Investigating Dynamic Changes in Morphology and Chemical State of Copper Catalysts for the Electrochemical Reduction of CO_2

Dissertation
to obtain the academic degree
Doctor rerum naturalium
(Dr. rer. nat.)

Submitted to the Faculty of Chemistry and Biochemistry
of the Ruhr-University Bochum

by
Philipp Grosse
born in Witten

MAX PLANCK GESELLSCHAFT

RUB

Berlin 2021

Die vorliegende Arbeit wurde im Zeitraum vom 01. März 2017 bis 01. November 2018 am Lehrstuhl für Experimentalphysik IV der Ruhr-Universität Bochum und vom 01. November 2018 bis 25. Februar 2021 in der Abteilung Grenzflächenwissenschaften des Fritz Haber Instituts der Max-Planck-Gesellschaft angefertigt.

Supervised by Prof. Dr. Beatriz Roldán Cuenya
2nd reviewer: Prof. Dr. Kristina Tschulik
3rd reviewer: Prof. Dr. Martin Muhler

Acknowledgements

I would like to thank everybody from the department of interface science involved in the development of this thesis. First of all, I thank Prof. Dr. Beatriz Roldan for supervising this work. As head of the ISC Department at the FHI, Beatriz Roldan has been very supportive and encouraging, and I thank her for nurturing a pleasant and fruitful work environment. Furthermore, I want to thank her for the invaluable advice, continuous support, and patience during my PhD study. Her immense knowledge and plentiful experience have triggered the ideas for the publications that this doctoral thesis is based on and with it she guided me throughout my academic research. I am very grateful to her for the attentively reading of my thesis and her helpful suggestions for corrections.

My special gratitude goes to Dr. See Wee Chee for being a particularly supportive mentor, never hesitating to assist and encourage the ongoing process. I thank him and the members of his liquid phase electron microscopy group deeply for cultivating the exceptionally cordial and positive working atmosphere and coherence that we had. Also to him goes a special thanks for reading the thesis and suggesting fruitful corrections.

Furthermore, I thank all members of the Interface Science Department for the pleasant work environment, for the helpful discussions, and for the generally cheerful mood. I highly appreciate the pleasant mixture of responsibility and lively work environment, combining high productivity with interludes of coffee or tea breaks with fruitful discussions. Another thanks goes to the Fritz Haber Institute for making this work possible in the first place, and for being such a marvelous place of work where I found a warm welcome and quickly felt at home. I also want to thank the technical staff for setting up and enabling the usage of the laboratories, enduringly helping even until very late in the evening when needed.

Furthermore, I want to deeply thank my parents, my sister, and my friends for staying close and supportive, always believing in me and my choice to pursue a doctorate. This work would not have been possible without them, granting me the privilege of their unfailing encouragement, inspiring soulfulness, and unlimited support.

Affidavit

I, *Philipp Grosse, born at 23.09.1990 in Witten*, hereby confirm that

(1) my thesis entitled

 Investigating Dynamic Changes in Morphology and Chemical State of Copper Catalysts for the Electrochemical Reduction of CO_2
 done at the Interface Science Department chair under the supervision of Prof. Dr. Beatriz Roldán Cuenya is the result of my own work;

(2) I did not receive any help or support from commercial consultants;

(3) All sources and / or materials applied are listed and specified in the thesis;

(4) This thesis has not yet been submitted as part of another examination process neither in identical nor in similar form.

I am aware that giving a false affidavit will have legal consequences.

Bochum, 12.04.2021

(Signature)

List of Publications

Articles

1. **Investigation of the plasma-assisted Oxidation of Cu**$\{1\,0\,0\}$ **and Cu**$\{1\,1\,1\}$
   S Kunze, L C Tănase, M Prieto, P Grosse, F Scholten, L Caldas, D van Vörden, T Schmidt, B Roldan Cuenya, **2021**, (to be submitted to Chemical Science)

2. **Steering the Structure and Selectivtiy of Electrocatalyst by Potential Pulses**
   J Timoshenko, A Bergmann, C Rettenmaier, A Herzog, R Arán-Ais, H S Jeon, F T Haase, U Hejral, P Grosse, T Jing, [...], O Magnussen, B Roldan Cuenya, **2021**, (to be submitted to Nature)

3. **Dynamic Re-structuring of Cubic Copper Catalysts during CO$_2$ Electroreduction and its Impact on Catalytic Selectivity**
   P Grosse, A Yoon, C Rettenmaier, A Herzog, S W Chee, B Roldan Cuenya, (under review in Nature Communications)

4. **Dynamic Imaging of Nanostructures in an Electrolyte with a Scanning Electron Microscope.**
   A Yoon, A Herzog, P Grosse, DH Alsem, SW Chee, B Roldan Cuenya, Microscopy and Microanalysis, 27.1 **2021** 121-128.

5. **Growth Dynamics and Processes Governing the Stability of Electrodeposited Size-Controlled Cubic Cu Catalysts**
   P Grosse, A Yoon, C Rettenmaier, SW Chee, B Roldan Cuenya, The Journal of Physical Chemistry C, **2020**, 124(49), 26908-26915.

6. *Operando* **NRIXS and XAFS Investigation of Segregation Phenomena in Fe-Cu and Fe-Ag Nanoparticle Catalysts during CO2 Electroreduction.**
   S Kunze, P Grosse, M T Bernal Lopez, I Sinev, I Zegkinoglou, H Mistry, J Timoshenko, M Y Hu, J Zhao, E E Alp, S W Chee, B Roldan Cuenya, Angewandte Chemie, **2020**, 132(50), 22856-22863

7. **Imaging electrochemically synthesized Cu$_2$O cubes and their morphological evolution under conditions relevant to CO$_2$ electroreduction**
   R M Arán-Ais, R Rizo, P Grosse, G Algara-Siller, K Dembélé, M Plodinec, T Lunkenbein, S W Chee, B Roldan Cuenya Nature Communications **2020** 11(1), 1-8

8. **Dynamic Changes in the Structure, Chemical State and Catalytic Selectivity of Cu Nanocubes during CO$_2$ electroreduction: Size and Support Effects.**

P Grosse, D Gao, F Scholten, I Sinev, H Mistry, B Roldan Cuenya Angewandte Chemie (International ed. in English), **2018**, 57(21), pp.6192-6197.

9. **Plasma-activated copper nanocube catalysts for efficient carbon dioxide electroreduction to hydrocarbons and alcohols**
D Gao, I Zegkinoglou, N J Divins, F Scholten, I Sinev, P Grosse, B Roldan Cuenya, ACS nano **2017** 11 (5), 4825-4831

Patent

1. **"Gößen- und formdefinierte lösungsmittel gesteuerte Nano-Strukturierung von Oberflächen und Nanopartikel-Synthese"**
P Grosse, D Gao, B Roldan Cuenya, **DE102017011341A1** (Application pending)

List of Constants

Avogadro constant (N_a) $= 6.022\,140\,857 \times 10^{23}\,\mathrm{mol}^{-1}$: Number of constituent particles contained in the amount of substance given by one mole

Elementary charge (e) $= 1.602\,176\,620\,8 \times 10^{-19}\,\mathrm{C}$: electric charge of a single electron

Faraday constant (F) $= 96\,485.332\,12\,\mathrm{C\,mol}^{-1}$: a physical constant describing magnitude (as absolute value) of electric charge per mole of electrons

Gas constant (R) $= 8.314\,462\,618\,153\,24\,\mathrm{J\,K}^{-1}\,\mathrm{mol}^{-1}$: a physical constant similar to the Boltzmann konstant, expressed in units of energy per temperatur increment per mole

Planck constant $(\hbar)$ $= 1.054\,571\,800 \times 10^{-34}\,\mathrm{J\,s}$: a physical constant describing the quantum of action

List of Acronyms

Abstract

The electrochemical reduction of carbon dioxide (CO_2RR) is a promising enabling technology for chemical energy conversion and storage, where the premise is to recycle industrial CO_2 emissions for the synthesis of useful chemical and fuels. Among the different metals that can be used as catalysts for this reaction, copper (Cu) is the only one known to facilitate the formation of hydrocarbons in relevant quantities. Specifically, the $\{1\,0\,0\}$ crystal facet of Cu has been shown to have superior selectivity for C2-C3 hydrocarbons. However, it is yet to be shown how one can translate such fundamental understanding obtained from bulk single crystals towards the design of high performance and stable catalysts that can be used on an industrial scale remains an active area of research. In this work, I explore electro-deposition as a scalable method to create cube-shaped Cu_2O catalysts and study how the properties of these catalysts are controlled by different synthesis parameters, such as size and support materials, and their transformations under reaction conditions.

This thesis is organized into ten chapters based on both published and submitted/in preparation papers. Chapters 1 to 3 delve into the motivation, background and methods used over the course of this work and the experimental work starts from Chapter 4 onwards. Chapter 4 explores the synthesis parameters that govern the electrodeposition of Cu cubes with $\{1\,0\,0\}$ facets on glassy carbon substrates and their influence on the size, shape, coverage, and uniformity of the cubes. Chapters 5 to 7 focus more on the changes that occur in the structure and elemental composition of these electrodeposited Cu_2O structures after (1) their introduction into an electrolyte, (2) the application of a reductive potential and (3) how these changes correlate to catalyst selectivity. In particular, the working structure of these model catalysts was investigated using an array of *in situ* and *operando* methods. Chapter 5 describes results where the chemical state of copper was probed on the surface by quasi *in situ* X-ray photoelectron spectroscopy (XPS) and in the bulk via X-ray absorption fine-structure spectroscopy (XAFS), whereas changes in morphology were tracked by electrochemical atomic force microscopy (EC-AFM). It was also clear from these studies that significant changes in the catalyst morphology already occur during the initial application of the potential, which could not be tracked with the limited temporal resolution of atomic force microscopy, and these changes had profound implications on the catalytic properties of the cubes.

Chapters 6 and 7 focus on efforts to use liquid cell electrochemical transmission electron microscopy (EC-TEM) to follow these changes in the initial seconds and minutes at higher temporal resolution. First, it was shown in Chapter 6 that it was possibly to synthesize and study the catalysts with the microfabricated reaction cells used in EC-TEM. More importantly, it was demonstrated that the dynamical morphology of these catalysts under operating conditions were extraordinarily complex. Chapter 7 discusses submitted work aimed at correlating the working morphology of differently-sized Cu_2O cubes with their observed changes in time-dependent product distribution.

Chapters 8 and 9 cover research that is still in preparation. In chapter 8, the cubes are electrochemically deposited on a variety of support materials and benchmarked for CO_2RR selectivity. A further discussion on the influence of the support material based on electrochemical characterization is presented. In chapter 9, ways to change the catalyst properties *ex situ* by plasma treatment and a beneficial influence of the plasma for the production of C2+ products are discussed. Finally, in Chapter 10, the future outlook of this work is discussed.

Contents

1 Introduction and Motivation

Since the beginning of the industrial revolution, humanity's energy consumption has increased exponentially. More than two-hundred years of development later, at the peak of fossil fuel consumption, carbon oxidation still stands at the center of our energy infrastructure.

However, the increase in the concentration of carbon dioxide (CO_2) in Earth's atmosphere has severe implications for our climate. It is estimated that the burning of Earth's fossil fuel reserves will increase the global temperature on average between 6.4 °C-9.5 °C and in the Arctic even up to 19.5 °C.[1] Furthermore, at our current rate of consumption, fossil fuels like crude oil, gas, and coal are estimated to run out by the end of this century. Some models predict coal being the only available resource as early as 2042[2], others estimate it almost a century later at 2126[3]. This has other important consequences, because the majority of today's chemical industry relies on some form of hydrocarbons as a feed stock - from drug production to plastics and polymers. Therefore, alternatives that can recycle emitted CO_2 by converting it into long-term chemical energy storage media and raw materials for the chemical industry are being actively pursued by the scientific community. The goal here is to make it more sustainable and economically viable by re-introducing the oxidized carbon species in the form of valuable chemicals and fuels, while powering the process with renewable energy in a manner analogous to photosynthesis.

In 1890, Mond, Langer, and Quincke discovered the formation of volatile nickel tetracarbonyl ($Ni(CO)_4$) by reacting nickel powder in CO atmosphere at 100 °C as well as the analogous iron reaction. This caught a lot of attention and sparked great interest in a lot of scientists at the time. One of which was Paul Sabatier, who subsequently tried to bind other unsaturated gaseous molecules to various metals. During these experiments Sabatier and his coworker Senderens discovered that it is possible to hydrogenate gaseous organic molecules over metal catalysts.[4,5] The catalytic hydrogenation of CO to methane, in particular, attracted enormous interest in industry and the scientific community and ultimately lead to his Nobel prize in chemistry in 1912.

Based on Sabatier and Senderens work, a commercially viable application was developed by Franz Fischer and Hans Tropsch in 1925.[6] This reaction named Fischer-Tropsch synthesis is able to convert CO into hydrocarbons over metal catalysts at typical temperatures of 150 °C-300 °C and high pressures. To this day, it remains an extremely important process in the chemical industry. It has also inspired research looking at ways to start the direct conversion to synthetic fuels from CO_2 instead of CO.[7,8]

One promising approach is the electrochemical conversion of CO_2. The execution of such a reaction turns out to be extremely challenging. The formation enthalpy of CO_2 ($-393\,\mathrm{kJ\,mol^{-1}}$)[9] is close to twice that of water ($-285\,\mathrm{kJ\,mol^{-1}}$)[10], meaning that the energetic costs of reversing carbon oxidation will be similarly higher than the alternative water splitting reactions. The question here

is if the reaction pathway can be made more favorable through the discovery of more selective catalysts.

The major breakthrough on the field of CO_2 reduction was made by Yoshio Hori and coworkers in 1985[11], who were working on a different approach to thermocatalytic CO_2 hydration. Hori reported the electrocatalytic reduction directly from CO_2 to methane in relevant amounts and high current densities in inorganic aqueous electrolytes for the first time. The attractiveness of this reaction lies in the fact that it works at ambient temperature and pressure and uses CO_2 directly as a feedstock. However, it also suffers from drawbacks such as low product selectivity and a low energy efficiency due to the required high overpotentials.[12–14] Among the potential catalyst materials, Cu has shown superior catalytic selectivity for hydrocarbons and alcohols due to its moderate CO binding energy.[15] Up until today, the field is still trying to develop more selective catalysts that can work at high currents and low overpotentials, with the primary strategy being targeted nanoscale structuring of the metal catalysts to improve their surface area-to-volume ratios and to tailor the active sites on their surfaces.

2 Theoretical Background

2.1 The Electrochemical Reduction of CO_2

The electroreduction of carbon dioxide (CO_2RR) in inorganic aqueous electrolytes was already intensively investigated for over three decades, but it is still a contentious topic. An industrially applicable catalyst with high activity and selectivity has yet to be developed. In 1989, Hori, Murata & Takahashi reported about the efficiency and potential-dependent selectivity of Cu catalysts.[16] In comparison to other catalysts that only produce CO, hydrogen, or formate, Cu catalysts generate a broad variety of products; the most common products are summarized in table 1. Here, the

Table 1: Liquid and gaseous products of the electroreduction of CO_2 with the number of electrons associated to the different reaction pathway.[17]

Product	Chemical state	Associated electrons
CH_4	gaseous	8
C_2H_4	gaseous	12
C_2H_6	gaseous	14
CO	gaseous	2
H_2	gaseous	2
HCOOH	liquid	2
MeOH	liquid	6
EtOH	liquid	12
1-PrOH	liquid	18

desired products are C_2H_4 and C_2H_6 as feedstock for the chemical industry and CH_4 and EtOH for fuel. The higher the carbon content in the products, the higher their value for the chemical industry. However, it also means that the reaction involves more than one electron associated with the conversion. This complex reaction pathway with multiple electron transfer makes it difficult to tune the selectivity of a catalyst and specifically target certain products.

2.2 Influence of Surface Facets on CO_2 Reduction

It is generally accepted that the binding distance and strength of adsorbed CO_2 molecules on Cu influences the product selectivity. Thus, different crystalline orientations are expected to produce different product selectivities. On this basis, numerous studies have been conducted on single crystal model systems.

2.2.1 The Influence of Facets on Product Distribution

The pioneering work on single crystals of different crystal orientations has been conducted by Hori et al. A selection of the most common low index examples Cu{100}, Cu{110}, and Cu{111} after an electropolishing treatment are presented in Table 2 with their respective Faradaic efficiencys (FE(%)) at $5\,\mathrm{mA\,cm^{-2}}$ in CO_2 saturated $0.1\,\mathrm{M}$ $KHCO_3$ (at 25 °C).Since then, the electrochemical analysis and benchmarking of the single crystal facets has been verified with different electrochemical methods like linear sweep voltammetry (LSV)[18–23] and chronoamperometry (CA)[18,24,25] as well as characterization tools, often in conjunction with *in situ* product analysis like differential electrochemical mass spectrometry (DEMS)[22,26,27].

Table 2: Faradic efficiency of different faceted Cu single crystals after an electropolishing treatment studied by Hori et al.[19,28]

Crystal orientation	Potential V_{RHE}	Faradaic Efficiency in %						
		H_2	CO	CH_4	C_2H_4	$HCOO^-$	Aldeh.	Alcohols
{100}	−1.0 V	6.8	0.9	30.4	40.4	3.0	4.4	12.0
{110}	−1.15 V	18.8	0	49.5	15.1	6.6	6.6	7.4
{111}	−1.15 V	16.3	6.4	46.3	8.3	11.5	11.5	3.3

According to the studies by Hori et al., Cu{100} is the crystal orientation with the highest faradaic efficiency for ethylene (table 2)[18–23], whilst methane is the most commonly formed product on the other two crystalline orientations Cu{110} and Cu{111} according to studies by Frese et al.[29] This is only true as long as mass limitations do not occur, which typically starts to influence the reaction around −1.1 to −1.2 V_{RHE} for morphologically flat catalysts[22,30,31]. Furthermore, the presence, amount, and faceting of atomic steps, step bunches, and defects on the surface can have a drastic effect on the product distribution for CO_2RR.[32,33] This has been initially shown by Hori et al.[20] and was later confirmed by others[25,34,35]. Most recently, active control over the amount of defects and *in situ* generation of morphological motifs has been utilized in pulsed CO_2 electroreduction to enhance the product selectivity of C_{2+} hydrocarbons and alcohols.[36]
However, these studies are generally done on electropolished copper single crystals that have been exposed to air. Moreover, due to oxidation and the generally high mobility of Cu atoms at room temperature, the assumption of a ultra high vacuum (UHV) clean and flat crystal surface is not a valid representation of the single crystal surfaces studied by Hori and others and it is not clear, if these findings translate to the particular catalysts used in industry. Considering the influence of steps and defects that form, electropolished surfaces are hardly comparable to a flat atomically ordered single crystal under reaction conditions. Indeed, it has been shown by Simon et al.[37] that the surface of UHV cleaned crystals cycled under CO_2RR conditions change drastically. With increasing negative potentials, the amount of undercoordinated Cu sites increases, indicating complex relationship and dynamic interplay between morphology, structure, defect density depending on the potential. Hence, the need for advanced *operando* techniques to investigate these changes.

2.2.2 The Influence of Facets on Activity

In terms of activity, strong differences have been predicted depending on the crystalline facet according to theoretical calculations[38]. Cu{1 0 0} has a lower CO dimerization barrier than Cu{1 1 1}, which leads to a higher activity in addition to selectivity changes. A few studies conducted under mass transport limitations also suggest deviations from the theoretically expected differences in activity under such conditions[20,22,25]. The cause for this is presumed to be the formation and increased density of steps, grain-boundaries, and defects.

Transferring this knowledge to the discovery of new catalysts is by no means a trivial task. Single crystals are not viable for industrial applications and thus, nanostructured catalysts with selective terminated facets and high surface area-to-volume ratio are the most promising approach to produce well defined but also active catalysts.

2.2.3 Experimental Implications

In the previous sections it was mentioned that the restructuring of Cu single crystal facets plays a big role on selectivity and activity. However, the dynamic nature of the Cu surface structure-property makes studies extremely challenging and the exact pathways of CO_2 reduction towards C_{2+} products remain elusive. For example, many different surface morphologies have been reported in KOH[22,23,39–44], which might originate from irreversible reconstructions due to oxidation, as it has been reported for platinum[45,46]. The studies by Hori et al. relied on cyclic voltammetry characterization of the surface structure. The first *in situ* probing of Cu surfaces was from Kim et al.[47] who used *in situ* electrochemical STM (EC STM) techniques to measure Cu{1 0 0} single crystals in 0.1 M KOH at −0.5 V_{RHE}. Their results showed the significant defect formation and changes in the surface morphology. The surface reconstructions observed by *in situ* EC STM also appeared in the absence of CO_2 or CO, indicating that they are not a direct consequence of the reaction[27,40,47–49]. Soriaga et al. also showed the formation of Cu{1 1 1} facets on a polycrystalline copper foil after 30 min at −0.5 V_{RHE} in 0.1 M $KHCO_3$ that subsequently transformed into Cu{1 0 0} facets after another 30 min[27,49]. This emphasizes the highly dynamic nature of Cu surfaces. Scott et al.[50] further used *operando* grazing incidence X-ray diffraction (GIXRD) to identify these transformations.

2.3 The Search for Intermediates to Elucidate the CO_2RR Mechanism

Although the mechanism of CO_2RR is not yet fully understood and appeared to be strongly dependent on the catalyst material selected, a number of reaction intermediates were already postulated on Cu surfaces, giving insight into the different pathways leading to the respective products.

2.3.1 The 1st Step: CO as an Intermediate

The first key intermediate that has been identified was CO[16,51–54]. Two distinctive pathways have been shown for the initial 2e$^-$ CO_2 reduction step. Depending on the binding mode, either a

(terminal) formation of formate ($HCOO^-$) or the intermediate CO forms, which can react further to C_1-C_3 products. Independent studies on CO reduction have shown that a similar product distribution as for CO_2 reduction can be found[52,55,56], confirming the role of CO as a key intermediate.

Experimental evidence for the existence of surface bound (CO^*) has also been provided by spectroscopic techniques[57–63] and mass spectrometry based techniques like DEMS.[26,36] The subsequent direction of the reaction varies, depending strongly on the catalyst. In particular, the binding strength of CO plays a crucial role in determining the subsequent pathway. If CO binds strongly, it reduces fully to elemental carbon and poisons the catalytic sites. On the other hand, if CO binds too weakly it desorbs before it reacts to yield the desired products. Thus, it is important, to find a good balance between these two extremes following the Sabatier principle[64]. Figure 2.1 shows this graphically by plotting e.g. the CO binding energy (G_{CO^*}) against the current density (i) in a volcano plot[56]. On the extremes, metals like Ni, Pt, or Pd produce mainly H_2 and very little CO, whilst on the other end transition metals like Au and Ag produce mainly CO.
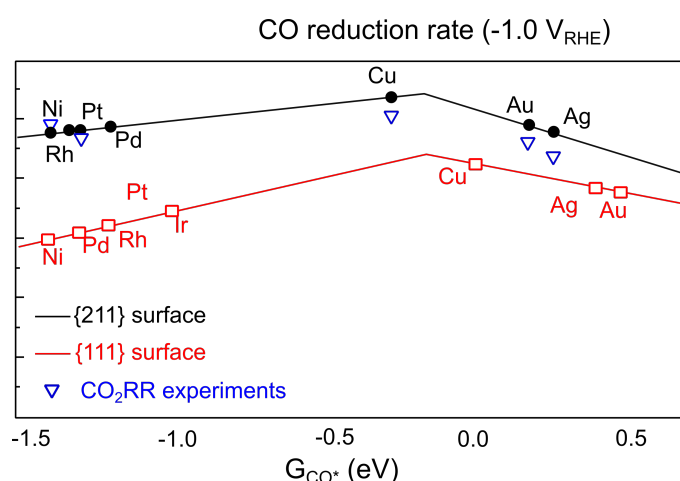
Figure 2.1: Activity volcano plot of the CO binding energy versus the current density at $-1.0\,V_{RHE}$ for a selection of catalyst materials simulated by microkinetic modelling on $\{2\,1\,1\}$ and $\{1\,1\,1\}$ surfaces. Redrawn from Kuhl et al.[65]

In addition, it has been shown experimentally that specifically on Cu, the binding of CO can suppress the parasitic hydrogen evolution (side) reaction (HER) by changing the binding energy or blocking active sites.[15,16,66,67]

2.3.2   Reduction of Oxygenated C_1 and C_2 Species as a Proxy to Determine Pathways

After the initial reaction step from CO_2 to CO, up to 16 possible products have been identified[30]. Among these are hydrocarbons, aldehydes, alcohols, ketons, and carboxylic acids. A schematic overview of potential pathways is displayed in Figure 2.2 based on the discussed observations. A few observations regarding the mechanism have been empirically made by directly reducing specific products.
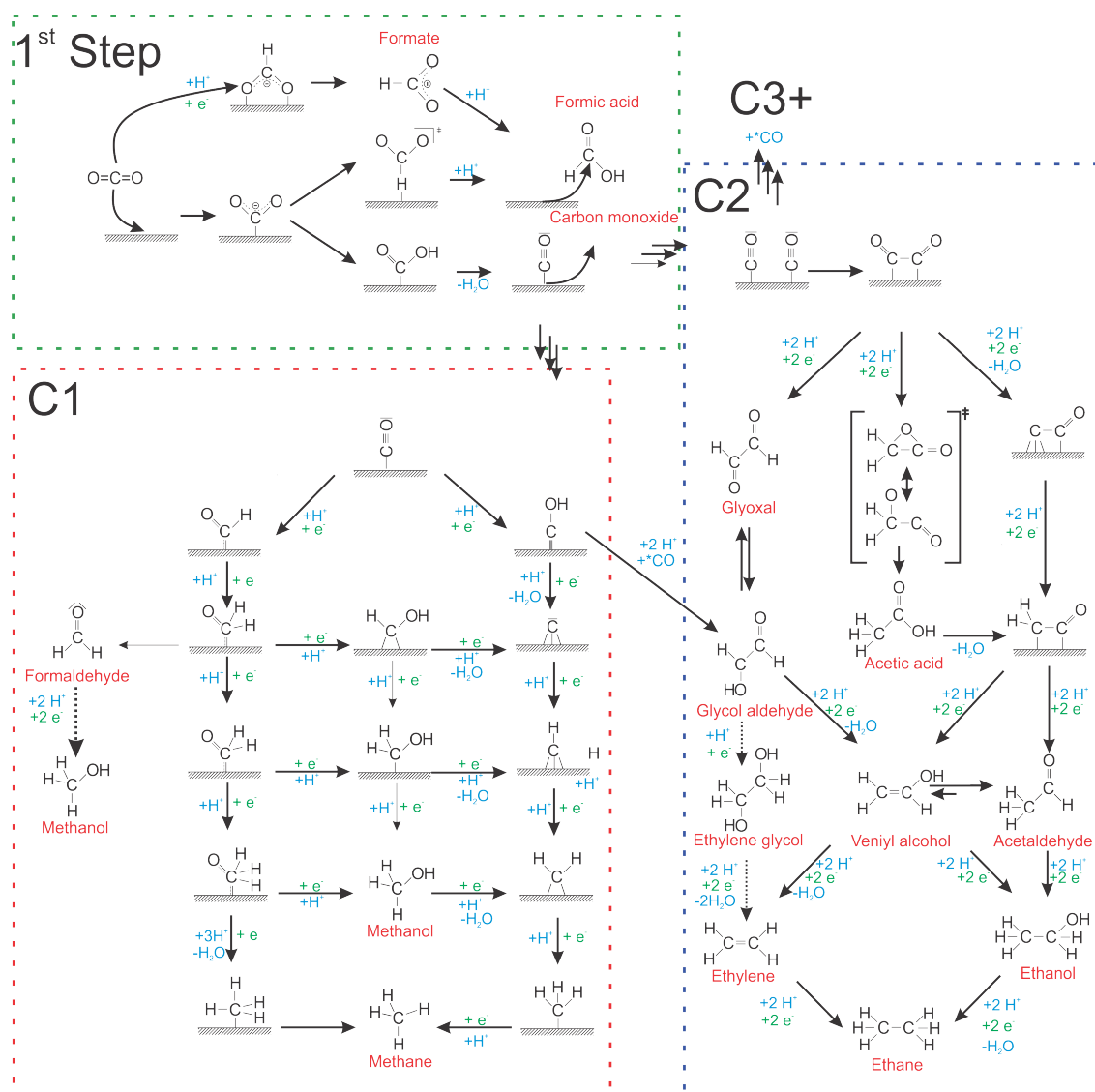
Figure 2.2: An overview of the potential pathways for the CO_2RR towards C1 and C2 productbased on the works discussed in this chapter. Dotted arrows indicate possible pathways, that have been shown as unlikely by the experiments discussed above. This schematic is by no means complete and does not consider kinetic energetic barriers.

1. **Formate/formic acid:** As discussed before, formate is a terminal step in the CO_2RR. Although some studies found methane by reducing formic acid directly, only small amounts were found and the required overpotentials were far higher than typical CO_2RR potentials[16,51,68].

2. **Formaldehyde:** Reducing formaldehyde yields methanol as the primary product and small amounts of methane[51,52,68–70]. Intriguingly, methanol is a product which is only sparsely found in conventional CO_2RR (in aqueous electrolyte, at atmospheric pressure, and ambient temperature). It leads to the question if methanol is a product resulting from the further reduction of formaldehyde. This would make it another intermediate of CO_2RR.

3. **Glyoxal/glycol aldehyde:** Acetaldehyde and ethanol can be found by reducing glyoxal or glycol aldehyde[70,71]. The absence of ethylene as a product indicates, that this is an

intermediate in the pathway of forming C2 product that is different from the ethylene forming route.

4. **Ethylene glycol/oxalic acid:** The reduction of ethylene glycol or oxalic acid yields no typical CO_2RR products, thus it is unlikely to be an intermediate but rather a terminal product instead[70].

These experiments give valuable marker for building a reaction mechanism. Another important observation is the high amount of carbonyl and hydroxyl moieties that indicate a relatively early C-C coupling step[30]. Due to this reason, it is assumed that enol-like adsorbed species such as enediol or enediolate are the intermediates towards multicarbon products[30,70].

2.4 Electrolyte Effects

One approach is to modify the electrolyte that is used. Usually, a buffer-solution of potassium bicarbonate ($KHCO_3$) is used in a concentration ranging from 0.1-0.5 M, which is constantly saturated by CO_2. Kas et al. showed that the Faradaic efficiency heavily changes depending on the concentration of the electrolyte[72,73]. At lower concentrations (0.1-0.2 M), the Faradaic efficiency (FE(%)) is clearly shifted towards ethylene, with a FE(%) of about 35%. The amount of methane and carbon monoxide produced by their Cu nanoparticles does not exceed 2.5%. Increasing the concentration of $KHCO_3$ results in a shift towards methane, with a FE(%) about 22% whilst the overall FE reduces.

2.4.1 pH Effects

One explanation for the influence of the electrolyte on the product selectivity lies in the effect of the pH. Different mechanisms were proposed with a pH dependent formation of methane and methanol, and a pH independent formation of ethylene[52,74,75]. The methane production was determined to be the thermodynamically favored product[15] whilst methanol is the kinetically favored product[76]. To understand this, it is important to discuss the pH dependency of CO_2-related reactions in aqueous electrolytes. CO_2 forms carbonate (CO_3^{2-}) or it's conjugated acid bicarbonate (HCO_3^-) when introduced in an alkaline liquid environment. This limits the use of electrolyte solutions to the acidic or neutral pH range with buffers like potassium bicarbonate to keep the pH stable (pH 6.2). On the other hand, highly acidic environments are unsuitable due to the intrinsic buffering capabilities of CO_2. A basic overview of the reactions taking place when purging CO_2 in acidic or neutral aqueous environments are given in the chemical equation 1.

$$CO_{2(g)} \rightleftharpoons CO_{2(aq)}$$
$$CO_{2(aq)} + H_2O \rightleftharpoons H_2CO_3$$
$$CO_{2(aq)} + H_2O \rightleftharpoons HCO_3^- + H^+ \qquad (1)$$
$$H_2CO_3 \rightleftharpoons HCO_3^- + H^+$$
$$HCO_3^- \rightleftharpoons CO_3^{2-} + H^+$$
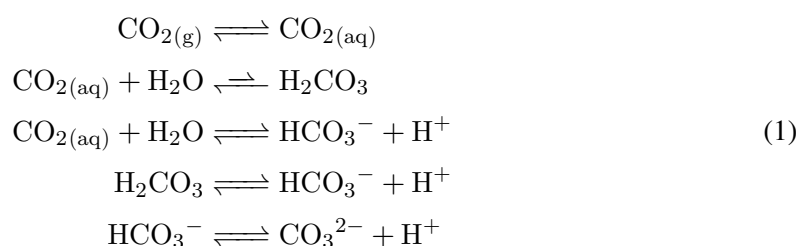
Hori et al. investigated the pH dependency on the formation of methane and ethylene and found them to be directly (or indirectly) linearly correlated[52]. He found that the logarithm of the partial current density of ethylene is proportional to the applied potential when changing the pH. For methane, a linear relation between these two could only be found by additionally adding the pH to the logarithm of the partial current density of methane, thus indicating a relevance of proton activity in this reaction[52]. These observations led him to propose a branching of the respective reaction pathways at an early stage, which has been later corroborated by single crystal studies from Koper et al.[34,35,74] However a second pathway was proposed within the scope of these studies dependent on pH, surface structure, and applied potential.

The pH can also indirectly influence the selectivity of a catalyst by impacting the parasitic hydrogen evolution reaction. At neutral to alkaline pH, the concentration of hydronium ions (H_3O^+) is low and thus the reaction is dominated by water reduction instead of proton reduction. Goddard et al. also found that the surface of noble metals tends to repel water at negative voltages causing enhanced hydrogen binding.[77] In the typical CO_2RR conditions used in this work, the pH is close to neutral, thus we expect it to be competing primarily with water reduction based HER, which is kinetically slower compared to proton reduction based HER.[67] This is relevant for CO_2RR, because a large amount of protons (produced at the anode by oxygen evolution reaction OER) is required for the formation of hydrocarbons. The competing HER does not significantly suppress CO_2 reduction, but the selectivity for hydrocarbons reduces due to the stronger driving force towards proton reduction. A good balance of these pH dependent effects is needed to get the best selectivity for C_{2+} products.

2.4.2 Cation Effects

The cation of the bicarbonate buffer can also influence the selectivity in different ways. Hori and Murata discovered a cation size dependent effect, where they observed an increase in C_{2+} products with the use of larger cations.[78] Although these observations have been corroborated by independent studies[71,79–82], the explanation is still debated. According to Hori and Murata, the large cations shift the outer Helmholtz plane potential, causing less hydration (e.g. they block each other less) which in return allows a higher quantity of adsorbed cations. This effect has been rationalized by Frumkin's adsorption theory for the adsorption kinetics at metal electrode interfaces.[83] However, this might not be applicable to the larger negative overpotentials required for CO_2RR, where the cations do not typically adsorb on the interface. Instead it remains partially solvated according to Strmcnik et al.[84,85], although this has yet to be verified experimentally.

A different approach to rationalize the effect of cation size is to consider the electrostatic influence on the Helmholtz layers. It has been proposed that the presence of larger cations at the interface can lower the acid dissociation (pk_a) and thus balances out the concentration polarization that induces the increase in local pH.[80] This, in turn, can increase the CO_2 concentration close to the interface by opening up blocked adsorption sites. Furthermore, the changes in the electrostatic field caused by the presence of larger cations can decrease the CO_2 adsorption. In this case, experimental evidence has been provided in the form of attenuated total reflection Fourier-transform infrared spectroscopy (ATR FTIR). An increase in cation size causes the $C{\equiv}O$ stretch frequency to shift

to lower energies, indicating a change in the interfacial electrostatic field.[86] Additional insights into the catalytic implications from the presence of alkali-metal cations have been investigated by Gao et al.[87] Here, the increase in cation size led to a higher production of C_{2+} products on a highly polarized interface of an O_2-plasma treated Cu foil. In this study, in addition to the cation driven electrostatic effects, the presence of Cu^+ on the surface accentuated the promoting effect further from the electrode side of the interface.

2.4.3 Anion Effects

Other anions like chloride (Cl^-), perchlorate ($HClO_4^-$), and sulfate (SO_4^{2-}) were also previously investigated[16,88]. It was found that these anions, unlike bicarbonate, buffer the electrolyte solution and will slowly lead to an increase in hydroxide ions (OH^-) from the CO_2 electroreduction, causing a shift induced by changes of the pH[72,89]. Thus, anion effects are also generally considered to be indirect pH effects. Ongoing discussions also postulate an involvement of the (bi-)carbonate as a potential source of CO_2, which in return would result in less availability in non-carbonate containing electrolytes[90,91].

Besides the electrostatic effects and pH influences discussed so far, the presence of halide anions can also have an effect on the morphology. Later in this work, the influence of chloride on the nanostructuring of copper is demonstrated for the electrodeposition of cubic particles. Besides chloride, other halides also result in structural modifications by targeting anion-specific adsorption sites on copper, leading to growth on the unoccupied sites/facets[92–99].

2.4.4 The Potential

The applied potential is a determining factor that controls the Faradaic efficiency of the products. Hori et al. measured the amount of products generated and their respective Faradaic efficiencies of a Cu electrode at multiple potential steps between -0.4 V and -1.1 V vs. reversible hydrogen electrode (RHE). The resulting plot can be seen in Figure 2.3. It can be seen, that at -1.1 V_{RHE}, the ethylene production is highest, while the production of other byproducts (except methane) diminishes. The next step would be to shift the potential closer to the theoretical potential for ethylene production, whilst simultaneously enhancing the selectivity. This might not be possible for a flat Cu-electrode, but instead, a modified catalyst with large surface area and roughness and a specific shape favouring the formation of the desired products would need to be found.
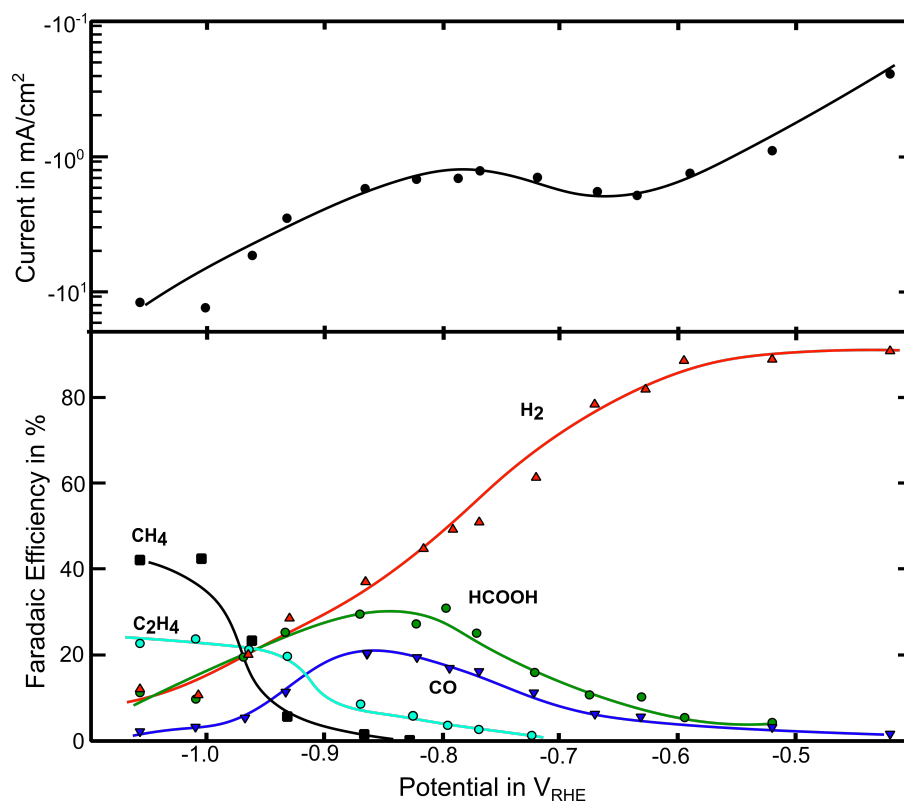
Figure 2.3: Current density and product yield as Faradaic efficiency of a polycrystalline Cu electrode at various onset potentials *versus* RHE. Data redrawn from[15].

2.5 Nanoparticles

Nanoparticles (NPs) by definition considers all supported (or unsupported) particles with an overall size of less then 100 nm in any direction. There have been many controversies over the years regarding the role of the NP structure on activity and/or selectivity. The rationale for nanostructuring materials for CO_2RR application lies in the possibility to tailor facets towards preferential orientations like e.g. Cu{1 0 0} on cubic particles, making them in theory ideal model catalysts. Furthermore, it opens the opportunity to control the number of coordinated sites on the surface in relation to bulk material used by tuning the size of the NPs.

2.5.1 Nanoparticle Size Effects

Nanoparticles with spherical shape as well as nanocubes show promising results in terms of catalytic performance[100–102]. As discussed in the previous sections, the {1 0 0} facets (on Cu-nanocubes) seem to be highly beneficial for the C-C coupling and thereby, favor the formation of higher carbon containing products like ethylene[92]. The reason behind these observations, however, is not as straightforward. The particle size heavily affects the coordination of surface atoms, which in turn leads to strained structures. This affects the electronic structure and hence the binding properties of CO_2 and the reaction intermediates. The strain can lead to a shift in the d-band that has strong implications for the reactivity[103–106]. However, it could lead to a modified stability of the structures, especially on the support interface or the improvement of one reaction step in exchange

11

for other reaction steps on the pathway to C_{2+} products[107–110]. The size dependent changes in selectivity and reactivity have been investigated by multiple groups[101,111–113], and these studies have found conflicting results. All of them also use different preparation methods, which can have an effect on the selectivity if for example synthesis-related residues are left on the NP surface. In the aforementioned studies, NPs smaller than 5 nm have shown an increased production rate for C_1 products, while C_{2+} products were enhanced for larger particles as shown in the studies by Reske et al.[111]. Manthiram et al. has synthesized 7 nm particles, that have shown strong agglomeration behavior after short times but still expressed an improved methane production[112]. Lastly, for cubic particles Loiudice et al. found an optimal size on 44 nm and proposed a size dependent face-to-edge ratio as the product determining factor[113]. All these studies, however show only a pristine state and a post mortem state of the catalyst. It is well known, that Cu, in the presence of CO_2/CO, is a highly dynamic system[114] where *operando* studies on the actual working morphology would be of immense value. Kim et al. demonstrated how closely packed 6 nm spherical particles transform into cubic particles that are highly selective for C_{2+} products[115]. Osowecki et al. has shown, that even without CO_2 a restructuring into cubes can occur via particle migration and coalescence[116]. However, with argon purged solutions, no individual crystalline grains were observed. Contrary to these findings, the opposite effect can also occur where larger Cu_2O particles with well defined facets (like cubes) split into smaller particles, which can affect the selectivity[117] towards C_{2+} products as shown in chapter 7. This again only highlights the complex interplay of factors that need to be accounted for to fully understand the size and shape effect on CO_2RR and the need for advances in imaging and spectroscopy during reaction.

2.5.2   Loading and Interparticle Distance

More complexity sets in, if we also consider interparticle distance (IP) and catalyst loading effects. Our group has investigated the change on catalytic activity and selectivity by different interparticle distances, where Mistry et al. prepared Cu nanoparticles of the same size with different interparticle distances[102]. A trend was observed, with smaller IP distance, for similarly-sized NPs, resulted in high selectivity for C_1-C_2 products versus CO and H_2.The origin of such trend is still unclear, but a complex interplay of local CO_2 depletion and pH effects must be accounted for. The aforementioned study by Kim et al.[115] also investigated different loading of nanoparticles, but with the focus of increased restructuring with higher loading which in turn changed the product selectivity.

2.5.3   Shape Effects

CO_2RR on faceted nanoparticles has been conducted by many groups to determine facet-dependent changes in selectivity. So far, Cu{1 0 0} has been shown to be the superior facet for Cu NPs, similar to the single crystal findings by Hori et al.[20,25,34,35,118] Wang et al. investigated the catalytic behavior of rhombic dodecahedral particles, which consist mainly of {1 1 0} facets. They found the decrease of CO selectivity and an enhanced selectivity for hydrocarbons[119]. According to Hori's single crystal study[21], an increase in oxygenates is also expected, however, no liquid products were provided in the study. It is important to note that the increase in number of corner sites as

compared to cubic particles could influence the activity due to the increase in undercoordinated sites.

2.5.4 Support Effect and Catalyst-Ionomer Interaction

In terms of support effect, less studies have been conducted and the ones that exist are challenging to compare. Supports such as nitrogen-doped high surface area carbon[120] or graphene (N-doped[121] and un-doped[120]) show an enhanced C_{2+} product selectivity. Furthermore, metallic supports like gold or silver lead to an enhanced C_{2+} product selectivity likely due to CO spillover or cascade effects, and a better support interface has been proposed as a reason for the effect[122,123].

2.6 Electrochemical Conditions

One of the key benefits of CO_2RR as a technology for sustainable chemical conversion is its ability to reduce CO_2 to hydrocarbons at ambient pressure and temperature. Nevertheless, there are some other factors that can be adjusted to improve selectivity and they will be discussed in the following sections.

2.6.1 Temperature

First of all, Henry's law states that the amount of dissolved gas in a liquid is proportional to the partial pressure of this gas above the liquid. However, if the temperature of the system changes, Henry's constant (H) changes as well. This correlation can be expressed by the van't Hoff equation (equation 2).

$$\frac{d \ln H}{d(1/T)} = \frac{-\Delta_{sol} H}{R}$$

$$R : \text{ideal gas constant}$$

$$T : \text{temperature}$$

(2)

This means that the concentration of dissolved CO_2 is increased at lower temperatures which can enhance CO_2RR. A number of studies have been conducted on the influence of temperature on CO_2RR[51,54,124–129], and an enhanced selectivity for methane at lower temperature was reported. In the same studies, the selectivity for HER was also strongly enhanced with increasing temperature, which could be a result of a lower CO_2 concentration in the electrolyte. Furthermore, temperature induced changes in (local) pH, CO adsorption strength, and ohmic resistance all lead to indirect temperature effects.

2.6.2 Pressure

As briefly stated in the previous section, the pressure of the system can have implications on CO_2RR by limiting or enhancing the concentration of CO_2 in the electrolyte. Thus, corresponding studies have observed an enhanced activity for CO_2RR with increasing pressure[72,125–130]. Though

not directly correlated, these studies can give insight on the importance of CO_2 concentration on the activity of catalysts, which could vary depending on the experimental setup.

2.7   Oxide and Confinement Effects

The role of oxygen and effects of confinement in larger three-dimensional catalyst structures are a topic of strong debates for many years in the field of CO_2RR. In this part, a brief overview of potential effects is given.

2.7.1   Role of Oxides in CO_2RR on Copper

The role of oxygen as an active participant in CO_2RR is one of the most controversially discussed topics. Oxides or interstitial oxygen are unlikely to exist for prolonged times under reaction conditions. Under the strongly reductive conditions in CO_2RR, lattice oxide is expected to be released, causing a strong multiplication of the electrochemical surface area (ECSA) by restructuring. Furthermore, this results in a rise of defects and undercoordination at the catalyst interface, which can have an influence on the selectivity. Plasma treatments can also result in an enhanced selectivity towards C_{2+} products. Our group has utilized oxygen- and other gas-plasmas to induce defects and to form thick oxide layers on copper films[131]. The plasma-treated samples show enhanced catalytic performance for CO_2RR. In the above mentioned study, the formation of defects alone was not sufficient to explain the enhanced Faradaic efficiency for C_{2+} products. However, the existence of oxide species on the interface during the reaction has been elusive to prove. More recently, the junction of metallic and oxidized Cu (on an atomic level) has shown potential for higher C_{2+} selectivity by asymetric CO coupling.[132] This indicates an involvement of oxides in the reaction process, which needs to be better studied by appropriate techniques like pulsed chronoamperometry to stabilize these oxides under reaction conditions.[36]

2.7.2   Oxide-Derived Copper

Oxide-derived copper catalysts prepared by anodic, thermal, or other oxidation techniques have also been studied by multiple groups[94,133–136]. The results of these studies, although interesting, are not consistent in terms of their selectivity changes. The amount of oxide, the degree of restructuring, and the dimensions of the resulting three-dimensional framework all differ, which makes a comparison of the results challenging. One important aspect to consider is how these structure alter the reaction kinetics. The observed changes can be a result from the increase of ECSA in junction with confinement, although the possibility of localized oxide species still exists. In general, the ECSA increase will result in a faster depletion of CO_2 due to the increased number of binding sites, and lead to enhances HER selectivity.

2.7.3   Confinement

The effect of confined spaces was studied by Yang et al. on templated nanopores[137]. They found that small pores of 30 nm diameter exhibited an enhanced selectivity for ethylene, although a

corresponding increase in the ECSA may be the reason for this increase. Moreover, deeper pores showed better selectivity for ethane (C_2H_6), which could indicate the involvement of re-adsorption processes in confined spaces. Scholten et al. also showed similar behavior from samples where gas products are confined under (polarized) oxygen-derived copper dendrites[138]. Besides re-adsorption, changes in the local pH are a factor to be considered in these confined spaces. The effect of confinement on catalysis has also been demonstrated for zeolites[139,140] and carbon nanotubes[141] with other catalytic systems.

3 Methods

3.1 *In situ* and *Operando* Microscopy

For the rational design of highly optimized catalysts, the structural correlations to their activity and stability need to be understood, especially if the structural properties change under reaction conditions. These changes can be reversible or irreversible, where the former will be impossible to identify from *ex situ* investigations[142,143]. As discussed in the previous chapter, the morphology plays a crucial role, and changes can occur under reaction conditions like sintering[144–148] and agglomeration[149], deactivation of the active sites[144,149–152], corrosion[149,153–155], as well as surface reconstruction[149,156–158] or segregation[159–161].

In situ and *operando* microscopy techniques are frequently used to elucidate such effects[162] and are extensively used throughout this work. The term *operando* describes here a more specific branch of *in situ* microscopy, where the microscopy data are collected with catalytic data in the same system and under reaction conditions to correlate structure and catalytic performance[163,164]. Each technique comes with its advantages and challenges, as discussed in the following sections. A short comparison of the characteristics of AFM to other commonly used microscopy techniques are listed in table 3.

Table 3: Comparison of AFM with SEM and TEM. Adapted from[165]

	AFM	SEM	TEM
Sample preparation	little or none	from little to significant	from little to significant
Resolution	0.1 nm	5 nm	0.1 nm
Relative cost	low	medium	high
Sample environment	any	vacuum/gas	vacuum
Depth of field	poor	good	poor
Sample type	conductive/insulating	conductive	conductive
Time per image	2-15 min	0.1-1 min	0.1-1 min
Maximum field of view	100 μm	1 mm	100 nm
Maximum sample size	unlimited	30 mm	2 mm
Measurements	3 dimensional	2 dimensional	2 dimensional

3.2   Atomic Force Microscopy

Scanning probe microscopy (SPM) was a breakthrough in the fields of microscopy and surface science when it was first invented. With SPM, it is possible to investigate surfaces and interfaces with very high accuracy and unprecedented resolution. In contrast, classical light microscopes that are limited by the Abbe diffraction limit. Nowadays, this limit can be bypassed by stimulated emission depletion (STED) microscopy and similar techniques[166], but SPM was the first technique to enable the analysis and manipulation of non-periodic structures, like surfaces and interfaces, on an atomic scale in real space. Additionally, SPM measures lateral as well as axial direction to the probe, resulting in a three dimensional representation of the investigated surface.

SPM can be further sub-divided into various techniques, for example scanning tunneling microscopy (STM)[167] and atomic force microscopy (AFM)[168], which are used in this work. Nonetheless, the basic principle is the same, differing only in the measured signal. SPM techniques, as the name suggests, always consist of a small and sharp tip which is called the "probe". This probe is brought into close proximity to the sample surface or interface (in the range of a few Å), allowing us to probe its interaction with the sample in a specific way. The z-direction movement is regulated by the feedback loop and ensures a constant measurement parameter (depending on the method). Furthermore, the movement is realized by an actuator in combination with this feedback loop, in the x-y-direction. The regulation is usually done by giving the feedback loop a setpoint value S that is then compared to the actual value I. If the difference between both values S and I is greater than the predefined threshold, the actuator adjusts the Z value until the actual value is again within the threshold. Additionally, the probe can be set to stay at a fixed position and the changes in the measurement parameter are recorded. The described setup for SPM then maps the three dimensional movement of the probe over a sample. The measurement parameter can also provide additional information about the sample like topography, force, and conductivity. One drawback of the technique is that the scanning of bigger areas (*i.e.* greater than $100\,\mu m$) would take a very long time due to the mechanical scanning of the whole surface.

Atomic force microscopy (AFM) has been widely established as a technique in surface science since it's development by Quate et al. in 1986[169,170]. It requires little sample preparation and can achieve up to atomic resolution, whilst being comparatively non-invasive. Thus, it is an ideal technique to study morphology. With the development of AFM for liquid environments in 1994[171–174] the study of catalytic systems opened new opportunities to better understand the morphology-related mechanisms in catalytic processes. Especially (electro-)chemical processes like growth, corrosion, and dissolution have contributed greatly to scientific advancements in the respective fields[175–179]. Also, highly dynamic Cu surfaces could be studied in liquid[180,181] and under CO_2RR conditions[37,182]. However, the technique comes with drawbacks as it has a temporal resolution in the range of a few minutes per frame, depending on the size of the sample. This makes it hard to capture fast processes like fragmentation or agglomeration, which could play a major role for the catalytic performance.

3.3 Electron Microscopy

A general description of an SEM, STM, and STEM setup is given in figure 13.1 and figure 13.2 in the appendix.

3.3.1 Electron Microscopy

Contrary to AFM, electron microscopy can achieve high spatial resolution while capturing images at frame rates of a few frames per second or better, albeit within confined liquid layers with thicknesses in the tens to hundreds of nanometres. The field of electron microscopy was started following the development of the electron lens in 1926 by Hans Busch[183] and the subsequent development of the first transmission electron microscope (TEM) by Ernst Ruska and Max Knoll in 1931[184]. Ruska was awarded the Nobel Price in Physics for this development. Modern TEMs with aberration-correction can attain sub-angstrom spatial resolution, depending on the acceleration voltage[185]. The group of Zworykin built the first scanning electron microscope (SEM) in 1942[186] for the purpose of observing the surface of samples, contributing to the first prototype of a commercial scanning electron microscope in 1965[187]. Although TEM and SEM are both electron-based microscopy techniques, they differ in how the images are formed and their requirements in terms of sample geometry.

In conventional TEM, a parallel electron beam illuminates the sample, and the electrons that are transmitted through the sample are collected with an electron camera to create an image. This typically limits the thickness of the samples to a few hundred nanometers. Alternatively, the electron beam can be focused to a fine sub-nanometer spot and scanned across the thin sample, also known as scanning transmission electron microscopy (STEM). The electrons scattered by the sample are then collected by different detector as a function of beam position, forming the image pixel by pixel. In terms of image formation mechanisms, the TEM image generally consists of phase and/or amplitude contrast, whereas STEM images are dependent on the detector used, with the most used being Z-contrast.

In SEM, the electron beam is also focused on a spot and scanned over the sample. Like STEM, the image formation mechanism also depends on the type of electrons detected, with the most common being the emitted secondary electrons, which are used to generate an image of the sample surface. In this case, the sample requirements are less stringent and even bulk samples can be imaged, provided they fit in to the microscope chamber. With thin samples, it is also possible to use a transmitted electron detector to form the image. Another significant advantage for the focused electron beam-based imaging approaches for concurrent chemical characterization. For example, it is possible to form compositional maps of the samples by collecting the characteristic X-rays (EDX) generated by electron-sample interactions.

The introduction of commercial environmental electron microscopes[188–190] and the development of microfabricated environmental (electrochemical) cells[191–194] lead to several advances in using electron microscopy to perform *in situ* observations. Williamson et al. reported first liquid cell for TEM in 2003[192]. It was followed by subsequent work by different groups such as Franks et

al.[191], Zheng et al.[195], and de Jonge et al.[196], which eventually led to the availability of liquid cell TEM holders from different manufacturers. Since then, the field of *in situ* TEM expanded rapidly evidenced by the large number of review papers in the 5 years[190,197–202]. Current *in situ* liquid cell holders are equipped with tubing that can be connected to fluid flow systems, and internal wiring that can be connected to electrodes that are deposited on the substrates and are thus capable of electrochemical measurements with an attached potentiostat.

The most significant concern for electrochemical TEM or SEM experiments are beam-induced artifacts due to the energetic electron interacting with the electrolyte and forming radiolytic radicals that interact with the sample[203]. The most basic interactions of the electron beam with water are displayed in figure 3.2. The current consensus in the field is to mitigate radiolytic effects by using the lowest possible electron flux and comparative control experiments where areas of the sample that are illuminated by the electron beam and those that are not illuminated are compared[32]. It should also be noted the need to maintain a reasonable liquid layer thicknesses for electrochemistry and low electron fluxes (i.e. poor signal-to noise ratios in the images) to minimize beam-induced effects, but both compromise the achievable spatial resolution to a nanometer or so even in the best microscopes[198,204].

3.3.2 Electron Microscopy in Liquid

Reactors for gas phase and liquid phase were developed alongside and resulted in the development of micro-electro-mechanical systems (MEMS), that combine electrical and mechanical components into a single chip. For electrochemistry, these chips combine reference, counter, and working electrode with microfluidic channels for the electrolyte and a silicon-nitride window for microscopy access. The chips are exchangeable in a dedicated TEM or SEM holder, which allows the easy exchange between individual measurements. The liquid volume can be controlled and adjusted by a spacer and the liquid channels are sealed with rubber o-rings from the vacuum. A basic schematic of the assembled liquid phase reactor is displayed in figure 3.1. In liquid phase EM, additional interactions of the electron beam with the liquid have to be considered. If electrons of high enough energy hit molecules, they can ionize them, introducing additional chemical reactions to the system. Possible pathways for the dissipation of energy on the example of ionization in water are displayed in figure 3.2
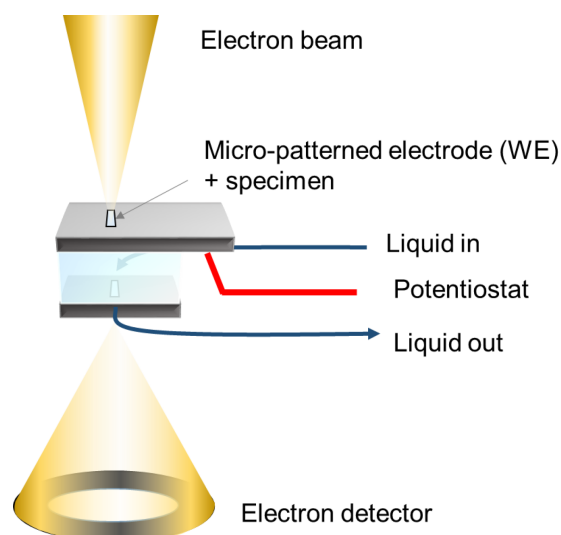
Figure 3.1: "**Schematic of the experimental geometry.** The *in situ* imaging is achieved by encapsulating the electrolyte in between two chips with an electron transparent silicon nitride membrane window. The electrolyte is flowed into the cell using a syringe pump, whereas the electrochemical biasing is achieved through a micropatterned carbon film that is connected to the working electrode of a potentiostat." (Made by Dr. Aram Yoon)[205]
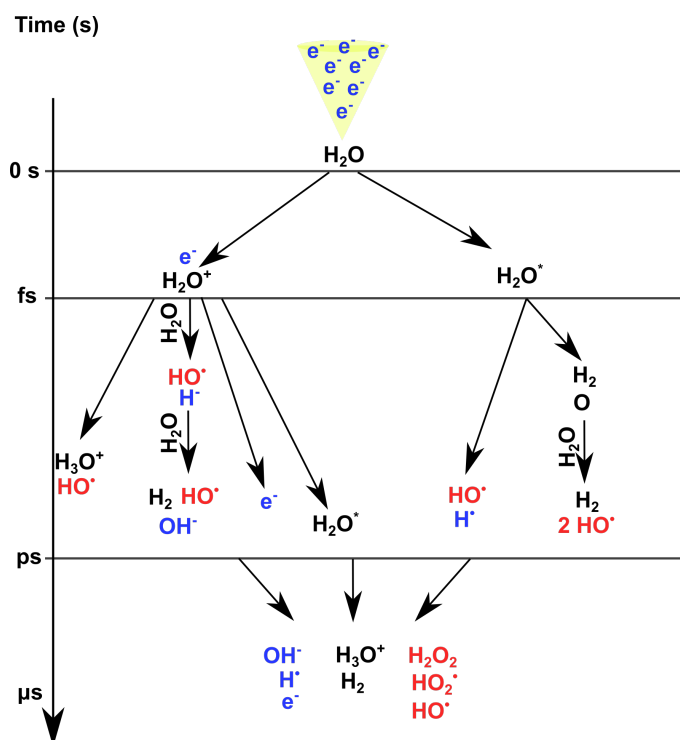
Figure 3.2: **Electron beam induced radiolysis processes upon interactions with water.** Within femtoseconds, radical and ionized water molecules are produced that trickle down towards more stable molecular species. Around the microsecond timescale after the initial electron interaction with water, stable species have formed, that can then react with other reactants or catalyst material in the cell.

3.4 X-Ray Spectroscopy

3.4.1 Extended X-Ray Absorption Spectroscopy

Extended X-ray absorption fine structure (EXAFS) spectroscopy is a type of absorption spectroscopy capable of (*operando*) measurements under electrochemical reaction conditions. The technique is based on the ionisation of individual atoms by absorption of X-ray photons of matching energy. As a result, a photoelectron with a kinetic energy depending on the incident X-ray photon is released.[206] The ejected photoelectron has an energy equal to the incident photon minus the binding energy of the released electron in its corresponding orbital (equation 3).

$$E_{kinetic} = h\nu - E_{binding} = \frac{\hbar^2 k^2}{2m} = \frac{(2\pi)^2 \hbar^2}{(2m\lambda)^2}$$

ν : frequency

λ : wavelength

k : wavenumber

m : mass

$h, \hbar$: (reduced) Planck constant

(3)

The absorption itself can be used to characterize the elements in a sample. For additional information like the crystalline lattice, the interference of the released photoelectrons with surrounding electrons from non-excited atoms is utilized. The ejected photoelectron can be seen as a propagating wave which interacts with point scatterers, *i.e.* the non-excited atoms. Consequently, the backscattered wave interferes in a constructive or destructive way with the propagating wave, leading to an oscillation visible in the absorption spectrum.[207] In reality, a combination of multiple-scattering effects and curved-wave corrections have to be taken into account. Modern methods like FEFF[208–210] (name derived from the effective curved wave scattering amplitude in the modern EXAFS equation) consider these effects. By fitting the (pre-processed) data with a combination of the most commonly occurring scattering paths predicted by FEFF, an accurate model for the bulk sample can be derived. Nevertheless, the level of theory involved in such analysis is beyond the scope of this work. Further informations for this topic can be found in the corresponding literature.[211]
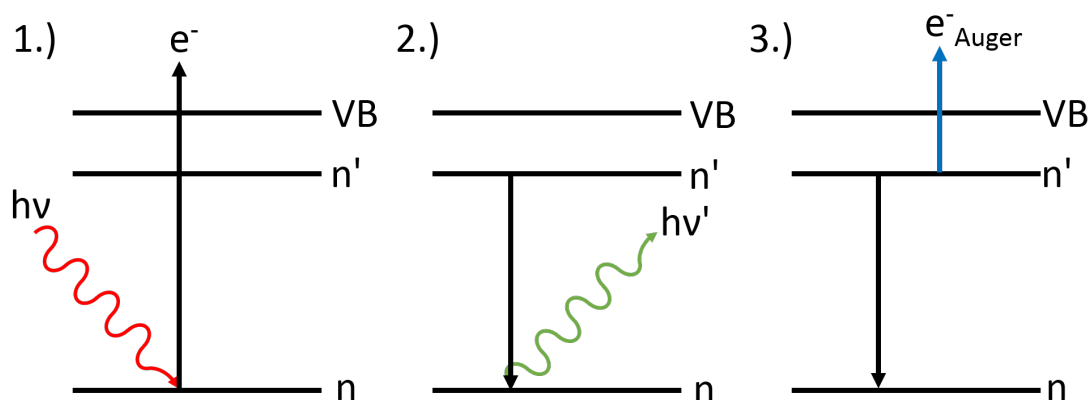
Figure 3.4: 1.) Excitation beyond the ionization energy; photoelectron utilized only in EXAFS. 2.) Recombination with release of a photon below the ionization energy; utilized in EXAFS and XANES. 3.) Auger effect; utilized in EXAFS and XANES.
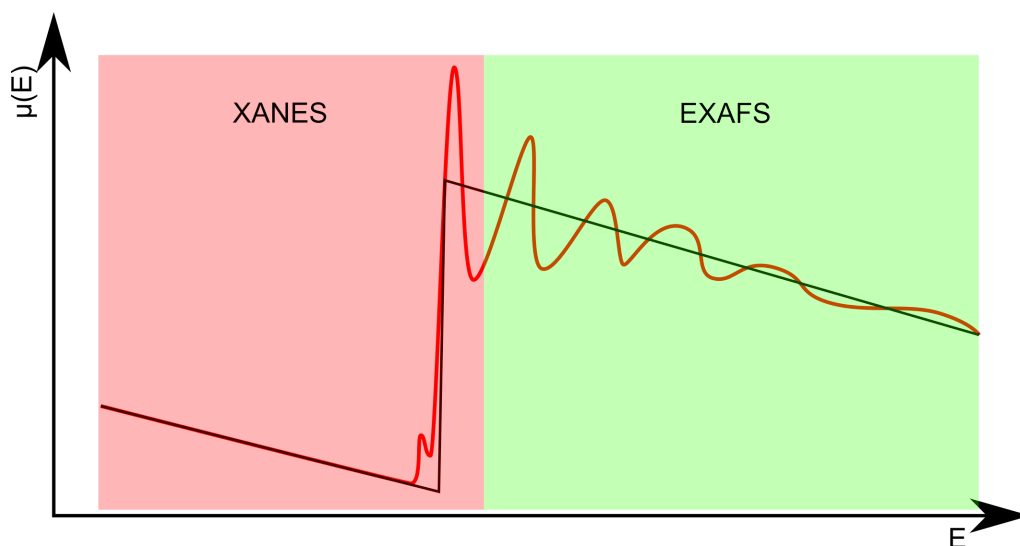
Figure 3.3: Red: region for XANES (pre-edge, near edge) and green: region for EXAFS (past edge).

Besides EXAFS, X-ray absorption near edge structure (XANES) can be used to get additional information about the components inside a sample and their chemical state under *operando* conditions. XANES is based on the same principle as EXAFS, but considers the pre-edge region of the spectrum. The near-edge spectra are sensitive to oxidation states. The XANES region starts about 5 eV above the absorption threshold and goes up to 150 eV (figure 3.3). XANES is typically dominated by multiple scattering processes compared to the mainly single scattering dominated EXAFS. Additionally, only photons and no photoelectrons are measured because it is below the ionization energy, whereas in EXAFS, both can be detected. Furthermore, after excitiation by the X-ray a recombining electron can transfer its energy to another electron, causing it to exceed the ionization energy and leave the shell, leading to the Auger effect.[212] Figure 3.4 shows all involved transitions that are utilized for XANES and EXAFS.

To get information about the coordination number and the atom position in the crystal lattice of the sample, the raw spectra have to be processed. First, a background subtraction is performed on the raw spectra. Therefore, a polynomial function is fitted onto the pre- and post-edge region. This procedure determines the normalization constant, for the fitting. A second function is fitted through the data points of the edge itself. A mathematical expression for the processing of the raw data is shown in equation 5.

$$\chi(E) = \frac{\mu(E) - \mu_0(E)}{\Delta\mu(E)} \approx \frac{\mu(E) - \mu_0(E)}{\Delta\mu(E_0)}$$

χ : normalized oscillatory part of the absorption coefficient

$\mu(E)$: measured absorption coefficient

$\mu(E_0)$: absorption coefficient without contributions from neighboring atoms (fit)

(4)

$\Delta\mu E_0$ can be evaluated at the edge step (E_0) and the approximation seen in equation 4 is used. The subtraction leaves an interferogram that represents the interference between the propagating wave and its backscattering part; this is referred to as the "k-space" or wavevector space (the vector space of possible values of momentum for a particle) with:

$$k = \sqrt{\tau(E - E_0)}$$

$$\tau \approx 0.2625$$

(5)

The next step is the Fourier transformation of the interferogram in k-space into the R-space (half path length) representation. Fast oscillations in the spectrum, which correspond to longer path lengths, are represented as R-space peaks located at higher r and *vice versa*. Onto the R-space spectrum, a fit consisting of multiple oscillations can be applied to gain more information like neighboring atoms in a Cu crystal lattice (FEFF-theory). Additionally, a reverse Fourier transformation can be done to get a "noise free" spectrum in k-space. An example for a transformation of raw data back and force between the real and the reciprocal spaces can be found in figure 3.5.

3.4.2 *Operando* XAFS

To enable XAFS measurement under CO_2RR *operando* conditions, a specifically designed cell is necessary. The absorption of X-rays in water (and water based electrolytes) makes electrochemical measurements challenging. Therefore, the specimens need to be deposited on a thin substrate, which is then used to seal off one side of the electrochemical cell. The X-rays enter the cell from the back of the substrate-sealed side, and the emitted fluorescence signal is collected from the front. A schematic of the electrochemical cell equipped with reference, counter, and working electrode are shown in figure 3.6.
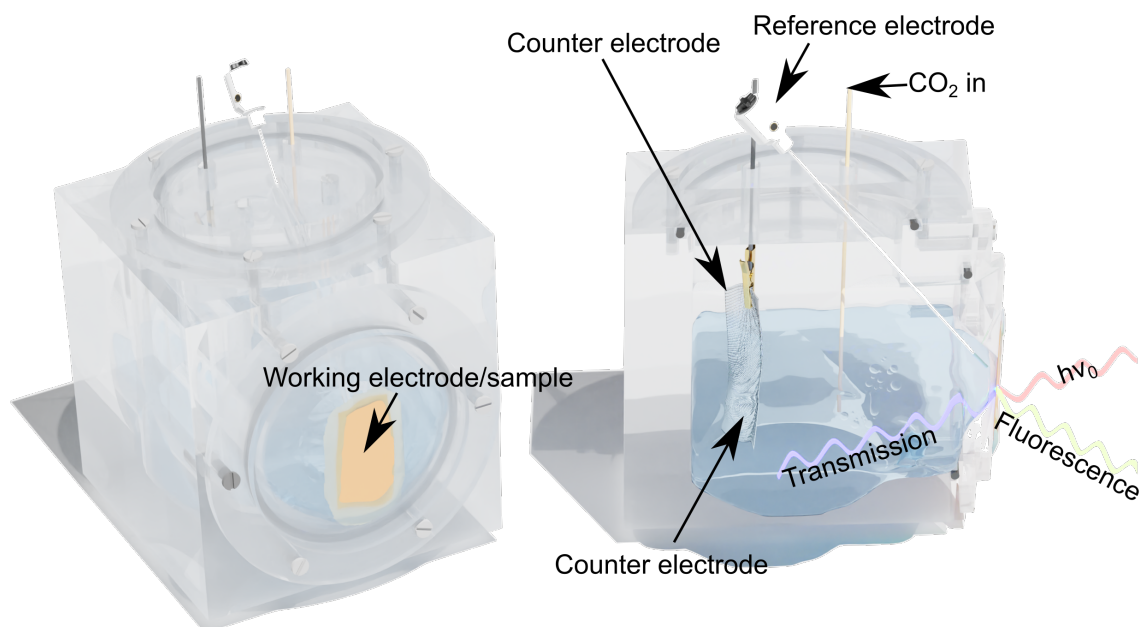
Figure 3.6: EC-cell used for XAFS measurements in liquid under CO_2RR conditions. The sample seals one
side of the cell and the X-rays are going in from the backside. The emitted fluorescence signal is
collected perpendicular to the incident beam.

3.4.3 X-Ray Photoelectron Spectroscopy

X-ray photoelectron spectroscopy (XPS) is a surface sensitive technique with a probing depth of only a few nanometers. This technique utilizes the photoelectric effect to analyze the atomic composition of surface atoms. The photoelectric effect originates from the phenomenon elucidated by Einstein, where a photon of sufficient energy (X-ray range) can eject an electron from the core level of an atom. To analyze the composition of a sample, the kinetic energy of the ejected electron is measured, which is characteristic for different elements. Although the X-ray photons can penetrate deep into the sample, only the surface level electrons can escape it, hence the high surface sensitivity. The kinetic energy of the electron depends on three components out of which one is known: the energy of the X-ray photon, typically from a Al/Mg Kα source (1486.3 eV and

1253.6 eV, respectively). The other two are the binding energy of the ejected electron and the work function between the vacuum and the sample surface, both of which are element specific. Equation 6 shows the relation between kinetic and binding energy.

$$E_k + \phi = E_b - h\nu$$

$$E_k : \text{kinetic energy}$$
$$E_b : \text{binding energy}$$
$$\phi : \text{work function}$$
$$E_{photon} : \text{energy of photon with frquency } \nu$$

(6)

From the electron vacancy left in the core level after the photoelectron was emitted, a secondary electron can be emitted via the Auger effect. The Auger effect describes the relaxation of a higher shell electron into the ground shell. The energy difference is released by emitting a second electron from the same shell that the first electron relaxated from and can be used for chemical characterization. Both, the photoelectric effect and the Auger effect are shown in figure 3.7.
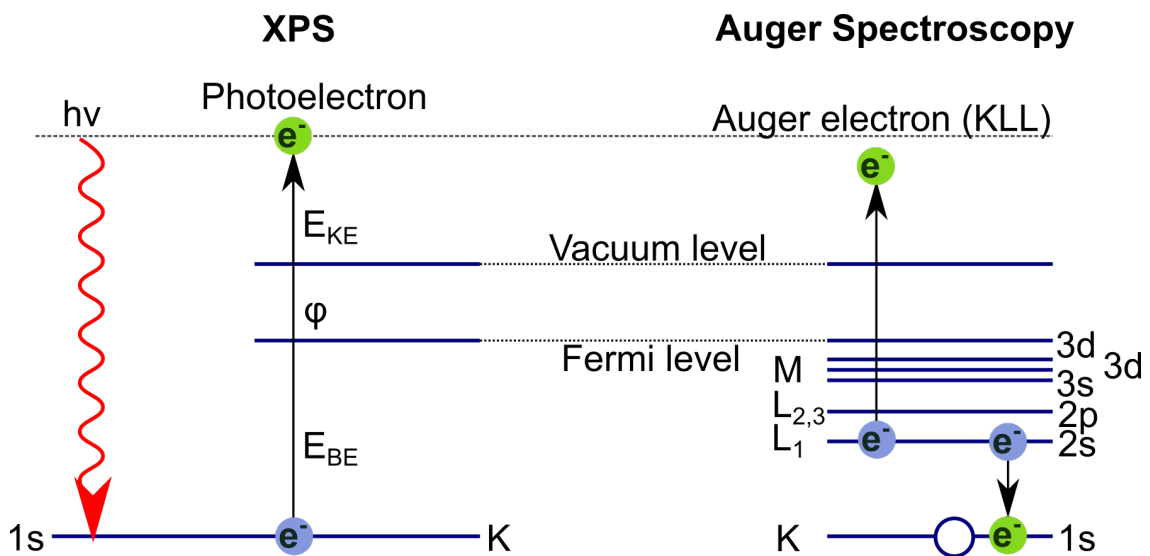
Figure 3.7: Schematic of the photoelectric- and Auger effect. A X-ray photon emitts a core level electron, leaving an electron vacancy that is filled by relaxating another electron from a higher shell and thereby emitting a second electron.

3.5 Electrochemistry

The following part covers all electrochemical techniques used in the characterization of the catalysts and the respective theory behind them, for an in depth introduction to the topic, readers are referred to various textbooks that this section is based on[213–216]. In this work, the emphasis is placed on electrically driven chemical effects and their measurement using various techniques. The processes discussed here take place on the solid-liquid interface of a heterogeneous system consisting of an electronic conductor (*electrode*) and liquid ionic conductor (*electrolyte*) when a

charge is transported through the interface by the movement of electrons (or holes). The electrolyte is (in most cases) a solution of ionic species in water or non-aqueous solvents and the charge is transported by the movement of these ions. The setup to measure the transport of these charges is collectively called an electrochemical cell.

3.5.1 Basics of Electrochemistry

Two types of processes occur on an electrode interface. First, there is the transfer of charges (e.g. electrons) across an electrode-electrolyte interface that causes the oxidation or reduction. This process is governed by Faraday's law, meaning that there is a proportionality between the amount of chemical reactions (caused by the flow of current) that occur, to the electricity passed, thus they are classified as *Faradaic processes*. The corresponding electrodes are in turn called *charge transfer electrodes*. If the electrons on the electrode-electrolyte interface are not transferred (e.g. if the reaction is thermodynamically or kinetically unfavorable) it will not show an electrical response in the system. However, there are processes like adsorption and desorption happening which can alter the solid-liquid interface. These processes can cause a current to flow when the applied potential, concentration of the electrolyte or the electrochemical surface area (ECSA) is altered. As a result, these *non Faradaic* processes cause an offset from the zero current line.

3.5.2 Electrode Setup
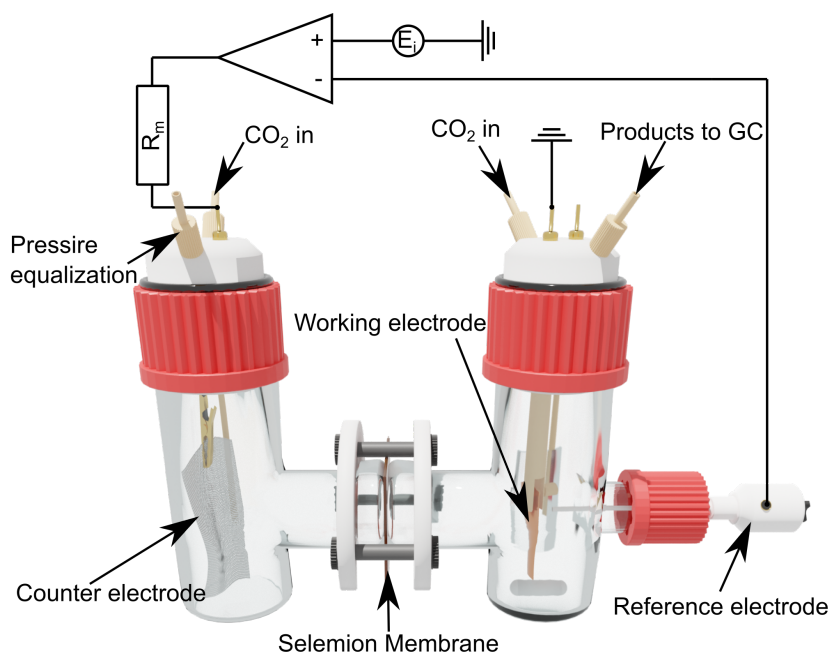
Figure 3.8: **Electrochemical Cell.** H-type electrochemical cell with a working electrode (WE) and counter electrode (CE) compartment which is separated by Selemion anion exchange membrane. Both compartments have a CO_2 inlet and outlet, with the one on the working electrode compartment connected to the GC. Additionally, a pass-through for the reference electrode (RE) is next to the working electrode. All three electrodes are connected to a potentiostat, which consists of three base components: a control amplifier (CA) to maintain the voltage, a series resistor (R_m) to measure the voltage drop and an input source (E_i).

The electrode setup depends on the type of experiment, the number of electrodes, the direction in which the current goes needs to be considered. Whether an oxidation or reduction reaction is measured, the reaction environment, and if the potential or current are tracked.

An electric cell potential between two electrodes (in Volts) describes the energy which is available to drive a charge between the electrodes by external forces. The potential is the cumulative energy of charge transfers due to potential differences on all interfaces in the electrochemical cell and the crossing almost exclusively occurs directly at the interface. Furthermore, the absolute difference in potential at an interface controls the direction and rate of charge transfer by affecting the relative energies of charge carriers in the individual phases.

In a typical electrochemical experiment, the potential between the working and counter electrode is applied by an external power supply. The setup used for the electrochemical characterization in this work is shown in Figure 3.8. As reactions occur, changes in the potential (E) are measured by an external circuit, which can be directly correlated to the stoichiometrical amount of product generated and reactant consumed at the interface. The number of electrons is expressed in the total amount of charge (Q) that passes the circuit. The relationship of product formed and charge can be described by Faraday's law.

$$\text{F} = eN_a = \frac{Q_1}{1mol}$$
$$\text{Q} = n_i z F$$

n_i : Number of associated electrons with the reduction

z : charge number

F : Faraday constant

N_a : Avogadro constant

(7)

In the basic case of two electrodes separated by a single-phase electrolyte, the reactions can be separated into nominally independent half cells. In the reactions discussed here, we focus on only one of the half-reactions, we call the corresponding electrode at which this reaction takes place the *working electrode* (or *indicator electrode*). The other half-cell is consists of a counter electrode with a surface area about 2-10 times that of the working electrode. The electrochemical potential can be measured between the working- and the counter-electrode. However, the counter electrode is usually not fully inert and can change over the course of the reaction. Thus, a third dedicated reference electrode is typically introduced into the system that has a stable phase and essentially constant composition. Historically, the potential of the reference electrode was set to that of the standard hydrogen electrode (SHE) or normal hydrogen electrode (NHE), but in particular substitute electrodes such as silver-silver chloride electrode (Ag/AgCl) or saturated calomel electrode (SCE) are usually used due to their stability for different reactions. The potential is corrected in relation to the SHE, for example the potential of Ag/AgCl/KCl (sat) is 0.242 V vs SHE.

3.5.3 Electrochemical Techniques Used

In this work, we focus on experiments that either keep the potential constant and track the current over time or investigate the current changes with changing potential.

Chrono Amperometry

Chronoamperometric (CA) measurements are one of the most commonly applied techniques in electrocatalysis and corrosion research. Here, the potentiostat keeps the applied potential between the working electrode and the counter electrode at a constant voltage and the changes of the current over time are measured.

Linear Sweep Voltammertry

The most basic potential sweep method is linear potential sweep chronoamperometry which is more commonly known as linear sweep voltammetry (LSV), where the current is tracked and plotted versus the changes in potential (i-E-curve, figure 3.9). In this case, the potential is changed with a fixed sweep rate (v) ranging between $10\,\text{mV}\,\text{s}^{-1}$ to $1000\,\text{mV}\,\text{s}^{-1}$ and up to $10 \times 10^6\,\text{V}\,\text{s}^{-1}$ with UMEs.

The starting point of LSVs is usually chosen close to E_0, such as to prevent Faradaic processes to occur right from the start. For a short time, only non-Faradaic processes are present on the electrode interface. With an increasingly more negative electrode potential, reduction processes become the charge transfer governing mechanism. Beyond this reduction onset, the reaction rate is increasing and the reactant concentration close to the surface drops whilst approaching the formal potential (E_0'). After passing E_0', the reactant mass transport to the surface reaches a maximum rate, and beyond that point the rate declines as the depletion effect sets in. The result is a peak shaped i-E curve that can be observed in the LSV.
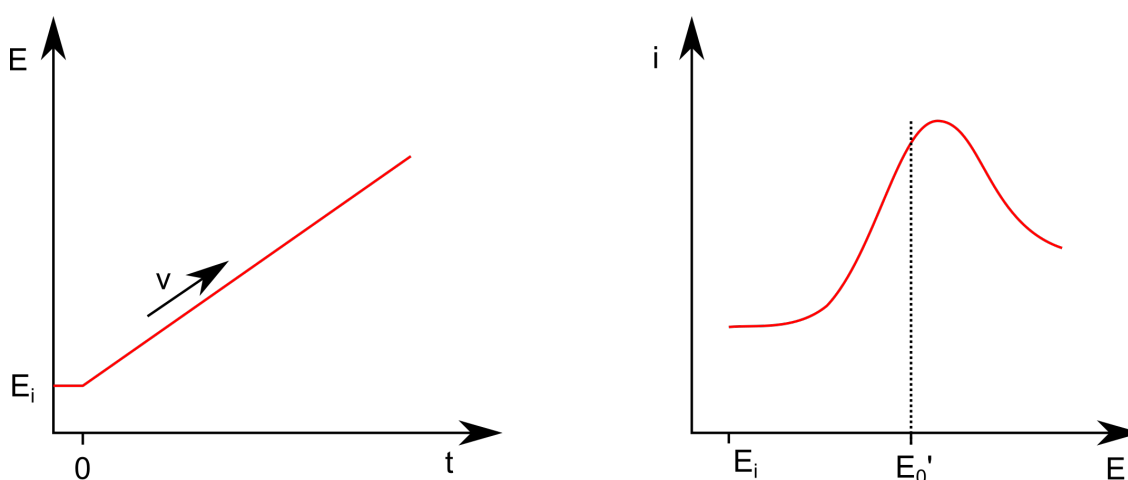
Figure 3.9: **Left:** linear potential increase (sweep) starting from E_i. **right:** resulting i-E-curve.

Cyclic Voltammetry

Following the peak shaped current response described in the previous section, the reverse potential at a defined sweep rate (usually the same as before) can be applied as shown in figure 3.10. Close to the surface, a high concentration of the previous product is present, which is now the educt for the reverse reaction (in a fully reversible redox reaction). In the current response, an analogue peak shape to the previous reduction can be observed with the main difference that the potential is shifted. The reasons for the peak-shape are essentially the same, with the exception of the direction in which the potential is swept, thus the peak center appears on the opposite side of E_0'. This experiment is typically referred to as cyclic voltammetry (CV) and is the potential scan equivalent to double potential step chronoamperometry.
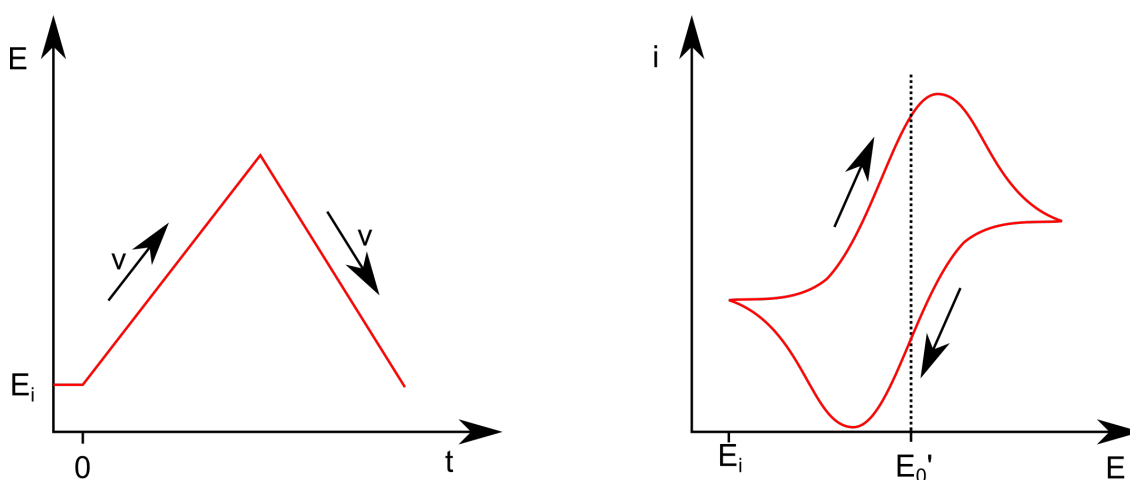
Figure 3.10: **Left:** linear potential increase (sweep) starting from E_i with subsequent reverse at the same speed. **right:** resulting i-E-curve.

CVs are a powerful tool that enable insight into fairly difficult electrode reactions as well as adsorption and desorption processes.

3.5.4 Double Layer Capacitance

This aforementioned non-Faradaic processes provide valuable information about the sample properties. One is the estimation of the electrochemical surface area (ECSA) by measuring the double layer capacitance (C_d). In case of CO_2RR, there are two common methods. The total applied current (I) consists of two components, the current used in faradaic processes (i_f) and in non-faradaic processes (i_c). The non-faradaic current contributes to charging the double layer

capacitance and can thus be used to probe it. Under the assumption that the surface area (A) does not change (e.i. $dA/dT = 0$), the current can be expressed by

$$i_c = -AC_d(d\eta/dt) = -AC_d(dE/dt)$$

i_c : non-faradaic current

A : area

C_d : double layer capacitance

(8)

dE/dt is time dependent, the resulting current changes over time. If an explicit dE/dt is known e.g. by measuring cyclic voltammetry with different scan rates (v), i_c can be calculated from the slope of the i_c-v-plot. In real world applications, the formation of oxide films and electrolysis of adsorbed species add additional components to the current.

The second approach is based on impedance spectroscopy. Impedance ($Z = R - jX_C$) describes a vector that links voltage and alternating current ($e = Esin(\omega t)$). It consists of a real component (Z_{Re}) and an imaginary component (Z_{Im}). In the field of electrochemistry, the imaginary part is almost always capacitive. Impedance is generally defined as

$$Z[\omega] = Z_{Re} - jZ_{Im}$$

ω : angular frequency of an alternating current

$j : \sqrt{-1}$

(9)

An electrochemical system can be modeled by an (Randles) equivalent circuit consisting of resistors and capacitors as presented in figure 3.11a. The resistance of the electrolyte (R_ω) is affecting all currents, thus the equivalent resistor element is put in series. After that are the double-layer-capacitance (C_d) and a general faradaic impedance (Z_f) in parallel, where the capacitive (i_c) and faradaic current (i_f) are taking different routes. The faradaic impedance is divided into further elements that are in parallel or series configuration. These elements are (in a simplified model system) the Warburg element (Z_W) which models diffusion processes, the charge transfer resistance (R_{ct}), and an adsorption pseudo capacitance and resistance (C_{ps} and R_{ads}, respectivley). Figure 3.11b shows how a Nyquist plot (Z_{Re}-Z_{Im}-plot) of such a system would typically look. The initial zero passing at high angular frequencies represents the resistance of the electrolyte, the second zero passage is the sum of the charge transfer resistance and electrolyte resistance, though due to diffusion limit resistance (Warburg resistance), the plot continues linearly in a $\approx 45°$angle.
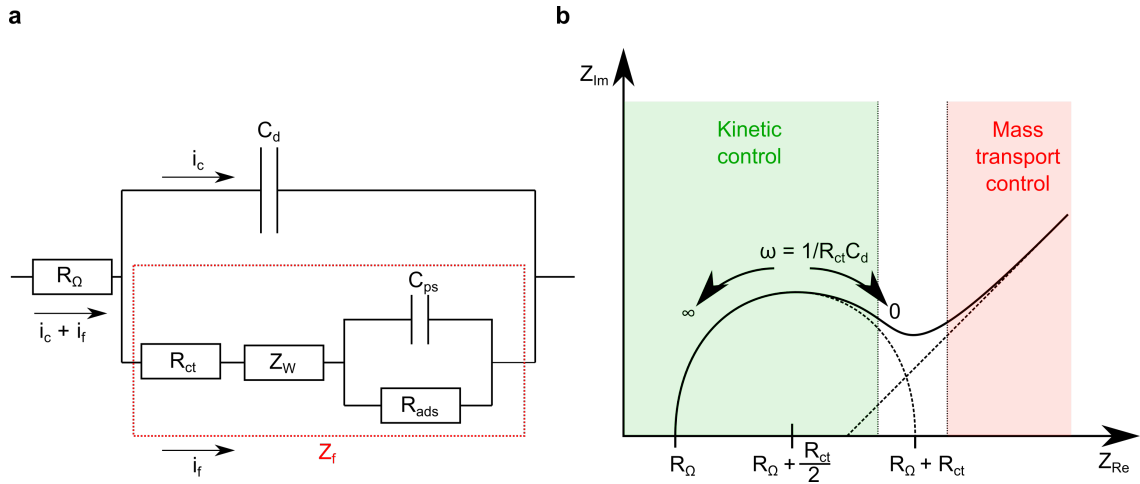
Figure 3.11: **a)** Equivalent circuit for a simplified electrochemical system consisting of electrical elements in series and parallel. **b)** Nyquist plot of an electrochemical model system.

At high frequencies. diffusion cannot manifest and thus Warburg resistance is not existent. The relation of these electrical elements to the angular frequency of a sinusoidal alternating current, as summarized in equation 10.

$$R_s = R_{ct} + \frac{\sigma}{\omega^{\frac{1}{2}}}$$

$$C_s = \frac{1}{\sigma \omega^{\frac{1}{2}}}$$

$$R_{ct} = \frac{nRT}{Fi_0}$$

R_s : series resistance

R_{ct} : charge transfer resistance   (10)

σ : Warburg coefficient

ω : angular frequency

R : gas constant

T : temperature

n : number of electrons involved

With these equations, the impedance of a system can be measured in dependence of the applied frequency and the resulting Nyquist plot modeled and fitted by an equivalent circuit to determine the double-layer-capacitance (among other sample properties). An in-depth explanation and discussion about how to derive the formula in this section is available in literature[214,217,218].

3.5.5 Faradaic Efficiency

To determine the effectiveness of a catalyst, it is important to have a representative value for comparison between samples. In the case of CO_2RR, this is the Faradaic efficiency (FE(%)) for gaseous and liquid products. The Faradaic efficiency is a value that determines the amount of

electrons that are used for the specific reaction (by applying a potential) over the electrons that do not (e.g. by going into other reactions like HER). First of all, the amount of products has to be determined. These are obtained by gas chromatography (GC) for the gaseous products as well as high-pressure liquid chromatography (HPLC) and nuclear magnetic resonance spectroscopy (NMR) for the liquid products. The equation that was used for the calculation of the Faradaic efficiency is shown below (equation 11).[219]

$$\text{FE}_i(\%) = \frac{n_i F \phi_i F_m}{I}$$

n_i : Number of electrons

F : Faraday constant

ϕ_i : Volume fraction of the gases (11)

F_m : Molar CO_2 flow rate

I : Current

The amount of electrons associated to the reduction of a certain product can be taken from table 1 from the previous section *Electroreduction of CO₂*. As for the Faraday constant (F), it is the absolute value of the electric charge per mole of electrons and is derived from physical constants; the electric charge e and the Avogadro constant (N_a). This relation is displayed in equation 12.

$$F = eN_A$$

N_A : Avogadro's constant (12)

e : elementary charge

From this, the partial current density (i_a) can be derived as shown in equation 13

$$i_a = \frac{\text{FE}_i(\%)}{100} \times \frac{i_{total}}{A}$$

i_{total} : total electrolysis current (13)

A : area of the sample

The molar flow rate F_m of CO_2 is predetermined by the experimental setup and is set to $20\,\text{mL}\,\text{min}^{-1}$ in all experiments. From the peak area of the signals in the GC, the volume fraction of the respective gases ϕ_i is determined. Finally, the current that is necessary for the calculation, is recorded throughout the experiment by the potentiostat. Therefore, for each injection into the GC, the current can be exactly determined. After inserting these values, the measured current, and respective product rate into equation 11, the Faradaic efficiency for each product is calculated. The sum of all Faradaic efficiencies $\text{FE}_i(\%)$ should be 100 %.

$$\text{FE}_{total}(\%) = \sum_i \text{FE}_i(\%)$$ (14)

To get information of the activity associated with each respective product, the partial current density is calculated according to equation 13.

4 Growth Dynamics and Processes Governing the Stability of Electrodeposited Size-controlled Cubic Cu Catalysts

The following chapter is based on my paper in Journal of Physical Chemistry C on the "*Growth Dynamics and Processes Governing the Stability of Electrodeposited Size-controlled Cubic Cu Catalysts*".[99] I have planned and conducted all experiments and prepared the draft. The liquid phase SEM measurements have been done in collaboration with Dr. Aram Yoon from our electron microscopy group. In this chapter, the synthesis parameters and mechanism that governs the electrodeposition of Cu cubes used in the later chapters are discussed.

"[...] Here, we explore the phase space of synthesis parameters required for the electrodeposition of Cu cubes with $\{1\,0\,0\}$ facets on glassy carbon substrates and elucidate their influence on the size, shape, coverage, and uniformity of the cubes. We found that the concentration of Cl^- ions in solution controls the cube size, shape, and coverage, whereas the ratio of the reduction versus oxidation time and number of cycles in the alternating potential electrodeposition protocol can be used to further tune the cube size. Cyclic voltammetry experiments were complemented with *in situ* electrochemical scanning electron microscopy to follow the growth dynamics and *ex situ* transmission electron microscopy and electron diffraction. Our results indicate that the cube growth starts from nuclei formed during the first cycle, followed by a layered deposition and partial dissolution of new material in subsequent cycles."[99]

4.1 Introduction

"[...] It is known from single-crystal studies that $Cu\{1\,0\,0\}$ has superior selectivity toward ethylene and ethanol production vs other crystalline orientations.[220] On the basis of theoretical calculations, it has been hypothesized that the bonding distance of two or more adsorbed CO molecules on the $\{1\,0\,0\}$ surface favors the C-C coupling and thus influences the desired selectivity toward C_{2+}** products.[221–223] Hence, cubic nano-particles exclusively made of $\{1\,0\,0\}$ facets have arisen significant interest for future industrial applications.[224]

There are various approaches to create size- and shape- controlled particles for use as electrocatalysts, such as colloidal synthesis,[225] laser ablation,[226] sol-gel,[227,228] chemical vapor deposition,[229] and electrochemical synthesis methods.[131,230] Among these techniques, the electrochemical deposition of copper particles has the following advantages: (1) the catalysts are directly deposited on the working electrode, which ensures good adhesion; (2) the catalyst shape and hence their surface

---

** Changed C2+ to C_{2+} for consistency to the other chapters.

34

exposure are easily tuned through the addition of halide ions to the copper precursor solution;[97,231] and (3) the use of surfactant ligands to achieve shape control is avoided, which otherwise requires additional chemical treatments to remove them to achieve a pristine catalyst surface. Moreover, the presence of halide ions in the electrolyte may act as another factor that can be used to tune the catalytic selectivity.[232] However, the phase space of synthesis parameters that needs to be explored to obtain catalysts with narrow size and shape distributions is large. These include, the optimum Cu precursor salt, optimum Cu concentration in the electrolyte, optimum Cl^- concentration (and how this affects the resulting average particle size), the potential range employed, and the duration of the electrodeposition as well as the pH of the electrolyte.

Recently, we reported a protocol that achieves the direct growth of copper particles from solution onto carbon-based supports with a narrow shape distribution using alternating potentials, where the potential window is tuned such that only the noncubic particles dissolve.[231] In the present study, we discuss the role of other important synthesis parameters namely, the Cu/Cl^- concentration, the number of cycles, speed, potential, and how they affect the final electrocatalyst shape and size distribution. In particular, we found that the Cl^- concentration[233] had the most drastic effect on the catalyst size distribution and coverage. We further studied the dynamic morphology of the electrodeposited Cu particles via *in situ* electrochemical scanning electron microscopy (SEM) to gain insight into the details of the growth pathways. Our results show that nuclei for the cubes are formed during the first pulse electrochemical cycle, which progressively grow into cubes in the subsequent alternating reductive-oxidative cycles as new material is deposited and partially removed. In addition to achieving shape selection,[182] here we attempt to explore the parameters and conditions required to grow uniformly dispersed, size-controlled Cu cubes from a solution of $CuSO_4$ and KCl.[182]

4.2 Experimental Methods

4.2.1 Synthesis

A mixture of 5 mM copper sulfate-pentahydrate ($CuSO_4 \cdot 5H_2O$) (Sigma-Aldrich, 99.7-100.5 %) and 5, 10, 30, or 50 mM potassium chloride (KCl) (Sigma-Aldrich, 99%) has been used as electrochemical deposition solution. The synthesis was performed in a three-electrode configuration, equipped with an Ag/AgCl (sat.) reference electrode (Gaoss Union), a Pt counter electrode, and a polished glassy carbon (vitreous) plate (SPI) as working electrode. Electrochemical cycling between an anodic (+0.0 V vs Ag/AgCl) and a cathodic potential (−0.5 V vs Ag/AgCl) within a total of 10 cycles results in the electrodeposition of size- and shape-controlled Cu cubes. Initially, a potential of −0.5 V vs Ag/AgCl was held for 8 s followed by a potential jump to +0.0 V vs Ag/AgCl for 4 s. The cyclic voltammetry is completed by returning to the initial potential.

4.2.2 Morphological Characterization

The samples were characterized by using a 200 kV Talos transmission electron microscope (TEM) from Thermo Fisher. The *in situ* electrochemical scanning electron microscopy (SEM)

experiments were performed in an 30 kV Apreo scanning electron microscope from Thermo Fischer using a customized liquid flow cell setup from Hummingbird Scientific with dedicated Ag/AgCl (3 M) reference and Pt counter electrodes. The electrodeposition studies were performed by using liquid cell chips from Hummingbird Scientific that are patterned with a carbon working electrode. The image sequences following the electrodeposition process were acquired by using the transmission electron detector.

For each precursor solution containing a defined ratio of Cu to Cl, three samples were produced, and the microscopy measurements were conducted in several different locations of the sample to check the homogeneity of the electrodeposition process. An automated particle detection and counting algorithm from the Gwyddion software was utilized. The respective SEM size distributions were calculated based on data obtained from at least three different positions on the sample. The interconnected cubes are counted as individual cubes for statistics, whereas the size distributions are obtained only from isolated cubes. The distributions were fitted with a Gaussian curve to yield the average sizes displayed in Tables 4 and 5.

4.3   Results and Discussion

Although it was previously established that the presence of Cl^- ions in solution is crucial for the electrochemical growth of the Cu cubes,[231] no information was yet available on how to simultaneously tailor their size, distribution, and coverage on the support. Because during the electrodeposition process the growth speed is governed by the availability of ionic metal species (M+), which is given by the concentration of the metal salt in solution, we have kept this parameter constant (5 mM $CuSO_4$) for a more direct comparison of the role of other parameters.
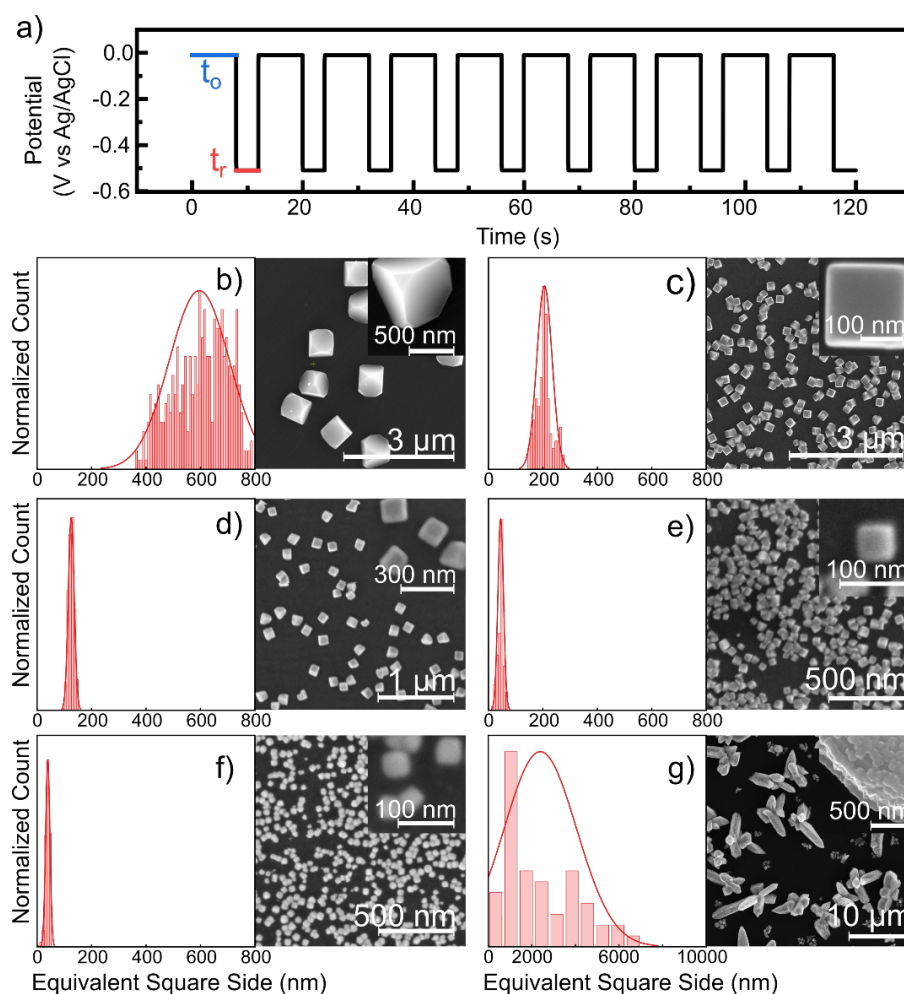
Figure 4.1: (a) Synthesis protocol with alternating potentials of 0 and −0.5 V vs Ag/AgCl and fixed oxidizing (t_o) and reductive (t_r) time length (t_o = 8 s and t_r = 4 s). SEM images and respective size distributions of Cu cubes synthesized with a 5 mM CuSO$_4$ solution mixed with a KCl solution of the following concentrations: (b) 0 mM KCl (1:0, no Cl$^-$), (c) 5 mM KCl (1:1), (d) 10 mM KCl (1:2), (e) 30 mM KCl (1:6), and (f) 50 mM KCl (1:10). In (g) 50 mM CuSO$_4$ + 5 mM KCl (10:1) were used to see the effect of further increasing the CuSO$_4$ concentration. The respective current response can be seen in Figure 4.2.

Figure 4.1 shows how the morphology of electrodeposited particles, obtained from SEM, varies as a function of the Cl$^-$ concentration from 5 to 50 mM, leading to different Cu-to-Cl ratios in the precursor solution. The alternating potential cycles used for the electrodeposition are depicted in Figure 4.1a. Figure 4.1b shows that such protocol can still yield cubelike structures without the presence of Cl$^-$ ions in solution but that their average size is much larger and exhibits a broader size distribution as compared to the samples where Cl$^-$ was added. Moreover, the cube corners are truncated. Figures 4.1c-f show that with increasing concentration of Cl$^-$ and constant Cu$^+$ concentration (5 mM CuSO$_4$), cubes with sharp corners are obtained, and the cube size was found to decrease while the surface density of the cubes on the support increased. At a Cu-to-Cl ratio of 1:6 (5 mM CuSO$_4$ to 30 mM KCl), the cubes start to interconnect as shown in Figure 4.1e. Furthermore, the cube coverage is the highest for this Cu/Cl ratio. For a KCl concentration

of 50 mM, the cubes no longer maintain a sharp cubic shape and the corners start to become rounded (Figure 4.1f). Increasing the concentration of $CuSO_4$ to 50 mM, while keeping the KCl concentration at 5 mM KCl (10:1) (Figure 4.1g), leads to a significant change in the deposited morphology, with large micrometer-sized branched structures. A closer examination of these flower-like structures further suggest that they are made up of merged cubes (inset in Figure 4.1).

On the basis of the size distributions, we calculated the exposed electrochemical Cu surface (specific $area_{Cu\text{-}cubes}$) assuming a cubic geometry. The results are summarized in Table 4. For all Cl^--containing samples synthesized under identical conditions, the exposed surface area of Cu is similar, while without the addition of Cl^-, the surface area is significantly smaller. This estimation does not account for the loss of exposed facets due to the interconnection of the cubes; thus, it may lead to an overestimation of the surface area for those samples.
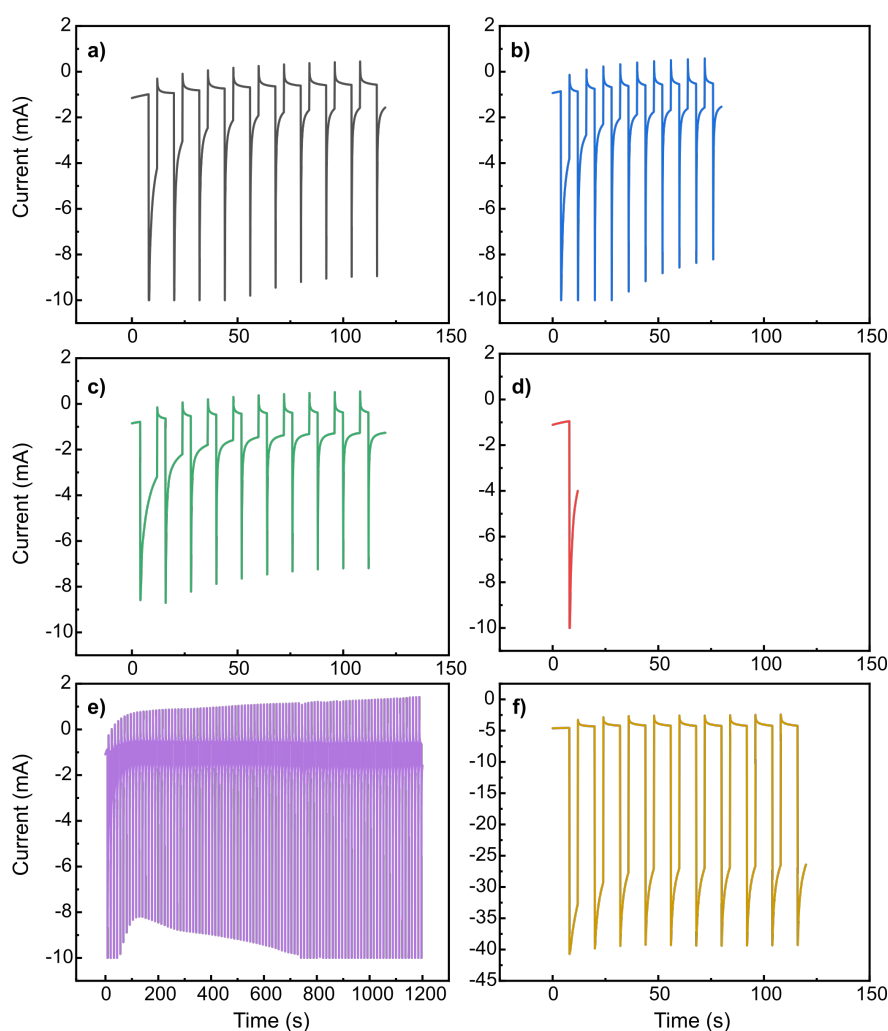
Figure 4.2: Current response for different applied synthesis protocols. Panels (a-c) show changes in the times t_r and t_d with (a) $t_r < t_o$, b) $t_r = t_o$, and (c) $t_r > t_o$. In (d,e) the variation of applied cycles is shown with (d) 1 cycle and (e) 100 cycles. Lastly, in (f) the concentration of $CuSO_4$ was increased from 5 mM to 50 mM, whilst the KCl concentration remained at 5 mM. The electrochemical protocol is the same as in (a).

Table 4: Size Distribution of the Different Electrodeposited Cu Samples with Varying Precursor Concentrations Ranging from 5 to 50 mM Cu-to-Cl Ratio Fitted by a Gaussian Peak Shape[a]

CuSO$_4$ conc (mM)	KCl conc (mM)	Cu:Cl$^-$ ratio	Size (nm)	no. of cubes/cm^2	Cu surface area (cm^2)
5	0	1:0	596 ± 47	9.0x10^6	1.6x10^{-1}
5	5	1:1	291 ± 32	1.6x10^8	6.6x10^{-1}
5	10	1:2	125 ± 5	9.1x10^8	7.1x10^{-1}
5	30	1:6	44 ± 4	1.8x10^{10}	17.3x10^{-1}
5	50	1:10	39 ± 3	5.5x10^9	4.2x10^{-1}
50	5	10:1	87 ± 7[b]	-	-

[a]The times t$_r$ and t$_o$ were kept at 4 and 8 s, respectively, and the number of cycles was kept constant and set to 10 cycles. The column (no. of cubes/cm^2) indicates the number of Cu Cubes detected per cm^2 of the support, while the last column describes the specific Cu surface area per cm^2 of sample.[b]Size of cubes in the branched structures.

In Figure 4.3, we summarize the effect that changing the duration of the applied reductive potential (E$_r$), oxidative potential (E$_o$), and the number of applied cycles have on the morphology. Previously, we had shown with *in situ* TEM that noncubic particles dissolve earlier than the cubic ones during the oxidative part of the cycle.[231] By cycling repetitively within a potential window where the noncubic particles dissolve and the cubic ones do not, we could induce selection toward cubic shapes. Now, we use Figure 4.1c as the reference point for comparison (5 mM CuSO$_4$ and 5 mM KCl) with 10 alternating potential cycles of t$_o$ = 8 s and t$_r$ = 4 s. Our results indicate that a longer oxidative potential is preferred to dissolve noncubic particles completely.[231] An increase in the reductive potential results in larger cubes, but it comes at the expense of the growth of noncubic particles that do not fully dissolve during the oxidative potential. In Figure 4.3a, we show that applying the same duration for both the oxidative and the reductive potential (t$_r$ = t$_o$ = 4 s) surprisingly leads to smaller cubes (roughly half the size of those shown in Figure 4.1c) with triple surface coverage. The calculated specific area of Cu is in this case approximately two-thirds of that of the 1:1 sample with t$_o$ = 8 s shown in Figure 4.1c. If t$_r$ is longer than t$_o$, the size distribution shifts to larger cube sizes together with the formation of branched structures (Figure 4.3b). Additionally, the specific area of the Cu cubic particles is reduced to approximately one-third. The size distribution and surface area calculation results, normalized to 1 cm^2 sample size, are summarized in Table 5.

Table 5: Size Distribution and Specific Cu-Cube Area Estimation Results Normalized to 1 cm^2 as a Function of the Electrochemical Protocol Applied (Fitted by the Gaussian Peak Shape)[a]

t_r (s)	t_o (s)	Size (nm)	no. of cubes/cm^2	Cu surface area (cm^2)
4	8	291 ± 32	6.6×10^8	27.9×10^{-1}
4	4	130 ± 3	21.9×10^8	18.5×10^{-1}
8	4	340 ± 10	1.6×10^8	9.6×10^{-1}

[a]Here the concentration was kept at 5 mM for KCl and CuSO$_4$ (1:1), and only the times are altered. The column (no. of cubes/cm^2) indicates the number of Cu Cubes detected per cm^2 of the support, while the last column describes the specific Cu surface area per cm^2 of sample.
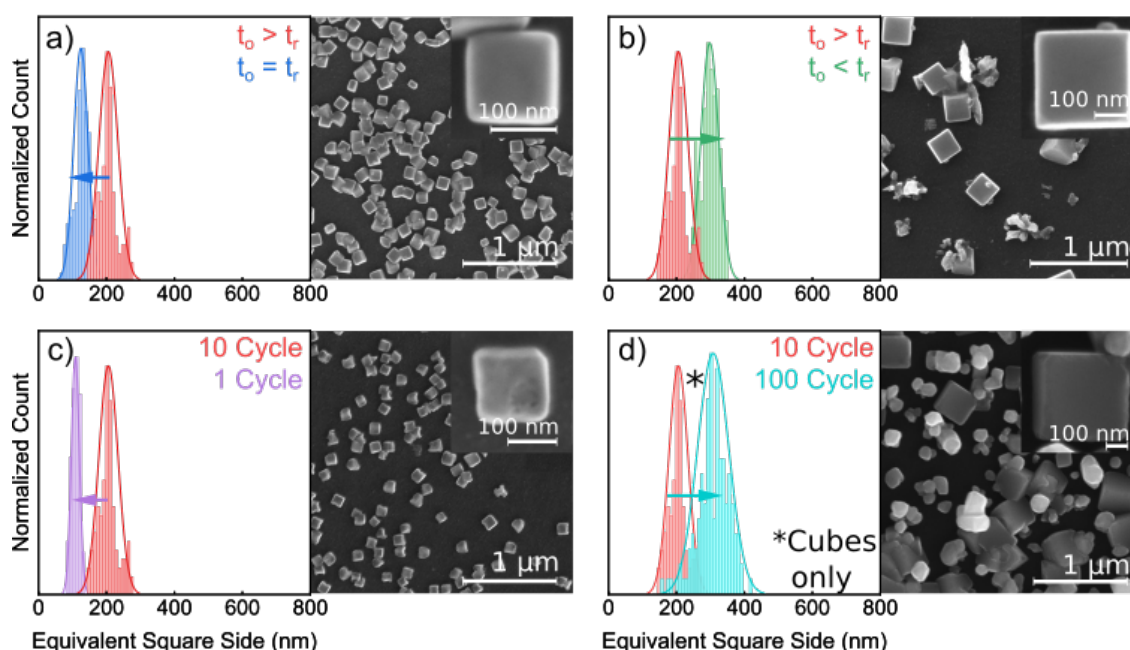

Figure 4.3: Effect of varying the time length and number of cycles of the synthesis protocol with constant precursor concentrations (5 mM CuSO$_4$ and 5 mM KCl). Different times for t_r and t_o with (a) t_r = t_o and (b) t_r > t_o as well as change in the number of cycles with (c) 1 cycle and (d) 100 cycles compared to the t_r < t_o, 10 cycle reference.

Lastly, we varied the number of cycles while using the same cycling parameters as in Figure 4.1c of t_o = 8 s and t_r = 4 s. From Figure 4.3c, we can see that applying only a single oxidative-reductive potential cycle leads to the formation of smaller, but poorly shaped cubes, suggesting that these are the initial nuclei from which the larger cubes are formed in the subsequent cycles. On the other hand, increasing the number of cycles to 100 (Figure 4.3d) leads to a densely covered surface, but with significant dispersion in terms of both particle size and shape.

For a better understanding of the parameters that enable a high surface coverage of size- and shape-controlled Cu$_2$O cubes, we further examined the electrochemical characteristics of the deposition process using cyclic voltammetry (CV) and the deposited structures using electron

microscopy. Figure 4.4a compares the CV curves of a glassy carbon support in a solution of 5 mM CuSO$_4$ and 5 mM KCl as well as a second solution with 50 mM KCl, both in Ar-saturated ultrapure water. In our protocol for the electrodeposition we alternated between two potentials, a reductive potential (E$_r$) at -0.5 V vs Ag/AgCl and a slightly oxidative potential (E$_o$) at +0.0 V vs Ag/AgCl, indicated by the dotted lines in Figure 4.4a. E$_r$ lies at a potential higher than the maximum of the two cathodic peaks, and E$_o$ lies at the onset of the anodic peaks. With increasing concentration of Cl$^-$ (and K$^+$) ions the conductivity increases, which reduces the distance between the cathodic and anodic peaks A1/2 and C1/2, respectively. Hence, changing the Cl$^-$ concentration also resulted in modifications of the deposition and dissolution currents and, thereby, in changes in the growth rate of the cubes. As shown in Figure 4.4b, the deposition and dissolution currents in the 50 mM KCl cycling experiment are about 4 times larger than those in the 5 mM KCl experiment.

Figure 4.4c shows high-resolution TEM images and the selected area electron diffraction (SAED) pattern of a 1:1 Cu-to-Cl ratio sample obtained by depositing the cubes directly on the carbon working electrode of the liquid cell chips used in the *in situ* SEM experiments described later in this article. Figure 4.4d shows the corresponding scanning TEM (STEM) image and energy-dispersive X-ray (EDX) spectroscopy map of a cube. The TEM and STEM images indicate that we form solid cubes with small pores near the surface. The SAED pattern shows that the cube is a Cu$_2$O single crystal. The strong diffraction spots at the $\{3\,1\,1\}$ and $\{\overline{4}\,\overline{2}\,0\}$ positions together with diffuse spots at $\{2\,2\,0\}$ and $\{\overline{2}\,\overline{2}\,0\}$ are consistent with the pattern of a tilted crystal which is not orientated close to a zone axis. A closer inspection of the image also reveals subtle layering in the internal structure of the cube (second panel in Figure 4.4c). The STEM image provides more detail regarding the structure, where one can distinguish a slightly porous cubic core with uniform contrast, followed by alternating layers of brighter and darker contrast, before ending with a thicker layer of darker contrast. These changes in contrast are likely caused by small changes in the density between an oxidized layer and the subsequently deposited layer.
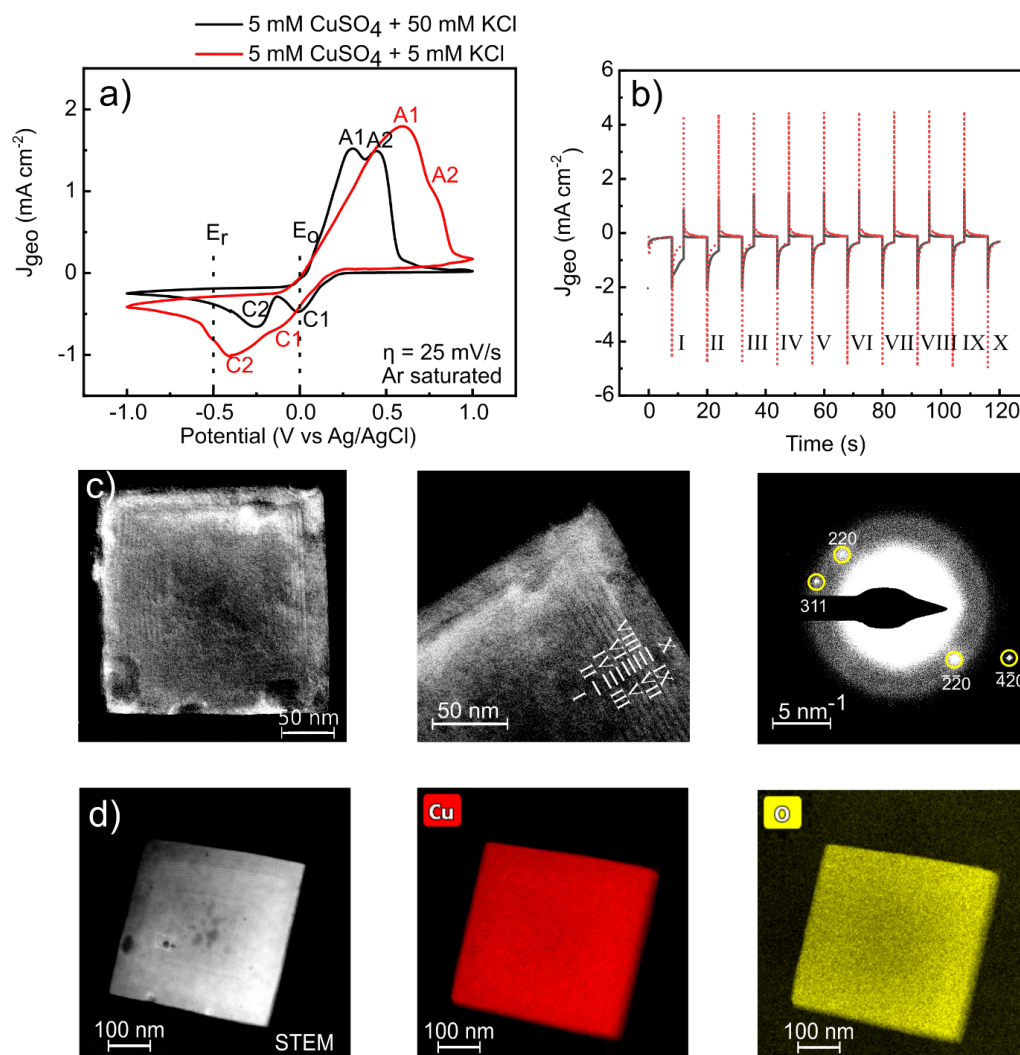
Figure 4.4: (a) Cyclic voltammograms (CV) in 5 mM $CuSO_4$ and 5 mM KCl/50 mM KCl at 25 mV s^{-1} to show the current response at the potentials E_r and E_o. The anodic peaks A1 and A2 represent the oxidation to Cu_2O and CuO, and the cathodic peaks are typically interpreted as the corresponding reductive counterparts.[234] In (b), the current responses for 1:1 and 1:10 Cu-to-Cl ratio samples (t_r = 4 s, t_o = 8 s, 10 cycles labeled I-X) at the potentials E_r and E_o are shown. TEM images and electron diffraction patterns of 1:1 cubes prepared with the same procedure are shown in (c), with the Roman numbers indicating layers correlated to the respective cycle in (b). The colors are inverted for better visibility. In (d), the EDX mapping of the same pristine Cu cubes on the carbon working electrode of the liquid cell chips used for TEM are shown.

These results, together with the poorly formed cubes after a single deposition cycle that was shown in Figure 4.3(c), suggest a cube growth pathway where the poorly formed cube serves as nuclei for subsequent growth. The thickness of the final surface layer indicates that the reductive part of the cycle actually increases the thickness of the cube by a substantial amount, which is removed to a large degree during the oxidative part of the cycle, leaving behind only a portion of the deposited layer. The last layer is thicker because the applied protocol ends at the reductive potential. This mechanism is summarized as a schematic in Figure 4.6(a). To confirm this growth

mechanism, we acquired electrochemical SEM images to follow the nucleation and growth of the particles during potential cycling. Images extracted from the first three cycles of the *in situ* image sequence are shown in Figure 4.6b, and the full movie sequence covering 11 cycles is provided as Movie 13.3*. Consistent with the proposed mechanism, we only observe small, partially developed cubic structures with truncated corners and broken edges during the first cycle (enlarged image in Figure S4.5).
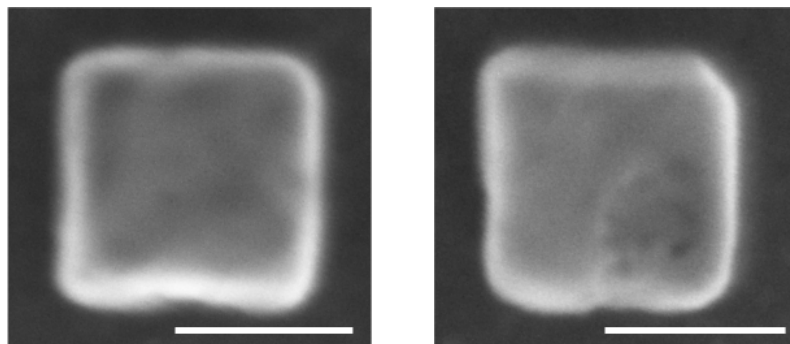

Figure 4.5: Magnification of the insets shown in Figure 4.3 (c) that displays the cubes after one deposition cycle. The scale bars are 100 nm.

The nucleation process itself was not possible to observe due to limitations in the microscope resolution. The *in situ* image sequence revealed that the cubes are nearly fully formed by the end of the third cycle. Furthermore, we were able to see the dynamic formation and dissolution of noncubic particles during each potential cycle, as we reported previously via TEM.[231] A comparison of the images acquired at the second and fourth deposition cycles also indicates that 80% of the final cubic structures were formed from the initial semicubic nanostructures. We could measure a slight increase 5-10% in size with each deposition step, corroborating our proposed mechanism. On the basis of these results, we can rationalize why our standard protocol appears to be optimal for generating size- and shape-controlled Cu_2O cubes and provide general principles for modifying the protocol to achieve tuning of the cube morphology. First, it is clear that the Cl^- ion concentration influences both the nucleation of the Cu_2O cubes and the stabilization of the cubic shape. It is known that both Cl^- and SO_4^- ions can act as modifiers to stabilize specific crystal orientations.[235] Cl^- ions stabilize the $Cu\{1\,0\,0\}$ facet, whereas SO_4^- ions stabilize both $Cu\{1\,1\,1\}$, and $Cu\{1\,0\,0\}$ facets. Hence, the formation of truncated cubes in the absence of Cl^- can be easily attributed to the effect of SO_4^-. When KCl is however added, the effect of chloride dominates due to the stronger adsorption of Cl^- ions to the Cu surface.[235]

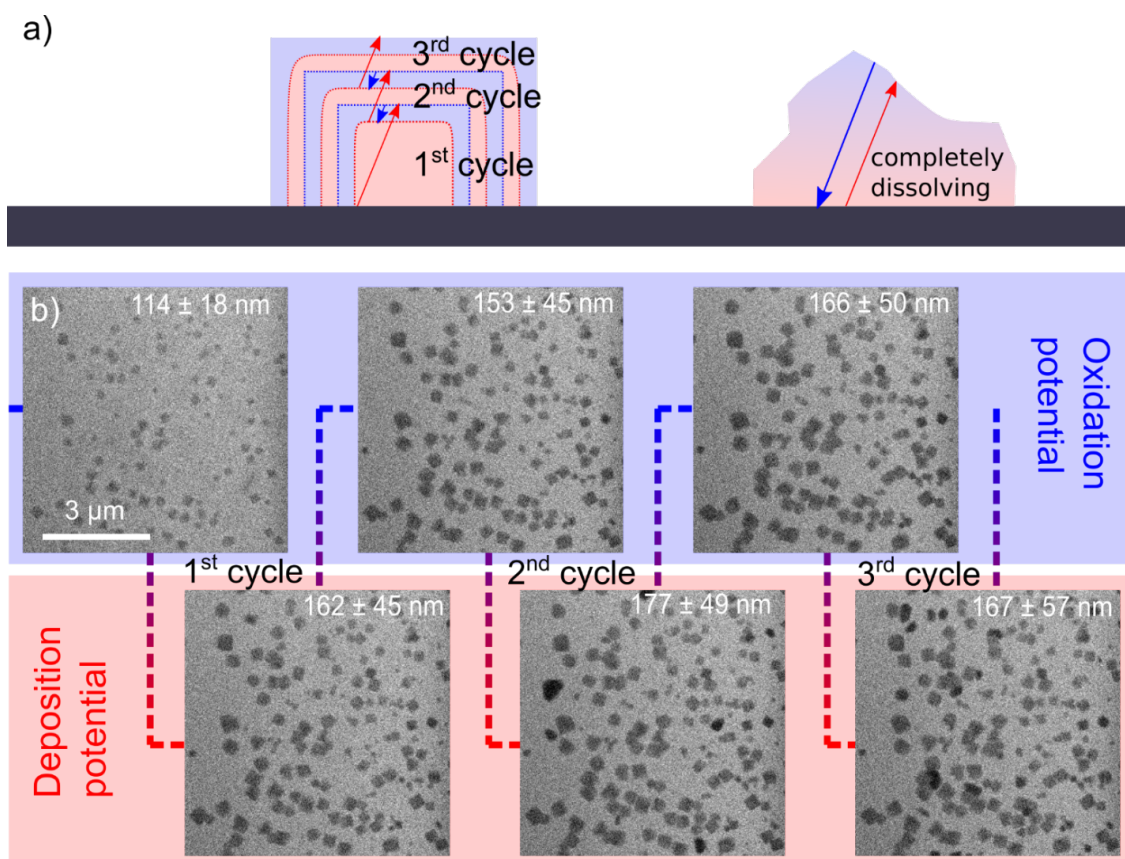* Here in form of a figure in the appendix

Figure 4.6: (a) Scheme of the proposed mechanism for the growth of Cu cubes by electrodeposition, with layer growth during E_r and shrinkage during E_o. The noncubic particles dissolve completely after growth during E_r. (b) Operando SEM images of the second to fourth electrochemical cycles in a 5 mM CuSO$_4$ + 5 mM KCl solution synthesized by the electrochemical protocol discussed in Figure 4.4.

The increased coverage of cubes on the glassy carbon surface and the reduction in size of the cubes are, on the other hand, attributed to the increased conductivity of the electrolyte due to the added KCl and the relatively low concentrations of CuSO$_4$ used in our deposition solutions. The higher deposition currents at higher KCl concentrations lead to the formation of more CuSO$_4$ nuclei, as indicated by the increasing density of cubes on the support surface with increasing KCl concentration. Presumably, the higher cube density also aggravated the local depletion of Cu^{2+} during the reduction cycle, resulting in a reduced growth and smaller initial cube sizes. We note here that this trend is not sustained at the highest Cu:Cl ratio of 1:10, where we also start to see poorly formed cubic structures, suggesting that at 50 mM KCl, the nucleated cubes start to be etched from the support surface by the high dissolution currents present during the oxidative cycles. Within these limits, the final size distribution can be then tuned by adjusting the durations of t_o and t_r and the number of cycles. Increasing the number of cycles by a significant amount, however, appears to have a detrimental effect on the monodispersity of the deposited catalysts (Figure 4.3d). This is likely due to the increase in the probability of the new nuclei formation with additional cycles.[231] It is also interesting that increasing the CuSO$_4$ concentration to 50 mM does not cause an increased coverage of the support surface by Cu structures. Instead, it causes branching of the

initial cubes, as seen in Figure 4.1f. A significant increase of branching has been reported for electrodeposition at high currents or high potentials.[236] In this case, the branching can be attributed to either the mass transport arguments that correlate the Cu concentration to the surface free energy of the particles previously put forth by Radi et al.[237] or the overpotential induced concentration gradients proposed by Siegfried and Choi.[238]

4.4 Conclusion

In this work, we explored the synthesis parameters governing the electrodeposition of size- and shape-controlled cubic Cu_2O structures for catalytic applications. We found that the concentration of Cl^- ions in solution controls the formation of cubic shapes, the cube size, the initial coverage, and the dispersion of the cubes on the support. The ratio of reductive and oxidative times in our alternating potential electrodeposition protocol can be used to tune the coverage of the Cu catalysts on the support surface, whereas the number of cycles determines the size of the cubes and monodispersity. The mechanisms responsible for the Cu cube growth are further investigated by using *ex situ* and *in situ* electron microscopy, featuring the importance of applying successive cycles. These results reveal the role of the alternating potential cycles in controlling the cube growth. In particular, after the Cu nuclei are formed during the first deposition cycle, new layers of material are progressively added and then partially removed in subsequent cycles. The principles described here provide guidelines for obtaining and controlling the growth of monodisperse cubic Cu_2O catalysts."[99]

5 Dynamic Changes in the Structure, Chemical State and Catalytic Selectivity of Cu Nanocubes during CO_2 electroreduction: Size and Support Effects

This chapter is based on the publication "*Dynamic Changes in the Structure, Chemical State and Catalytic Selectivity of Cu Nanocubes during CO_2 electroreduction: Size and Support Effects*", in which I developed the electrochemical preparation of the samples, planned and carried out the experiments, the data analysis, and preparation of the draft. The electrochemical measurements have been supported by Dr. Dunfeng Gao, who also contributed to writing the draft. Fabian Scholten measured the quasi *in situ* XPS and I performed the analysis. The other authors participated in the synchrotron experiments. The code for the wavelet transform analysis was written by Dr. Janis Timoshenko et al. and was modified for our analysis by me. In this chapter, "*in situ* and *operando* spectroscopic and microscopic methods were used to gain insight into the correlation between the structure, chemical state, and reactivity of size- and shape-controlled ligand-free Cu nanocubes during CO_2 electroreduction (CO_2RR). Dynamic changes in the morphology and composition of Cu cubes supported on carbon were monitored under potential control through electrochemical atomic force microscopy, X-ray absorption fine-structure spectroscopy and X-ray photoelectron spectroscopy. Under reaction conditions, the roughening of the nanocube surface, disappearance of the $(1\,0\,0)$[sic][**] facets, formation of pores, loss of Cu and reduction of CuO_x species observed were found to lead to a suppression of the selectivity for multi-carbon products (i.e. C_2H_4 and ethanol) versus CH_4. A comparison with Cu cubes supported on Cu foils revealed an enhanced morphological stability and persistence of Cu^{+}[‡] species under CO_2RR in the former samples. Both factors are held responsible for the higher C_2/C_1 product ratio observed for the Cu cubes/Cu as compared to Cu cubes/C. Our findings highlight the importance of the structure of the active nanocatalyst but also its interaction with the underlying substrate in CO_2RR selectivity."[182]

5.1 Introduction

"In recent years, interest in understanding the parameters that govern the electrochemical reduction of CO_2 (CO_2RR) has increased. The knowledge is used to design catalysts with high selectivity for valuable chemicals and fuels.[239] Among these parameters, the catalyst structure and chemical state are of particular importance.[101,240,241] Compared to polycrystalline Cu elec-

---

** For consistency, this was corrected from $(1\,0\,0)$ to $\{1\,0\,0\}$ here and in the rest of this chapter.

‡ Changed Cu^{I} to Cu^{+} for consistency to the other chapters here and in the rest of the chapter.

trodes, nanostructured Cu catalysts have shown a significantly improved CO$_2$RR performance, attributed to grain boundaries,[242,243] Cu{1 0 0} facets,[35,92,113,115,244,245] increased roughness,[246] defects,[247–249] low-coordinated sites,[102,111,250] and the presence of subsurface oxygen and Cu$^+$ species.[97,131,251–258]

Previous studies[244,245,259] on Cu single crystals have shown the improved C-C coupling performance of {1 0 0} facets, which was further confirmed by the high selectivity towards ethylene observed on cube-shaped Cu catalysts.[131,224,249,260–267] However, the presence of {1 0 0} facets is not the only factor responsible for the superior activity and selectivity of cube-shaped Cu catalysts, with surface roughness, subsurface oxygen and Cu$^+$ species or Cu/Cu$^+$ interfaces formed and/or stabilized under reaction conditions also playing a very important role.[97] The function of oxygen in such structures is particularly intriguing, since on Cu{1 0 0} surfaces it was discussed to contribute to the formation of oxygenated hydrocarbons.[268] The complexity arising from the multiple factors affecting the catalytic performance of cube-shaped Cu catalysts requires a systematic study of the evolution of their structure and oxidation state under *operando* CO$_2$RR conditions.

This work focuses on the understanding of the relative importance of the different factors responsible for specific selectivity trends observed for Cu catalysts during CO$_2$RR, namely, the presence and stability of Cu{1 0 0} facets, defect sites, and the content of Cu$^+$ species and/or subsurface oxygen. By electrochemically growing ligand-free Cu cubes on C supports and comparing with analogous samples supported on Cu foils, we were able to reveal the intrinsic behavior of the cube-shaped Cu NPs catalysts and their dynamic evolution under CO$_2$RR conditions.

5.2 Experimental Methods

5.2.1 Sample Preparation

"A mixture of 5 mM copper sulfate-pentahydrate (CuSO$_4$ x 5 H$_2$O) and 5 mM potassium chloride (KCl) was used as starting material. Electrochemical cycling between an oxidizing (0.55 V vs. RHE) and a reducing potential (0.22 V vs. RHE) with varying number of cycles (1–100), depending on the desired cube size and coverage, lead to the electrodeposition of size- and shape-controlled Cu cubes with a narrow size distribution. Initially, a potential of −0.2 V versus Ag/AgCl was held for 8 s with a subsequent ramp to 0.4 V versus Ag/AgCl for 4 s at a ramp rate of 700 mV s^{-1}. Returning to the initial potential completes the cyclic voltammetry. Cu cube sizes ranging from 80 nm to 1.2 μm were obtained depending on the 1 mM–100 mM KCl and CuSO$_4$ x 5 H$_2$O concentration, the number of cycles, and applied potential. High surface area carbon paper was used as substrate (Toray Carbon Paper TGP-H-060). The Cu cubes on Cu foil were prepared as described in ref.[269].

5.2.2 Surface Characterization

For a thorough investigation of the surface morphology, composition, and changes during the reaction, a variety of characterization techniques were used. For morphological analysis, scanning electron microscopy (SEM) using a Quanta 200 FEG from FEI with a field emitter as electron source as well as an atomic force microscopy (AFM) using a Bruker MultiMode 8 were applied.

The SEM images were acquired in vacuum utilizing a secondary electron detector (Everhart-Thornley). The images were taken with an acceleration voltage of 10 keV at a working distance of 10 mm. With these parameters, the best spatial resolution, field depth, and signal to noise ratio were achieved. For AFM, operation in air was conducted to image the initial morphological state of the samples, with subsequent imaging in liquid under potential control using 0.1 M KHCO$_3$ as electrolyte.

The sample surface was investigated by *in situ* X-ray photoelectron spectroscopy (XPS) in an ultra-high vacuum setup. The XPS setup was equipped with a non-monochromated Al X-ray source (hν = 1486.6 eV) as well as a hemispherical electron analyzer (Phoibos 100, SPECS GmbH). The XPS analysis chamber was connected to an *in situ* electrochemical cell (SPECS GmbH) with an Autolab potentiostat (PGSTAT 302N) to conduct the measurements, so that in between XPS measurements, the sample was not exposed to air. The Auger spectra (Fig. 5.5) were deconvoluted with reference signals from metallic Cu*, Cu$_2$O (from Ref.[239]), CuCl* and CuCl$_2$*. (* Indicates reference spectra measured in our system).

To determine the surface composition of the pristine Cu cubes before and after CO$_2$RR for 1 h at −1.1 V vs RHE, X-ray photoelectron spectroscopy (XPS) data from the Cu-2p (Supplementary Fig. 13.4) and Cu LMM Auger region (Fig. 5.5 in the main text) were acquired in an ultra-high vacuum-(UHV) XPS system directly attached to an electrochemical cell, allowing the transfer of the samples in vacuum to avoid reoxidation. Although no distinction between metallic Cu and Cu$^+$ species can be made in the analysis of the Cu-2p region (Supplementary Fig. 13.4), our fits confirm a content of 64% Cu(I/0), and 36% Cu(II) in the as prepared sample and almost no Cu(II) after reaction (4%). The Cu LMM AES data (Fig. 5.5) were deconvoluted using reference spectra for metallic Cu, Cu$_2$O, CuCl and CuCl$_2$ measured in the same system together with reference spectra by Biesinger et al.[270]. Our quasi *in situ* XPS data reveal that the surface of the pristine Cu nanocubes consisted of 51.7% Cu$_2$O, 21.8% CuCl$_2$, 23.5% CuCl, and 3.0% metallic Cu. After electrochemical treatment for 1 h at −1.05 V vs RHE, the XPS data (no potential applied on the sample during XPS) indicate that the cubes are mostly reduced, but 5% Cu$_2$O was still detected.

5.2.3 Bulk Characterization

Bulk characterization was experimentally realized by energy-dispersive X-ray spectroscopy (EDX) and X-ray absorption fine-structure spectroscopy measurements (XAFS). The EDX spectra were acquired in vacuum with a liquid-N$_2$ cooled detector that was attached to the previously described Quanta 200 FEG microscope. All data shown correspond to an average of at least three separate measurements and the error in the content of the different species was calculated from these. The samples after synthesis and reaction were washed thoroughly and transferred immediately into the SEM chamber to minimize the air exposure and thereby possible reoxidation. *Operando* XAFS measurements were conducted to solidify the findings and give better accuracy about the content of the different Cu, CuO and Cu$_2$O species in subsurface sample regions (volume-averaging technique). For each sample, the full spectrum consisting of the X-ray absorption near-edge structure region (XANES) and the extended X-ray absorption fine structure region (EXAFS) were acquired. After subtracting a baseline for pre- and post-edge as well as a

function for the edge-step, the remaining part of the spectrum in energy space (E-space) is then transferred to wavenumbers (k-space). The resulting spectrum is shown in Supplementary Fig. 13.5. These spectra can be Fourier transformed to get the spectrum in R-space which then can be fitted. These measurements were compared to references and fitted as well. Additionally, Morlet wavelet transform (WT) was performed to better analyze small amounts of oxide species after reaction. In contrast to the traditionally applied Fourier transform (FT), the WT allows two-dimensional separation in distance and frequency space domain simultaneously. The mathematical details regarding the application of WT are discussed by Timoshenko et al.[271]."[182]

5.2.4 Electrochemical Analysis

For electrochemical analysis, an H-type cell, with two compartments separated by a Selemion anion exchange membrane (by AGC), was used. The cell was gas-tight, both compartments were filled with 40 mL of electrolyte, and continuously purged with CO_2 at a flow rate of $20\,mL\,min^{-1}$. The electrolyte used in the experiments was a $KHCO_3$ (Sigma Aldrich, 99%) solution with a concentration of 0.1 M. This acts as a buffer to avoid significant bulk pH changes during the reaction, since this could influence the reaction pathway[52,74,232]. To ensure CO_2 saturation, the electrolyte was purged prior to the experiment to remove dissolved oxygen and saturate the solution. A leak-free Ag/AgCl/3.4 M KCl reference electrode by Innovative Instruments Inc., and a platinum gauze counter electrode by MaTeck ($3600\,mesh\,cm^{-2}$) were used. The sample, which acts as the working electrode in this setup, was fixed with a conductive clamp. Furthermore, all exposed parts of the clamp and the backside of the sample were covered by Kapton tape to exclude possible partaking in the reaction. Each sample was measured with a chronoamperometric step for 1 hour (if not stated otherwise) at each potential. Potential control was realized with an Autolab potentiostat (PGSTAT 302N). The measured potentials were iR-corrected as determined by current interrupt and converted to the reversible hydrogen electrode scale. The catalytic active area was determined by estimating the surface from the SEM images (by size distribution over multiple spots). The products from CO_2RR come in gaseous and liquid form. Gaseous products were measured every 17 min by an online gas chromatograph (GC, Agilent 7890A). The products were separated by different columns (Molecular sieve 13X, HayeSep Q, and Carboxen-1010 PLOT) and subsequently quantified with a flame ionization detector (FID) as well as a thermal conductivity detector (TCD). During the reaction, liquid products as carboxylates (e.g. formate and acetate) are formed. After 1 h of CO_2RR, the liquid products were analyzed by high performance liquid chromatography (HPLC, Shimadzu Prominence), which is equipped with a NUCLEOGEL Sugar 810 column for product separation as well as a refractive index detector (RID) for quantification. In addition, alcohols produced during the reaction were analyzed with a liquid GC (Simadzu 2010 plus) equipped with a silica capillary column and a FID. All offline product analysis was conducted directly after the experiment. From the measured product distribution and the current after 1 h (if not stated otherwise), the reported Faradaic efficiencies (FE(%)) were calculated."[182]

5.3 Results and Discussion

Size-dependent changes in the morphology and composition of Cu cube samples electrodeposited on carbon paper were investigated *ex situ* through scanning electron microscopy (SEM) and energy dispersive X-ray spectroscopy (EDX) before and after CO_2RR (Figure5.3 and Figures 5.1 and 5.2 [...]). In all samples the Cu cubes were found to decrease in size in the course of the first hour of the reaction. Furthermore, in this process the originally flat facets and sharp edges of the Cu cubes were found to roughen, resulting in a porous nanocube surface (see Figure 5.3).
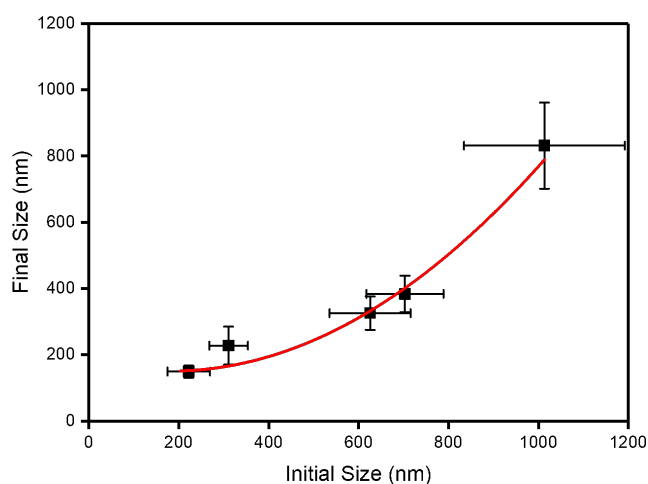

Figure 5.1: Cu-cube edge length measured via SEM before and after 1 hour of CO_2RR at -1.05 V vs RHE. A polynomial fit (2nd order) was applied to serve as guide for the eye. Our data indicate that the size decrease does depend on the initial cube size.
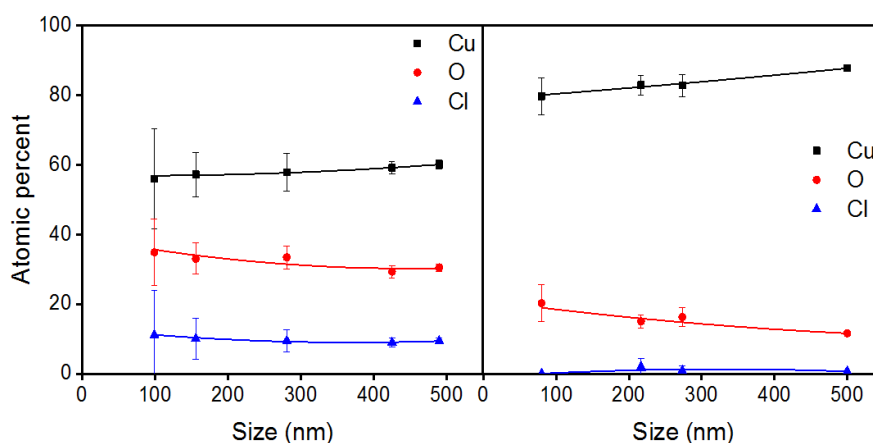

Figure 5.2: Comparison of single Cu-cube EDX before and after reaction and a correlation of their atomic percent. Polynomial fits of 2nd order indicate a size dependent trend, with smaller cubes containing more oxygen and initially more chlorine.
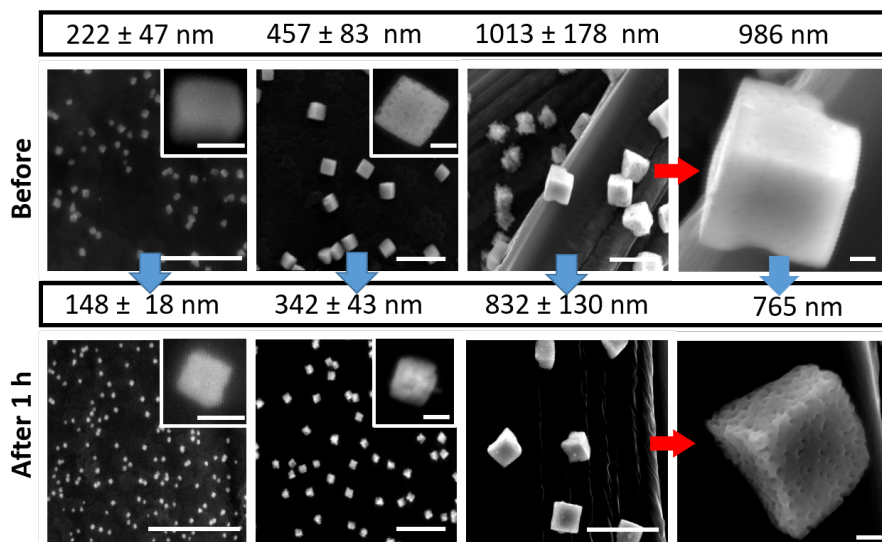
| 222 ± 47 nm | 457 ± 83 nm | 1013 ± 178 nm | 986 nm |

| 148 ± 18 nm | 342 ± 43 nm | 832 ± 130 nm | 765 nm |

Figure 5.3: SEM images from size-controlled Cu nanocube samples electrodeposited on carbon paper acquired before and after CO_2RR at $-1.05\,V$ for 1 h. The scale bars in the main panels are $2\,\mu m$, those in the insets and in the higher magnification image of the last column are $200\,nm$. *Operando* electrochemical EC-AFM measurements carried out on a sample with $100\,nm$-large cubes also revealed significant changes in their morphology already prior to the actual CO_2RR. Sample immersion in the aqueous $0.1\,M$ $KHCO_3$ electrolyte at open circuit potential was observed to lead to the formation of "cracks" on the cube facets. These cracks are likely the result of mechanical stress taking place during the solvation of Cl^- ions while being transferred from the cubes to the electrolyte.

Operando electrochemical atomic force microscopy (EC-AFM) measurements carried out on a sample with approximately $100\,nm$ large cubes also revealed significant changes in their morphology already prior to the actual CO_2RR (Figure 5.4). Sample immersion in the aqueous $0.1\,M$ $KHCO_3$ electrolyte at open circuit potential was observed to lead to the formation of "cracks" on the cube facets. These cracks are likely the result of mechanical stress taking place during the solvation of Cl^- ions while being transferred from the cubes to the electrolyte. SEM-EDX data revealed that Cl was present throughout the entire Cu volume in the as prepared samples and therefore, the loss of Cl leads to drastic structural changes in the entire cube volume.
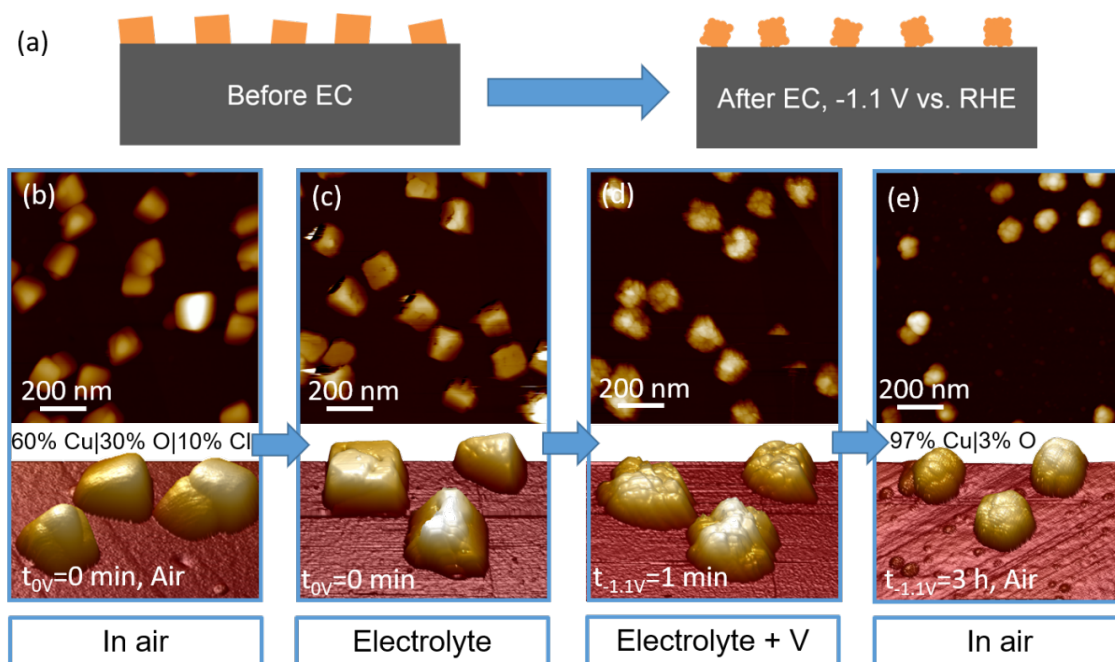
Figure 5.4: (a) Schematic representation of the morphological evolution of Cu nanocube catalysts. (b-e) AFM images of Cu nanocubes electrodeposited on highly oriented pyrolytic graphite (HOPG) acquired in air (b), and *operando* EC-AFM measurements in a CO_2-saturated 0.1 M $KHCO_3$ aqueous solution at open circuit potential (c), at -1.1 V vs RHE in the same electrolyte for 1 min (d), and after 3 h under the same conditions as in (d) and subsequent air exposure (e).

A 1 min potential pulse at 1.1 V versus the reversible hydrogen electrode (RHE) resulted in the further roughening of the nanocube surface, loss of sharp corners and edges, and a decrease in the edge length of approximately 10%. The latter is assigned to the initial reduction of Cu_2O to Cu as well as some loss of Cu. After 3 h CO_2RR at -1.1 V versus RHE, an additional 10% decrease of the NP size was observed, with rough spherical-like NP shapes.

X-ray-induced Cu LMM Auger electron spectra (XAES) were acquired from pristine C-supported Cu cubes (220 nm) before and after CO_2RR for 1 h at -1.1 V versus RHE in an ultrahigh vacuum (UHV) XPS system directly interfaced to an electrochemical cell. Thus, the sample could be transferred in vacuum to avoid re-oxidation.[97] Additional Cu 2p XPS data are also included in Supplementary Figure 13.4. A surface composition of the pristine C-supported Cu cubes of 52% Cu_2O, 22% $CuCl_2$, 23% CuCl, and 3% metallic Cu was obtained before reaction, Figure 5.5. After the electrochemical treatment, the cubes are mostly reduced, with only 4.6% Cu_2O detected. Interestingly, a higher content of Cu^+ species (13%) was detected after CO_2RR on similarly synthesized Cu cubes supported on a Cu foil, and no Cu^+ at all in the pristine Cu foil support after CO_2RR (Supplementary Figure 13.5). The latter finding highlights the key role of having a Cu cube/Cu foil interaction for the stabilization of Cu^+ species.
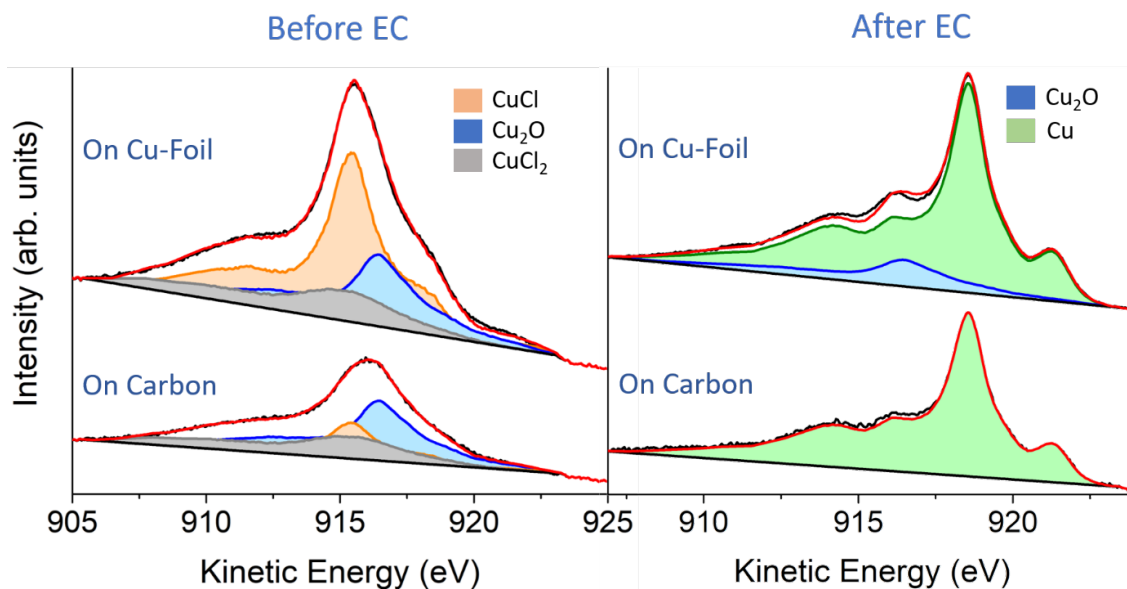
Figure 5.5: Quasi *in situ* Cu Auger LMM XAES spectra of 220 nm Cu cubes electrodeposited on C paper and 250 nm cubes deposited on a Cu foil acquired before (left) and after 1 hour of CO_2RR at -1.1 V versus RHE (right).

To gain further insight into the stability of Cl, Cu^I species, and subsurface oxygen in our Cu cubes under CO_2RR, *operando* X-ray absorption fine-structure (XAFS) measurements were conducted on 120 nm Cu cubes, Figures 5.6 and 5.10 (see also Figures 5.7, 5.8, and 5.9 [...] for more details). As compared to XPS and XAES, probing about 10 nm below the surface, XAFS is a bulk sensitive technique that reveals the overall change in the structure and composition of the Cu cubes.
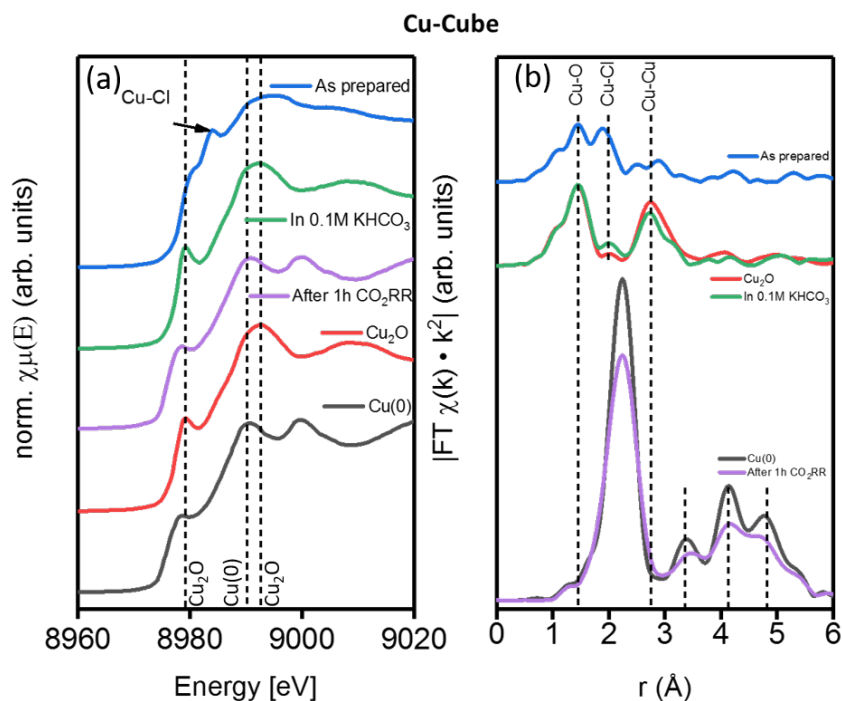
Figure 5.6: Normalized XANES region (a) and Fourier-transform magnitudes of k^2-weighted EXAFS data of pristine Cu cubes (b) measured as prepared, in 0.1 M $KHCO_3$ at open circuit potential and in the same electrolyte after 1 h of CO_2RR at -1.1 V vs RHE.
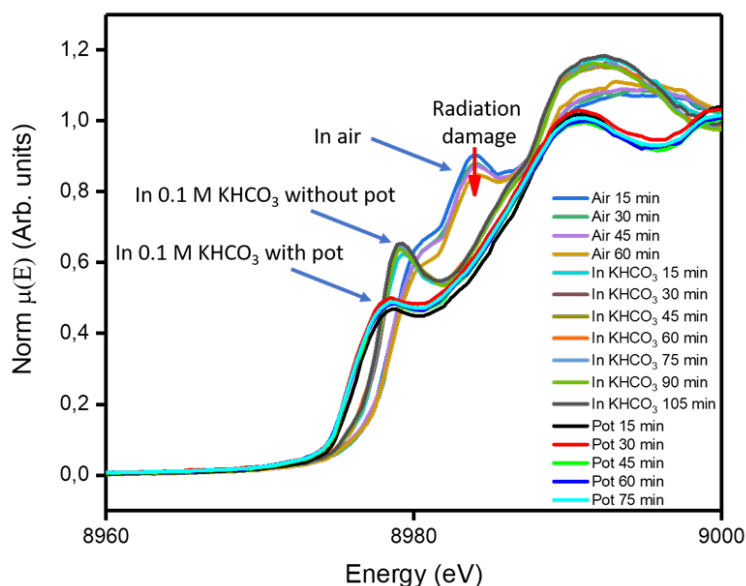
Figure 5.7: *Operando* XANES data acquired on 120 nm Cu-cubes deposited on C conducted in 15 min time steps. The individual measurements in air, in electrolyte (0.1 M $KHCO_3$) without potential and in electrolyte with potential are shown. The potential of the data shown is -1.1 V vs RHE.

Figure 5.8: k-space EXAFS data of pristine Cu nanocubes acquired under *operando* conditions during CO_2 electroreduction at $-1.1\,\mathrm{V}$ vs. RHE in $0.1\,\mathrm{M}$ $KHCO_3$. Data from the as prepared sample, a metallic Cu reference, and a Cu_2O reference sample, all measured in air, are also included for comparison.

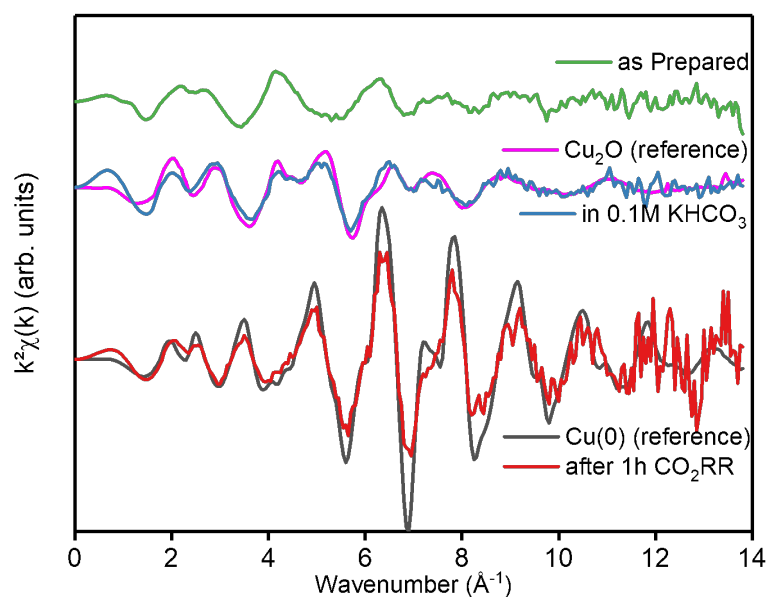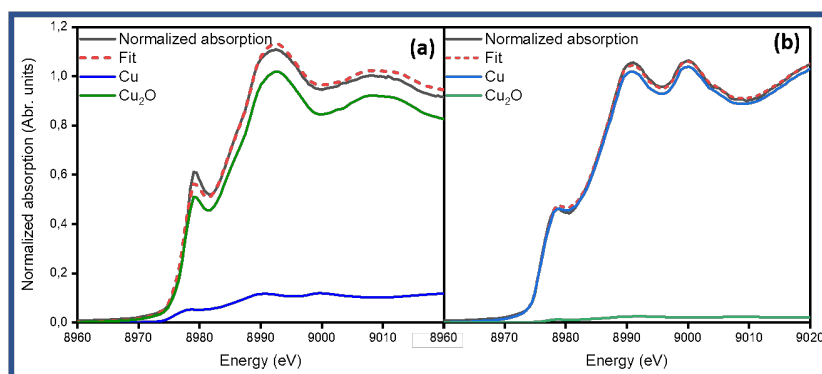Figure 5.9: Deconvolution of the XANES region of Cu nanocube samples. On the left, a linear combination fit of the pristine Cu-cubes in $0.1\,\mathrm{M}$ $KHCO_3$ before and on the right after $1\,\mathrm{h}$ of CO_2RR at $-1.1\,\mathrm{V}$ vs RHE is shown.

The as prepared state of the Cu cubes shows a mixture of Cu_2O and $CuCl_x$, which almost immediately changes fully into Cu_2O upon becoming in contact with the electrolyte. In CO_2-saturated $0.1\,\mathrm{M}$ $KHCO_3$, the spectrum resembles greatly the Cu_2O reference, with only a very small difference where the Cl-feature was previously observed and a small decrease of the Cu-O feature. After $1\,\mathrm{h}$ at $-1.1\,\mathrm{V}$ versus RHE, the spectrum obtained for the Cu cubes resembles that of metallic Cu. The Fourier Transform (FT) data obtained for the Cu cubes in the electrolyte after $1\,\mathrm{h}$ CO_2RR at $-1.1\,\mathrm{V}$ versus RHE are less intense in comparison to a bulk Cu foil, indicating a lower atomic coordination and/or enhanced disorder. From the first shell Cu-Cu fit after $1\,\mathrm{h}$ of

applied potential, a coordination number (CN) of 10.8 was obtained for the Cu cubes (vs. 12 expected for bulk fcc-Cu). The lower CN values might be indicative of the formation and growth of pores on the Cu cubes under reaction conditions or the partial disruption of the nanocubes, leading to an increased surface roughness. The *operando* EC-AFM data also revealed the formation of cracks (defects) on the Cu cubes even before applying the potential once they were exposed to the electrolyte. The porous structure seen by SEM can also be a result of the progressive CuO_x reduction during the reaction. Under reaction conditions, these pores as well as the cube corners and edges appear more prone to dissolution than the higher coordinated flat facets.

Since Cu^+ species[268] have been suggested to play an important role in CO_2RR selectivity, in order to better detect small amounts of Cu-O species an additional analysis of the XAFS data by wavelet-transform[271] (WT) was applied (Figure 5.10). Details on this analysis are given in the Suppl. documents. After processing the measured spectra and doing the Morlet WT, the spectra were normalized to the highest signal, allowing subtraction of measured reference materials. The Cu cubes on C in their as prepared state display a large feature at R≈1.4 Å and k≈3.9 Å^{-1} which represents the Cu-O shell, whereas at a slightly higher distance (R≈2 Å, k≈7 Å^{-1}) the interaction of Cu with the heavier Cl atoms is visible. For the as prepared sample, only a faint Cu-Cu 1st and 2nd neighbor interaction is observed after the subtraction of a Cu_2O reference from the pristine Cu cubes, indicating that the sample consists almost exclusively of Cu_2O and $CuCl_x$. In the electrolyte, the $CuCl_x$ feature immediately disappears and a Cu-O-Cu feature arises at R≈3 Å and k ≈4 Å^{-1}. In addition, the magnitude of the Cu-O component decreases slightly. After 1 h of CO_2RR, the most prominent feature is that of the Cu-Cu first shell (R≈2.3 Å, k ≈7 Å^{-1}). The pristine Cu cubes resemble almost exactly the metallic Cu reference after 1 h of CO_2RR. A deconvolution of the Cu XANES region of pristine Cu cubes in 0.1 M $KHCO_3$ with Cu, Cu_2O, and CuO standards, Figure 5.9, yields a composition of 99% Cu and 1% (within the error margin) Cu_2O after 1 h of CO_2RR. CuO could not be reasonable fitted. These findings are in good accordance with the XPS surface analysis indicating that for the Cu cube/C system, no Cu_2O species remain after 1 h of reaction either at the surface (XPS) or in sub-surface regions (XAFS), which is in clear contrast with previous findings for Cu cubes/Cu foil (Figure 5.5).[97,131]
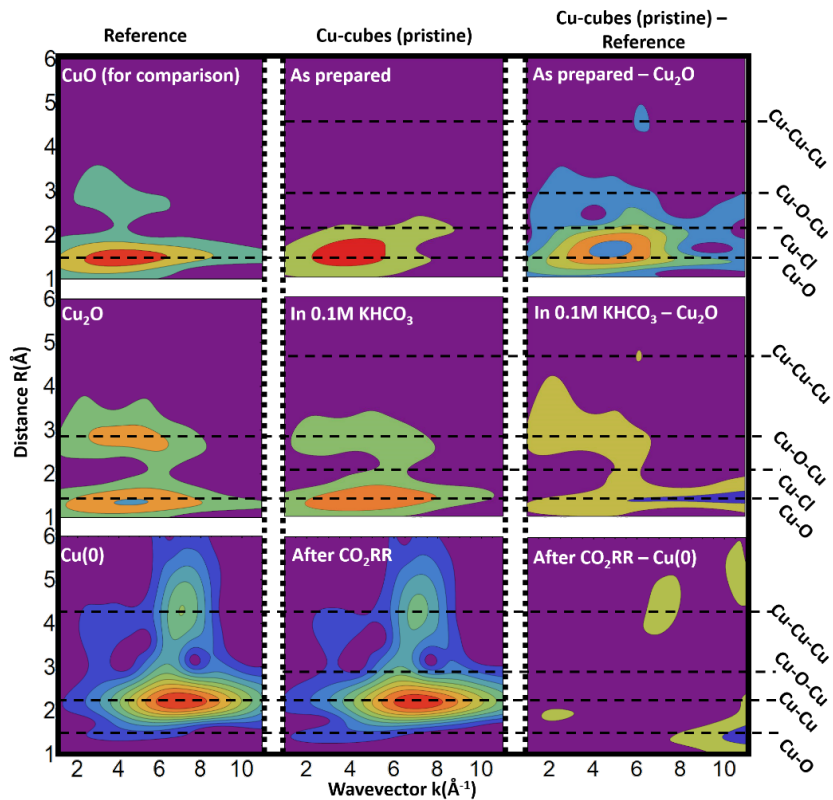
Figure 5.10: Wavelet transform of Cu nanocubes as prepared, in 0.1 M KHCO$_3$, and after 1 h of CO$_2$RR as well as the references used. The height is normalized to 1 (based on the highest peak) and the subtracted images scaled by a factor of two for better visibility.

After observing drastic changes in the morphology and chemical composition of the samples under *operando* reaction conditions within the first 1–3 hours, the electrochemical performance was studied in order to gain insight into structure/chemical-state/reactivity correlations. The background signal from the C-paper support was subtracted from all data presented as shown in Figure 5.11.
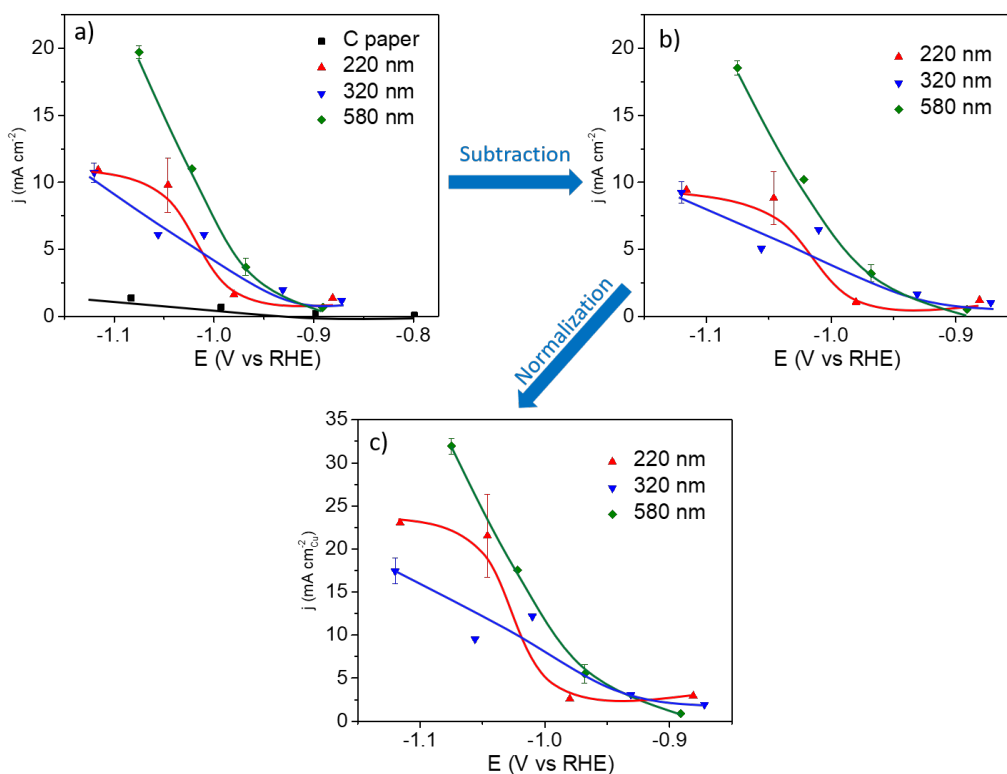
Figure 5.11: (a) Geometric current density of pristine Cu-cubes with an average size of 220, 320, and 580 nm and the clean C-paper support at potentials between -1.15 V and -0.85 V vs RHE. The contribution from the C-paper support was subtracted in (b). The data in (a) and (b) are shown normalized by the total sample area, which includes the cubes and the carbon support. In (c), the data are normalized by the real Cu surface area extracted from the analysis of SEM images.

A comparison between HER Faradaic efficiency (parasitic reaction) and the sum of the Faradaic efficiency of all products from CO_2RR is displayed in Figure 5.12. Detailed information on the different products detected can be found in Figure 5.13 for the 220 nm Cu cubes and in Figures 5.14, 5.15 and 5.16. Similar trends for small Cu-Au cubic NPs were reported in ref.[272].
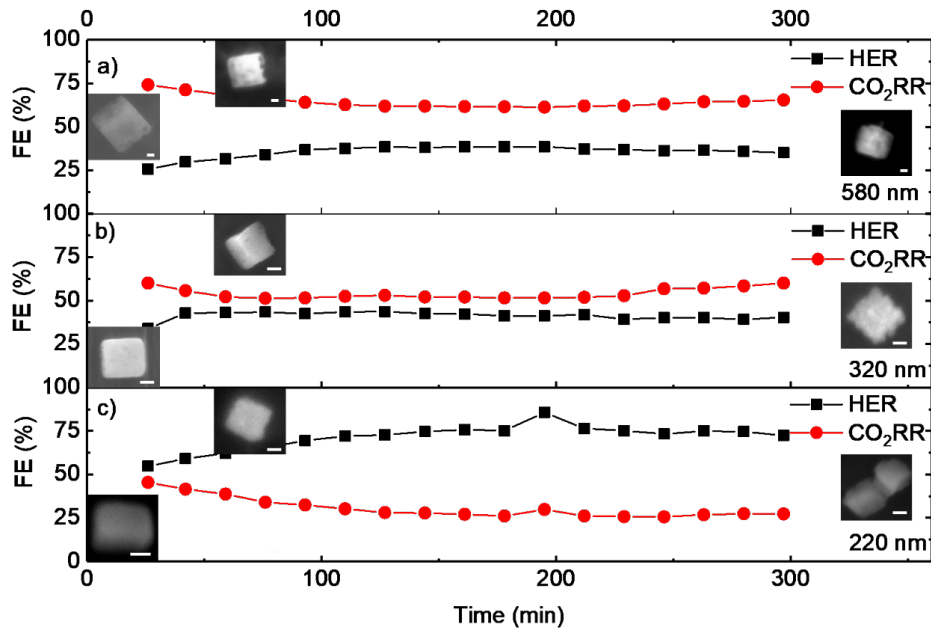
Figure 5.12: Faradaic efficiency for CO$_2$RR and HER at approx. -1.05 V vs RHE recorded during 5 h for samples with different Cu-cube sizes (580 nm, 320 nm and 220 nm). The insets display SEM images of typical Cu cubes measured after different reaction times. The size of the scale bars is: 100 nm.
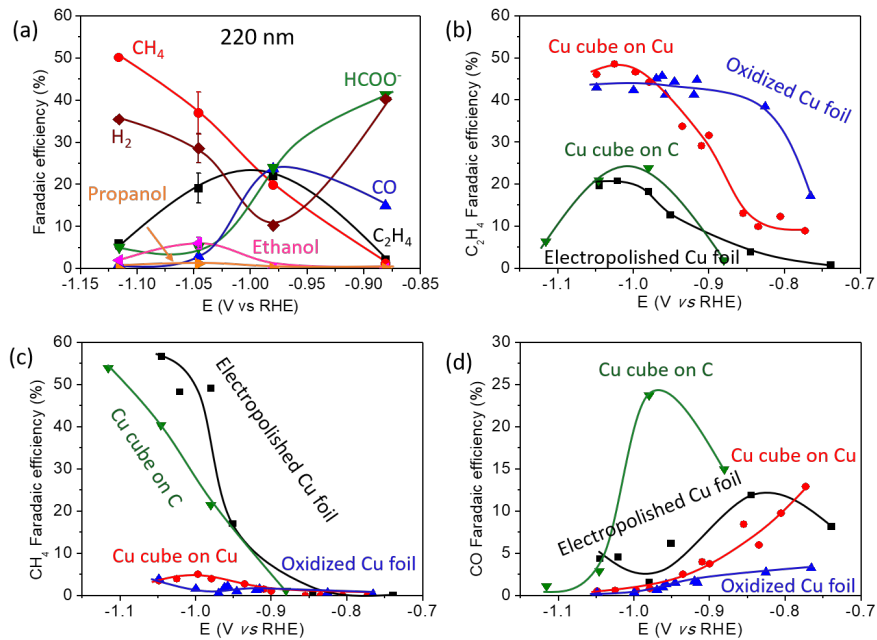
Figure 5.13: (a) Faradaic efficiency of pristine 220 nm Cu-cubes on C as a function of the applied potential obtained after 1 h of CO$_2$RR. Faradaic efficiencies for C$_2$H$_4$ (b), CH$_4$ (c), and CO (d) are also shown for the pristine 220 nm Cu cubes on C, analogously prepared 250 nm Cu cubes on Cu foil and two reference Cu foils electropolished and O$_2$-plasma treated (20, 20 W, 400 mTorr[97,131]).
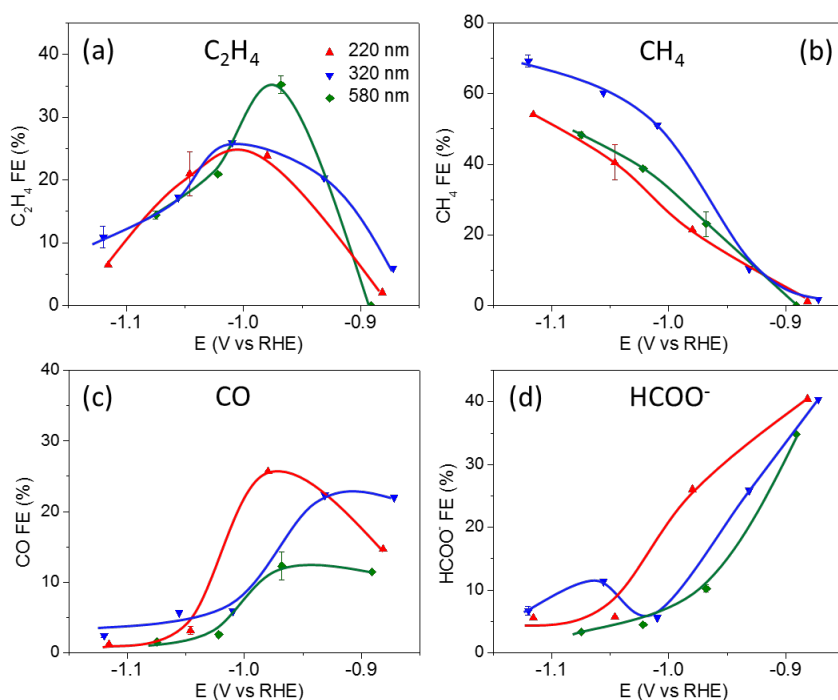
Figure 5.14: Faradaic efficiency for ethylene (a), methane (b), carbon-monoxide (c), and formate (d) obtained after 1 hour of CO_2RR at different potentials. The products produced by a reference blank substrate scaled to the (approximate) unoccupied carbon paper in the samples was subtracted to show only the products from the Cu-cubes.
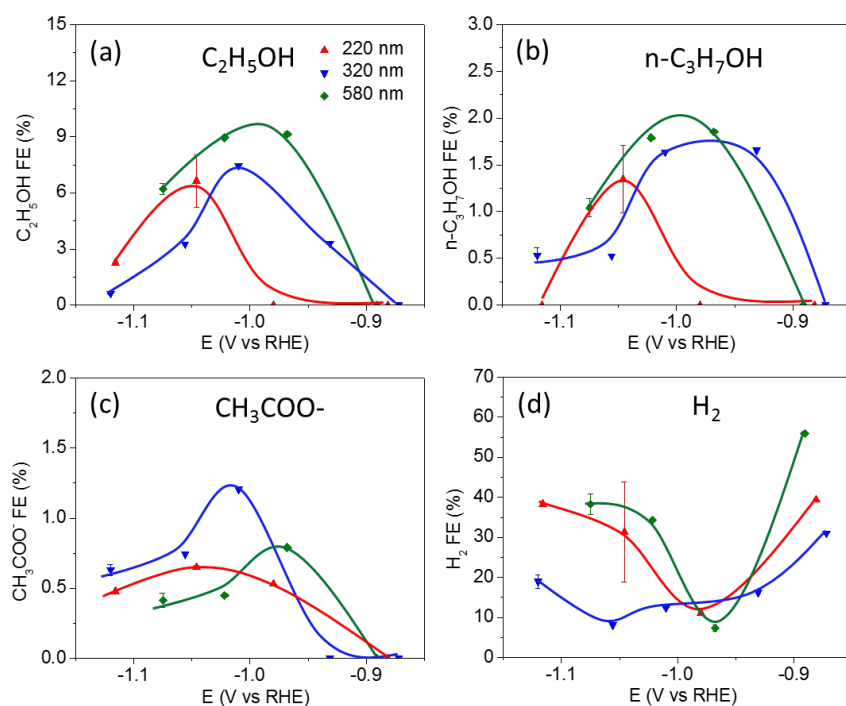
Figure 5.15: Faradaic efficiency for ethanol (a), 1-propanol (b), acetate (c), and hydrogen (d) after 1 hour of CO_2RR at different potentials.
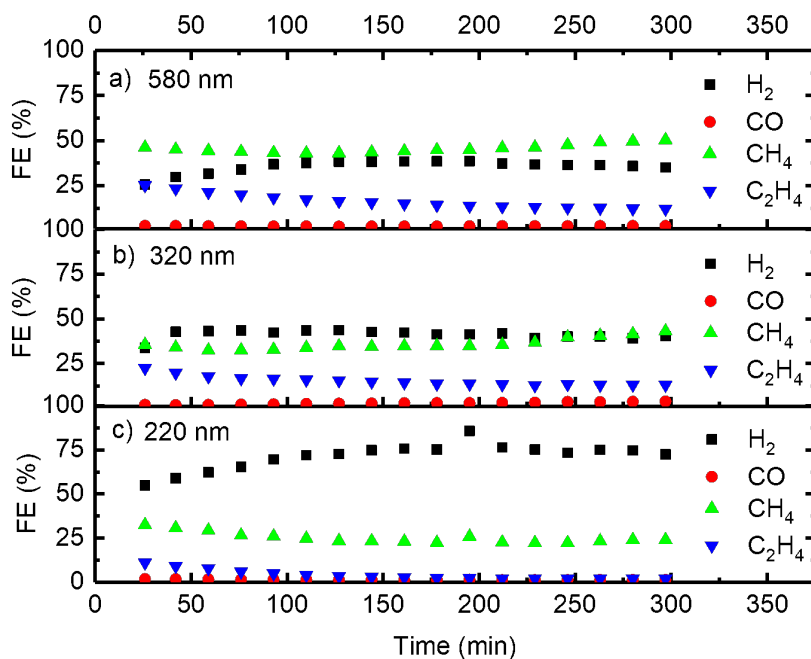
Figure 5.16: Temporal evolution of the product selectivity during CO_2RR for 580 nm (a), 320 nm (b), and 220 nm (c) Cu nanocubes measured at -1.05 V vs RHE for 5 h. For smaller cube sizes, H_2 production outweighs the production of hydrocarbons, whilst on the bigger and more morphologically stable Cu-nanocubes this trend reverses.

For the stability tests, Cu cubes of three different initial sizes were investigated at -1.05 V versus RHE, Figure 5.12. This potential was chosen since we expect to see the highest selectivity towards C2-C3 products.[16] The total CO_2RR FE was found to increase with increasing Cu cube size, and achieves an initial value of approximately 75% on the 580 nm cubes. This is assigned to the enhanced morphological stability of the larger cubes. A second general trend, independent of size, is a decrease in Faradaic efficiency for CO_2RR and increase in HER over time. An exception is the sample containing 220 nm Cu cubes, which starts already with higher Faradaic efficiency for HER over CO_2RR. The smaller cube size on the weakly binding C support leads to a lower stability of the Cu cubes, leading to the loss of material into the electrolyte and possible subsequent re-deposition as small clusters on the support and Cu cubes. Such low-coordinated structures were found to result in an increase in the H_2 and CO production and decrease in the formation of hydrocarbons, that is, they favor HER over CO_2RR.[100,273] This correlates with the observed morphological changes shown in Figures 5.3 and 5.4, where a rounding of corners and edges and roughening of the facets is observed.

Figure 5.13a displays the FE data for the pristine 220 nm Cu cubes on C measured as a function of the applied potential after 1 h of CO_2RR. The production of C2 and C3 products peaks around -1.0 V versus RHE, whilst hydrogen evolution is the lowest at this potential. At potentials more negative than -1.0 V versus RHE, C2/C3 products decline, whilst methane production keeps increasing.

The FE for C_2H_4, CH_4 and CO as a function of the applied potential for the pristine 220 nm Cu cubes on C together with similarly synthesized 250 nm Cu cubes supported on a Cu foil as well as electropolished and O_2-plasma-treated Cu foils are shown in Figure 5.13(b–d). A very strong support-effect is evident, with the Cu cubes grown on the weakly-interacting C support displaying a higher overpotential and much lower FE for C2-C3 products than the similarly-sized Cu cubes on the Cu foil. In fact, as can be seen in Figure 5.13(c), the production of CH_4 of the Cu cubes on C resembles the metallic electropolished Cu foil, although the CO production of the Cu cubes on C is much higher, Figure 5.13(d). It is remarkable that the pristine Cu cubes on the Cu foil, which were found to better stabilize Cu^+ species under reaction conditions (Figure 5.5), behave similarly to the O_2-plasma treated Cu foils. Therefore, we can confirm a direct correlation between the stabilization of Cu^+/Cu interfaces (Cu cubes on Cu foil) and the selectivity for C2-C3 products, since metallic Cu cubes supported on C are more selective for C1 products. This is however not the only reason for the change in the selectivity. Even more important are the drastic structural changes observed for the Cu cubes on C. The roughening of the Cu$\{1\,0\,0\}$ facets, partial loss of the cubic shape and formation of pores as well as detachment from the surface play a critical role in the selectivity switch reported here.

A simple electrochemical method for the synthesis of cube-shaped nanoparticles of tunable size supported on carbon substrates is presented here. Dynamic morphological and chemical transformations of Cu cubes during CO_2RR were monitored using *operando* EC-AFM and XAFS. Drastic changes in the cube morphology were found to take place for the Cu cubes on C under CO_2RR conditions, including the roughening and loss of $\{1\,0\,0\}$ facets, loss of Cu atoms from edge and corner sites, and the reduction of CuO_x species.

5.4 Conclusion

The selectivity for CO_2RR versus HER was found to decrease with decreasing cube size, which was assigned to more drastic changes in the cube morphology taking place under CO_2RR conditions over smaller cubes. In contrast with the findings previously reported for Cu cubes grown on Cu foils, a surprisingly high selectivity for CH_4 as compared to C_2H_4 was observed when deposited on C. The observed morphological instability of the Cu cubes on C versus those deposited on Cu, together with the absence of stable Cu^+ species in the former samples are considered responsible for the preferred selectivity for C1 products."[182]

6 Imaging electrochemically synthesized Cu$_2$O cubes and their morphological evolution under conditions relevant to CO$_2$ electroreduction

This chapter is based on the publication "*Imaging electrochemically synthesized Cu$_2$O cubes and their morphological evolution under conditions relevant to CO$_2$ electroreduction*", where I developed the electrochemical preparation of the samples, planned the experiments and actively participated in carrying out the experiments, the data analysis, and the preparation of the draft. "[...] Here, using liquid cell transmission electron microscopy, we show the formation of cubic copper oxide particles from copper sulfate solutions during direct electrochemical synthesis and their subsequent morphological evolution in a carbon dioxide-saturated 0.1 M potassium bicarbonate solution under a reductive potential. Shape-selected synthesis of copper oxide cubes was achieved through: (1) the addition of chloride ions and (2) alternating the potentials within a narrow window where the deposited non-cubic particles dissolve, but cubic ones do not. Our results indicate that copper oxide cubes change their morphology rapidly under carbon dioxide electroreduction-relevant conditions, leading to an extensive re-structuring of the working electrode surface."[231]

6.1 Introduction

"Metal nanoparticles (NPs) are important catalyst materials for various energy harvesting applications because of their unique structural and electronic properties[274–277]. Therefore, there has been significant research into ways to engineer the detailed structure of NPs in order to create electrocatalysts with improved activity and selectivity for various electrochemical reactions. In particular, designing an effective electrocatalyst for the selective reduction of CO$_2$ (CO$_2$RR) into valuable products, such as ethylene or ethanol[268,277,278], is still an on-going challenge. CO$_2$RR powered by renewable energy sources is an attractive strategy for the sustainable production of chemicals and fuels. In this reaction, it is known that Cu-based nanostructures with cubic morphology have increased selectivity toward the desired C$_{2+}$ reaction products[131,182,260,277]. It has also been shown that the detailed morphological parameters of cubic NPs, such as size and surface structure, can be used to further control the selectivity and stability[131,182,260]. Nevertheless, we still lack the precise control needed to fine-tune the structure of these NPs and optimize their electrocatalytic properties, despite the range of synthesis methods we have at our disposal to create NPs of different size, shape and composition, because it is not always clear which synthesis parameter is responsible for a certain morphology[279]. Another key question related to the use of shape-selected NPs in catalytic applications is their morphological stability under reaction conditions, and whether the favorable structural motifs that are expected to lead to specific activity and selectivity trends persist

during electrocatalysis. This question can be addressed through *in situ* and *operando* microscopic observations.

The synthesis of cubic-shaped Cu NPs can be achieved by wet chemical methods[260,280,281] or by electrodeposition[182,282,283]. In chemical synthesis, shape selection is often achieved via the addition of facet-stabilizing ligands[260,280]. It is also commonly accepted that chloride ions (Cl^-) in the precursor solution encourage nanocube formation because they stabilize the $\{1\,0\,0\}$[sic]** facets of Cu[235,284]. However, how such effects lead to cube formation during electrochemical synthesis is yet to be clarified. The electrochemical synthesis of shaped-controlled NPs through halide additives is interesting for a few reasons. First, this method generates well-dispersed, shape-controlled NPs directly anchored to the support without the need of organic surfactants to keep the shape. In contrast, colloidal chemical synthesis usually needs organic surfactants[260,285] which might be strongly attached to the catalyst surface, leading to catalytic properties that might be altered with respect to those from the underlying metal. Second, these halide anion species can also play a role in modifying the CO_2RR selectivity[97]. A better understanding of the shape-selection mechanism(s) during electrochemical synthesis will allow us to develop strategies to control the formation of Cu-based nanocubes for subsequent CO_2RR applications.

Liquid cell transmission electron microscopy (LC-TEM) is a relatively new technique that allows us to directly image nanostructures in a liquid environment with the high spatial resolution of a TEM[192,286,287]. By integrating thin film electrodes into the cells, we can study the dynamic behavior of materials in an electrolyte and under applied potential[155,192,288–295]. Although LC-TEM has been previously used to investigate shape-control mechanisms during colloidal synthesis[296–298], it also constitutes a promising approach for the *in situ* study of electrocatalyst stability under reaction conditions[155,295]. In electrochemical LC-TEM studies, the electrocatalysts are usually synthesized using wet chemistry and then drop-casted on the working electrode of the liquid cells (LCs). While nonuniform Cu electrodeposition has already been shown in liquid TEM cells[192,288,299–301], the electrochemical synthesis of shape-controlled particles within LCs is more challenging, due to their small volume and nonstandard thin film electrodes, and has not yet been demonstrated.

In this study, we show that we can electrochemically deposit Cu_2O cubes directly from an aqueous $CuSO_4$ solution within the LCs, and follow their subsequent stability in a CO_2-saturated $KHCO_3$ electrolyte under electrochemical reduction conditions. We further demonstrate that the shape-selection is due to Cl^- ions encouraging the formation of Cu_2O particles, together with the enhanced stability of the Cu_2O $\{1\,0\,0\}$ facets, which protect the cubic Cu_2O particles from dissolution at mildly oxidative potentials. Subsequently, we illustrate that fast morphological changes take place in the electrodeposited particles under conditions relevant to CO_2RR. The latter results have significant implications for our understanding of the catalytic structures that exist under the actual reaction conditions and determine the selectivity trends.

** For consistency, this was corrected from $(1\,0\,0)$ to $\{1\,0\,0\}$ here and in the rest of this chapter.

6.2 Experimental Methods

6.2.1 Chemicals and Materials

Potassium chloride (KCl, 99.0–100.5%), copper sulfate pentahydrate (CuSO$_4$ x 5 H$_2$O, 99.995%) and potassium bicarbonate (KHCO$_3$, 99.9%) were obtained from Sigma-Aldrich. All chemicals were used as received.

6.2.2 LC-TEM Experiments

For these experiments, a liquid biasing DENSsolution Stream holder and a flow cell chip equipped with a silicon nitride window and three Pt electrodes were employed. An overview of the electrode is displayed in Fig. 6.2. A pressure based-liquid pump was used to flow the working electrolyte (CuSO$_4$ + KCl and/or CuSO$_4$ solutions) inside the microfluidic cell and a CompactStat potentiostat (Ivium Technologies, Netherlands) was connected to the holder for conducting the electrochemical deposition of copper particles on the working electrode. The LC-TEM holder was leak tested in a vacuum pump station provided by DENSsolutions.

The *in situ* microscopy was performed using a FEI Titan 80-300 kV transmission electron microscope operated in scanning (STEM) mode at 300 kV. Electron beam conditions were selected to optimize the imaging conditions while maintaining a low overall electron dose rate of no more than 20 e$^-$ nm^{-2} s^{-1} during image acquisition. At these dose rates, we did not see obvious effects of the electron beam on the experiment, dynamic changes were only observed during the application of the potential. The movie acquisition rate was 1 frame per second.

Cu$_2$O cubic particles were grown in a 5 mM CuSO$_4$ + 5 mM KCl solution by electrochemical cycling in a potential window of 0.3 V between the starting points of the Cu reduction and oxidation processes at a sweep rate of 5 mV s^{-1}. The limits of the scan were determined *in situ* by finding the potentials at which extensive Cu deposition/dissolution were observed on the working electrode. Such approach was implemented because there were shifts in the potentials between *in situ* experiments of up to ∼200 mV, which we partially assigned to the microfluidic electrochemical cell configuration and the Pt pseudo-reference electrode. Hence, the potentials we used for the *in situ* imaging show small deviations from the potentials we employed in the benchtop set-ups. Similar deviations have also been reported by other researchers[302].

6.2.3 *Ex situ* SEM and TEM Imaging

A Thermo Fisher Apreo scanning electron microscope was used to collect *ex situ* images of the chip. TEM, HRTEM, and EDX elemental mapping of the cubic particles deposited on the TEM grid were acquired on a high resolution analytical transmission electron microscope (JEOL, JEM-2800)."[231]

6.3 Results and Discussion

6.3.1 Observation of Cubic-Shaped Cu$_2$O Particle Growth.

First, we discuss the synthesis of cubic-shaped Cu$_2$O particles. A scheme of the cell setup, with a cross-section of the TEM LC and the top view of the chip which contains the three Pt electrodes (working electrode, reference electrode and counter electrode) is shown in Fig. 6.2. The LC was first filled by flowing the precursor solution (aqueous 5 mM CuSO$_4$ or 5 mM CuSO$_4$ + 5 mM KCl solution)[182] through the internal tubing prior to loading the holder into the TEM. Subsequently, the Pt working electrode was held at open circuit potential (OCP). Figure 6.1a shows the image sequence that was captured with scanning transmission electron microscopy (STEM) and the cyclic voltammetry recorded a potential range of −0.10 and 0.20 V vs. a Pt pseudo-reference at 5 mV s^{-1}, respectively. The first image clearly reveals that there is no copper deposited on the working electrode at the start of the experiment.
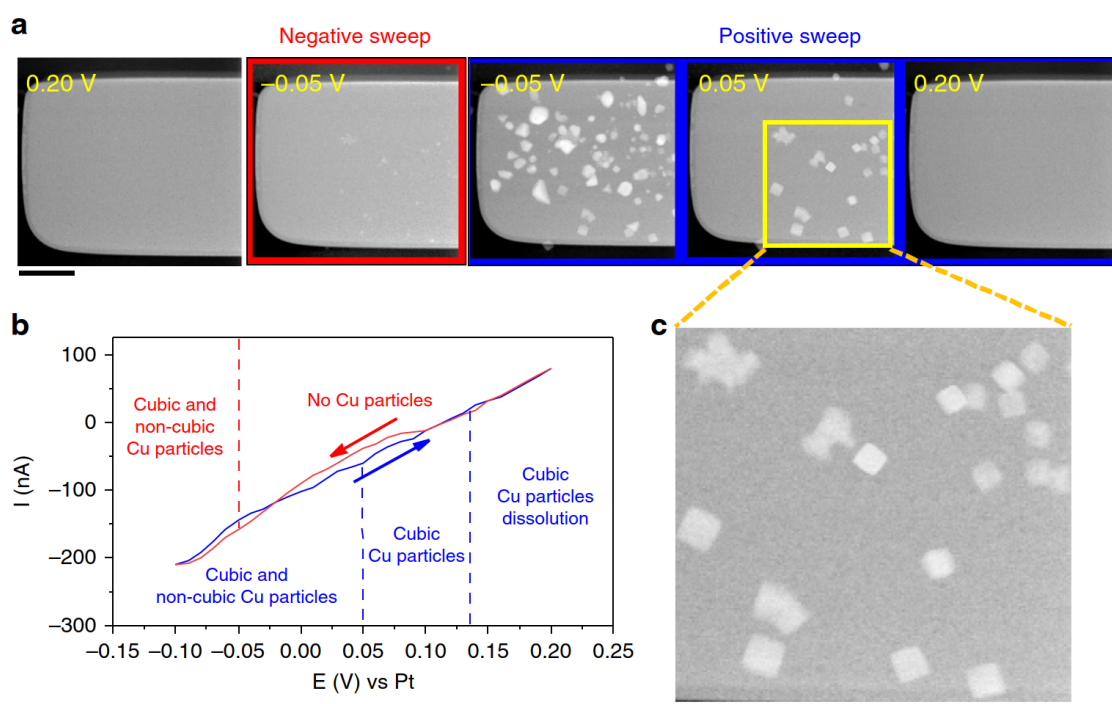
Figure 6.1: **Electrochemical deposition of Cu$_2$O cubes. a** STEM images of the Pt working electrode at different potentials. The scale bar corresponds to 2 μm. **b** Cyclic voltammetry recorded at a scan rate of 5 mV s^{-1} in 5 mM CuSO$_4$ + 5 mM KCl solution. **c** Expanded image extracted from the STEM image of the working electrode at −0.05 V during the positive-going scan clearly identifying Cu$_2$O cubes on the electrode. The scale bar corresponds to 500 nm.
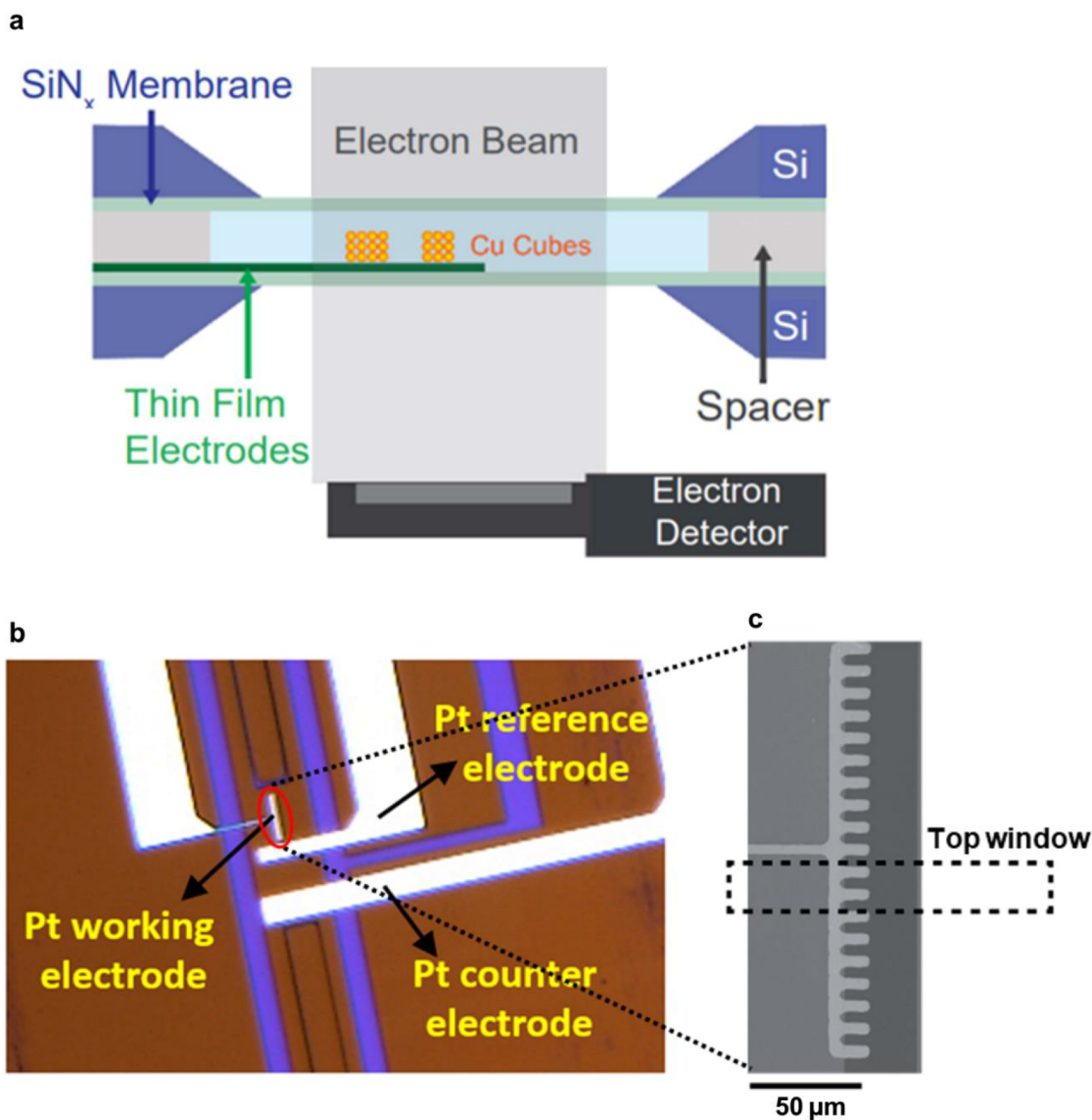
Figure 6.2: **Overview of an electrochemical cell setup**, with **a**, a cross section of the TEM liquid cell on the top and **b**, view of the electrodes on the electrochemistry chip from DENS solutions on the bottom. As shown in the schematic, the liquid cell isolates the electrolyte from the vacuum of the TEM column by enclosing the liquid between two electron-transparent silicon nitride membrane windows. **c**, SEM image of the working electrode in the liquid cell. The dashed box denotes the approximate size of the top window.

The second and third images show that particles nucleated and grew as the potential was ramped toward negative values. At these potentials, the shape and size distribution of the electrochemically deposited particles were inhomogeneous. As the potential was ramped to positive values once again, the non-cubic structures dissolved and only cubic particles remained on the working electrode (fourth image from Fig. 6.1a, c). Eventually, the cubes also dissolved as the potential approached 0.20 V. A movie describing the entire sequence is provided as Appendix Movie* 13.6. Appendix Movies 13.7 and 13.8 show extended videos of the electrode under OCP at two magnifications, one

---

∗ Here in form of a figure in the appendix

at our typical imaging magnification and the second at a higher magnification. SEM images taken *ex situ* after synthesis also show the formation of cubes on other areas of the working electrode that had not been illuminated by the electron beam (Fig. 6.3). These results indicate that there was no beam-induced nucleation at our imaging conditions and that the particle formation/dissolution were controlled by the applied potential.
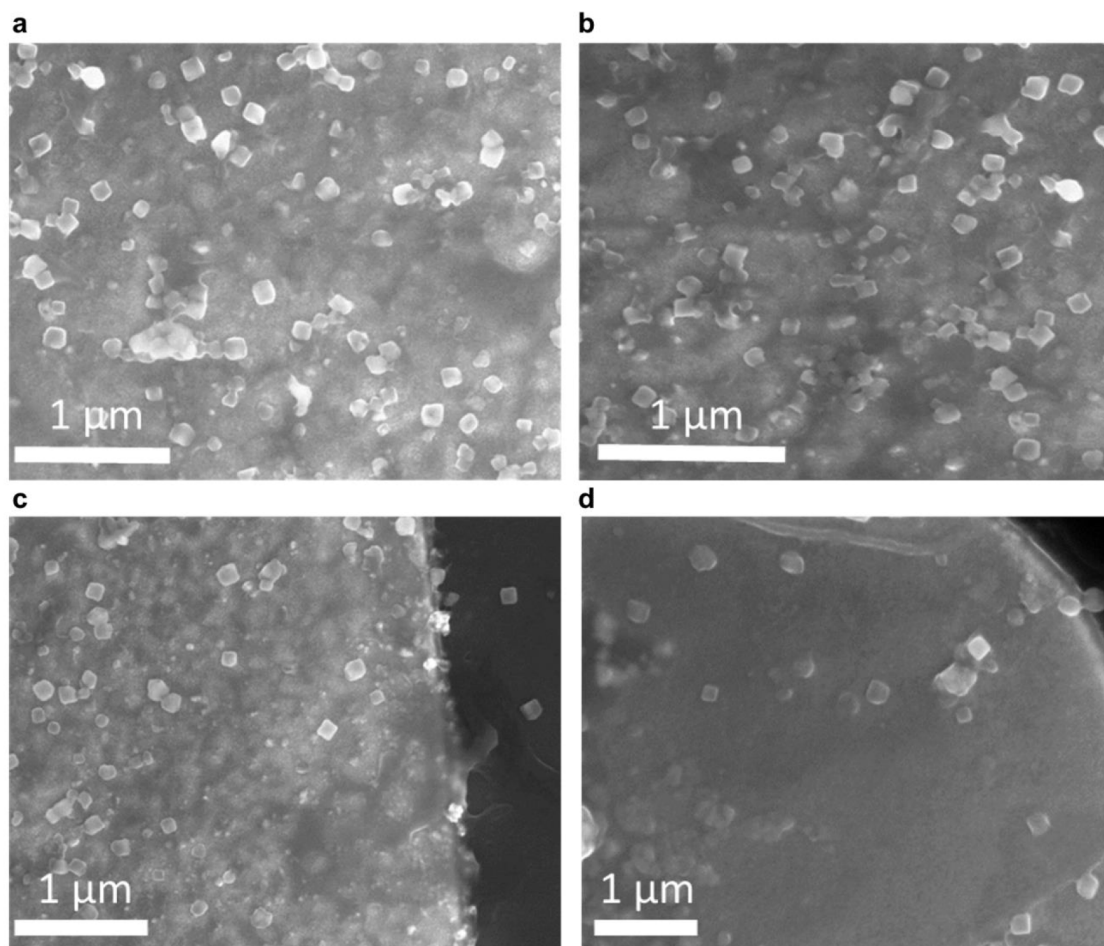
Figure 6.3: **a-d**, *Ex situ* SEM images of the working electrodes in an experiment where we carried out the synthesis outside the TEM, i.e., the samples were not exposed to the electron beam.

Figure 6.4 shows electron diffraction patterns collected *in situ* from the particles deposited on the working electrode. These results suggest that the as-deposited particles are a mixture of metallic copper and copper oxide. We also performed *ex situ* characterization of similar cubes deposited on a TEM grid with lacey carbon support (Fig. 6.5). High-resolution TEM images show that the cubes are predominantly Cu_2O with faint fringes that may be attributed to Cu $\{2\,0\,0\}$ or CuCl $\{1\,0\,\overline{1}\,4\}$. Energy dispersive X-ray (EDX) spectroscopy analysis of one of such cubes indicates an overall composition of 61% Cu, 31% O, and 5% Cl. The mapping results also suggest that there is segregation of Cl within the particle, where higher intensity of the Cl signal is seen in the middle of the cube and a square band within the cube. These areas of segregated Cl also correspond to darker

contrast in the STEM image and lower intensity in the Cu map. These results are in agreement with the cube composition previously reported[182].
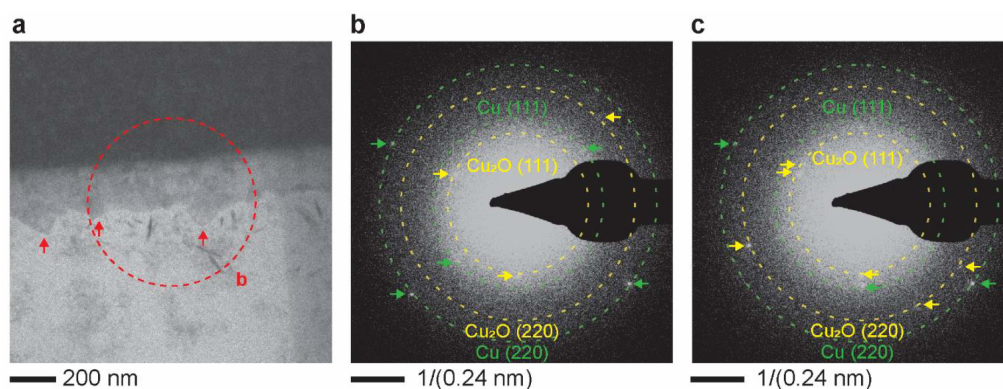
Figure 6.4: *In situ* **electron diffraction patterns of electrodeposited Cu particles. a**, Cubic-shaped Cu particles deposited on the edge of the working electrode. The selected area used for the electron diffraction is outlined with a red dashed circle. Red arrows denote the cubic particles. **b**, Electron diffraction pattern from the area selected in (a). **c**, Electron diffraction pattern from a different area further along the working electrode out of the field of view of (a).
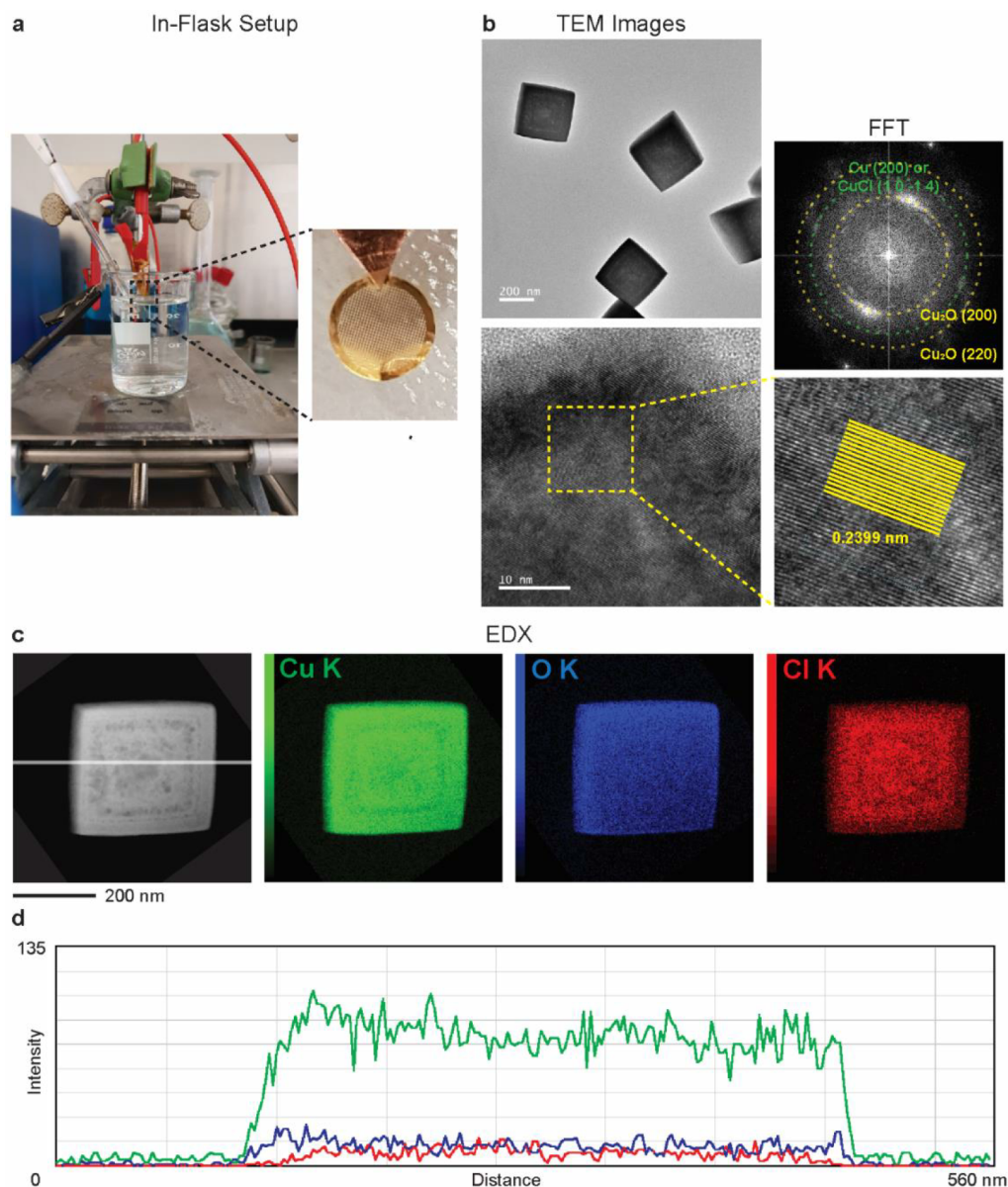
Figure 6.5: *Ex situ* **characterization of electrodeposited Cu₂O particles. a**, Experimental setup for the electrodeposition of Cu_2O cubes on different substrates, consisting on a beaker containing the precursor solution, a Pt counter electrode, a Ag/AgCl reference electrode and a TEM grid acting as working electrode. **b**, TEM, HRTEM and Fast Fourier Transform (FFT) of the cubic particles deposited on the TEM grid. **c**, STEM image and EDX elemental mapping for copper (green), oxygen (blue) and chlorine (red). The overall composition of the particle from EDX is 61% Cu, 31% O and 5% Cl. The Cl K map suggests there is segregation of Cl within the particle, with more Cl in the middle of the cube and a square band within the cube. These areas of segregated Cl correspond to darker contrast in the STEM image and lower intensity in the Cu map. The line in the STEM image denotes the location of the line profile displayed in (d). **d**, Line profile of characteristic X-ray intensity across the particle. The colors are the same as in (c).

Figure 6.6a describes the size evolution of a Cu_2O cube (red line) and a non-cubic (blue line) particle during the cyclic voltammetry in detail. Cu_2O cubes started to form on the working electrode at −0.05 V during the negative-going scan. These cubes reach a maximum size of 345 nm

at 0.03 V and start dissolving at 0.07 V during the positive-going scan, and a potential of 0.20 V is required to completely dissolve them. In contrast, the growth of non-cubic particles started at −0.08 V during the negative-going scan and reached a maximum particle size of 800 nm at −0.05 V during the positive-going scan. After ramping to more positive potentials, the non-cubic structures decrease in size rapidly and are completely etched from the working electrode surface at 0.05 V, a potential that is lower than the one needed to remove the cubic particles. Thus, Cu_2O cubes were not only deposited at a lower overpotential than the non-cubic particles, but they were also stable over a broader potential range.
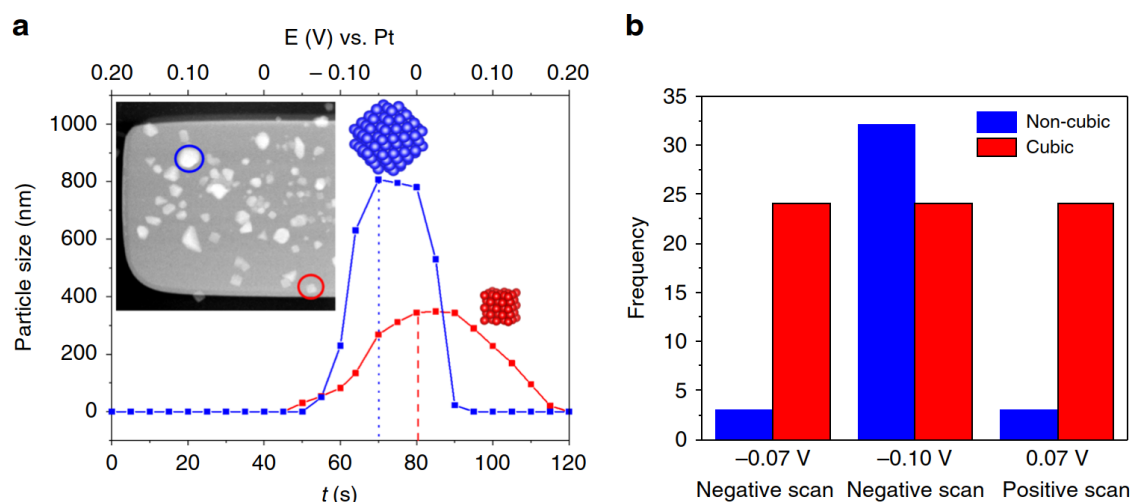
Figure 6.6: **Potential-induced changes in particle size and morphology. a** Non-cubic (blue solid line) and cubic (red solid line) particle size evolution of the selected particles marked in the STEM image with a circle of the corresponding color as a function of time and applied potential. **b** Evolution of the frequency of non-cubic and cubic particles deposited on the working electrode with the applied potential.

The populations of cubic and non-cubic particles at three different potentials are compared in Fig. 6.6b. These data confirm that the behavior described in Fig. 6.6a for a single particle is consistent across all the particles on the working electrode. Even though more non-cubic particles were formed during the negative-going scan, they also dissolved earlier when the potential reached positive values. Figure 6.7 shows another image sequence from a different experiment where the same behavior was observed. It should be mentioned here that the potentials at which particles could be deposited and dissolved can vary between LCs, presumably due to differences in the properties of the thin-film pseudo-Pt reference electrodes and the ohmic drop across the length of the working electrode. Nevertheless, the Cu_2O cubes are consistently more stable than the non-cubic particles across all experiments. The stabilization of Cu_2O $\{1\,0\,0\}$ facets by Cl^- during electrodeposition has been previously reported[284]. The enhanced stability of our Cl-rich $Cu_2O\{1\,0\,0\}$ cubes against oxidative dissolution is assigned to the shorter length of the Cu–O bond on the $\{1\,0\,0\}$ plane as compared to $\{1\,1\,1\}$ and $\{1\,1\,0\}$, leading to a stronger bond[303]. Our observations are in agreement with previous findings[303,304].
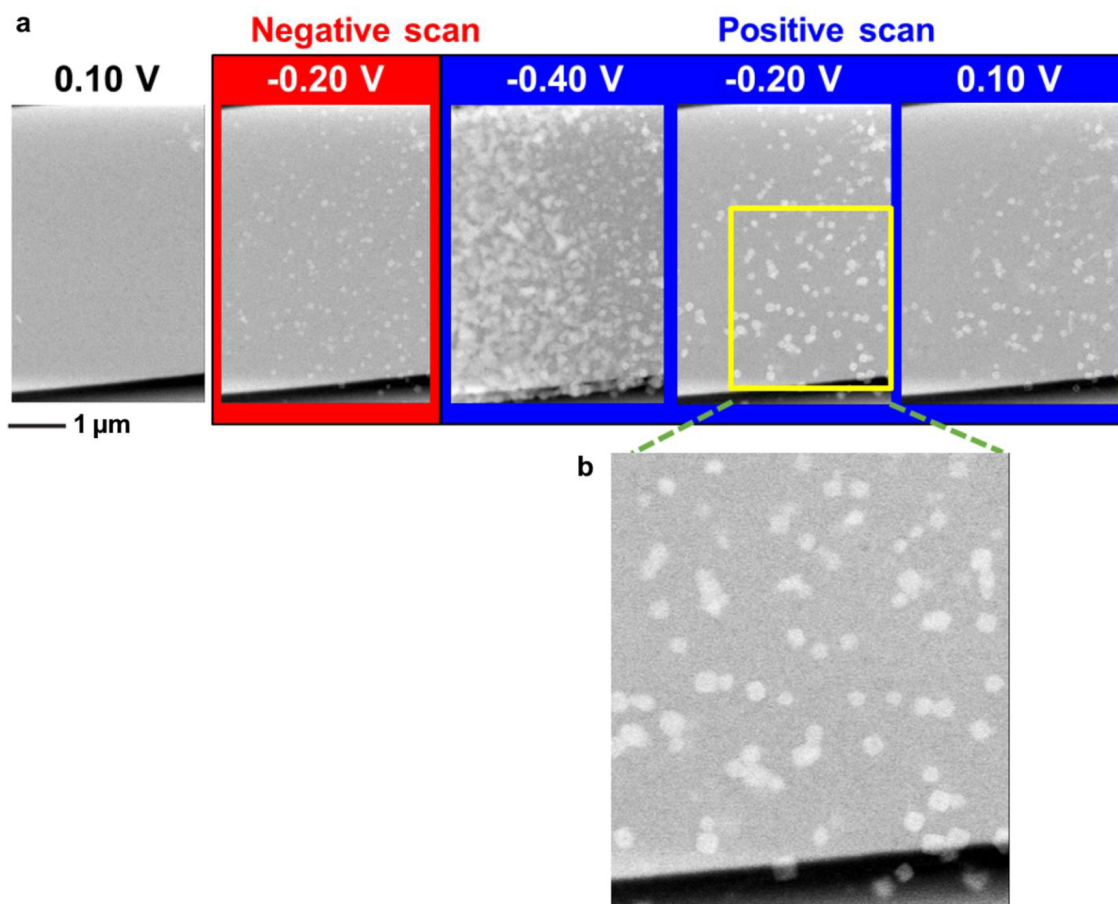
Figure 6.7: **a**, STEM images of the working electrode at different potentials during cyclic voltammetry recorded at a scan rate of $5\,mV\,s^{-1}$ in 5 mM $CuSO_4$ + 5 mM KCl solution. These images correspond to a different experiment (different pair of chips assembly) with respect to the one presented in the main paper but with similar results. **b**, Magnified area of the −0.20 V image showing the cubic-shaped particles.

The number of Cu_2O cubes also increased upon repeatedly cycling the potential. Figure 6.8 shows the results from one such experiment where we cycled the potentials at an upper potential where the particles did not fully dissolve from the working electrode (Appendix Movie* 13.9). Again, particles with different shapes nucleated and grew during the negative-going scan of the first cycle. The cubes largely survived the positive-going scans. In this case, the number and size of cubic particles increased with successive cycles (images in Fig. 6.8), as new cubic architectures were nucleated and the retained cubes grew larger. This behavior resulted in increasing shape-selection as the synthesis process continued.

---

* Here in form of a figure in the appendix
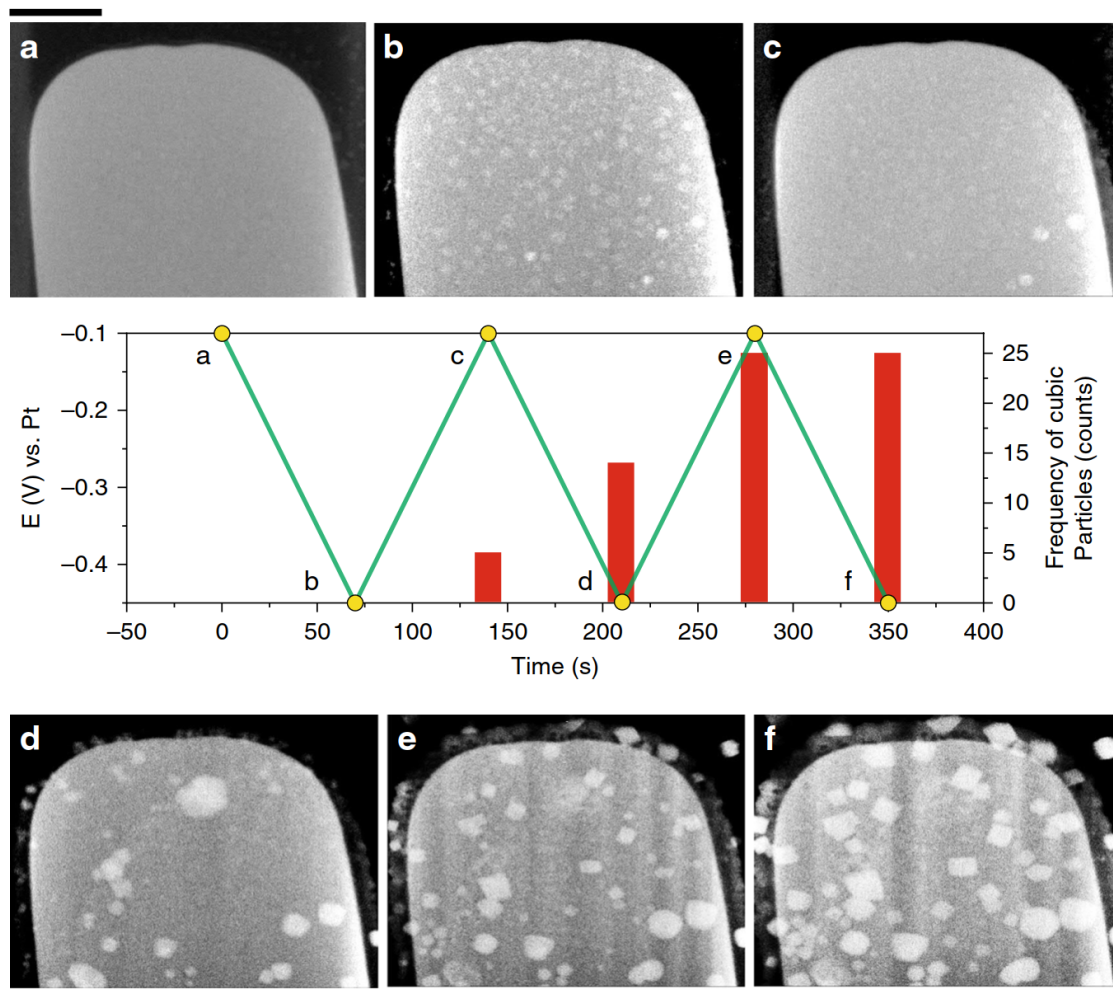
Figure 6.8: **Number of cubic particles observed with potential cycling.** Potential (green line) and frequency of cubic particles (red columns) as a function of experimental time during electrochemical cycling. The images labeled as **a-f** correspond to STEM images of the working electrode acquired at different pote ntials as indicated by the yellow circles in the plot. The vertical bars indicate the number of cubic-shaped particles observed at each point. The scale bars correspond to 1 μm.

6.3.2 Influence of Cl⁻ Ions on the Particle Morphology.

In colloidal particle synthesis, it is considered that the addition of Cl^- ions leads to shape-selection toward cubic NPs via kinetic control and oxidative dissolution of non-cubic, twinned NPs[305–307]. Kim et al.[308] discussed that Cl^- favors the formation of cubic Cu_2O particles during colloidal synthesis by slowing down the nucleation and growth rate. Chloride ions in the precursor solution also encourage nanocube formation by stabilizing the $\{1\,0\,0\}$ facets of Cu[235,284] and Cu_2O[303]. The shape of Cu nanocrystals in a solution containing different ions (Na^+, NH_4^+, SO_4^{2-}, Cl^-, dodecyl sulfate) was also investigated[284]. Interestingly, regardless of the initially exposed crystal facets, only $\{1\,0\,0\}$ planes remained after exposing these crystals to Cl^--containing solutions for a few minutes, leading to cubic shapes. Moreover, the electrochemical nanostructuring of Cu foils into cubic facets was observed in the presence of Cl^-, while flatter larger morphologies and

needle-like structures were obtained when cycling in the presence of Br^- and I^-, respectively[309]. We also showed recently[182] that Cu cubes can be grown by electrodeposition on a carbon substrate (HOPG) using $CuSO_4$ as Cu source to create NPs and KCl to reshape them. However, the former study only contained *ex situ* atomic force microscopy (AFM) data of the final state of the samples after the synthesis, while here we present an *in situ* microscopy study that allows us to follow in detail the electrochemical parameters influencing the formation of the cubes, and even more importantly, the potential regimes in which the cubic shapes are most stable. In addition, by employing a different support material (Pt), we are able to demonstrate now that the previously described synthesis is not only restricted to carbon-based substrates.

The question now is if the presence of Cl^- ions in fact influences the particle morphology during nucleation. The image sequence in Fig. 6.9 of particles grown using a 5 mM $CuSO_4$ solution with no KCl added (Appendix Movie* 13.10), demonstrates that no cubic particles are formed in the absence of Cl^- ions. Hence, it suggests that KCl is in fact necessary for the shape-selection toward Cu_2O cubic particles. As further control experiments to verify the role of Cl^- ions, we performed benchtop electrodeposition on glassy carbon supports with 5 mM $CuSO_4$ solutions containing either 5 mM KCl, 5 mM NaCl, or 5 mM HCl (Fig. 6.10) as additive to check if the cations had any effect on the particle morphology. Cubes were seen in both KCl and NaCl, but not when HCl was used. The absence of cubes in the HCl experiment can be rationalized from the Pourbaix diagram of Cu in aqueous solutions containing Cl^{-}[310], where the Cu_2O phase is destabilized at the lower pH, thus leading to the loss of the cubic morphology. Hence, these results confirm that the specific alkali metal cations had no influence on the electrodeposition and that the cubes are nucleated from Cu_2O.
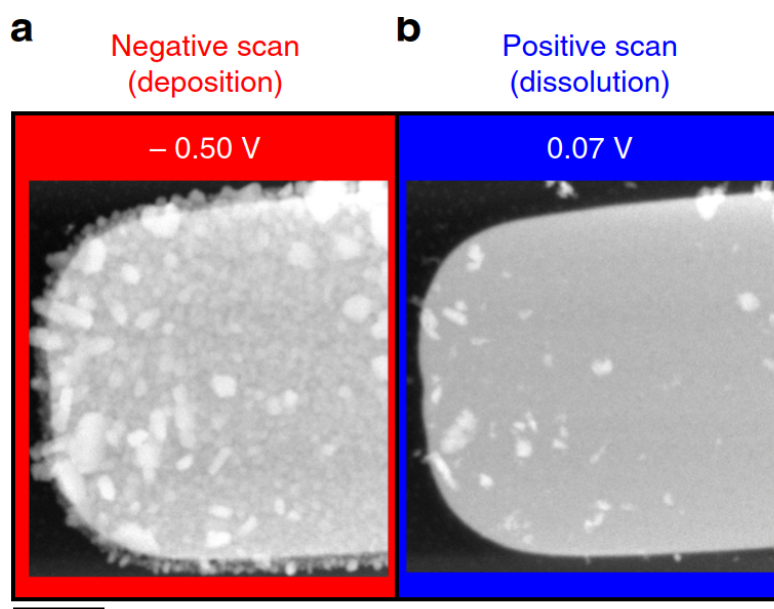
Figure 6.9: **Particle growth in the absence of Cl^- ions.** STEM images of the working electrode at different potentials during cyclic voltammetry recorded at a scan rate of $5\,mV\,s^{-1}$ in a 5 mM $CuSO_4$ solution. The scale bar corresponds to $2\,\mu m$.

---

* Here in form of a figure in the appendix
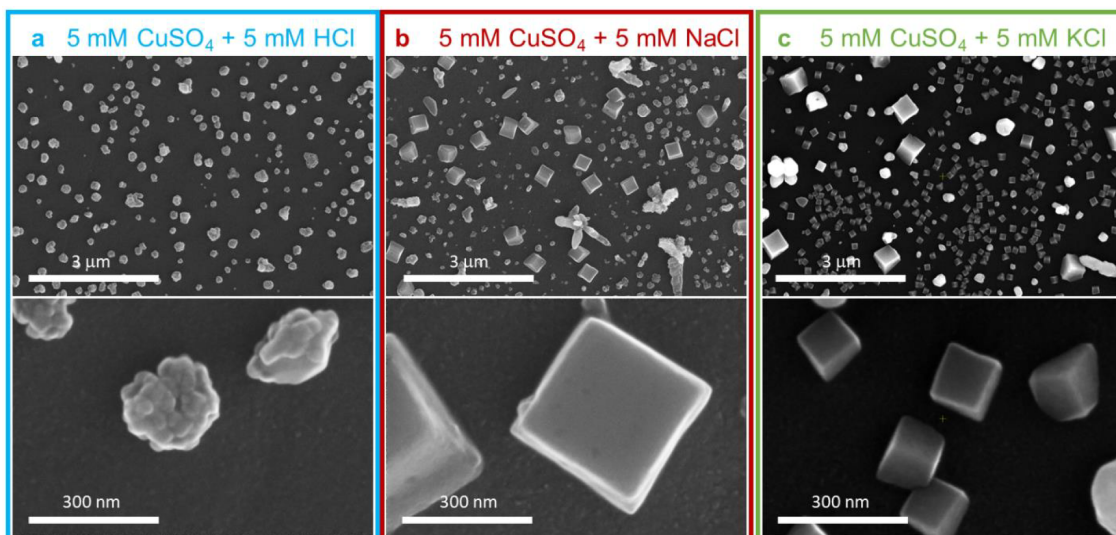
Figure 6.10: ***Ex situ* SEM images of Cu structures** electrodeposited on a glassy carbon electrode using **a**, 5 mM $CuSO_4$+ 5 mM HCl; **b**, 5 mM $CuSO_4$+ 5 mM NaCl and **c**, 5 mM $CuSO_4$+ 5 mM KCl solutions. The particles were electrodeposited by sweeping the potential between −0.5 V and −0.2 V vs Ag/AgCl.

More importantly, our *in situ* observations show that the presence of Cl^- ions does not directly lead to the solely nucleation of cubic particles. Instead, mixed morphologies are formed during the initial nucleation stage, and a second dissolution mechanism and the optimum applied potential are required to refine the particle shape distribution. This adds valuable insight for the further optimization of the synthesis recipes towards catalysts with narrow size and shape distributions.

6.3.3 Dynamic Changes under Reducing Conditions in 0.1 M $KHCO_3$.

We further exposed these as-synthesized cubes directly to reducing conditions where CO_2 electroreduction takes place and were able to monitor drastic changes of the catalyst structure in real time. Figure 6.12 shows one set of results from these experiments. Here, we exchanged the electrolyte by flowing CO_2-saturated 0.1 M $KHCO_3$ through the cell for at least 30 min while keeping the potential of the working electrode at −0.1 V to avoid particle dissolution at OCP. It can be seen from Fig. 6.11 that the cubes did not exhibit significant changes during the fluid exchange. Then, a potential of −0.7 V was applied to the working electrode, which led to dynamic morphological changes taking place on the working electrode within the cell (Fig. 6.12, Appendix Movie* 13.11). Between t = 1 s and 61 s, we can see that some of the cubes were not strongly attached to the surface and they started moving across the electrode surface when the potential was applied. At the same time, we see concurrent size reduction of the original cubes and the formation of new copper structures on the working electrode, some in the form of dendritic structures (t = 61 s to 246 s). It should be noted here that the potentials reported may be up to 0.2 V off from the applied values due to the electrochemical cell configuration of these *in situ* TEM studies and the pseudo-Pt reference electrode.

∗ Here in form of a figure in the appendix
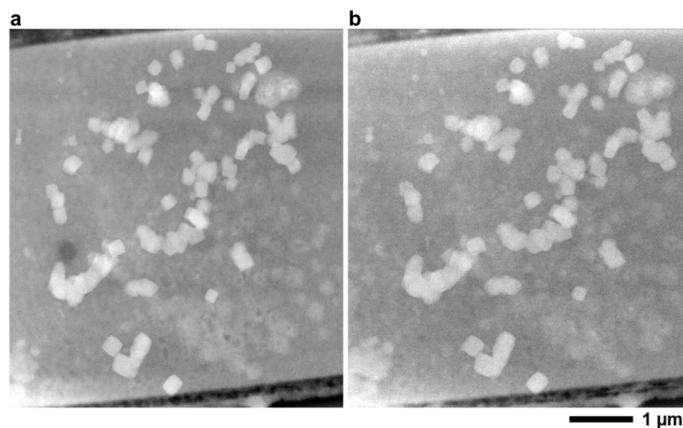
Figure 6.11: *In situ* **TEM images comparing the electrodeposited Cu cubes described in Figure 6.12. a**, before and **b**, after the flow of a CO_2-saturated 0.1 M $KHCO_3$, but before the application of −0.7 V.
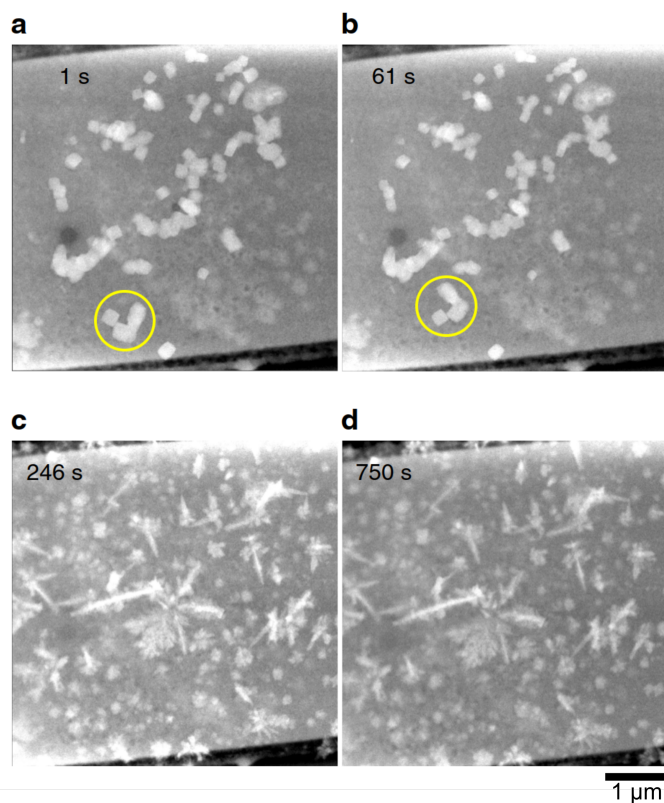
Figure 6.12: **Evolution of Cu$_2$O cubes during reducing conditions.** STEM images of the working electrode at different experimental times, **a** t = 1 s, **b** t = 61 s, **c** t = 246 s, and **d** t = 750 s, acquired while keeping the potential at −0.7 V in a CO_2-saturated 0.1 M $KHCO_3$ solution. It can also be seen that many cubes have started to reduce in size. A cluster of cubic particles that moved between t = 1 s and t = 61 s is highlighted with a yellow circle. After t = 245 s, no further changes in the nanostructure morphology were apparent. The scale bar corresponds to 1 µm.

The morphological changes directly observed here in the Cu$_2$O particles by *in situ* LC-TEM under CO_2RR conditions are expected to lead to changes in the product selectivity, as previously

discussed based on *ex situ* SEM data[131,138,182]. The progressive loss of the $\{1\,0\,0\}$ facets leads to an increase in H_2 production at the expense of the CO_2RR products. However, a higher stability and C_2–C_3 product yield was observed during CO_2RR for Cu NCs electrochemically grown on Cu foils[131]. Even more importantly, the highest ethylene yield was obtained when the Cu NCs/Cu samples were pretreated with an oxygen plasma which lead to a drastic change in the structure and the loss of the cubic shape after reaction, while the same samples pretreated in Ar-plasma retained the cubic structure but resulted in a significantly lower C_2–C_3 product selectivity. In general, the loss of Cu$\{1\,0\,0\}$ facets is correlated with a decrease in the yield of ethylene[131,224,309], although other factors such as the content of subsurface oxygen or Cu(I) species have also been mentioned to play a role[131,311]. Unfortunately, correlating the observed structural transformations with their impact on reaction product selectivity is still a nontrivial technical challenge for LC-TEM, and outside the scope of this work.

Our *in situ* TEM observations of highly dynamic Cu catalysts are consistent with a recent study using identical location SEM also reporting significant restructuring of Cu NP catalysts within minutes of applying the potential to initiate CO_2RR[116]. The formation of dendritic structures has been attributed to the simultaneous dissolution and redeposition of Cu under CO_2 reduction conditions[265]. A similar mechanism may be at play in our experiments. We speculate that the Cu species that end up forming dendrites originate from material (Cu atoms and small Cu clusters not visible during the *in situ* TEM) that was deposited on the working electrode during *in situ* electrodeposition but not nucleated as cubes. These Cu species on the electrode surface become mobile when the potential is applied, leading to a redistribution of the as-deposited Cu and the consequent dendritic nanostructure growth. In other areas of the working electrode, we can also observe a size reduction in the original as-synthesized cubes, similar to that previously reported via electrochemical atomic force microscopy for Cu_2O cubes grown on graphite, albeit at much higher rates. The fact that the size reduction of the cubes and additional particle growth occurred at the same time in our experiments also suggests that the behavior we observe is not due to the reduction of residual Cu ions in solution. The differences between the dynamic morphological changes observed for the electrochemically grown Cu cubes versus the former study[182] might be due to the different supports used, graphite (HOPG) vs. Pt, as well as the different configurations of the electrochemical cells employed. The cell geometry can influence the flow rate of the electrolyte and determine the local chemical concentration and potential gradients at the working electrode. Our future work will focus on fine-tuning our synthesis protocol such that size-selected cubic-like structures are also generated *in situ* for more detailed studies looking at the effects of both shape and size in these catalysts during CO_2RR.

We also briefly address the possibility of electron beam-induced artifacts in the particle growth and CO_2 electroreduction experiments in the bicarbonate electrolyte. We have used a low electron dose rate of $20\,e^-\,nm^{-1}\,s^{-1}$[sic]** in these experiments and thus, such effects are not apparent. Fig. 6.13 shows that the morphological changes seen in the Cu_2O structures in Fig. 6.12 and in Appendix Movie* 13.11 were not due to artifacts from sustained imaging with the electron beam.

** Correction from $20\,e^-\,nm^{-1}\,s^{-1}$ to $20\,e^-\,nm^{-2}\,s^{-1}$

* Here in form of a figure

In this control experiment, we imaged the as-deposited particles for 750 s after electrolyte exchange to CO_2-saturated 0.1 M $KHCO_3$ before applying the −0.7 V potential. As expected, and regardless of the prior electron beam irradiation, Cu restructuring and dendrite growth was only seen when the potential was applied.
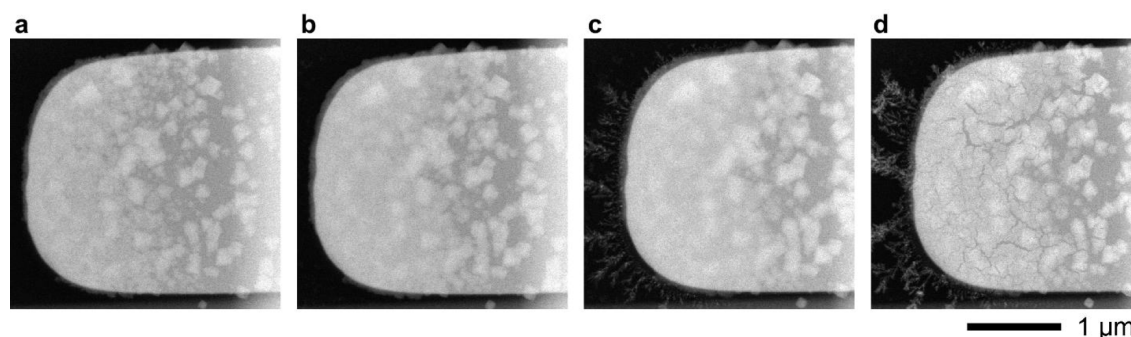
Figure 6.13: **An image sequence from a control experiment** where we checked that the re-structuring shown in Figure 6.12 was not caused by artifacts related to the electron beam. The electrodeposited cubic-like Cu_2O structures were imaged in a CO_2-saturated 0.1 M $KHCO_3$ solution for 750 s before the application of the −0.7 V potential. Images of the working electrode after **a**, electrodeposition and electrolyte exchange, **b**, 750 s of imaging, **c**, 5 s after applying −0.7 V against the pseudo-Pt reference, and **d**, 58 s after applying −0.7 V.

6.4 Conclusion

The present study emphasizes the advantages of using *in situ* LC-TEM for monitoring the nanoscale evolution of electrocatalysts at timescales of seconds. Nevertheless, the resolution degradation associated with imaging through a liquid[286] makes it difficult to capture small structural changes in the *in situ* image sequences. Furthermore, key technical challenges still remain to be solved before one can directly correlate the morphological modifications observed with the catalytic performance. These include the minute liquid volumes held in the TEM cells, the small size of the electrodes in the microfabricated set-ups, the low catalysts loading, and the need for product detection instrumentation with faster time–response and improved sensitivity. Nevertheless, we expect that future improvements of the experimental set-ups will eventually provide us with the ability to relate the evolution of the structure of an electrocatalyst with changes in its activity, selectivity and stability, providing in depth insight for rational electrocatalyst design.

In conclusion, we demonstrated that we can directly synthesize shape-controlled catalyst particles on the working electrode of a microfluidic TEM LC and follow their subsequent dynamics under reaction conditions. In particular, the *in situ* TEM observations during synthesis show that the addition of Cl^- ions into the precursor $CuSO_4$ aqueous solution induces the nucleation of cubic structures among non-cubic particles and stabilizes these cubes against dissolution. The cubes require a lower overpotential to be deposited and are stable over a larger range of potentials. Additional potential cycles lead to an increase in the number of cubic particles and growth of the cubes deposited in the previous cycles. These experiments provide new insights into the electrodeposition parameters required to custom-tune the synthesis of size- and shape-selected NPs.

Moreover, the ability to directly deposit cubic particles on the working electrode of a LC provides a straightforward way to create these electrocatalysts for subsequent *in situ* studies of their behavior during CO$_2$RR.

The observation of the *in situ* synthesized Cu$_2$O cubes under conditions relevant to the electrochemical reduction of CO$_2$ also revealed that fast and extensive restructuring takes place within a few minutes of applying a reductive potential in a CO$_2$-saturated bicarbonate solution. The results shown here emphasize the highly dynamic nature of electrocatalysts under reaction conditions, including their mobility and their ability to serve as nucleation sites for the growth of Cu dendrites. Finally, this study highlights the advantages of using *in situ* LC-TEM for the mechanistic investigation of the parameters affecting the electrochemical synthesis of catalytically relevant materials and the excellent possibilities of monitoring their performance *in situ* during an electrocatalytic process."[231]

7 Understanding Stability of Cubic Copper Catalysts during CO$_2$ Electroreduction and its Impact on Catalytic Selectivity

This chapter is based on our upcoming publication titled "*Understanding Stability of Cubic Copper Catalysts during CO$_2$ Electroreduction and its Impact on Catalytic Selectivity*" where we explore the dynamic behavior of state of the art copper catalysts under *operando* conditions in real time on the nanoscale. My involvement in this project include the synthesis of Cu$_2$O cubes on the TEM chips, the *ex situ* electrochemical benchmark and characterization, as well as the electrochemistry during the TEM and SEM measurements. This project is a cooperation with our liquid phase electron microscopy group, who helped and were part of all microscopy experiments. I was strongly involved in writing the draft. As of now, this is still unpublished work but we are making revisions after review. "[...] Here, we present real-time electrochemical liquid cell transmission electron microscopy studies showing how Copper(I) oxide cubes restructure under reaction conditions. In particular, fragmentation of the solid cubes and re-deposition of new nanoparticles are observed as a function of the applied potential and time. We further correlate this dynamic morphology with the catalytic selectivity through time-resolved scanning electron microscopy measurements and product analysis. Comparative studies using cubes with different initial sizes show that both, the morphological stability of large, fragmented cubes and a dense coverage of re-deposited nanoparticles contribute to the enhanced C$_{2+}$ selectivity observed.

7.1 Introduction

The conversion of simple molecules, such as CO$_2$ and H$_2$O, into valuable products by use of renewable energy is a key strategy towards a sustainable society[312,313]. However, many of these technologies are not yet industrially viable because they are hampered by the lack of functional catalysts with good performance and stability. Among these processes, CO$_2$RR is particularly appealing because it transforms a greenhouse gas into useful fuels and base chemicals, such as ethylene and ethanol at ambient temperature and pressure[12,13].

Developing a catalyst with the optimal balance of activity, selectivity and stability is, however, a non-trivial task. Although some catalysts may show better initial performance than others, they often lose their activities over time. Copper is the most attractive material for CO$_2$RR because of its unique ability to generate C$_{2+}$ products, but it suffers from poor selectivity[12–14]. Several studies have also suggested that restructuring under applied potential can alter the catalytic properties of Cu-based nanostructures[36,112,115,117,182,265,314–316]. Unfortunately, these conclusions are largely

drawn from samples that have been removed from the electrochemical environment and evaluated in the absence of an applied potential. Detailed understanding of the specific morphological features responsible for a given activity and selectivity remains elusive due to insufficient of insight into the dynamic evolution of Cu catalysts under reaction conditions[12,149,317].

Liquid cell transmission electron microscopy (L-TEM) is a powerful technique for capturing the dynamics of nanostructures within a liquid environment[198,286,318]. Electrochemical experiments can also be performed within the TEM (EC-TEM) by incorporating thin film electrodes on the microfluidic chips[192]. Thus, the morphological evolution of electrocatalysts can be monitored under reaction conditions[117,155,231,295,302,319–321] and, in combination with electrochemical measurements, used to establish structure-property relationships[318,322]. Such information is key to inform theoretical models for the rational catalyst design and can provide the much needed understanding of the parameters influencing the reaction pathways required for generating multi-carbon products.[143,323]

Here, we track the dynamic evolution of electrochemically synthesized Cu_2O cubes in real-time under CO2RR conditions with EC-TEM and correlate the changes with the catalyst behavior obtained from benchtop electrochemical measurements. Our *in situ* observations revealed that under applied potential, nanoporous cubic frames and re-deposited nanoparticles (NPs) coexist. By tracking the reaction products generated by Cu_2O cubes with different initial sizes for several hours in parallel to the extended *in situ* imaging of those cubes, we could show that a dense network of stable nanoporous cubes and re-deposited NPs is required to sustain high selectivity towards C_{2+} products.

7.2 Methods

7.2.1 Cubic Cu_2O Synthesis

The synthesis protocol involves a mixture of 5 mM copper sulfate-pentahydrate ($CuSO_4x5H_2O$, Sigma Aldrich) and different concentrations of potassium chloride (KCl, Sigma Aldrich)[182,231]. Polished glassy carbon (vitreous, SPI) plates, as well as Hummingbird TEM EC-chips, were used as substrate. The largest Cu_2O cubes of 390 nm are obtained using 5 mM KCl and the smaller cubes of 170 nm and 80 nm by increasing the KCl concentration to 30 mM and 50 mM, respectively[99]. The starting cubes were synthesized by electrochemical cycling between an oxidizing (+0.6 V_{RHE}) and a reducing potential (+0.1 V_{RHE}) with in total 10 cycles, which led to the electrodeposition of size- and shape-controlled Cu cubes with a narrow size distribution depending on the Cu to Cl ratio used in the precursor. Initially, a potential of 0.6 V_{RHE} was held for 8 s with a subsequent potential jump to 0.1 V_{RHE} for 4 s. Returning to the initial potential completes the protocol. After the synthesis, the samples were rinsed with Milli-Q water and then used for subsequent CO2RR experiments.
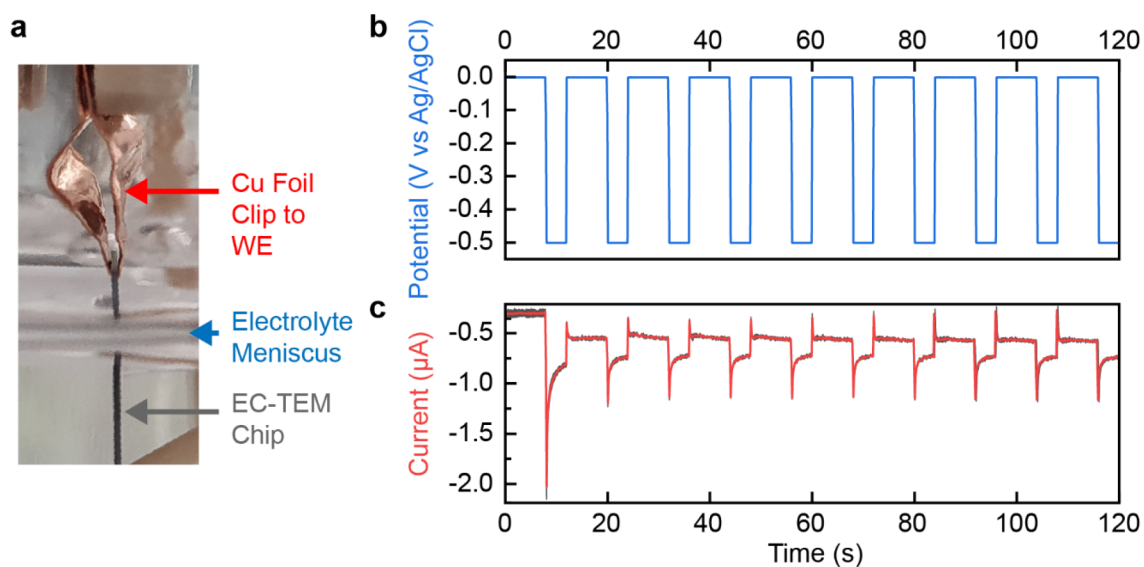
Figure 7.1: ***Ex situ* synthesis of Cu₂O cubes on EC-TEM chip.** (a) Photograph of our setup for the electrodeposition of cubes on the EC-TEM chips in a standard H-type cell. Contact to the carbon working electrode (WE) of the chips is made using copper foil clips. (b) Alternating potential profile used for the electrochemical deposition. (c) Corresponding current traces obtained from four different depositions using the same synthesis conditions.

7.2.2 Electrolyte (KHCO₃) Preparation

All electrochemical experiments for CO₂RR were performed in a 0.1 M KHCO₃ solution as the electrolyte. The solutions were prepared by dissolving potassium bicarbonate (KHCO₃, Sigma Aldrich) in ultrapure water ($18\,\mathrm{M\Omega\,cm^{-1}}$, from Veolia Purelab Flex Pure Water). Before use, purification of the solution with Chelex 100 resin (Bio-Rad) was performed for 24 h. Directly prior to the measurement, the electrolyte was saturated with CO₂ for at least 45 min for a full saturation.

7.2.3 *In situ* transmission electron microscopy

The *in situ* EC-TEM experiments were performed in a Thermo Fisher 300 kV Titan TEM (Thermo Fisher Scientific) operated in STEM mode using a Hummingbird Scientific Generation V Bulk Liquid Electrochemistry TEM holder (Hummingbird Scientific) with Pt counter and Ag/AgCl (3M KCl) reference electrodes. A schematic of the experimental configuration can be found in Figure 3.1. The image sequences were acquired using an electron probe current of ~220 pA and at a frame rate of 1 frame per second with 1024×1024 pixel image resolution. The EC-TEM chips with a 50 nm thick silicon nitride membrane window were also produced by Hummingbird Scientific. The EC-TEM chips have a carbon film covering approximately half the window as the working electrode. The electrochemistry experiments were performed using a Biologic SP-200 potentiostat. The potentials were measured against the built-in Ag/AgCl reference and then converted to RHE. [...] Subsection 7.2.8 discusses the electrochemical performance of the EC-TEM holder compared to a standard H-type cell.

The TEM holder was pre-filled with 0.1 M KHCO$_3$ during cell assembly to ensure that the electrolyte fills the entire fluid path. After loading into the TEM, the syringe was filled with freshly saturated KHCO$_3$ and introduced at a flow rate of 0.76 ml min^{-1} for 60 mins. Cyclic voltammetry from -0.3 V$_{RHE}$ to -1.1 V$_{RHE}$ was first used to determine the onset potential for the CO$_2$RR, followed by chronoamperometry for up to one hour at -0.9 V$_{RHE}$ or -1.1 V$_{RHE}$. The flow rate was maintained at 0.76 ml min^{-1} unless a bubble forms, at which point we increased the flow rate to 7.6 ml min^{-1} to push out the bubble. Due to the limited volume of 25 ml of our syringe, multiple syringe changes were required during the extended experiments. The intermittent bubble formation can be seen as jitters in the Appendix Movies.

In situ imaging was always performed under conditions with electrolyte in the cell, as determined from the image contrast, and we stayed under an electron flux of $7 \, e^- \, Å^{-2} \, s^{-1}$ at all times to minimize electron beam-induced artifacts. The presence of liquid in the electrochemical cell was also confirmed using electron energy loss spectroscopy (a representative spectrum is provided in Figure 7.2). A rough estimate puts the liquid layer thickness at 500 nm or more in our experiments. Also, at least two *in situ* experiments were performed at each size distribution for reproducibility [...]. The influence of the electron beam induced is discussed in [...] the Appendix 13.6.
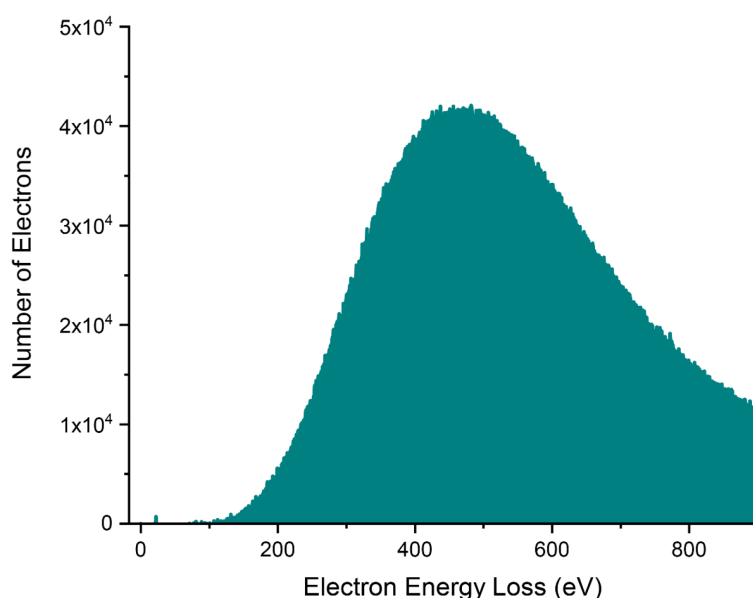
Figure 7.2: **A representative EELS spectrum acquired during our *in situ* TEM experiments.** The spectrum profile indicates significant scattering of the primary electrons as they propagate through the electrochemical cell. Note the absence of the zero-loss peak, which indicates that the liquid thickness exceeds at least a few inelastic mean free paths of the 300 kV electrons, i.e. we have a layer thickness of at least 500 nm.

The image segmentation for the in situ TEM movies was executed by using built-in functions and scripting in MATLAB. The analysis was performed in the following steps: 1) drift correction 2) bandpass filtering, 3) binarization, 4) particle detection and 5) classification of the cubes and

re-deposited particles. The band filter size and binary cutoff threshold were determined by visual inspection. For the NP size and NP number density plots in Figure 7.17, each point is an average of 60 frames, and the error bars represent the standard deviation of 60 frames (segmentation error). The classification of NP type was based on the particle size. A particle larger than a pre-determined size was categorized as a cube. Particles that were smaller than the threshold were categorized as re-deposited. The size criteria were 200, 500, and 1000 pixels (57 nm, 90 nm, and 127 nm) for the Cu cubes of average size of 80 nm, 170 nm, and 390 nm, respectively. The size criteria were determined by manual testing to find the size that results in the most correctly labelled particles. We also applied an extra shape limiting criteria, such that the eccentricity and the perimeter-to-area ratio could exclude the occasional mislabeling during segmentation when necessary.

7.2.4 *Ex Situ* Electrochemistry and Product Analysis

Ex situ electrochemistry and product analysis measurements were carried out in a benchtop electrochemical setup using an Autolab potentiostat (PGSTAT 32N). An H-type two compartment electrochemical cell with anolyte and catholyte separated by an ion-exchange membrane (Selemion AMV, AGC Inc.) was used with a Pt-mesh counter electrode (MaTecK, 3600 mesh cm^{-2}), a leak-free Ag/AgCl (sat.) reference electrode (Innovative Instruments Inc.) in a three-electrode configuration. The working electrode compartment was stirred at 800 RPM. For each data point, at least three identical samples were measured. The volatile gas products were analyzed via online gas chromatography (GC, Agilent 7890A) equipped with a thermal conductivity (TCD) and a flame ionization (FID) detector. Here, the headspace of the cell was directly connected to the GC, allowing online analysis after ∼30 min of product accumulation. An injection was performed approximately every 17 minutes during the measurements. A continued supply of CO_2 was ensured by constant bubbling of the anolyte and catholyte with CO_2 at 20 mL min^{-1}. Carboxylates such as formate and acetate were measured after the experiment by high performance liquid chromatography (HPLC, Shimadzu Prominence) equipped with a NUCLEAOGEL SUGAR 810 column and a refractive index detector (RID). Alcohols and other liquid products were analyzed by liquid gas chromatography (L-GC, Shimadzu GC-2010 Plus with auto sampler) equipped with a TCD and FID. We mention here that the first 1-2 injections at the beginning of the experiments tend to be less accurate due to limited product accumulation. All measurements were repeated three times on identically prepared and independent samples for statistical significance. [...]

7.2.5 *Ex situ* transmission electron microscopy

The *ex situ* TEM imaging and STEM-EDX mapping were performed using a Thermo Fisher 200 kV Talos F200X TEM. The EC-TEM chips were loaded on a Hummingbird Scientific Tomography holder with a customized tip for the chips. For the after-reaction samples, the electrochemical cells were rinsed in Milli-Q water after they were disassembled from the holder and immediately transferred into the TEM.

7.2.6 Scanning electron microscopy

The *ex situ* SEM imaging was performed using a Thermo Fisher Apreo SEM with the in-lens secondary electron detector.

7.2.7 Time-Resolved *Ex Situ* SEM Imaging of Cubes Reacted in a Standard H-Type Cell

To confirm that the EC-TEM observations can be indeed extrapolated to the behavior in a standard electrochemical cell, we further followed *ex situ* the morphological evolution of the Cu_2O cubes deposited on the glassy carbon plates during CO_2RR. The samples were extracted periodically over one hour and investigated by SEM. Figure 7.3 shows a sequence of SEM images from a sample with 170 nm cubes acquired after different CO_2RR times at $-0.9\,V_{RHE}$. Indeed, the SEM images show the restructuring of the cubes and NP re-deposition similar to that observed in the *in situ* experiments. As shown in the histograms in Figure 7.3(b), the cubes in our standard cell also did not change significantly in size and number density during the experiments, whereas the re-deposited NPs increased in size and number. The size trends from these experiments are plotted in Figure 7.3(c).
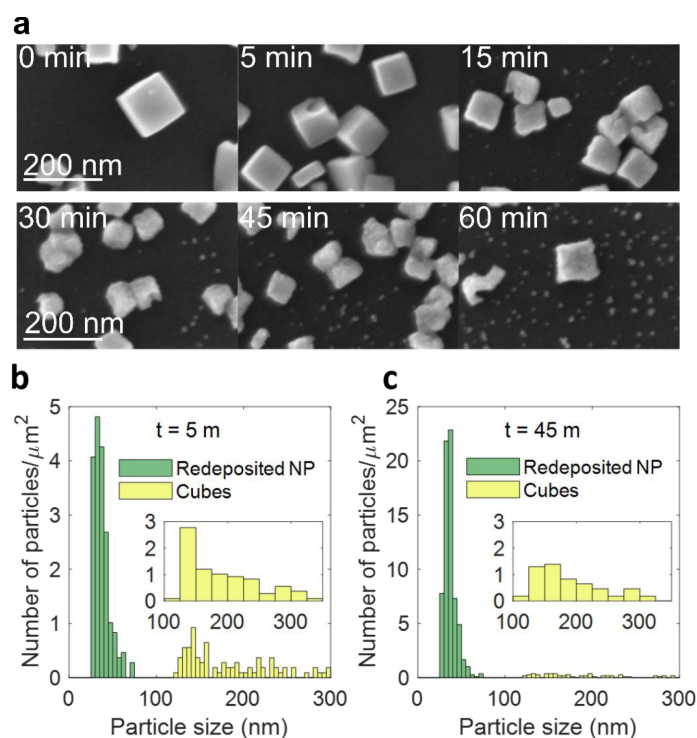
Figure 7.3: **Time-resolved *ex situ* SEM of Cu_2O cubes.** (a) SEM of 170 nm cubes extracted at different time points of CO_2RR at constant potential ($-0.9\,V_{RHE}$). The reaction was stopped at 5-15 minute intervals, and the glassy carbon support with the specimen was removed from the electrolyte solution for imaging. The histograms compare the size distribution of cubes and re-deposited particles after (b) 5 minutes and (c) 45 minutes.
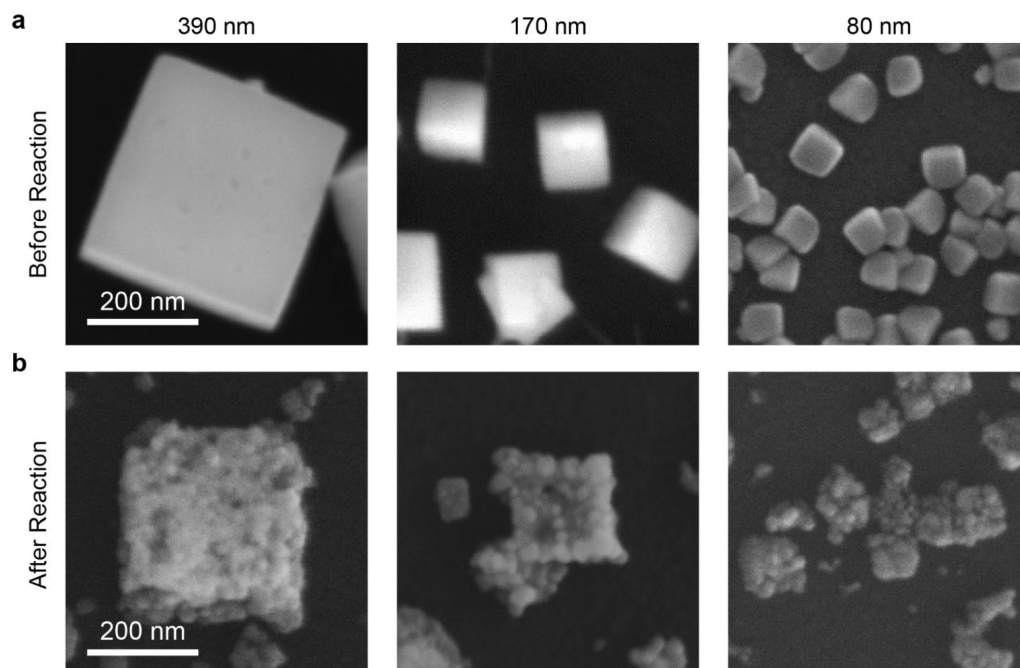
Figure 7.4: ***Ex situ* SEM images of Cu₂O on the EC-TEM chips before and after the CO₂RR reaction.** The reaction time was 60 minutes at a potential of $-0.9\,V_{RHE}$. All images are at the same magnification.

7.2.8 Comparison of the Electrochemical Performance of the EC-TEM Cell and a Standard H-Type Cell

To determine if the electrochemical data obtained from the EC-TEM cell accurately reproduce the behavior found in the benchtop measurements, we compared the current densities that are obtained after correcting for the surface area of the Cu catalysts. The exposed surface area of Cu (area$_{Cu}$) was estimated from the size and distribution of the as-synthesized cubes in the electron microscopy images. Here, we assume that each cube has 5 exposed facets of similar size, with the sixth one covered in contact with the support. The contribution to the current from the pure glassy carbon plate is negligible compared to that of the Cu catalysts. For the *ex situ* experiments, SEM images of at least three different locations have been taken on the sample and the number of cubes per μm^2 as well as their average size have been determined. For the *in situ* experiments, the same has been done using the STEM images. The linear sweep voltammetry currents and chronoamperometric traces have been normalized by dividing the measured currents by the total surface area of Cu. We are aware that such normalization is not ideal, since the total Cu surface area is changing under reaction conditions due to the morphological changes in the catalysts, as shown our *in situ* experiments. Nevertheless, we consider that this approach is a reasonable approximation as it captures the differences that are caused by the initially distinct cube size and loading, which would be otherwise ignored if the support geometrical surface area is used for the normalization. Our preliminary experiments also indicate that there is a reproducible offset of $\sim-0.4\,V$ between the reference potentials in the EC-TEM cell and the standard H-type cell, which we corrected for in the experiments presented in the manuscript. We attribute this offset to the

86

ohmic potential drop caused by the longer (fixed) separation between the reference and working electrodes in the EC-TEM cell. Figure 7.5 superimposes the initial linear sweep voltammograms for catalysts of similar sizes after correcting for the reference potential offset and normalization over the exposed surface area of Cu for the samples in the two setups. It is clear that the current densities compare well against each other. Hence, both time-resolved imaging [...] (subsection 7.2.7)and electrochemical data from both *in situ* TEM and benchtop setups indicate a robust correspondence between the two systems, allowing us to extrapolate the *in situ* findings and associate them with the real changes in catalytic performance measured from the identically prepared samples deposited on the bulk electrodes.
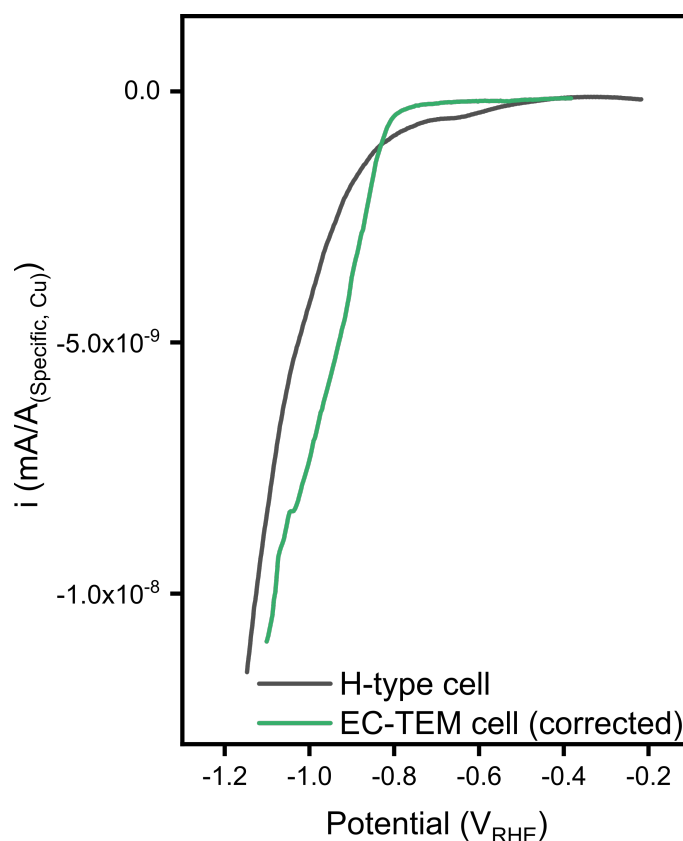
Figure 7.5: **Linear sweep voltammogram from *ex situ* and *in situ* experiments.** The currents have been normalized over the estimated exposed surface area of Cu on the working electrode, which is a glass carbon plate in the H-type cell and a carbon thin film in the EC-TEM experiments, respectively.

7.3   Results and Discussion

In the EC-TEM studies, we followed the morphological evolution of Cu_2O cubes with three size distributions, 80 ± 5 nm, 170 ± 40 nm and 390 ± 60 nm. The cubes were synthesized directly on the carbon working electrode of an EC-TEM chip *ex situ* from an aqueous mixture of $CuSO_4$ and KCl[99] in a standard benchtop electrochemical setup (Figure 7.1). In Figure 7.7(a), we show a STEM image sequence where we imaged several $\sim$170 nm Cu_2O cubes *in situ* under different electrochemical conditions, (i) at open circuit potential in CO_2-saturated 0.1 M $KHCO_3$, (ii) after

applying $-1.1\,V_{RHE}$, and (iii) after ~9 min at $-1.1\,V_{RHE}$ where a bubble formed. The image sequence shows that a few morphological changes occur during the application of the reductive potential: new NPs (~40 nm) form, and the cubes become porous and decrease in size by 10%. The size decrease can be attributed to the reduction of Cu_2O towards metallic Cu as previously determined from operando spectroscopy studies[132,182,324]. The data acquired during the linear sweep from open circuit potential to $-1.1\,V_{RHE}$ are provided as Appendix Movie 13.13*. The re-deposited NPs form first at about $0.5\,V_{RHE}$, before the size reduction of the cubes takes place at about $-0.7\,V_{RHE}$ (Figure 7.8).

This suggests that the small NPs are not produced by the reduction of Cu_2O, but originated from Cu species leached from the cubes after they were immersed in the electrolyte[182,321]. The high-resolution image in Fig. 7.7(a)(iii), acquired after bubble formation, reveals more clearly the nanoporous nature of the cubes. A comparison of Fig. 7.7(a)(ii) and (iii) further shows that the nanoporous cubes remained stable under sustained applied potential, whereas the small NPs started to agglomerate into interconnected structures.

Figure 7.7(b)-(d) shows *ex situ* TEM data, selected area electron diffraction, scanning transmission electron microscopy (STEM), and energy-dispersive X-ray spectroscopy (EDX) maps of a ~390 nm Cu_2O cube acquired (b) before and (c) after CO_2RR at $-1.1\,V_{RHE}$ for 1 hour in CO_2-saturated 0.1 M $KHCO_3$. In agreement with the image sequence in Figure 7.7(a), the single crystalline Cu_2O cube is fragmented and porous after reaction. EDX spectra acquired from the cubes (Figure 7.6(a)) indicate a significant decrease in both O and Cl signatures in these Cl^--stabilized Cu_2O cubes after reaction. The electron diffraction pattern exhibits strong Cu and weak Cu_2O diffraction spots after reaction, where the Cu_2O signatures may be due to re-oxidation during the *ex situ* sample transfer. The smaller NP agglomerates that are formed during reaction were identified as Cu (Figure 7.6(b)).

∗ Here in form of a figure in the appendix
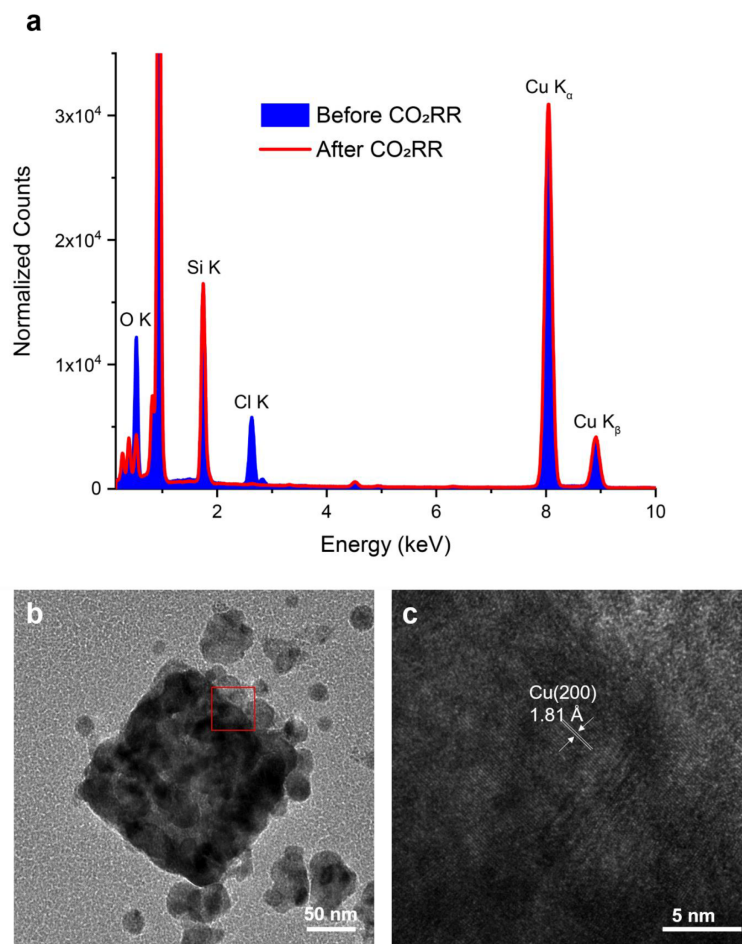
Figure 7.6: **Copper reduction after CO₂RR** (a) Comparison of the EDX spectra obtained during the acquisition of Figure 7.7(c). The results indicate a decrease in both Cl and O after reaction. The spectra are normalized to the Si K peak of the silicon nitride membrane. (b) Cu cubes after CO₂RR. (c) The $\{1\,0\,0\}$ facet of the magnified area within the Cu NP marked by a red square in (b). The lattice parameter 1.81 Å corresponds to Cu$\{2\,0\,0\}$.

Since it was challenging to prevent the formation of gas bubbles and to remove them at $-1.1\,\mathrm{V}_{RHE}$ during the *in situ* investigations, we applied a lower potential of $-0.9\,\mathrm{V}_{RHE}$ in subsequent experiments. This allowed us to extend the continuous observation window up to about an hour. Figure 7.12 depicts the morphological evolution of cubic-shaped Cu₂O catalysts with different initial sizes where the image sequences track the same cubes at four different reaction times after the application of the reductive potential: t = 0 min, 5 min, 25 min and 45 min. The corresponding movies with wider fields-of-view for the size distributions of (a) 390 nm, (b) 170 nm and (c) 80 nm are provided as Appendix Movies 13.14, 13.15 and 13.16*, respectively. In [...] section 13.6 , we discuss the control experiments we performed to rule out electron beam induced effects in these extended imaging experiments.

∗ Here in form of a figure in the appendix
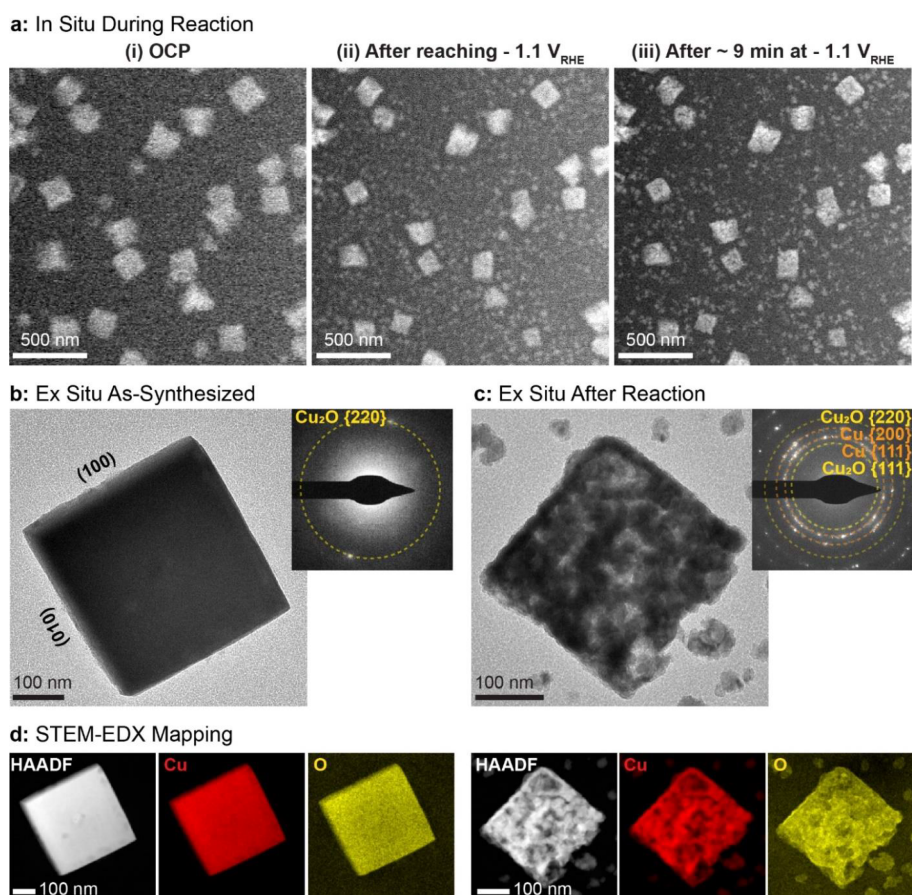
Figure 7.7: **Morphology of Cu₂O cubes and their evolution during CO₂RR.** (a) An imaging sequence illustrating the morphological changes observed in $\sim$170 nm cubes after (i) introducing CO_2 saturated 0.1 M $KHCO_3$ under open circuit potential, (ii) applying a reductive potential of $-1.1\,V_{RHE}$ and (iii) after $\sim$9 min at $-1.1\,V_{RHE}$, where a large bubble formed. The image sequence was acquired with an electron flux of $1.7\,e^-\,\text{Å}^{-2}\,s^{-1}$. Comparison of Cu₂O cubes (b) before and (c) after reaction using *ex situ* TEM imaging and electron diffraction (upper right inserts). (d) STEM-EDX mapping of the same cubes showing the Cu and O maps.
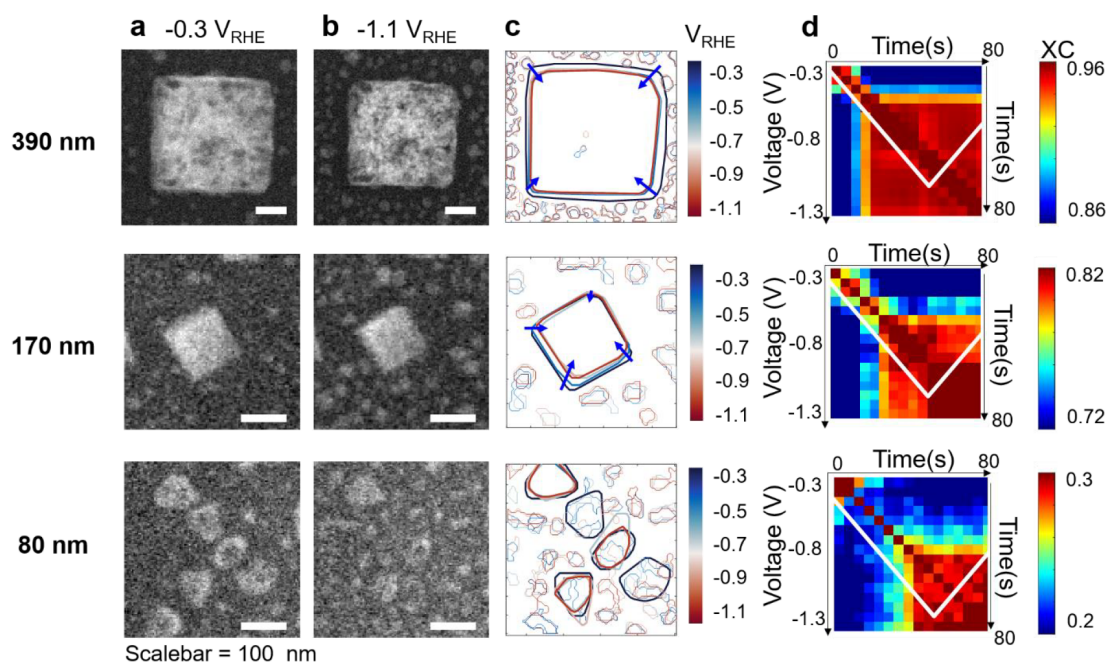
Figure 7.8: **Cube size changes and particle re-deposition during initial cyclic voltammetry.** (a). TEM images of Cu cubes at −0.3 V$_{RHE}$. (b). TEM images of the Cu cubes and redeposited particles at −1.1 V$_{RHE}$. (c). Line profiles showing the outlines of cubes and re-deposited particles at different applied potentials. The arrows highlight the shrinking of the cubes. (d). Cross correlation coefficient (XC) maps comparing each image frame and its subsequent frame. The more similar each pair of images are, the higher the XC number is. The white line indicates the applied potential over time. The map shows that the changes occur mostly at the beginning of the potential sweep (−0.5 V$_{RHE}$ to −0.7 V$_{RHE}$), where the cubes shrink, and then, the morphology is relatively stable over the rest of the voltage sweep.

The image sequences show a drastic difference between the larger (390 nm and 170 nm) and the smaller (80 nm) cubes studied. Although fragmentation and a size decrease were found to occur under reductive potential regardless of the initial cube size, the cubic nanoporous frames from larger cubes were largely stable and did not show significant mobility. On the other hand, the 80 nm cubes decreased in number after the introduction of electrolyte. Different areas of the working electrode showed either a noticeably lower cube loading or remnant cube fragments. To confirm this observation, we imaged the Cu$_2$O cubes *ex situ* with TEM, after synthesis, after a 30-minute immersion in 0.1 M KHCO$_3$ and after reaction at −0.9 V$_{RHE}$ in our standard H-type cell (Figure 7.9). While large cubes ($\geq$ 170 nm) only showed subtle changes after immersion in the bicarbonate solution, the smaller cubes underwent significant degradation and a reduction in their number, corroborating the poorer stability of these cubes. The *in situ* TEM image sequence in Figure 7.12(c) describes the dynamics of the structure of the 80 nm cubes under applied potential, where catalyst aggregation and detachment can be seen. Results from another experiment where we mostly found cube fragments is provided as Figure 7.10 and Appendix Movie 13.17*, respectively.

∗ Here in form of a figure in the appendix
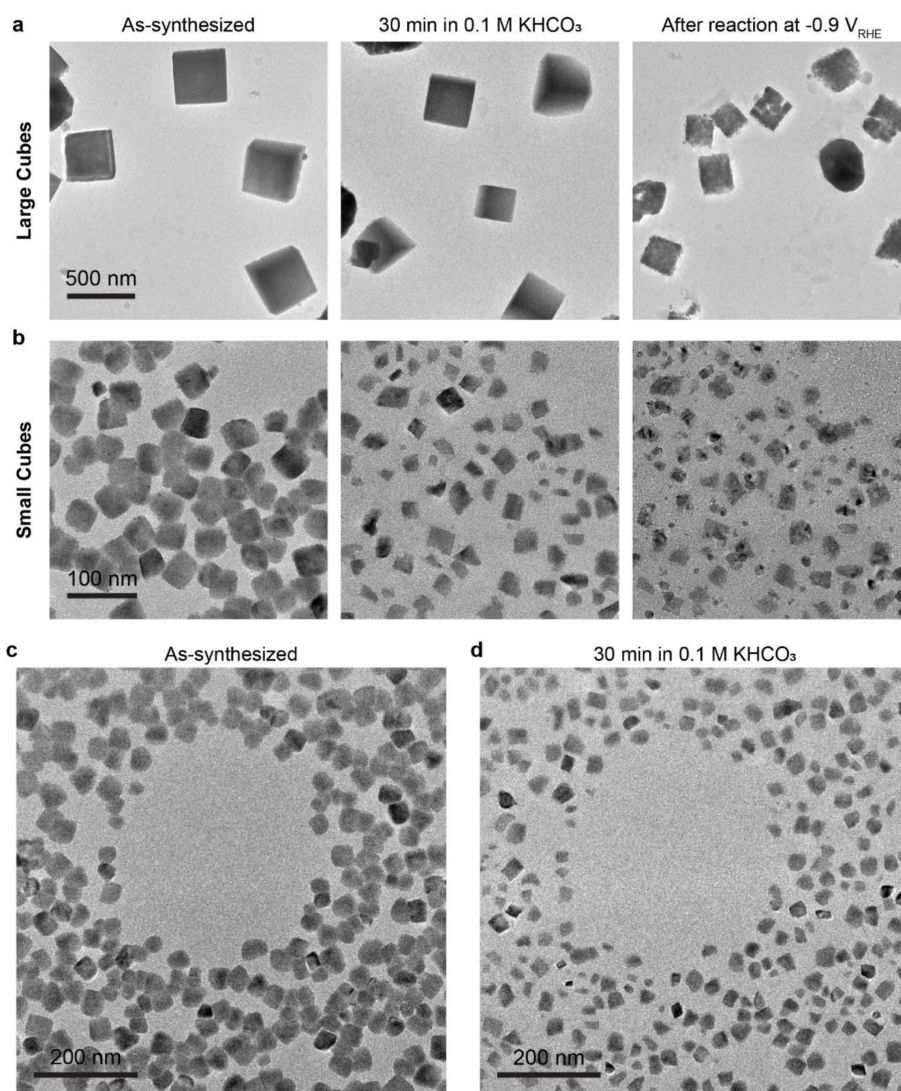
Figure 7.9: ***Ex situ* TEM images of areas comparing Cu$_2$O cubes synthesized on the EC-TEM chip but subject to CO$_2$RR in the benchtop setup.** Image sequence in (a) displays the larger cubes and in (b) the smaller cubes. To mimic the *in situ* experiments, the chips were immersed in 0.1 M KHCO$_3$ (not connected) for 30 minutes followed by 1 hour reaction in CO$_2$-saturated 0.1 M KHCO$_3$ at $-0.9\,\mathrm{V}_{RHE}$. A comparison of the images acquired after immersion in 0.1 M KHCO$_3$ of the smallest as-synthesized cubes also suggests that the KHCO$_3$ can alter the morphology and surface density of the cubes as shown by (c) and (d). Our previous work also suggested that similar changes in morphology also occur on the surface of the larger cubes, but these changes are difficult to observe with TEM[182].
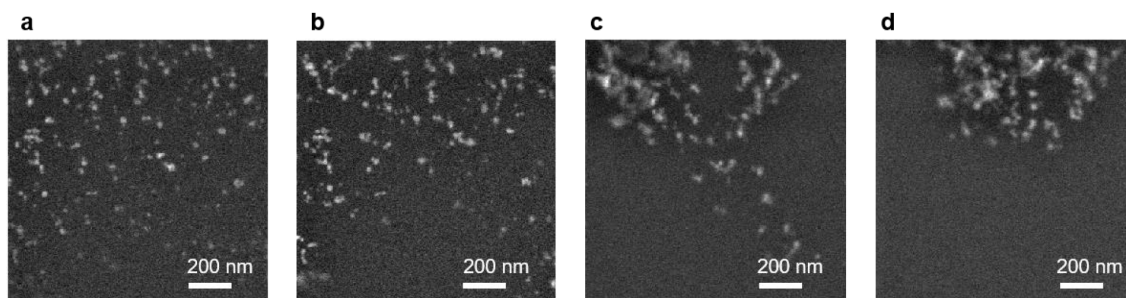
Figure 7.10: **EC-TEM images of fragments and redeposited NPs from the 80 nm cubes** acquired during CO_2RR at (a) 0 min, (b) 5 min, (c) 25 min, and (d) 45 min in CO_2-saturated 0.1 M $KHCO_3$ at $-0.9\,V_{RHE}$.

To understand how the morphological changes identified in the *in situ* experiments impact the overall catalytic properties of these samples, we repeated the synthesis of the Cu_2O cubes on conventional glassy carbon plates using the same protocol and measured their reaction products using online gas chromatography. Chronoamperometric traces obtained during these experiments are provided in Figure 7.11. Results from online gas chromatography analysis of these samples, measured at $-1.1\,V_{RHE}$, are shown in Figure 7.16. Here, Figure 7.16(a) shows SEM images of the samples after 12 hours of CO_2RR and Figure 7.16(b) plots the partial current densities for hydrogen (H_2), carbon monoxide (CO), methane (CH_4) and ethylene (C_2H_4) for samples with the different size distributions. It can be seen from Figure 7.16(a) that the cubic structure was preserved for the larger cubes, whereas extensive agglomeration was observed for the smallest ones, consistent with the *in situ* EC-TEM results. In general, the formation of multi-carbon products, such as C_2H_4, are expected from such Cu_2O cubes starting at $\sim-0.9\,V_{RHE}$[182]. A comparison of the sample morphologies reacted at $-0.9\,V_{RHE}$, $-1.1\,V_{RHE}$, and $-1.3\,V_{RHE}$, captured using SEM (Figure 7.13(a)), indicates that the general morphological evolution is comparable among the different potentials, and that the more negative potential only accelerated the dynamic changes in the morphology. Partial current densities for gaseous products at $-0.9\,V_{RHE}$ and $-1.3\,V_{RHE}$ are provided as Figure 7.13(b).

It can be seen from Figure 7.16(b) that over the course of 12 hours at $-1.1\,V_{RHE}$, CH_4 and C_2H_4 production decrease, which is explained by the observed degradation of the catalyst cubic morphologies, especially with the attachment of re-deposited NPs onto the fragmented cubes. The details, however, differ across the three samples. The sample composed of 170 nm cubes showed significantly higher currents for CH_4 and C_2H_4 compared to the other two samples, presumably due to the higher density of catalytic structures present on the working electrode surface in this sample as shown in Figure 7.12(b). On the other hand, the 80 nm cubes showed a precipitous drop in partial current density for CH_4 and C_2H_4, and an increase in the partial current density for CO within the first hours. While the yields of H_2 and CO stayed roughly constant for the 390 nm and 170 nm cubes, they reached a similar level for the three samples after the first hour of reaction. The 390 nm cubes also maintained the selectivity towards CH_4 and C_2H_4 that were close to those originally found in the 80 nm cubes, but with a more gradual drop over time.

Figure 7.16(c) further compares the Faradaic efficiencies (FE(%)) towards different products at 1 hour and 12 hours of reaction time for these three samples. Figure 7.14 provides the full datasets of the FEs for all products over 12 hours with a temporal resolution of about 17 min and Figure 7.15 compares the gaseous products in terms of the FE for the different cube sizes. It is evident from the product analysis that the 170 nm cubes were the only ones that retained significant hydrocarbon selectivity after 12 hours.
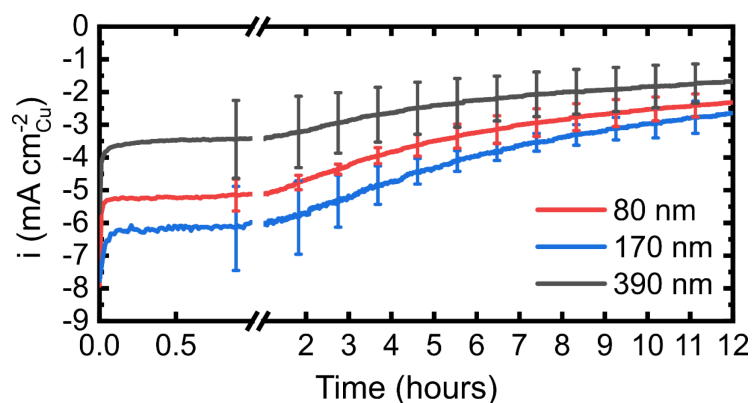
Figure 7.11: **Chronoamperometric traces obtained during the benchtop time-resolved product analysis experiments.** The plot shows the chronoamperometric traces for 80 nm, 170 nm, and 390 nm Cu cubes on glassy carbon plates measured for 12 h at $-1.1\,\mathrm{V}_{RHE}$. Each trace is the average of three independent measurements.
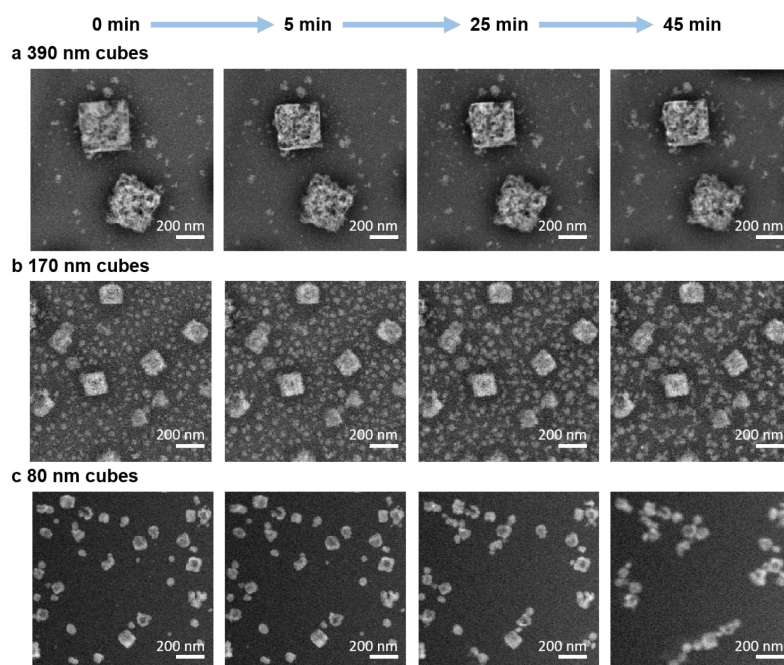
Figure 7.12: **Morphological evolution of Cu$_2$O cubes and re-deposited NPs captured under *operando* conditions over 45 min of CO$_2$RR by EC-TEM.** Snapshots extracted from the videos tracking the evolution of (a) 390 nm, (b) 170 nm, and (c) 80 nm cubes at 0 min, 5 min, 25 min and 45 min after applying a potential of $-0.9\,\mathrm{V}_{RHE}$. Each image is an average of 10 frames. The electron flux used is $3.5\,\mathrm{e^-\,\mathring{A}^{-2}\,s^{-1}}$.
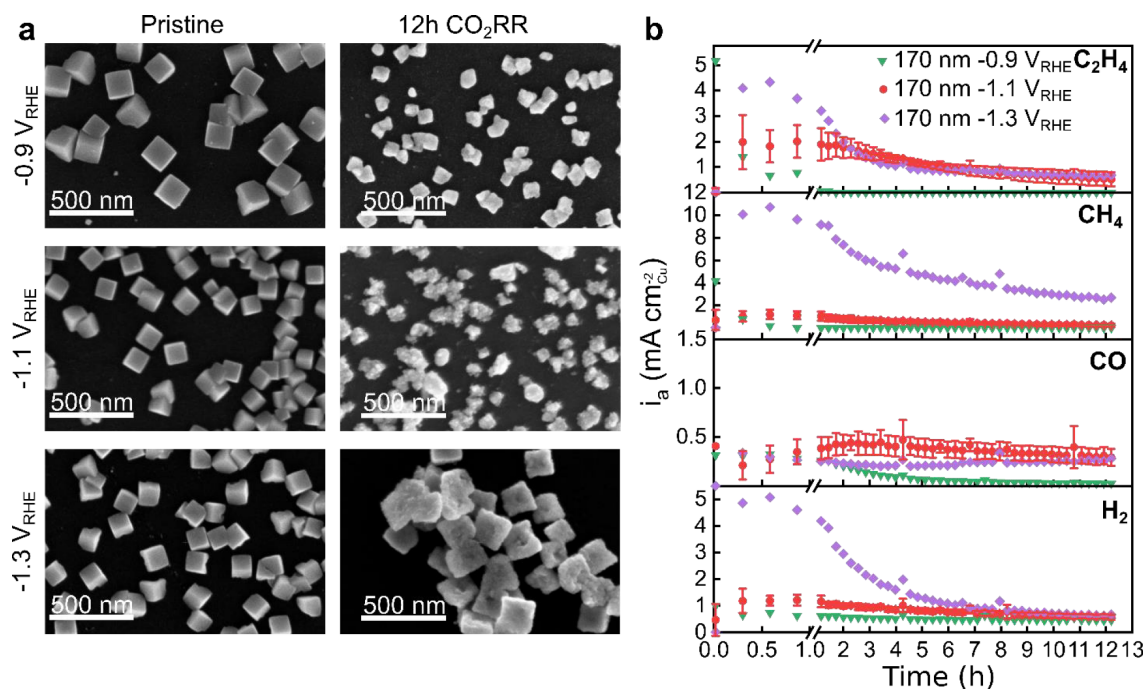
Figure 7.13: **Comparison of the time-dependent evolution of the morphology and gaseous products of CO₂RR at different reduction potentials.** (a) *Ex situ* SEM images of Cu_2O cubes deposited on glassy carbon plates before and after 12 hours of the reaction. Comparison of Cu cubes deposited on a glassy carbon plate before (pristine) and after CO₂RR at $-0.9\,V_{RHE}$, $-1.1\,V_{RHE}$ and $-1.3\,V_{RHE}$. (b) Partial current density of 170 nm Cu cubes measured at $-0.9\,V_{RHE}$, $-1.1\,V_{RHE}$, and $-1.3\,V_{RHE}$ for H_2, CO, CH_4, and C_2H_4. The biggest changes were observed within the first hour of reaction, with secondary long term stability changes.
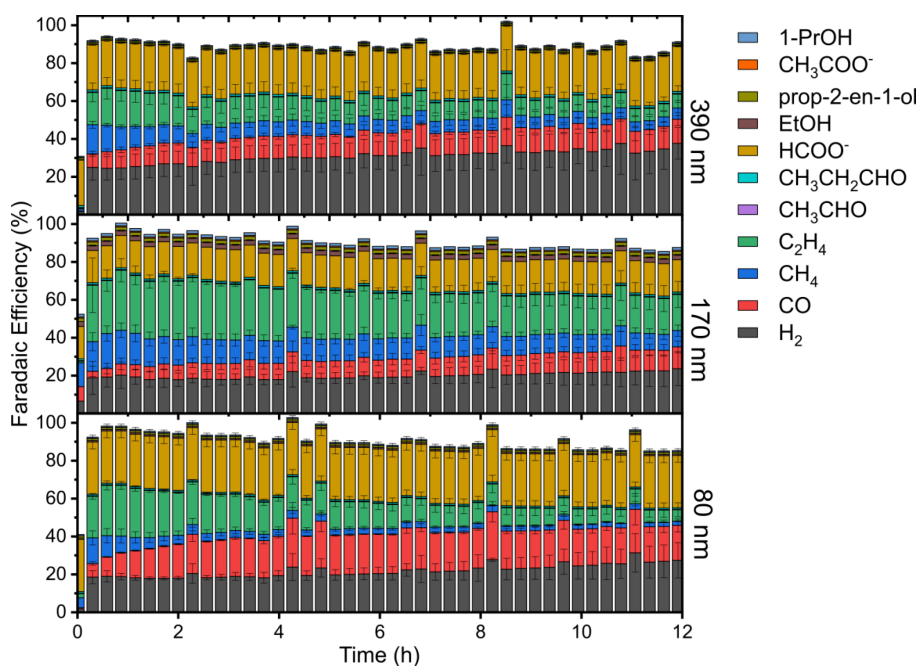
Figure 7.14: **Full product analysis over 12 hours of CO$_2$RR with Cu$_2$O cubes on glassy carbon plates.** Gaseous products were measured via online gas chromatography during the reaction and liquid products were measured with high performance liquid chromatography (HPLC) after the reaction.
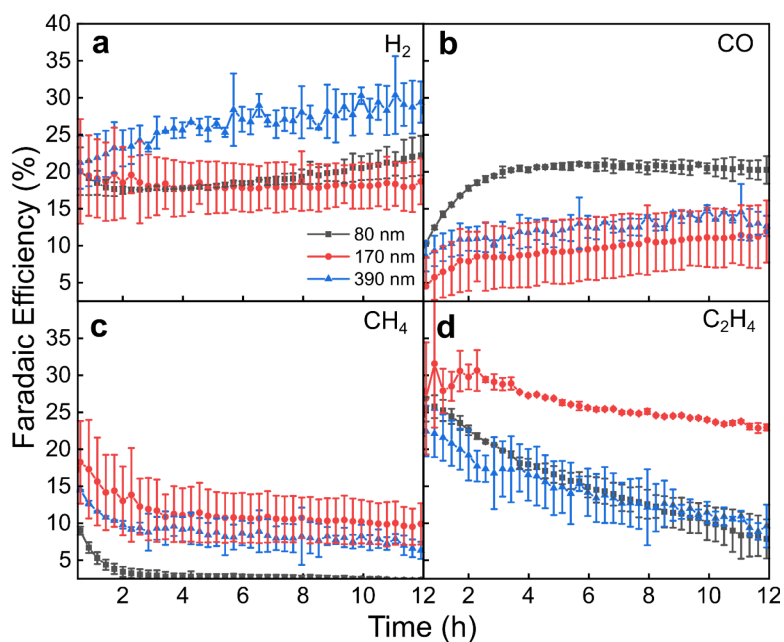
Figure 7.15: **Comparison of the time-dependent CO$_2$RR Faradaic Efficiency evolution for gaseous products.** Faradaic efficiencies of three cube sizes (80 nm, 170 nm, 390 nm) for (a) hydrogen, (b) carbon monoxide, (c) methane, and (d) ethylene.
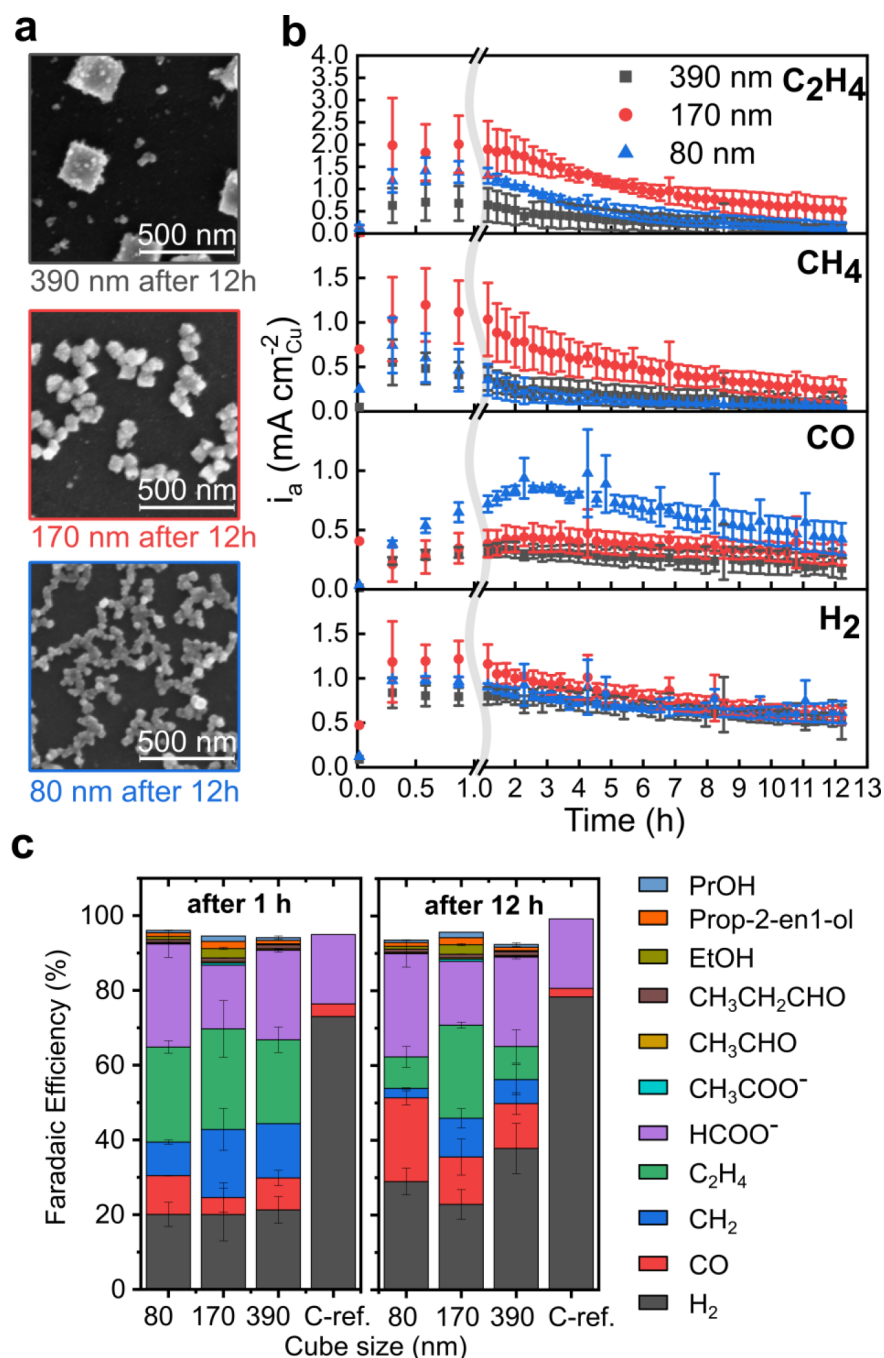
Figure 7.16: **Product analysis from CO$_2$RR over Cu$_2$O cubes deposited on glassy carbon.** (a) SEM images of Cu cubes with three different average size distributions measured *ex situ* after 12 h of CO$_2$RR. (b) Partial current densities for H$_2$, CO, CH$_4$ and C$_2$H$_4$ obtained from time-resolved gas chromatography data acquired over 12 hours. The currents are normalized by the exposed surface area of the as-synthesized Cu$_2$O cubes. Note that this normalization does not consider the dynamic morphological changes observed under reaction conditions. Faradaic efficiencies of all measured reaction products after (c) 1 hour and 12 hours of CO$_2$RR at $-1.1\,\text{V}_{RHE}$. The efficiency in (c) is slightly lower than 100% due to evaporation of liquid product and presumably non-linear product formation since we average the liquid products over 12 h. The reference sample is a glassy carbon plate without catalysts.

We further performed experiments where identically prepared cubes deposited on glassy carbon were extracted and examined at regular intervals during the first hour of the CO_2RR to track the time-resolved morphology changes of the cubes in the H-type cell. These *ex situ* imaging experiments are summarized in [...] subsection 7.2.7. In short, the main features of the EC-TEM observations; cube fragmentation, re-deposition of small NPs and their subsequent agglomeration were found in these samples and their trends as a function of the cube size were also reproduced, indicating that our EC-TEM experiments indeed mimic the behavior of the electrocatalysts in benchtop systems.

Hence, it is evident that the formation, motion, and aggregation of the re-deposited NPs are the main drivers of the morphological change on the working electrode surface. Figure 7.17 plots the time-resolved traces of the size of the cubes and re-deposited NPs extracted from the EC-TEM studies. After the reductive potential is applied, the size of the cubes decreased by 10 ~15% from their as-synthesized size as seen in Figure 7.17(b). Following this initial size change, the cubes remained stable in size but with an increasing spread in sizes as the small re-deposited NPs start to attach to the corners and edges of the cubes as presented in Figure 7.17(b). The cubes with an initial size of ~80 nm showed a steep increase of their size as compared to the larger ones because these small cubes became mobile, which lead to significant aggregation during sustained potential application. As can be seen in Figure 7.17(c), the number density of 390 nm and 170 nm cubes stay constant during the first hour, whereas the number density of 80 nm cubes decreases by ~50%. The latter is caused by the higher mobility and extended aggregation of the smallest cubes, which results from their poor adhesion to the working electrode surface.

The initial sizes of the re-deposited NPs were similar at ~40 nm for the three sample sets, Figure 7.17(d). As these small NPs aggregated with each other or attached to the surface of the existing cubes over time, their size further increased from 40 nm to 60 nm. The NP number density also decreased by ~25% over 45 mins for the 170 nm and 80 nm cube samples as shown in Figure 7.17(e). Such aggregation behavior seems to be similar to that reported for small Cu NP ensembles during CO_2RR[116,117]. The NPs in the 390 nm cube sample show only a minor change in NP surface density, probably due to the sparse distribution of NPs in the original as prepared sample, Figure 7.12(a).

These changes in the catalyst morphology can be further matched with overall trends in the activities of the differently sized cubes. The smallest cubes studied were clearly the least stable with significant aggregation and loss of catalyst material from the glassy carbon surface, which is reflected in the sharp decrease in their hydrocarbon production. Small Cu NPs are also known to be selective towards CO and H_2, instead of hydrocarbons[111]. On the other hand, the increased selectivity towards C_{2+} products in the 170 nm cube sample is surprising and requires us to consider how the catalyst loading changes under reaction conditions, since this is expected to impacts its selectivity[102,258]. In the as-synthesized sample, the highest catalyst loading was obtained for the 80 nm cubes and lowest for the 390 nm cubes[99]. However, the EC-TEM observations indicate that during CO_2RR, the number density of both, cubes and NPs formed during the reaction, is three times higher in the 170 nm sample as compared to the other two samples. Conversely, the density of nanocubes in the 80 nm nanocube sample dropped drastically during the reaction. It is likely that

the high coverage of the NPs generated during CO_2RR from the 170 nm cubes is responsible for the higher amount of multi-carbon products (e.g. C_2H_4) produced. A more facile C-C coupling leading to enhanced hydrocarbon selectivity (vs CO) was previously reported for Cu CO_2RR electrocalysts as a function of the interparticle distance[102] and Cu mass loading.[258] The fragmentation of the as-synthesized Cu_2O cubes also intrinsically creates a large number of defects (e.g. edge sites), which have been deemed favorable for the CO_2RR catalytic activity and selectivity[262,317]. The exact effect of such defects, however, remains to be clarified as very small NPs (<5 nm) with a large number of undercoordinated sites have also been shown to favor H_2 formation[116].

Moreover, the 170 nm cubes had the most stable catalytic performance. FE towards C_{2+} products only dropped by 24% for the 170 nm sample over 12 hours as compared to 46% for the 390 nm sample and 54% for the 80 nm sample. Previously, Jung et al.[316] had reported that 20 nm Cu_2O nanocubes synthesized by means of wet chemistry can gradually fragment over several hours, resulting in a corresponding increase in ethylene selectivity. In comparison, our larger (80-390 nm) cubes fragment almost instantaneously upon the application of a reductive potential, attain peak current densities for C_{2+} products within the first hour of reaction as shown in Figure 7.12 (and Figures 7.14 and 7.15), although only the 170 nm cubes sustain their selectivity. This long-term catalytic stability may be explained as a combination of the morphological stability of the larger nanoporous cubic frames during sustained potential application and the formation of additional densely packed re-deposited NPs, surrounding the cubes, giving rise to a reduction in interparticle spacing during reaction[102].
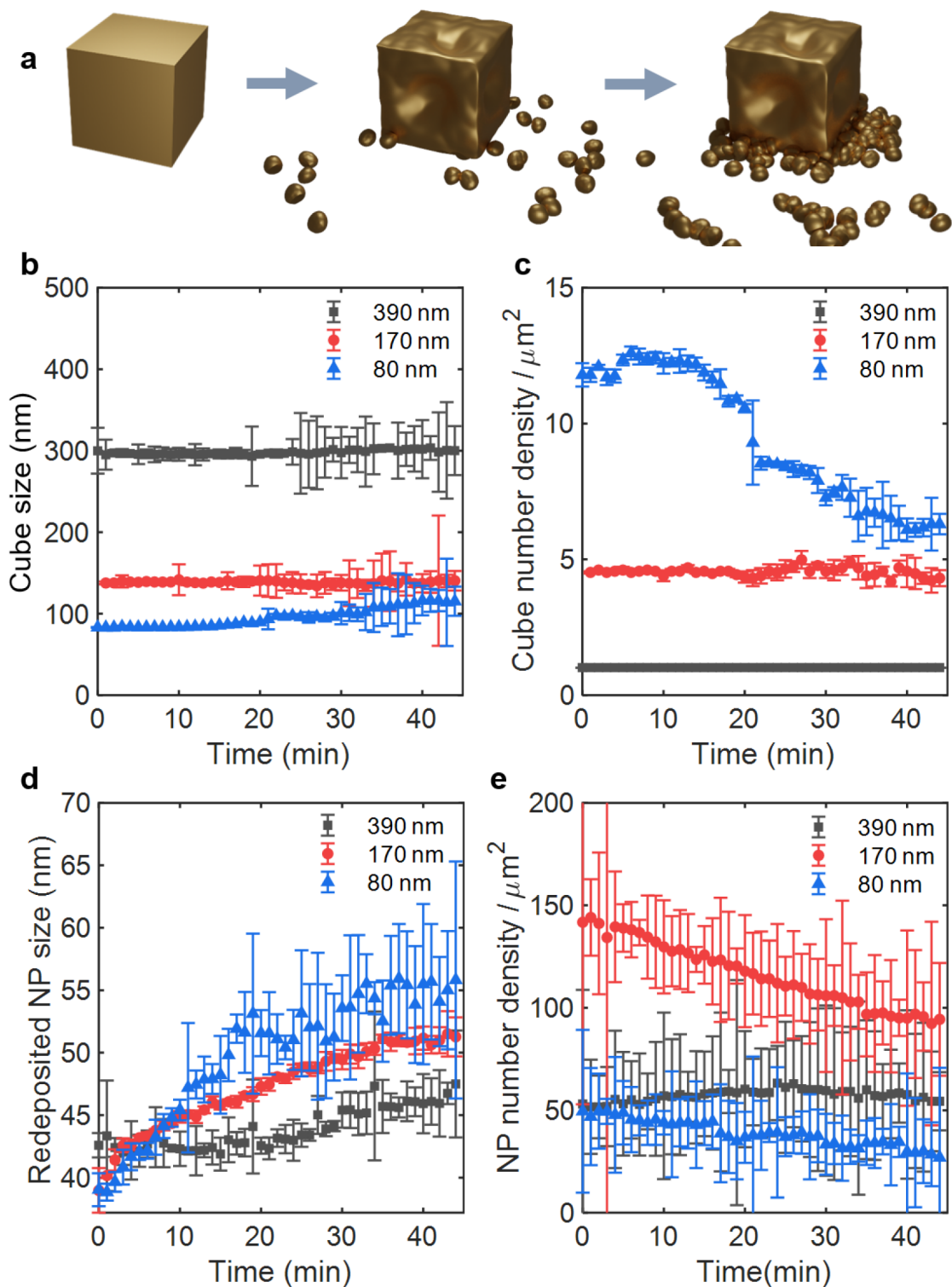
Figure 7.17: **Catalyst size changes over 45 min from *in situ* and *ex situ* imaging.** (a) Schematics describing the evolution of the cube morphology and the re-deposition of catalyst particles. (b) The average cube size, (c) the number density of cubes, and (d) re-deposited particle size and (e) the number density of the re-deposited particles extracted from *in situ* CO_2RR experiments collected over 45 minutes. The error bars represent the standard deviation of the average size of the cubes for the as-deposited samples, whereas for the sizes during reaction, the error bars represent the segmentation error from the automated NP detection processing routine.

So far, we have presented a detailed picture of how Cu_2O catalysts dynamically re-structure under CO_2RR reaction conditions using both *in situ* and *ex situ* electron microscopy, providing insight into the kinetics of different dynamical processes such as re-deposition, agglomeration, detachment, dissolution, and fragmentation[149]. Clearly, the catalytic properties of our system cannot be interpreted using concepts based on the flat surfaces of the well-defined as-prepared Cu_2O cubes. Instead, they must be rationalized based on the contributions of both Cu_2O cubes and re-deposited NPs (summarized in the cartoon in Figure 7.17(a)).

The catalytic stability of the cubic Cu_2O particles cannot be easily understood if one simply considers a size dependence, where neither the samples with larger, stable cubes nor the samples with smaller, rapidly aggregating NPs, showed the best performance. Instead, a combination of densely loaded, moderately sized cubes with a high density of re-deposited NPs yielded the best C_{2+} product selectivity and stability, alluding to a complex interplay between the initial catalyst parameters (cube size, cube loading) and their dynamic parameters (nanoporous frame stability, re-deposited NP size, re-deposited NP loading, re-deposited NP aggregation, and detachment). To check the generality of our results, we also performed EC-TEM experiments using $\sim$30 nm Cu_2O cubes synthesized via a colloidal chemistry approach (Figure 7.18 and Appendix Movie 13.18*). Similar re-structuring and re-deposition were seen in these samples. However, as in our electrochemically synthesized $\sim$80 nm cubes, these cubes did not attach well to the working electrode and were mobile during the extended reaction times employed. Lastly, further clarification using theory regarding how the different factors, especially the effect of confinement[325] due to the nanopores formed under CO_2RR on the fragmented cubes, influence the catalytic behavior can inform rational strategies that exploit the dynamic morphologies of these catalysts for improved performance.
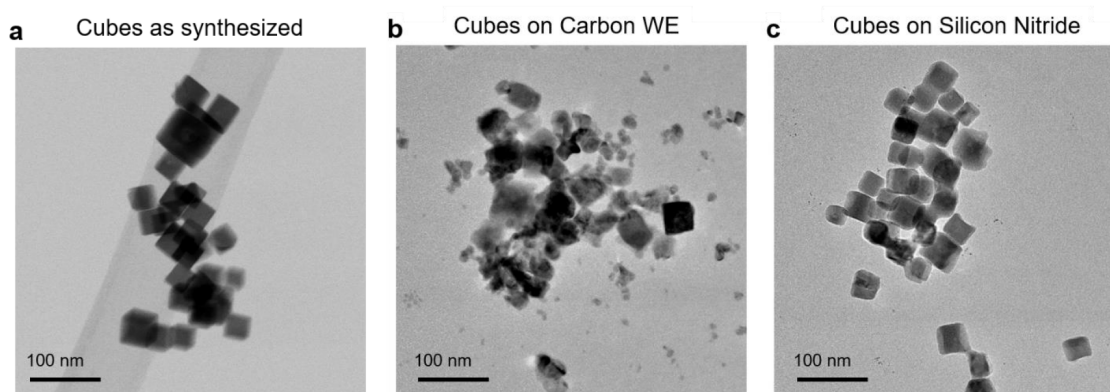
Figure 7.18: *Ex situ* **TEM images of 50 nm Cu_2O cubes synthesized with colloidal chemistry.** (a) Image of the as-synthesized cubes. Images of cubes after 1 hour of CO_2RR that are found in two areas of the silicon nitride window: (b) the carbon WE of the EC-TEM chip and (c) the bare silicon nitride membrane. Images on the carbon WE show significant restructuring and formation of small NPs whereas the cubes on the silicon nitride show only small changes in their shape (presumably un-reacted due to the absence of electrical contact).

---

* Here in form of a figure in the appendix

7.4 Conclusions

Using a combination of *in situ* and *ex situ* electron microscopy experiments, we showed that cubic Cu_2O catalysts restructure from a solid single crystalline form to a fragmented nanoporous structure under CO_2RR conditions. Furthermore, we observed the formation of small randomly shaped NPs originating from Cu leached out of the Cu_2O cubes, resulting in a dynamic morphology with two distinct structures: nanoporous cubic frames and redeposited NPs. By matching the morphological evolution of the cubic catalysts and the smaller NPs generated by the applied potential with the analysis of reaction products from identically prepared samples deposited on bulk carbon electrodes, we elucidated how the C_{2+} hydrocarbon selectivity is controlled by initial cube size and surface coverage. In particular, we revealed that nanoporous structures created from larger cubes are morphologically stable and catalytically selective. Our results also demonstrate the inherent complexity of real-world electrocatalysts and their dynamic morphology under reaction conditions. Understanding of several structural parameters is needed to rationalize the catalytic selectivity of samples with different initial morphology. A complex interplay of dynamic structural behavior, dynamic loading, and interface stability must be considered for the development of better CO_2RR catalysts. Gaining such insight into the long-term stability of nanoscale catalysts is especially important for the advancement of energy conversion technologies as it can lead to the development of novel strategies that make use of the inherent re-structuring dynamics of the catalysts. "[205]

8 Elucidating the Influence of the Support Material on the Catalytic Performance of Electrodeposited Cu-Cubes for Electrochemical CO_2 Reduction in Aqueous Media

This chapter is based on unpublished and ongoing work where I investigate the influence of the support material on the product selectivity of CO_2RR. The idea behind this project is taking support materials that are known for specific properties like reduction of CO_2 to CO to enhance the performance of the electrodeposited Cu cubes.

8.1 Introduction

There is an urgent need to advance technologies that can help counter the effects of anthropogenic climate change. A variety of approaches is being investigated in this rapidly expanding field of research. Carbon oxidation stands at the core of humanity's energy infrastructure, however there is a distinctive lack of industrial counter reactions that cause a perturbation to the system and an increase of the greenhouse gases in the Earth's atmosphere.

A key technology to prevent this is the catalytic conversion of industrial climate change gases, such as CO_2, that are emitted from industrial plants and converting them back into valuable chemicals, thus closing the industrial carbon cycle. A promising strategy to achieve this goal would be the CO_2RR[312,313] with the help of renewable energy sources. With this catalytic conversion, industrially desirable products can be yielded such as ethanol and ethylene[12,13], which can be either used directly as fuel or as precursors for established industrial processes. Contrary to thermally driven catalytic processes, the aqueous electrochemical CO_2RR can run at ambient temperature and atmospheric pressure and further combines electrochemical water splitting with carbon hydrogenation into one process.

Amongst all available catalysts investigated to this day, copper is unique as a material in its ability to produce C_{2+} hydrocarbons, alcohols, and aldehydes in significant amounts. However, with more than ten products, it suffers from bad selectivity towards the most desirable chemicals as well as from a low energy efficiency due to the required high overpotentials[12–14]. Furthermore, it is always competing with the parasitic hydrogen evolution reaction (HER).

A tremendous effort has been put into elucidating the processes that govern the electrochemical reduction of CO_2.[88] Among the investigated parameters, the catalyst structure and chemical

state are of particular importance.[17,101,241] Compared to polycrystalline Cu electrodes, nanostructured Cu catalysts have shown a significantly improved CO_2RR performance attributed to grain boundaries[242,243], Cu{1 0 0} facets[35,92,113,115,244,245], increased roughness[72], defects[135,248,249], low-coordinated sites[102,250,326], and the presence of subsurface oxygen and Cu(I) species[97,131,251–258]

However, a factor that has not been researched intensively is the role of the support material, which can have significant influence on a catalysis performance through spillover or cascade effects, synergistic effects or enhanced stability governed by the interface. From all the electrode materials that are active for CO_2RR, three groups can be classified based on their primary product[327]. Formate ($HCOO^-$) is produced as the main product by metals such as Pb, Hg, Ti, In, and Sn[328,329]. Transition metals like Zn, Pd, Au, and Ag[65] produce mostly carbon monoxide (CO), whilst some others are almost inert for CO_2RR and only participate in HER, like Pt, Fe, and Ni[65,329]. In order to modify the selectivity of Cu catalysts, the combination of two (or more) catalyst materials can have beneficial effects on selectivity or activity[330,331]. Adding a primarily CO producing material can enhance the reaction through spillover effects, such as surface diffusion of CO or the increase of local CO concentration[18,332,333]. Additionally, electronic effects can change the electronic structure of the catalyst material which alters binding strengths on the surface, ultimately leading to a lower energy barrier of the rate determining step (CO_2 to CO)[334].

In this study, we make an effort to better understand the influence that the support has on our electrodeposited Cu-cubes[99] and correlate this to the selectivity. We have prepared cubic catalysts by electrodeposition on primarily H_2, CO, and $HCOO^-$ producing transition-metal supports and compared their selectivity to that of a pure Cu-foil. Online gas chromatography (GC) allowed us to observe the products of the reaction, whilst SEM provided information of the morphology of our catalysts. Lastly, potentiometric impedance spectroscopy (PEIS) was used to investigate the catalyst/support/electrolyte interface.

8.2 Results

To study the effects of the support material, a selection of supports has been made. Ag and Au were chosen as they provide carbon monoxide at relatively low potentials and with high currents. The lattice parameter of these transition metals are close to that of Cu, thus a more stable interface will be formed between the cubes and the support. In addition, Fe was chosen a contrast since it is very active for HER. Formate-producing supports are excluded in this study to avoid having an easy route for a terminal product in CO_2RR. Lastly, two types of carbon supports were chosen, one with high roughness (carbon paper) and one that is flat (carbon foil) to have a support that is not strongly active for CO_2RR. For these, the only difference should be caused by support topography effects.

First of all, the cubes were synthesized on the aforementioned support materials according the the procedure described in[99]. SEM images were taken before and after 1 h of CO_2RR at $-1.0\,V_{RHE}$ as shown in Figure 8.1.
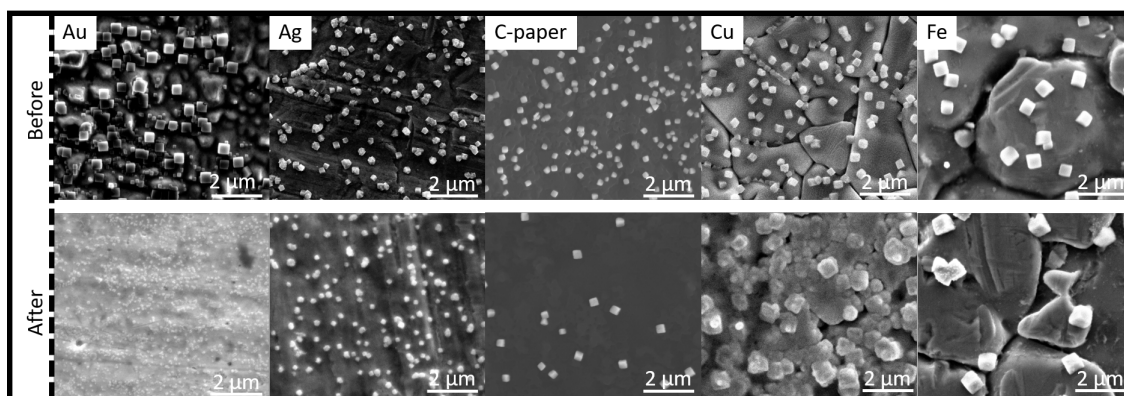
Figure 8.1: Cu cubes electrodeposited on Au foil, Ag foil, carbon paper, Cu foil, and Fe foil as support materials before and after 1 h of CO_2RR at $-1.0\,V_{RHE}$ in CO_2 saturated 0.1 M $KHCO_3$

The images indicate that the cubes have different stability under CO_2RR conditions, depending on which support they are deposited on. To gain more information on the respective contribution for CO_2RR and to distinguish the reactivity of the support and the cubes, linear sweep voltammetry (LSV) was conducted before and after electrodeposition in a defined area. The electrolyte was CO_2-saturated 0.1 M $KHCO_3$ and the sweep rate was set to $20\,mV\,s^{-1}$. We found that in all cases the onset of the LSV was shifted to more negative potentials. The smallest difference was found for the Cu-cubes on Cu and the largest difference for Cu cubes on Fe. Additionally, we compare the second and tenth cycle to see how the current changes within the first few minutes. Again, the biggest change was observed for Cu cubes on Fe sample, the smallest in the Cu cubes on Cu. The results for all tested support materials are shown in Figure 8.2a-f.
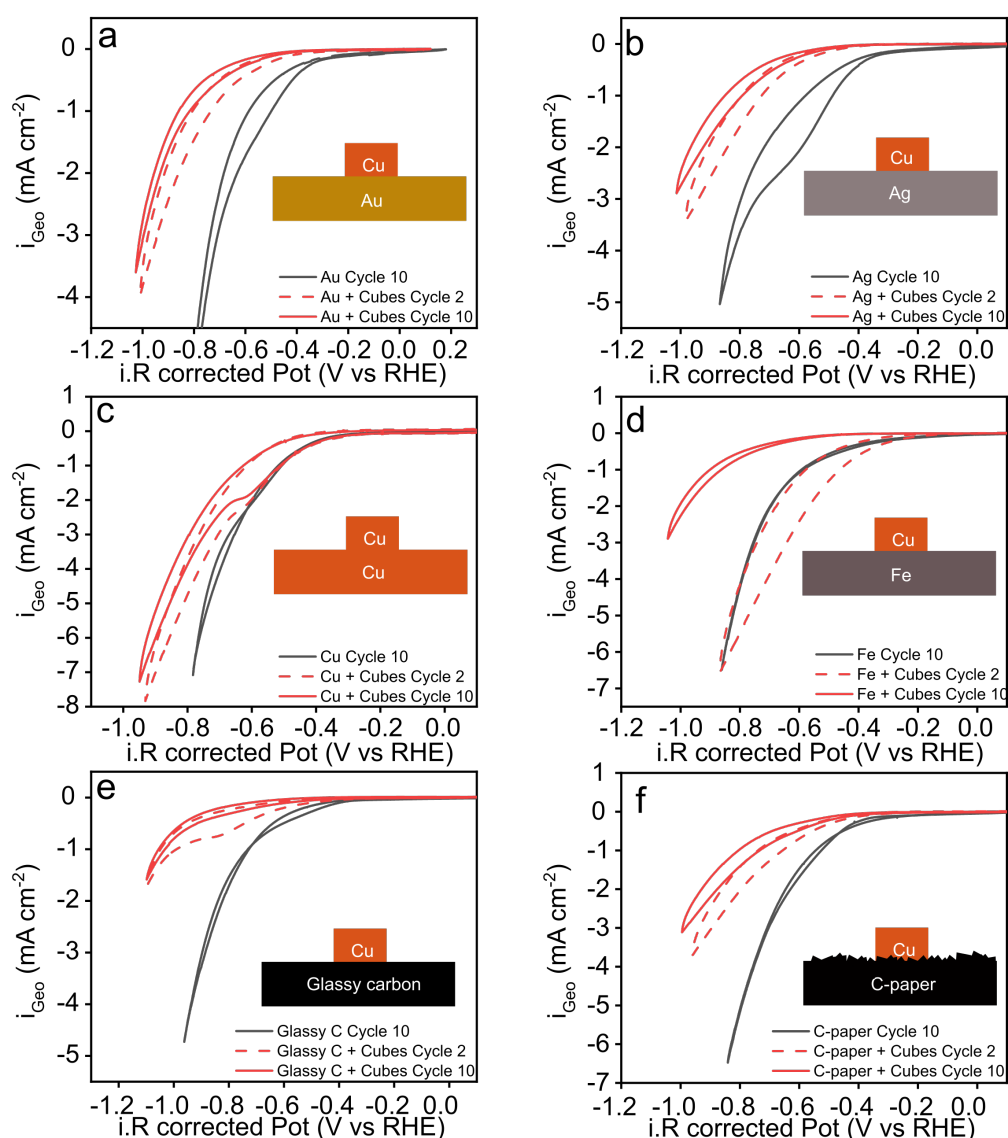
Figure 8.2: Linear sweep voltammetry of the pristine supports after 10 cycles and the Cu cube decorated supports in CO_2 saturated 0.1 M $KHCO_3$ on Au (a), Ag (b), Cu (c), Fe (d), glassy carbon (e), and carbon paper (f). The 10th cycle is compared to ensure the system is under stable conditions. For the Cu cubes on the respective support, the 2nd cycle is shown with a dotted line to see the strong changes within 10 cycles. All potentials are 90% iR corrected.

With the exception of the Cu cubes on Cu, we have observed a drop in current and a shift to more negative potentials for all other support materials. This phenomenon was further explored by conducting potentiostatic electrochemical impedance spectroscopy (PEIS) measurements. The results are shown in Figure 8.3, where the supports were again measured before and after electrodeposition of the Cu cubes. A total of three potentials were measured and to see the impedance response in the non-faradaic region ($-0.1\,V_{RHE}$), close to or at the onset ($-0.3\,V_{RHE}$), and at CO_2RR relevant potentials ($-0.9\,V_{RHE}$). We found that with increasingly negative potential, the charge transfer resistance (second 0 crossing) decreases to lower Re(Z) values. With the addition of Cu cubes, however, they overall increase again. In the case of the Cu cubes on glassy carbon, the onset shifts

so far to more negative potentials, that no charge transfer occurs at all at $-0.9\,V_{RHE}$. For Cu cubes on carbon paper, Ag, and Fe on the other hand, we observed mass transport limitations, indicated by the Warburg resistance (linear continuing plot at higher Re(Z) values).
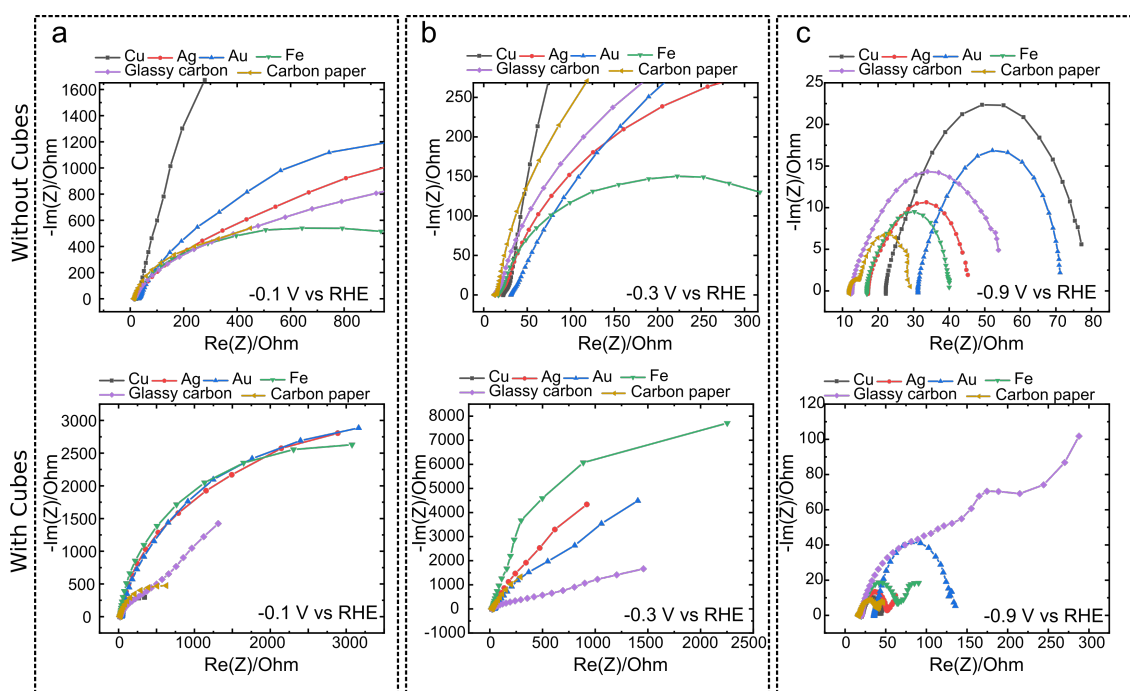
Figure 8.3: Impedance spectroscopy measurements of the pristine support materials and the same support materials with Cu cubes electrodeposited in CO_2 saturated 0.1 M $KHCO_3$. Niquist plot measured at a) $-0.1\,V_{RHE}$, b) at $-0.3\,V_{RHE}$, and c) at $-0.9\,V_{RHE}$. The frequency range is 1 Hz to 0.1 MHz.

Lastly, the performance for CO_2RR was measured by comparing the potential dependent formation of products by online gas chromatography (GC). Figure 8.4 shows the gas products for all measured supports with Cu cubes at different potentials. As can be seen from Figure 8.4a, in terms of hydrogen Fe performs the best with close to 100% faradaic efficiency, however, this also means that no CO_2RR could be achieved on this support material. This is in agreement with the performance we observed in the LSV in Figure 8.2. In the case of Cu cubes on Cu, Ag, Au, and C-paper we observed respective minimum points for H_2 production. From the faradaic efficiency for CO, we have observed that Ag and Au express superior performance, indicating that in these cases the support material is the major contributing catalyst and not the Cu cubes. Interestingly, we observe CH_4 and C_2H_4 for Cu cubes on Ag, indicating that here the Cu cubes are indeed participating in the CO_2RR and compete with the Ag support material. The maximum of the faradaic efficiency, however, is only about 50% to that of Cu cubes on Cu and the maxima are shifted to more negative potentials. Surprisingly, in case of Au, no faradaic efficiency for hydrocarbons could be observed.
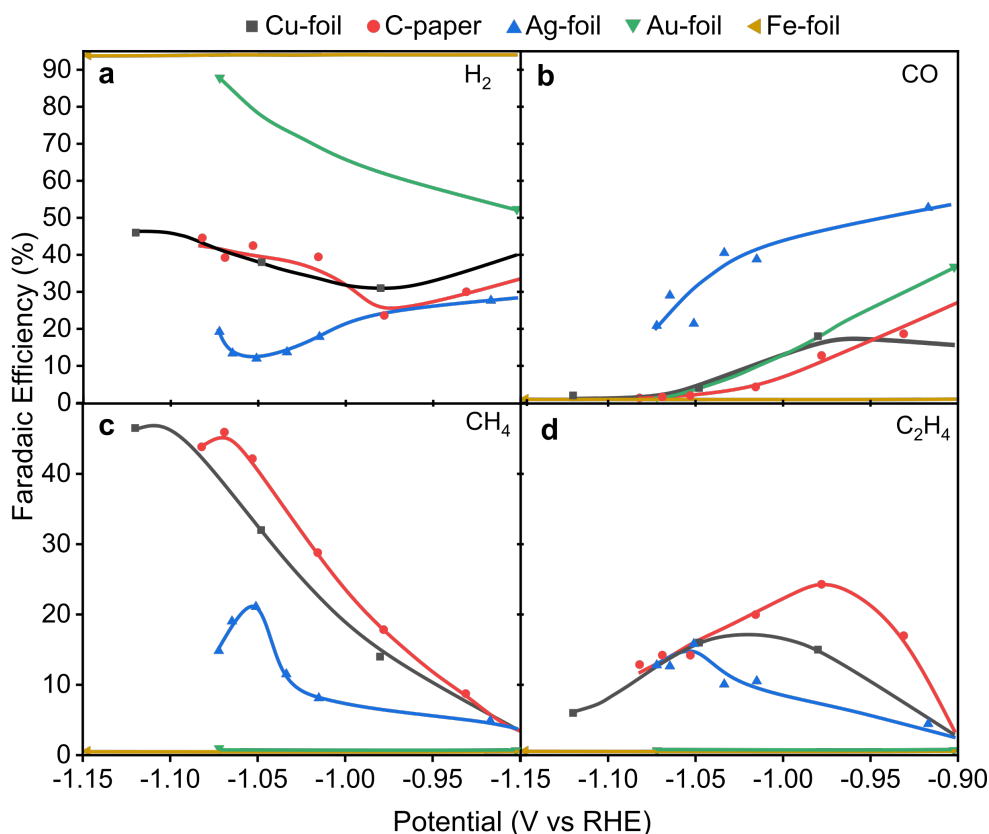
Figure 8.4: Faradaic efficiency for Cu cubes on different supports. a) shows faradaic efficiency for H_2, b) for CO, c) for CH_4, and d) for C_2H_4 as a function of the applied potential. The lines are guides for the eye and do not indicate a fit.

8.3 Discussion

We have also observed different morphological behavior after CO_2RR, depending on the support material used. From fragmentation of the Cu cubes on Au, shrinking on Ag, and sintering on Cu, the range of observed effects is broad and a unified explanation is close to impossible. However, from the data discussed in the previous section, we can derive an interaction of electrodeposited Cu cubes on the tested support materials. In the case of Cu cubes supported on Au and Fe we have not seen activity for hydrocarbons, only H_2 for Fe and H_2+CO for Au. These products are known to be coming from the support itself and dominate the selectivity trends, since no contribution from the Cu cubes could be observed.[65,329] The reason is the poor overlap of potentials, where the supports start to produce H_2 and CO respectively at far lower overpotential and with high current densities, as compared to the CO_2RR onset. The impedance measurements showed that the overall resistance (ohmic and charge transfer resistance) increases by adding the Cu cubes. An explanation for this observation could be the increased amount of electrons required to form products on the cubes (two or more electrons), whereas the blank supports can only produce simple molecules derived from one or two electron transfer processes. However, the cubes consist initially of Cu_2O, which has lower conductivity and thereby cause the observed increase in resistance. This needs to be studied in future experiments.

8.4 Conclusion

It can be concluded that the presented data show an interesting approach to enhance the performance of electrodeposited Cu cubes, however, understanding the complicated interplay and competitive reaction pathways require a more in depth analysis by spectroscopic means. Furthermore, a higher temporal resolution product analysis like DEMS could provide crucial information on the highly potential dependent product selectivity and thereby distinguish between support and Cu cube contributions. Lastly, an analysis of the bound surface species i.e. extracted from Raman spectroscopy measurements could provide information on the different binding of intermediate species on the catalyst and support. It is important, that all studies are conducted on the blank supports as well, ideally on the same piece of material that is subsequently used for the electrodeposition to enable a better comparable study.

9 Plasma Induced Surface Functionalization for Catalysis

9.1 Plasma-Activated Copper Nanocube Catalysts for Efficient Carbon Dioxide Electroreduction to Hydrocarbons and Alcohols

The following section is based on the publication "*Plasma-Activated Copper Nanocube Catalysts for Efficient Carbon Dioxide Electroreduction to Hydrocarbons and Alcohols*" in which I was involved in sample preparation and plasma treatment. In this publication, we "have developed highly active and selective copper (Cu) nanocube catalysts with tunable Cu{1 0 0} facet and oxygen/chlorine ion content by low-pressure plasma pretreatments. These catalysts display lower overpotentials and higher ethylene, ethanol, and n-propanol selectivity, resulting in a maximum Faradaic efficiency (FE) of $\sim$73% for C_2 and C_3 products. Scanning electron microscopy and energy-dispersive X-ray spectroscopy in combination with quasi-*in situ* X-ray photoelectron spectroscopy revealed that the catalyst shape, ion content, and ion stability under electrochemical reaction conditions can be systematically tuned through plasma treatments. Our results demonstrate that the presence of oxygen species in surface and subsurface regions of the nanocube catalysts is key for achieving high activity and hydrocarbon/alcohol selectivity, even more important than the presence of Cu{1 0 0} facets."[131]

9.1.1 Introduction

"The electrochemical reduction of CO_2 to useful chemicals and fuels provides a sustainable way to simultaneously address the environmental challenges caused by fossil fuel combustion and the global need for storage of electric power produced by renewable energy sources.[335,336] The activity and selectivity of CO_2 electroreduction over metal catalysts partly depend on the adsorption strength of carbon monoxide (CO) on the metal surfaces.[17,337] Among the metals used for CO_2 electroreduction, copper (Cu) is one of the most extensively studied.[28,101,338] Thanks to its moderate CO binding energy, Cu can efficiently reduce CO_2 to valuable hydrocarbons and alcohols, rather than to only yield CO and formic acid.[15] Polycrystalline Cu shows much higher selectivity for methane than ethylene, an important chemical feedstock.[28,80] There is an urgent need to develop novel, highly active electrocatalysts with enhanced selectivity for C_2/C_3 hydrocarbons and alcohols that could be economically employed in industrial applications. Nanostructured Cu catalysts have shown tunable activity and selectivity for CO_2 electroreduction.[94,101,111,137,253–255,267,339,340] Compared with polycrystalline Cu, oxide-derived Cu catalysts exhibit significantly improved CO_2 electroreduction at lower potentials,[242] which was initially attributed to a large amount of grain boundaries formed by successive oxidation and reduction.[341] The increase of the local pH on the

roughened Cu surface[247] was considered to be another factor contributing to the enhancement of catalytic activity.[74] Besides surface roughness, the crystallographic orientation of nanoscale structures on the surface of Cu-based catalysts has also been reported to affect their catalytic properties. The presence of cubic Cu-based nanostructures was shown to lower the onset potential for ethylene formation and to lead to high ethylene selectivity at the expense of methane.[92,94,113] The role of Cu^+ species and subsurface oxygen on pre-oxidized Cu foils has also been proposed to be a crucial parameter affecting the activity and ethylene/alcohol selectivity of Cu catalysts.[251,252,254,342] Despite intense recent work, the mechanism behind the improved activity and ethylene/alcohol selectivity of oxide-derived Cu-based catalysts for CO_2 electroreduction remains controversial. Disentangling the contributions of the crystallographic facets, roughness, and the presence of Cu^+ species and/or subsurface oxygen and determining the relative importance of each of them have not yet been possible. To shed light on the relative effect of these parameters, we designed a Cu nanocube catalyst with tunable Cu{1 0 0} facet morphology and ion (O_2- and Cl^-) content achieved by mild plasma treatments. By comparing the catalytic performance of samples with similar cubic morphology but different ion contents and samples with similar oxygen content but different morphology, we were able to demonstrate that the presence of oxygen in the ethylene- and alcohol-selective catalysts is key for achieving high activity and selectivity. It is postulated here that surface and subsurface oxygen species affect the binding of CO to the Cu nanocube surface, favoring the formation of multicarbon reduction products such as ethylene, ethanol, and n-propanol.[245]

9.1.2   Methods

Synthesis and Plasma Treatment

Commercial Cu foils (Advent Research Materials Ltd., 99.995%) were first cleaned with acetone and ultrapure water (18.2 MΩ) in an ultrasonic bath and then electropolished in phosphoric acid (VWR, 85 wt %) at 3 V vs Titanium foil for 5 min. Cu nanocubes were prepared by electrochemically anodizing the electropolished Cu foils in 0.1 M KCl (VWR, 99.9%) with five triangular potential scans ranging from 0.4 to 2.0 V vs RHE at a rate of 500 mV s^{-1}. During each cycle, the potential was held at the positive and negative limits for 10 and 5 s, respectively.18 The Cu nanocube samples were then rinsed with a large amount of ultrapure water to remove the electrolyte. Plasma pretreatments were then performed in a plasma etcher (Plasma Prep III, SPI Supplies) at a gas pressure of 400 mTorr of O_2, H_2, or Ar and power of 20 W for different periods of time.

Surface Characterization

The morphology of the cubic nanostructures and the surrounding foil surface was investigated by SEM using a Quanta 200 FEG microscope from FEI with a field emitter as electron source. The images were acquired in vacuum using a secondary electron (Everhart-Thornley) detector to ensure high surface sensitivity. An accelerating voltage of 10 kV and a working distance of 10 mm were found to yield the best balance between spatial resolution, surface sensitivity, signal-to-noise

ratio, and field depth. A separate, liquid-N_2-cooled EDX detector was employed for the elemental analysis of the sample surface. The acceleration voltage chosen for the EDX studies was also 10 kV. For every sample and every treatment condition (as-prepared, after plasma treatment and after electrochemical reaction), a large number of SEM images were acquired from different regions of the surface at magnification factors between 100x (overview images) and 160.000× (detailed morphology of a selected nanocube), to ensure that the obtained results were representative of the whole surface. For the elemental analysis, EDX spectra from at least 10 different nanocubes, as well as from nearby regions of the underlying foil, were collected. The average composition of the cubes and the foil was subsequently determined for every sample and condition. [...][131]

Electrochemical Measurements

"Electrochemical measurements were carried out in a gas-tight H-cell separated by a Nafion 115 membrane. Both working and counter compartments were filled with 40 mL 0.1 M $KHCO_3$ (Sigma-Aldrich, 99.7%) and purged continuously with CO_2 (20 mL min-1). A platinum gauze (MaTecK, 3600 mesh cm^{-2}) was used as the counter electrode and a leak-free Ag/AgCl electrode (Innovative Instruments) as the reference electrode. The Cu nanocube samples were used as the working electrode and contacted with a clamp wrapped by Kapton tape to avoid the unwanted reaction. A freshly prepared sample was measured with a chronoamperometric step for 1 h at each potential. The potentials were controlled with an Autolab potentiostat (PGSTAT 302N). All potentials vs Ag/AgCl were converted to the reversible hydrogen electrode (RHE) scale and corrected for iR drop as determined by current interrupt. The roughness factors were determined by measuring double-layer capacitance with cyclic voltammetry in CO_2-saturated 0.1 M $KHCO_3$ solution (pH 6.8) after 1 h of electrochemical reaction at -1.0 V vs RHE [...].[242,251]

Product Analysis

The gas products were analyzed by online GC (Agilent 7890A) every 17 min. CO, H_2, and hydrocarbons were separated by different columns (Molecular sieve 13X, HayeSep Q and Carboxen-1010 PLOT) and quantified by a thermal conductivity detector (TCD) and flame ionization detector (FID). Carboxylates (formate and acetate) formed during electrolysis were analyzed by HPLC (Shimadzu Prominence), equipped with a NUCLEOGEL SUGAR 810 column and refractive index detector (RID). Alcohols were analyzed by liquid GC (Shimadzu 2010 plus), equipped with fused silica capillary column and FID. An aliquot of the electrolyte after reaction was directly injected into HPLC and liquid GC without further treatment. All reported FEs were calculated based on the product distribution and current after 1 h of electrochemical reaction at constant potentials."[131]

9.1.3 Results and Discussion

Size-selected Cu nanocube catalysts were synthesized by electrochemical cycling of an electropolished Cu foil in an aqueous 0.1 M KCl solution. Characterization by SEM ([...]) showed that the as-prepared nanocubes have an average edge length of 250-300 nm and are evenly distributed across the Cu foil surface with no evidence of large-scale agglomeration. Some local clustering

of nanocubes occasionally occurs along domain borders of the underlying foil. The Cu nanocube samples contain 240 ± 80 nanocubes per $100\,\mu m^2$ of geometric surface area based on the acquired SEM images. Energy dispersive Xray spectroscopy (EDX) analysis indicates that the nanocubes consist of CuO_xCl_y with the ratio x:y typically being close to 1:1 ($\sim$20 at% for O and $\sim$24 at% for Cl), while the surface and near-surface regions of the surrounding (and underlying) foil consist of CuCl with no oxygen detected in those regions within the sensitivity of EDX [...].

Our SEM analysis revealed that, while long exposure of the samples to plasma destroys the nanocubes, short plasma treatments ($\sim$20 s O_2 plasma or 4-5 min H_2/Ar plasma) do not significantly modify the morphology of the as-prepared samples and only moderately affect the ion content of the cubes (moderate increase of O_2-ion content after O_2 plasma, analogous decrease upon H_2 plasma, and minimal change upon Ar plasma as compared to the as-prepared samples). The most significant effect of plasma treatment becomes evident after 1 h of the CO_2RR at -1.0 V vs RHE. While the nanocubes that do not undergo any plasma treatment (as prepared) have a significantly lower oxygen content ($\sim$14 at% O, O/Cu atomic ratio $\sim$0.2), the samples treated with O_2 plasma prior to the reaction retain more oxygen ($\sim$30 at% O, O/Cu atomic ratio $\sim$0.4) in their final state after the reaction. Although part of this oxygen consists of adsorbed species and is not in the form of copper oxides, there is spectroscopic evidence that O_2 plasma treatment before the reaction partially stabilizes the $O_2{}^-$ ions and results in oxygen-rich nanocubes even after long exposure to the strongly reducing electrochemical environment. The samples that are treated with H_2 plasma before the reaction end up with $\sim$14 at % O, and those pre-exposed to argon with only $\sim$6-7 at% O after the reaction. While an initial Cl content of $\sim$24 at% was detected on the as-prepared nanocubes, the amount of Cl both in the nanocubes and in the foil after the reaction is less than $\sim$2 at% in the O_2 and H_2 treated samples and negligible in the as-prepared and Ar treated samples.
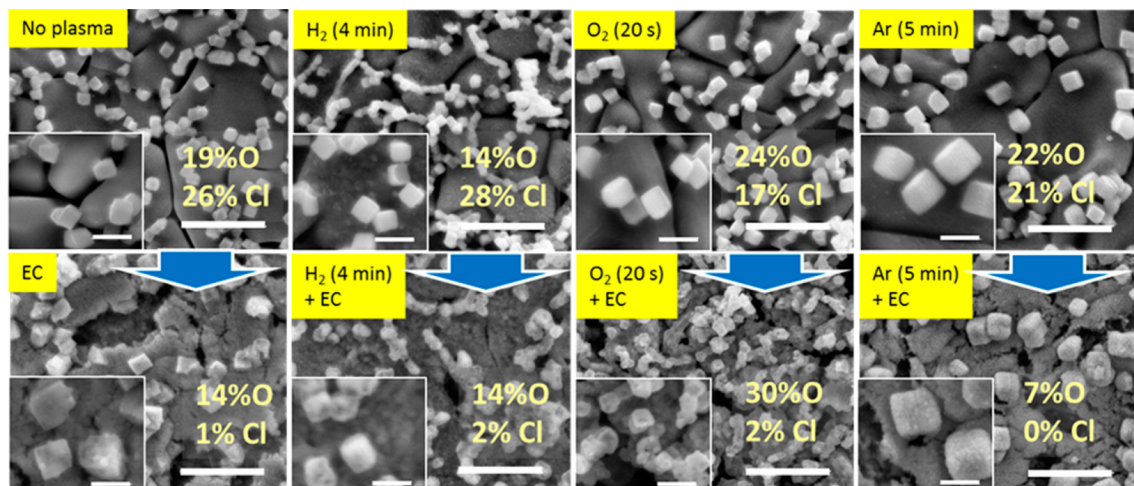
Figure 9.1: SEM images of Cu nanocube samples after plasma treatment (first row) and after 1 h of electrochemical reaction (EC) at -1.0 V vs RHE (second row). The scale bar in the main images is 2 μm. The insets show details of the nanocubes (scale bar: 500 nm). The atomic percentages determined by EDX shown are average values for each sample and refer to the elemental composition of the nanocubes themselves (not the surrounding Cu foil). Data acquired by Dr. Ioannis Zegkinoglou.

Under reaction conditions, a gradient in the oxygen content inside the Cu cubes is likely formed, with lower oxygen content near the surface. The catalytic activity and selectivity of the Cu nanocubes were obtained by performing chronoamperometry measurements in a CO_2-saturated 0.1 M $KHCO_3$ solution. The gas products were analyzed by online gas chromatography (GC), while liquid products were analyzed by high-performance liquid chromatography (HPLC) and liquid GC after electrolysis. Figure 9.2a shows the geometric current density of differently treated samples as a function of the applied potential. All Cu nanocube samples show significantly higher geometric current density than an electropolished Cu foil. To some extent, this can be attributed to the high surface area of the roughened Cu nanocube samples. Indeed, cycling the Cu foil in a KCl solution and successive plasma treatment significantly affects the roughness of the surface. [...] Despite the importance of the roughness effect, it cannot by itself explain the difference in the geometric current densities of the differently treated Cu nanocube samples. For example, although the as-prepared nanocube sample has an electrochemical roughness factor very similar to that of the 4 min H_2 plasma treated sample, its geometric current density is about 1.5 times higher than that of the H_2 plasma treated sample at -1.0 V vs RHE. The same observation can be made for the 20 s O_2 and 5 min Ar plasma treated samples, which also have similar roughness factors but very different catalytic activity.
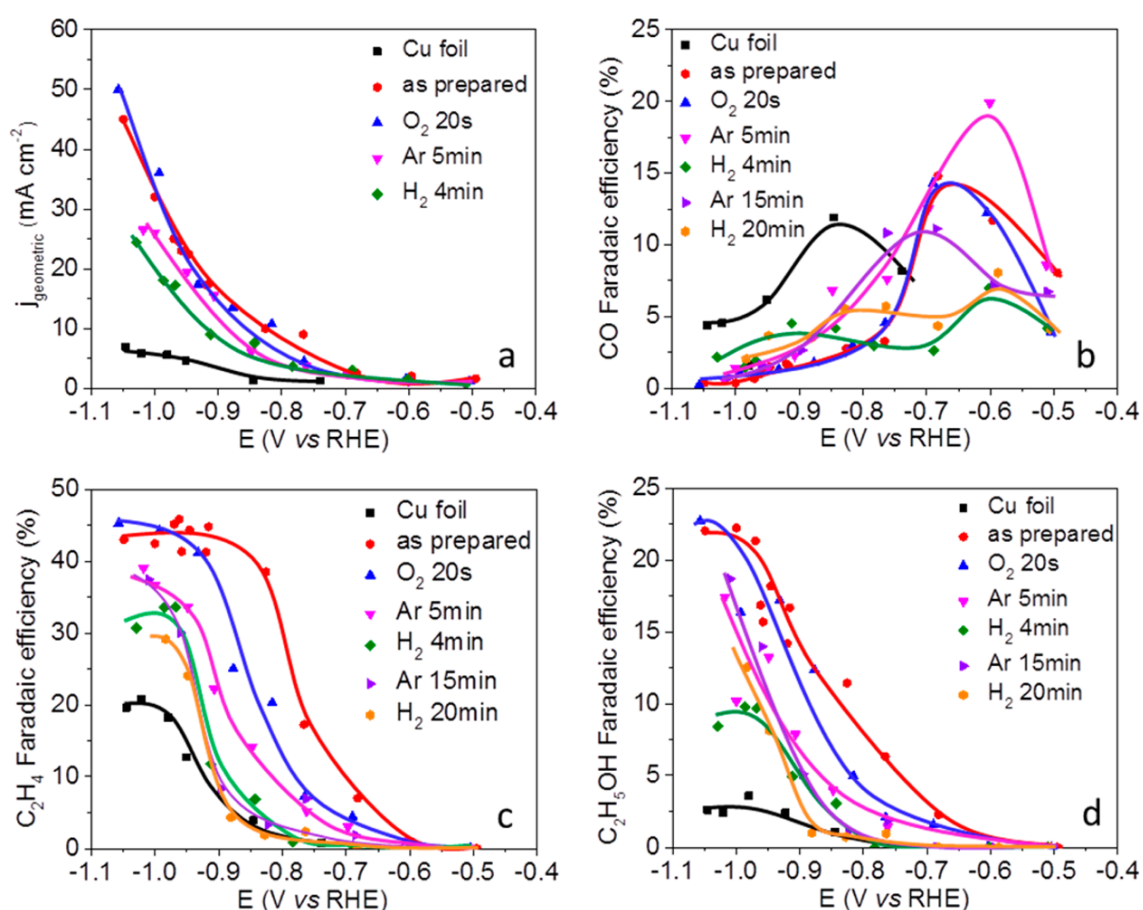
Figure 9.2: Potential-dependent geometric current density (a) and Faradaic efficiencies of (b) CO, (c) C_2H_4, and (d) C_2H_5OH after 1 h of electrochemical reaction in a CO_2-saturated 0.1 M $KHCO_3$ solution. Solid lines are guides for the eye. Data acquired by Dr. Dunfeng Gao.

Another way to demonstrate this is by plotting the current density normalized by the corresponding electrochemical roughness factor [...].[343,344] The O_2 plasma treated sample exhibits the highest normalized current density at -1.0 V vs RHE. Additional parameters need to be considered in order to interpret the observed differences in current density. As was previously shown via EDX and XPS, the enhanced intrinsic activity of the O_2 plasma treated sample is a result of its much higher surface area and subsurface oxygen content available during the reaction. Our study demonstrates that the role of oxygen species is even more important than that of specific crystalline facets for the catalytic activity. Despite having less well-defined Cu{1 0 0} facet geometry after 1 h of reaction, the 20 s O_2 plasma treated sample displays higher current density than the 5 min Ar plasma treated and nonplasma treated Cu samples.

Figure 9.2b-d [...] shows the Faradaic efficiencies (FE(%)) of various CO_2 reduction products as a function of applied potential. [...] All Cu nanocube samples show significantly different selectivity from an electropolished foil. Ethylene formation is facilitated (up to $\sim$45% at -1.0 V vs RHE in Figure 9.2c), while methane formation is drastically suppressed [...]. This variation can be attributed to the different active sites on Cu nanocube samples and the electropolished foil and the different pathways for ethylene and methane formation.[17] Remarkably, high ethanol ($\sim$22%) and propanol ($\sim$9%) FE, up to 10 times higher than on the electropolished foil, were also obtained for the O_2 plasma treated sample. These products are valuable liquid fuels with high-energy density, particularly useful for industrial applications. The total FE of $\sim$73% achieved at -1.0 V vs RHE for C_2 and C_3 products on as-prepared and O_2 plasma treated Cu nanocube samples ([...]) is significantly higher than those of previously reported Cu-based catalysts.[94,134,219,254,345] Furthermore, Cu nanocube samples exhibit lower onset potential (i.e., the potential required for achieving a production rate of 10% of the highest value at -1.0 V vs RHE) for ethylene, ethanol, and n-propanol formation compared to the electropolished foil [...]. Trace amounts (<1%) of ethane and acetate were also produced [...].

The important role of the oxygen content in achieving high ethylene/alcohol selectivity is demonstrated by comparing samples with similar cubic facet morphology but different oxygen content (Figure 9.3). The O_2 plasma treated sample shows higher FE for ethylene, ethanol, and propanol than the H_2 plasma treated sample, while having similar morphology. Compared with the 4 min H_2 plasma, a shorter (20 s) O_2 plasma treatment increases the O_2- content of the cubes and their stability during the reaction, while resulting in decreased roughness and similar facet morphology. Given that high roughness is considered to be favorable for ethylene formation,[74] the higher selectivity of the O_2 plasma treated sample despite its reduced roughness indicates that oxygen content affects ethylene formation more than roughness. The O_2 plasma treated sample also shows higher ethylene FE than the Ar plasma treated sample, although their roughness is similar. Given that the Cu{1 0 0} facets are generally considered as the active site for ethylene formation,[245,346] the superior ethylene FE of the O_2 plasma treated sample, despite its worse facet morphology compared to the Ar plasma treated sample, indicates that the oxygen content plays a more important role in ethylene formation than Cu{1 0 0} facets.

The results shown in Figure 9.3 indicate a clear correlation between the oxygen content of the nanocubes and the catalytic activity and ethylene selectivity. At the same time, the beneficial

effect of facet morphology also becomes evident as an upward shift of the current density and ethylene FE in the samples which maintain relatively good facet morphology after the reaction (i.e., the nonplasma treated and Ar plasma treated samples), as well as in comparison with the flat electropolished Cu foil. When comparing samples with the same oxygen content (e.g., 4 min H_2- and 5 min Ar treated samples), the sample with better maintained facet morphology, namely 5 min Ar treated Cu nanocube, shows higher ethylene selectivity. Similar observations are also made with respect to ethanol and n-propanol. Both the presence of cubic structure and the high oxygen content remaining on the nanocube sample after the O_2 plasma pretreatment are necessary to reach the high catalytic performance presented in Figure 9.2. The similarities among all C_2 and C_3 products with respect to the variation of onset potentials and FE with plasma conditions (i.e., the fact that their dependence on oxygen content and facet morphology is the same) indicate that the reaction pathways are similar for those products.

Summarizing, our experimental work evidences that the O_2 plasma oxidation of our samples gives rise to special defect sites and the stabilization of subsurface oxygen species inside the cubes which is beneficial to their catalytic performance. Although there is to date no *ab initio* theoretical support that can be directly correlated to our study, several plausible explanations based on past experimental and theoretical studies might be considered.[17,74,92,113,222,245,247,251,253,255,339,341,346][22,248,347–351] For instance, the surface and subsurface oxygen species generated and stabilized by our plasma pretreatment might act as oxygen reservoirs able to modify the electronic properties of the surface, and correspondingly the binding of CO and/or known reaction intermediates such as COOH*, upon surface diffusion.[253,348]
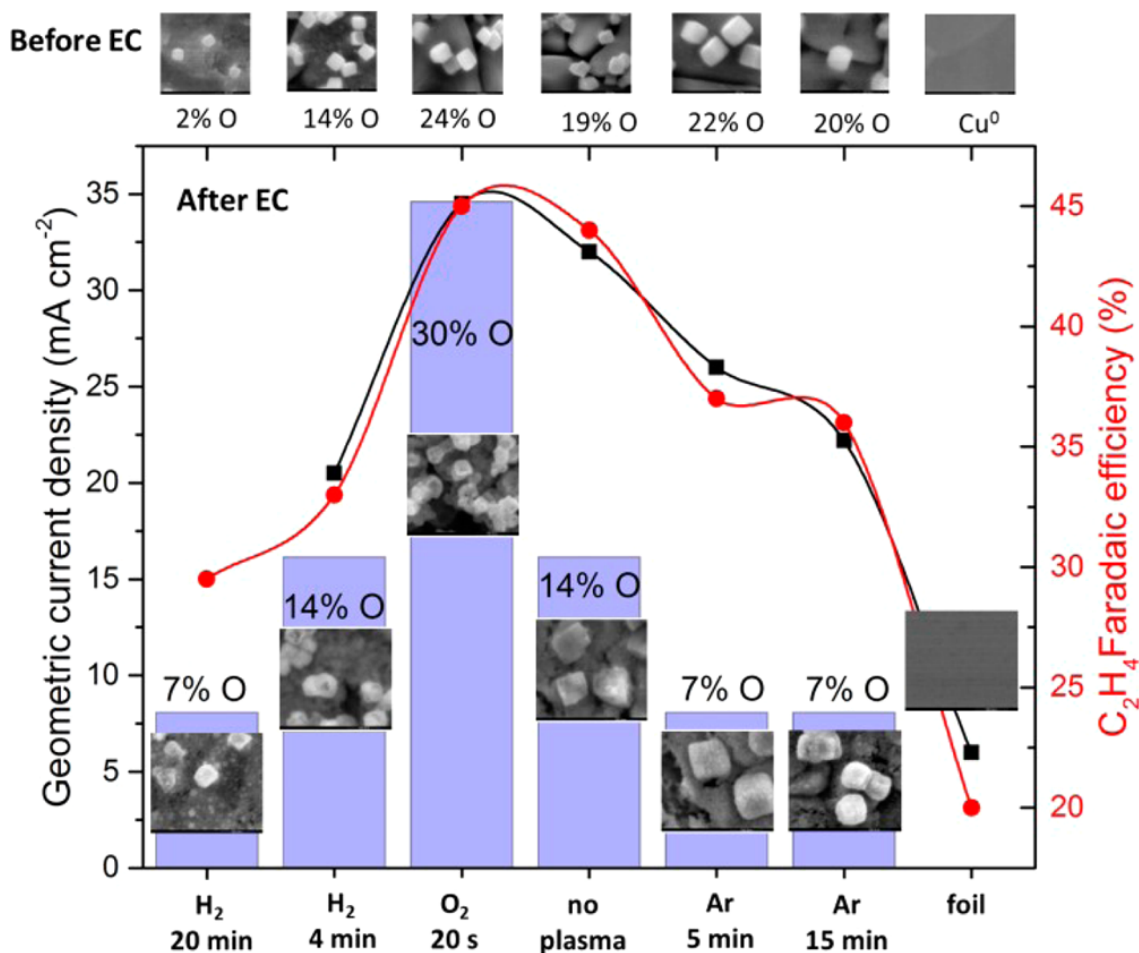
Figure 9.3: Geometrical current density (left axis) and Faradaic efficiency for C_2H_4 (right axis) after 1 h of electrochemical reaction at $-1.0\,\text{V}$ vs RHE in CO_2-saturated 0.1 M $KHCO_3$ for different plasma treatments as well as for a reference electropolished Cu foil. The oxygen content of the nanocubes after the reaction (from EDX) is indicated with column bars (blue). The oxygen content of the cubes before the reaction, as well as typical SEM images (lateral image size: 1.7 μm) before (top row) and after the reaction (images inside the blue columns), are shown as insets. The cubes contain $\sim$24 at% Cl before the reaction, which is depleted during the reaction [...]. Data acquired by Dr. Dunfeng Gao and Dr. Ioannis Zegkinoglu.

Alternatively, the presence of CuOx species or subsurface oxygen species might lead to lattice strain in the more oxygen-poor Cu nanocube surface layer.[248,349] Furthermore, our plasma pretreatments might lead to the generation of special defects, where a local enhancement of the electric field might take place.[247,248,350,351] Additional future experimental and theoretical work will be needed in order to fully understand the relative importance of the former parameters.

9.1.4 Conclusions

We have prepared Cu nanocube catalysts with tunable Cu{1 0 0} facet morphology, defect content, and oxygen content through an electrochemical synthesis in KCl combined with lowpressure plasma treatments. These catalysts exhibit drastically higher activity and ethylene/alcohol selectivity (with the highest FE of $\sim$45% for ethylene, $\sim$22% for ethanol, and in total $\sim$73% for

all C2 and C3 products) as well as lower onset potentials compared to the electropolished Cu foil. Their catalytic properties can be tuned by plasma-induced variation of their morphology and defect density, ion content, and surface roughness. By analyzing the correlation between the catalytic performance and the surface morphology and composition of differently treated catalysts, we were able to demonstrate that the presence of defects, surface and subsurface oxygen species, including oxygen ions associated with Cu^+ species, is a key parameter for achieving high activity and ethylene selectivity, even more important than the presence of $Cu\{1\,0\,0\}$ facets."[131]

9.2 Plasma-Induced Surface Functionalization and Regeneration under *Operando* Conditions

In the following section, a potential way to utilize and replenish the beneficial effects of plasma treatment are discussed. This work is conceptualized around the possibility to do surface modifications in *operando*, to retain surface oxides, and remove poisoning on the catalyst surface. Moreover, there is potential for the activation of reactant species that will lead to new or energetically more favorable product pathways.

This project is still in its early stage, thus a proof that the plasma in liquid does have an effect on the catalysis needs to be established. For this purpose, we have investigated HER, a less complex reaction with two electron transfers and two reaction steps. The catalyst performance is measured electrochemically by cyclic voltammetry and linear sweep voltammetry, with reaction onset and peak size as performance indicators. We have built a one compartment, five electrode electrochemical cell for the purpose of these experiments. Thee electrodes are used for the catalysis: working electrode, counter electrode (both Pt), and reference electrode plus additional two electrodes that are connected to a DC power supply (max. 250 V, 5 A) for the plasma generation.

9.2.1 DC Plasma in Liquid Generation

For the generation of a plasma "in liquid", we have decided to use contact glow discharge electrolysis (CGDE). We decided on this method, to have the most versatile setup for testing in terms of shape, position, and size of our plasma electrodes. Here, we immerse two metal electrodes of different size into our conductive medium (aqueous electrolyte). On the smaller electrode, which is a Pt wire, a gas sleeve forms around the tip of the electrode. If the current is high enough, a plasma ignites in the gas sleeve, which is directly in contact with the electrolyte. A schematic for the application of DC plasma in CO_2RR is shown in figure 9.4.

Figure 9.4: **DC Plasma generation in aqueous electrolyte.** (a) The DC-plasma electrode is covered by a glass pipette, except for the protruding Pt tip. CO_2 gas is flown through the pipette directly into the plasma. A Pt-mesh is used as a counter electrode. (b) Photo of the plasma electrode in operation.

This is technically not a plasma in liquid since it ignites inside a gas environment that is submerged in the electrolyte, but it makes a good model system for testing purposes. For the later stages of the project, we have a micro/nanosecond pulsed system developed and tested by K. Grosse et al.[352], which is able to produce plasma directly in liquid by direct discharge between two electrodes and we can implement these pulsed plasma in liquid into our electrochemical setup.

There are two major challenges for the combination of CDGE and electrochemistry. First, most of the input energy used in the generation of the plasma is consumed by Joule heating due to the resistivity of the electrolyte. To avoid this effect, we kept the plasma times small and used a large electrolyte volume to absorb the heat. Furthermore, we have measured the temperature of the liquid phase close to the electrochemistry electrodes to make sure that the observed changes are not caused by the temperature increase. The second challenge is the strong electric field emitting from the plasma. During plasma operation, the noise level is high and potential shifts are observed. For these preliminary tests, we disconnect the electrochemistry electrodes during plasma and measured the electrochemical behavior immediately after.

9.2.2 Results

Our initial test to find an effect coming from the plasma in liquid is to apply 5-10 s of plasma and measure CVs directly after the treatment. Both, after 5 s and 10 s of treatment, an additional

reductive (double-) peak can be found at $0.1\,V_{RHE}$. However, this peak disappears after the first CV. The results of 5 s and 10 s plasma treatment of a Pt wire in $0.1\,M\,HClO_4$ are shown in figure 9.5(a). At this point, it is unclear if the peak corresponds to two individual peaks or a single peak that shifts closer to the HER onset with increasing plasma and/or polarization times.
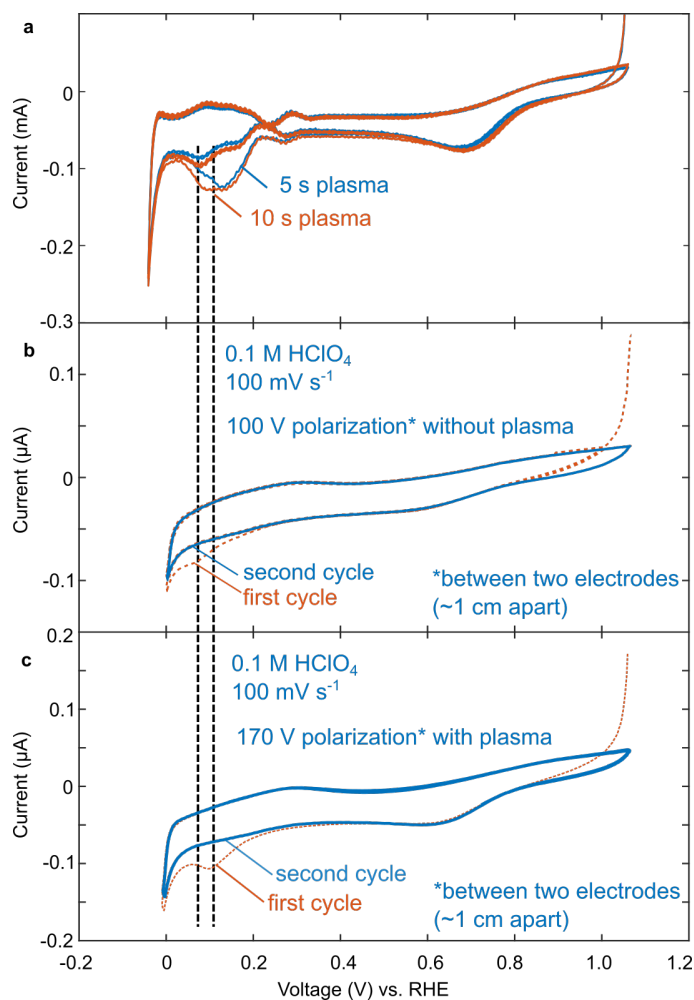
Figure 9.5: **Plasma treatment time dependent changes in HER activity.** The CVs have been measured in $0.1\,M\,HClO_4$ at a sweep rate of $100\,mV\,s^{-1}$ (a) shows the difference between 5 s and 10 s plasma treatment. The first cycle after plasma treatment shows a peak around 0.1 V vs. RHE (b) shows the effects of general polarization at 100 V applied to the plasma electrodes (just before the plasma ignites). (c) shows the effect of a higher potential (170 V) applied to the plasma electrodes and a subsequent ignition of the plasma before the CVs.

Figure 9.5(b-c) shows comparative experiments to distinguish the plasma effect from a pure polarization effect. In Figure 9.5(b), the polarization is done at a voltage of 100 V between the plasma electrodes, just before the plasma ignites. We observed a shoulder in the first CV cycle. In Figure 9.5(c), the polarization voltage is increased to 170 V, so that the plasma can ignite. Again, here we see a peak forming in the initial CV cycle that is increase but shifted to lower overpotentials.
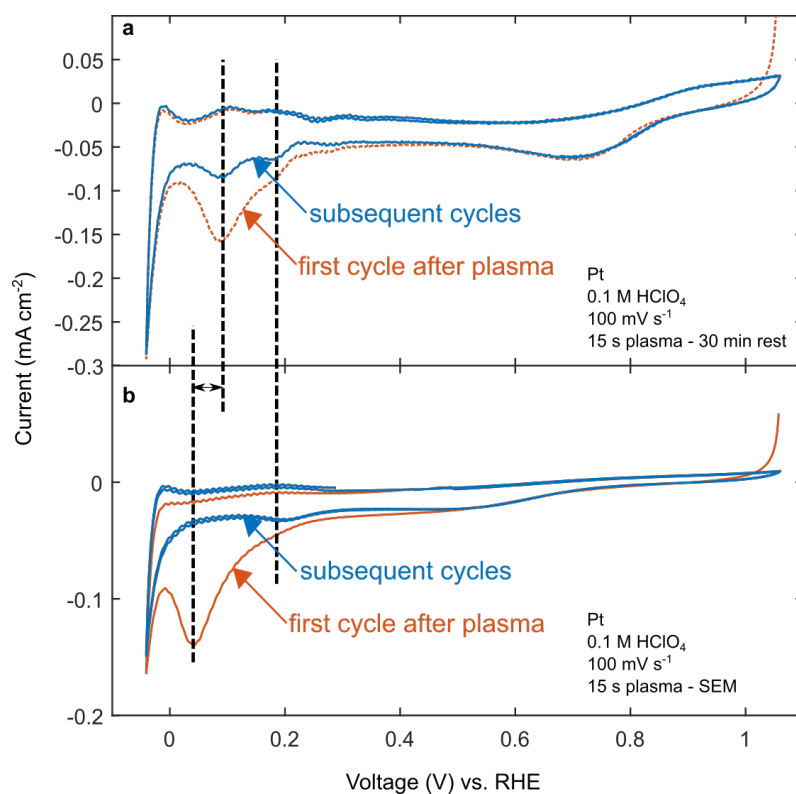
Figure 9.6: **Resting time after plasma dependent changes in HER activity.** (a) CVs after 15 s of plasma and subsequent 30 min resting period. (b) shows the same experiment, but instead of resting, the sample was subsequently measured by SEM under vacuum conditions.

Figure 9.6(a) shows cyclic voltammetry after 15 s of plasma and a subsequent waiting period. In Figure 9.6(a), the treated Pt wire was left in solution for 30 min and CVs were recorded after that. In the initial cycle, the peak is observable and well separated from the HER onset. Figure 9.6 shows a similar experiment, but here the wire was taken out and measured in an SEM (under vacuum conditions).

Lastly, I investigated the peak behavior in dependence of the pH. Fort this purpose, we measured CVs of a Pt wire after plasma in 0.1 M KOH (pH 13.5, Figure 9.7(a)) and 0.1 M HClO$_4$ (pH 1, Figure 9.7(b)). In these two cases, the interfacial double layer consists of H$^+$ in acidic and OH$^-$ in alkaline conditions. The charge transfer is influenced by the ionic species solvation in water in both cases, and kinetically coupled to the charge migration in this interface ensemble.
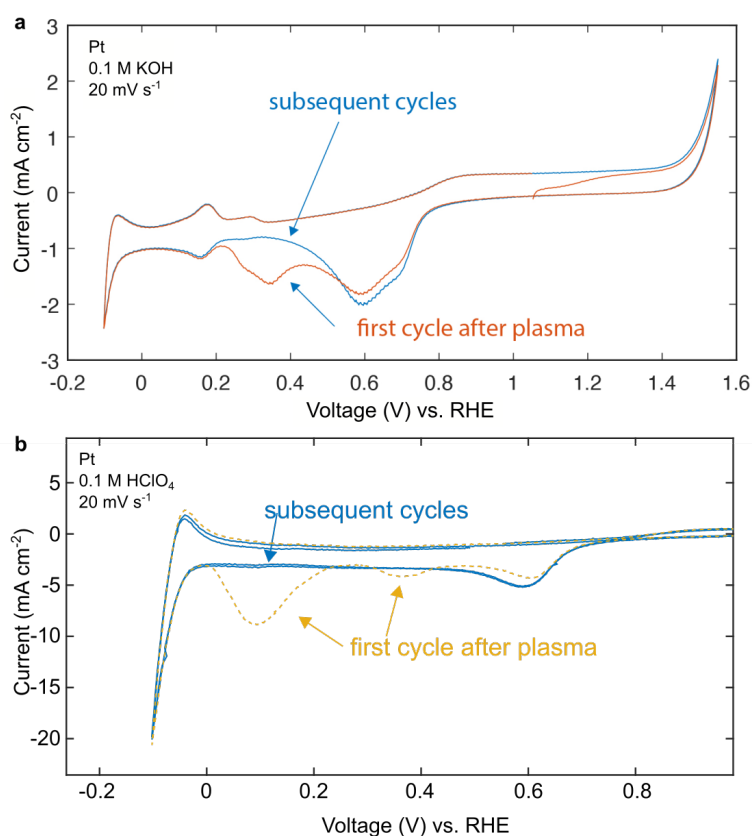
Figure 9.7: **pH dependent changes in HER activity.** Cyclic voltammetry after plasma in (a) 0.1 M KOH and (b) 0.1 M HClO$_4$.

9.2.3 Discussion

Changing peak intensities in the Pt voltammograms have been observed previously.[353] In particular, the effect of hydrogen exposure and flame annealing has been studied for Pt electrodes. For example, it has been found that certain treatments lead to the evolution of a third, "enigmatic" hydrogen peak in the Pt voltammogram. The origin of this peak is strongly debated in the literature, including speculation about subsurface hydrogen, but Koper and coworkers were able to convincingly ascribe it to the emergence to the evolution of the $(1\,0\,0)$-$(2\,x\,1)$ reconstructions on the Pt surface with the help of FTIR.[354] However, compared to these studies, here we observe the peak only in the cathodic scan direction. It is never enhanced in the anodic scan direction. Also, the preliminary results indicate that vacuum exposure leads to a shift in the peak position. Therefore, more experiments are needed to better understand the cause of the increasing peak intensities in these potential ranges. In particular, we need to understand the effect of the polarization itself, even without plasma treatment, and the effect of the plasma on surface cleaning. It is well known that the purity of the electrolyte and electrodes have a strong effect on the cyclic voltammogram curves of Pt. In the future, I will expand on these preliminary results, but also study the effect of the plasma on the reaction kinetics for reactions involving gases as reactants.

10 Summary and Future Outlook

In this work, my focus was mainly the development of electrochemical Cu_2O cube synthesis and the analysis of the dynamic morphology of Cu catalysts for CO_2RR. To this end, a variety of *in situ* microscopy techniques were used and comparative studies to *ex situ* product analysis were conducted. Additionally, X-ray spectroscopy was utilized to elucidate changes in the chemical state of the surface and bulk materials of the investigated catalysts, both *operando* and quasi *in situ*. We gained a comprehensive insight of the dynamic behavior of Cu cubes under CO_2RR conditions in real time and could correlate the observations to changes in the catalytic performance, in particular, the reaction selectivity.

As a consequence of the experiments conducted so far, many opportunities for further exploration and exciting research presented themselves.

1. In the present work, we have focused mainly on cubic shaped particles to utilize their $\{1\,0\,0\}$ facets for CO_2RR. We have observed a highly dynamic morphological behavior. Even though we started out from $\{1\,0\,0\}$ facets, the catalyst structure under *operando* conditions is substantially different. This opens up the question of whether other crystalline orientations might express a similar behavior, which would challenge the current shape-dependent product selectivity reported in many publications. It is plausible that the underlying effect in the formation and density of redeposited nanoparticles. Thus, a modification of the presented synthesis approach form chapter 4 to produce different shapes like octahedral ($\{1\,1\,1\}$) or rhombic dodecahedral ($\{1\,1\,0\}$) would enable interesting experiments. This can help understand and separate the effects of mass transport and shape-dependency for CO_2RR.

2. One should further work towards the transition of *in situ* electron microscopy to real *operando* experiments, i.e. those for which activity and product selectivity can be measured online. The realization for CO_2RR is tricky, but a combination of spectroscopic and mass spectrometry-based techniques is being tested to enable the measurement of catalytic properties whilst observing morphological changes in a catalyst. The characteristic fluorescence originating from the interaction of the electron beam and the specimen could be used to find surface species. Additionally, the chemical state of the catalyst (bulk) material could be probed by electron energy loss spectroscopy (EELS) to confirm the oxidation state. For CO_2RR, the best way to determine catalytic performance would be product analysis. However, the amounts produced inside a liquid phase EM holder are far too small, thus GC is not suited. Furthermore, the temporal resolution has to be high. I observed rapid morphological changes in the nanosized samples that are in the timescale of second and minutes. Thus, a high temporal resolution, high sensitivity technique that is compatible with our system is required. The solution that comes to mind would be mass spectrometry, similar to applications like in

DEMS.[26,355] The realization, however, will still need more time until the integration is fully realized.

3. From the results shown in chapter 6 and chapter 7 it became evident, that the support material plays a crucial role in the morphological stability of a catalyst. The synthesis approach from chapter 4 allows the electrodeposition of cubic Cu_2O particles on a broad variety of conductive support materials. This opens large amount of experiments, however, as discussed in chapter 8, the interpretation is not trivial and a comparative study on the same piece of support material is crucial. Here the investigation of the samples by DEMS, *in situ* Raman, or *in situ* infrared spectroscopy (IR) can provide key information on the possible support-dependent distinct stability of reaction intermediates observed in the study.

4. Lastly, we have seen in chapter 9 that the treatment of Cu foils by low pressure oxygen plasma can be highly beneficial for the CO_2RR performance. Based on the works of Katharina Grosse et al.[352,356,357] we have developed a cooperation to plasma treat samples in liquids under reaction conditions. Preliminary tests have already shown structural changes and growth of oxides on the surface. This project can yield a completely new way of functionalizing the surface *in situ* and under *operando* conditions as well as to modify the solubility in the electrolyte of reactants like CO_2.

11 Curriculum Vitae

Personal Data

Name:	Philipp Grosse
Date of birth:	23.09.1990
Place of birth:	Witten

University Education

01.03.2017 - today	Doctoral studies
10/2014 - 11/2016	M.Sc. Chemistry at Ruhr-University Bochum
10/2011 - 08/2014	B.Sc. Chemistry at Ruhr-University Bochum

School Education

25.06.2010	Abitur
08/2001 - 06/2010	Geschwister-Scholl-Gymnasium, Wetter
08/1997 - 07/2001	Osterfeldschule, Wetter-Wengern

February 25, 2021

12 Bibliography

Bibliography

1. Tokarska, K. B., Gillett, N. P., Weaver, A. J., Arora, V. K. & Eby, M. The climate response to five trillion tonnes of carbon. *Nature climate change* **6,** 851–855 (2016).

2. Shafiee, S. & Topal, E. When will fossil fuel reserves be diminished? *Energy policy* **37,** 181–189 (2009).

3. Peter, T. *A thousands barrel a second: The coming oil breakpoint and the challenges facing an energy development world* 2007.

4. Sabatier, P. How I Have Been Led to the Direct Hydrogenation Method by Metallic Catalysts1. *Industrial & Engineering Chemistry* **18,** 1005–1008 (1926).

5. Sabatier, P. & Senderens, J. Comptes Rendus Des Séances De L'Académie Des Sciences, Section VI–Chimie. *Paris: Imprimerie Gauthier-Villars* (1902).

6. Fischer, F. & Tropsch, H. Über die direkte Synthese von Erdöl-Kohlenwasserstoffen bei gewöhnlichem Druck.(Erste Mitteilung). *Berichte der deutschen chemischen Gesellschaft (A and B Series)* **59,** 830–831 (1926).

7. Wang, Y. *et al.* Direct conversion of CO_2 to aromatics with high yield via a modified Fischer-Tropsch synthesis pathway. *Applied Catalysis B: Environmental* **269,** 118792 (2020).

8. Kirsch, H., Lochmahr, N., Staudt, C., Pfeifer, P. & Dittmeyer, R. Production of CO_2-neutral liquid fuels by integrating Fischer-Tropsch synthesis and hydrocracking in a single microstructured reactor: Performance evaluation of different configurations by factorial design experiments. *Chemical Engineering Journal,* 124553 (2020).

9. Medvedev, V. A., Cox, J. & Wagman, D. D. *CODATA key values for thermodynamics* (Hemisphere Publishing Corporation New York, 1989).

10. Binnewies, M. & Milke, E. *Thermochemical data of elements and compounds* (Wiley-VCH, 1999).

11. Hori, Y., Kikuchi, K. & Suzuki, S. Production of CO and CH_4 in electrochemical reduction of CO2 at metal electrodes in aqueous hydrogencarbonate solution. *Chemistry Letters,* 1695–1698 (1985).

12. Handoko, A. D., Wei, F., Yeo, B. S., Seh, Z. W., *et al.* Understanding heterogeneous electrocatalytic carbon dioxide reduction through operando techniques. *Nature Catalysis* **1,** 922–934 (2018).

13. Birdja, Y. Y. *et al.* Advances and challenges in understanding the electrocatalytic conversion of carbon dioxide to fuels. *Nature Energy* **4,** 732–745 (2019).

14. Nitopi, S. *et al.* Progress and perspectives of electrochemical CO_2 reduction on copper in aqueous electrolyte. *Chemical reviews* **119,** 7610–7672 (2019).

15. Peterson, A. A., Abild-Pedersen, F., Studt, F., Rossmeisl, J. & Nørskov, J. K. How copper catalyzes the electroreduction of carbon dioxide into hydrocarbon fuels. *Energy & Environmental Science* **3,** 1311–1315 (2010).

16. Hori, Y., Murata, A. & Takahashi, R. Formation of hydrocarbons in the electrochemical reduction of carbon dioxide at a copper electrode in aqueous solution. *Journal of the Chemical Society, Faraday Transactions 1: Physical Chemistry in Condensed Phases* **85,** 2309–2326 (1989).

17. Kortlever, R., Shen, J., Schouten, K. J. P., Calle-Vallejo, F. & Koper, M. T. Catalysts and reaction pathways for the electrochemical reduction of carbon dioxide. *The journal of physical chemistry letters* **6,** 4073–4082 (2015).

18. Christophe, J., Doneux, T. & Buess-Herman, C. Electroreduction of carbon dioxide on copper-based electrodes: activity of copper single crystals and copper–gold alloys. *Electrocatalysis* **3,** 139–146 (2012).

19. Hori, Y., Wakebe, H., Tsukamoto, T. & Koga, O. Adsorption of CO accompanied with simultaneous charge transfer on copper single crystal electrodes related with electrochemical reduction of CO_2 to hydrocarbons. *Surface science* **335,** 258–263 (1995).

20. Hori, Y., Takahashi, I., Koga, O. & Hoshi, N. Electrochemical reduction of carbon dioxide at various series of copper single crystal electrodes. *Journal of Molecular Catalysis A: Chemical* **199,** 39–47 (2003).

21. Hori, Y., Takahashi, I., Koga, O. & Hoshi, N. Selective formation of C2 compounds from electrochemical reduction of CO_2 at a series of copper single crystal electrodes. *The Journal of Physical Chemistry B* **106,** 15–17 (2002).

22. Huang, Y., Handoko, A. D., Hirunsit, P. & Yeo, B. S. Electrochemical reduction of CO_2 using copper single-crystal surfaces: effects of CO* coverage on the selective formation of ethylene. *ACS catalysis* **7,** 1749–1756 (2017).

23. Takahashi, I., Koga, O., Hoshi, N. & Hori, Y. Electrochemical reduction of CO_2 at copper single crystal Cu (S)-[n (111)×(111)] and Cu (S)-[n (110)×(100)] electrodes. *Journal of Electroanalytical Chemistry* **533,** 135–143 (2002).

24. Yoshihara, N., Arita, M. & Noda, M. Electrochemical Reduction of Carbon Dioxide on Single-Crystal Copper Membrane. *ECS Transactions* **66,** 83 (2015).

25. Hahn, C. *et al.* Engineering Cu surfaces for the electrocatalytic conversion of CO_2: Controlling selectivity toward oxygenates and hydrocarbons. *Proceedings of the National Academy of Sciences* **114,** 5918–5923 (2017).

26. Javier, A. *et al.* A DEMS study of the reduction of CO_2, CO, and HCHO pre-adsorbed on Cu electrodes: empirical inferences on the CO_2 RR mechanism. *Electrocatalysis* **6,** 127–131 (2015).

27. Kim, Y.-G. *et al.* Surface reconstruction of pure-Cu single-crystal electrodes under CO-reduction potentials in alkaline solutions: A study by seriatim ECSTM-DEMS. *Journal of Electroanalytical Chemistry* **780,** 290–295 (2016).

28. Hori, Y. i. in *Modern aspects of electrochemistry* 89–189 (Springer, 2008).

29. Frese, J. *Electrochemical reduction of CO$_2$ at solid electrodes* (Elsevier: Amsterdam, 1993).

30. Kuhl, K. P., Cave, E. R., Abram, D. N. & Jaramillo, T. F. New insights into the electrochemical reduction of carbon dioxide on metallic copper surfaces. *Energy & Environmental Science* **5,** 7050–7059 (2012).

31. Singh, M. R., Clark, E. L. & Bell, A. T. Effects of electrolyte, catalyst, and membrane composition and operating conditions on the performance of solar-driven electrochemical reduction of carbon dioxide. *Physical Chemistry Chemical Physics* **17,** 18924–18936 (2015).

32. Masliuk, L. *et al.* Structural complexity in heterogeneous catalysis: cataloging local nanostructures. *The Journal of Physical Chemistry C* **121,** 24093–24103 (2017).

33. Taylor, H. S. A theory of the catalytic surface. *Proceedings of the Royal Society of London. Series A, Containing Papers of a Mathematical and Physical Character* **108,** 105–111 (1925).

34. Schouten, K. J. P., Qin, Z., Pérez Gallent, E. & Koper, M. T. Two pathways for the formation of ethylene in CO reduction on single-crystal copper electrodes. *Journal of the American Chemical Society* **134,** 9864–9867 (2012).

35. Schouten, K. J. P., Pérez Gallent, E. & Koper, M. T. Structure sensitivity of the electrochemical reduction of carbon monoxide on copper single crystals. *ACS Catalysis* **3,** 1292–1295 (2013).

36. Arán-Ais, R. M., Scholten, F., Kunze, S., Rizo, R. & Cuenya, B. R. The role of in situ generated morphological motifs and Cu (i) species in C 2+ product selectivity during CO$_2$ pulsed electroreduction. *Nature Energy* **5,** 317–325 (2020).

37. Simon, G. H., Kley, C. S. & Roldan Cuenya, B. Potential-dependent Morphology of Copper Catalysts During CO$_2$ Electroreduction Revealed by In Situ Atomic Force Microscopy. *Angewandte Chemie International Edition* (2020).

38. Jiang, K. *et al.* Metal ion cycling of Cu foil for selective C–C coupling in electrochemical CO$_2$ reduction. *Nature Catalysis* **1,** 111–119 (2018).

39. Schouten, K. J. P., Gallent, E. P. & Koper, M. T. The electrochemical characterization of copper single-crystal electrodes in alkaline media. *Journal of Electroanalytical Chemistry* **699,** 6–9 (2013).

40. Kim, Y.-G. & Soriaga, M. P. Cathodic regeneration of a clean and ordered Cu (1 0 0)-(1× 1) surface from an air-oxidized and disordered electrode: An operando STM study. *Journal of Electroanalytical Chemistry* **734,** 7–9 (2014).

41. Droog, J. M. & Schlenter, B. Oxygen electrosorption on copper single crystal electrodes in sodium hydroxide solution. *Journal of Electroanalytical Chemistry* **112,** 387–390 (1980).

42. Jović, V. & Jović, B. Surface reconstruction during the adsorption/desorption of OH species onto Cu (111) and Cu (100) in O. 1 M NaOH solution. *Journal of the Serbian Chemical Society* **67,** 531–546 (2002).

43. Jović, V. & Jović, B. EIS and differential capacitance measurements onto single crystal faces in different solutions: Part I: Ag (111) in 0.01 M NaCl. *Journal of Electroanalytical Chemistry* **541,** 1–11 (2003).

44. Matsuoka, O., Ono, S. S., Nozoye, H. & Yamamoto, S. Structure and dynamics of oxy-overlayer on Cu (1 1 1) electrode surfaces in alkaline aqueous solution revealed by electrochemical STM and quartz crystal microbalance measurement. *Surface science* **545,** 8–18 (2003).

45. Climent, V. & Feliu, J. M. Thirty years of platinum single crystal electrochemistry. *Journal of Solid State Electrochemistry* **15,** 1297 (2011).

46. Gomez-Marin, A. M. & Feliu, J. M. Pt (1 1 1) surface disorder kinetics in perchloric acid solutions and the influence of specific anion adsorption. *Electrochimica acta* **82,** 558–569 (2012).

47. Kim, Y.-G., Javier, A., Baricuatro, J. H. & Soriaga, M. P. Regulating the product distribution of CO reduction by the atomic-level structural modification of the Cu electrode surface. *Electrocatalysis* **7,** 391–399 (2016).

48. Schlaup, C. & Horch, S. In-situ STM study of phosphate adsorption on Cu (111), Au (111) and Cu/Au (111) electrodes. *Surface science* **608,** 44–54 (2013).

49. Kim, Y.-G., Baricuatro, J. H., Javier, A., Gregoire, J. M. & Soriaga, M. P. The evolution of the polycrystalline copper surface, first to Cu (111) and then to Cu (100), at a fixed CO_2RR potential: A study by operando EC-STM. *Langmuir* **30,** 15053–15056 (2014).

50. Scott, S. B. *et al.* Absence of oxidized phases in Cu under CO reduction conditions. *ACS Energy Letters* **4,** 803–804 (2019).

51. DeWulf, D. W., Jin, T. & Bard, A. J. Electrochemical and surface studies of carbon dioxide reduction to methane and ethylene at copper electrodes in aqueous solutions. *Journal of the Electrochemical Society* **136,** 1686 (1989).

52. Hori, Y., Takahashi, R., Yoshinami, Y. & Murata, A. Electrochemical reduction of CO at a copper electrode. *The Journal of Physical Chemistry B* **101,** 7075–7081 (1997).

53. Hori, Y., Murata, A., Takahashi, R. & Suzuki, S. Electroreduction of carbon monoxide to methane and ethylene at a copper electrode in aqueous solutions at ambient temperature and pressure. *Journal of the American Chemical Society* **109,** 5022–5023 (1987).

54. Kim, J., Summers, D. & Frese Jr, K. Reduction of CO_2 and CO to methane on Cu foil electrodes. *Journal of electroanalytical chemistry and interfacial electrochemistry* **245,** 223–244 (1988).

55. Bertheussen, E. *et al.* Electroreduction of CO on polycrystalline copper at low overpotentials. *ACS Energy Letters* **3,** 634–640 (2018).

56. Wang, L. *et al.* Electrochemical carbon monoxide reduction on polycrystalline copper: Effects of potential, pressure, and pH on selectivity toward multicarbon and oxygenated products. *ACS Catalysis* **8,** 7445–7454 (2018).

57. Ross, M. B. *et al.* Tunable Cu enrichment enables designer syngas electrosynthesis from CO_2. *Journal of the American Chemical Society* **139,** 9359–9363 (2017).

58. Gunathunge, C. M. *et al.* Spectroscopic observation of reversible surface reconstruction of copper electrodes under CO_2 reduction. *The Journal of Physical Chemistry C* **121,** 12337–12344 (2017).

59. Chernyshova, I. V., Somasundaran, P. & Ponnurangam, S. On the origin of the elusive first intermediate of CO_2 electroreduction. *Proceedings of the National Academy of Sciences* **115,** E9261–E9270 (2018).

60. Hori, Y. *et al.* Adsoprtion of carbon monoxide at a copper electrode accompanied by electron transfer observed by voltammetry and IR spectroscopy. *Electrochimica Acta* **39,** 2495–2500 (1994).

61. Hori, Y., Koga, O., Yamazaki, H. & Matsuo, T. Infrared spectroscopy of adsorbed CO and intermediate species in electrochemical reduction of CO_2 to hydrocarbons on a Cu electrode. *Electrochimica acta* **40,** 2617–2622 (1995).

62. Wuttig, A. *et al.* Tracking a common surface-bound intermediate during CO_2-to-fuels catalysis. *ACS central science* **2,** 522–528 (2016).

63. Gunathunge, C. M., Ovalle, V. J., Li, Y., Janik, M. J. & Waegele, M. M. Existence of an electrochemically inert CO population on Cu electrodes in alkaline pH. *ACS Catalysis* **8,** 7507–7516 (2018).

64. Sabatier, P. Hydrogénations et déshydrogénations par catalyse. *Berichte der deutschen chemischen Gesellschaft* **44,** 1984–2001 (1911).

65. Kuhl, K. P. *et al.* Electrocatalytic conversion of carbon dioxide to methane and methanol on transition metal surfaces. *Journal of the American Chemical Society* **136,** 14107–14113 (2014).

66. Hori, Y., Murata, A. & Yoshinami, Y. Adsorption of CO, intermediately formed in electrochemical reduction of CO_2, at a copper electrode. *Journal of the Chemical Society, Faraday Transactions* **87,** 125–128 (1991).

67. Ooka, H., Figueiredo, M. C. & Koper, M. T. Competition between hydrogen evolution and carbon dioxide reduction on copper electrodes in mildly acidic media. *Langmuir* **33,** 9307–9313 (2017).

68. Cook, R. L., MacDuff, R. C. & Sammells, A. F. Evidence for formaldehyde, formic acid, and acetaldehyde as possible intermediates during electrochemical carbon dioxide reduction at copper. *Journal of the Electrochemical Society* **136,** 1982 (1989).

69. Kyriacou, G. & Anagnostopoulos, A. Electroreduction of CO_2 on differently prepared copper electrodes: The influence of electrode treatment on the current efficiencies. *Journal of Electroanalytical Chemistry* **322,** 233–246 (1992).

70. Schouten, K., Kwon, Y., Van der Ham, C., Qin, Z. & Koper, M. A new mechanism for the selectivity to C 1 and C 2 species in the electrochemical reduction of carbon dioxide on copper electrodes. *Chemical Science* **2,** 1902–1909 (2011).

71. Resasco, J. *et al.* Promoter effects of alkali metal cations on the electrochemical reduction of carbon dioxide. *Journal of the American Chemical Society* **139,** 11277–11287 (2017).

72. Kas, R., Kortlever, R., Yılmaz, H., Koper, M. & Mul, G. Manipulating the hydrocarbon selectivity of copper nanoparticles in CO2 electroreduction by process conditions. *Chem-ElectroChem* **2,** 354–358 (2015).

73. Hashiba, H. *et al.* Effects of electrolyte buffer capacity on surface reactant species and the reaction rate of CO_2 in Electrochemical CO_2 reduction. *The Journal of Physical Chemistry C* **122,** 3719–3726 (2018).

74. Schouten, K. J. P., Gallent, E. P. & Koper, M. T. The influence of pH on the reduction of CO and CO_2 to hydrocarbons on copper electrodes. *Journal of Electroanalytical Chemistry* **716,** 53–57 (2014).

75. Gattrell, M., Gupta, N. & Co, A. A review of the aqueous electrochemical reduction of CO_2 to hydrocarbons at copper. *Journal of Electroanalytical Chemistry* **594,** 1–19 (2006).

76. Nie, X., Esopi, M. R., Janik, M. J. & Asthagiri, A. Selectivity of CO_2 reduction on copper electrodes: the role of the kinetics of elementary steps. *Angewandte Chemie International Edition* **52,** 2459–2462 (2013).

77. Cheng, T., Wang, L., Merinov, B. V. & Goddard III, W. A. Explanation of dramatic pH-dependence of hydrogen binding on noble metal electrode: Greatly weakened water adsorption at high pH. *Journal of the American Chemical Society* **140,** 7787–7790 (2018).

78. Murata, A. & Hori, Y. Product selectivity affected by cationic species in electrochemical reduction of CO_2 and CO at a Cu electrode. *Bulletin of the Chemical Society of Japan* **64,** 123–127 (1991).

79. Lum, Y., Yue, B., Lobaccaro, P., Bell, A. T. & Ager, J. W. Optimizing C–C coupling on oxide-derived copper catalysts for electrochemical CO_2 reduction. *The Journal of Physical Chemistry C* **121,** 14191–14203 (2017).

80. Singh, M. R., Kwon, Y., Lum, Y., Ager III, J. W. & Bell, A. T. Hydrolysis of electrolyte cations enhances the electrochemical reduction of CO_2 over Ag and Cu. *Journal of the American chemical society* **138,** 13006–13012 (2016).

81. Kyriacou, G. & Anagnostopoulos, A. Influence CO_2 partial pressure and the supporting electrolyte cation on the product distribution in CO_2 electroreduction. *Journal of applied electrochemistry* **23,** 483–486 (1993).

82. Pérez-Gallent, E., Marcandalli, G., Figueiredo, M. C., Calle-Vallejo, F. & Koper, M. T. Structure-and potential-dependent cation effects on CO reduction at copper single-crystal electrodes. *Journal of the American Chemical Society* **139,** 16412–16419 (2017).

83. Frumkin, A. Influence of cation adsorption on the kinetics of electrode processes. *Transactions of the Faraday Society* **55,** 156–167 (1959).

84. Strmcnik, D. *et al.* The role of non-covalent interactions in electrocatalytic fuel-cell reactions on platinum. *Nature chemistry* **1,** 466 (2009).

85. Strmcnik, D. *et al.* Effects of Li+, K+, and Ba2+ cations on the ORR at model and high surface area Pt and Au surfaces in alkaline solutions. *The Journal of Physical Chemistry Letters* **2,** 2733–2736 (2011).

86. Gunathunge, C. M., Ovalle, V. J. & Waegele, M. M. Probing promoting effects of alkali cations on the reduction of CO at the aqueous electrolyte/copper interface. *Physical Chemistry Chemical Physics* **19,** 30166–30172 (2017).

87. Gao, D. *et al.* Activity and Selectivity Control in CO_2 Electroreduction to Multicarbon Products over CuO x Catalysts via Electrolyte Design. *Acs catalysis* **8,** 10012–10020 (2018).

88. Hori, Y., Murata, A., Takahashi, R. & Suzuki, S. Enhanced formation of ethylene and alcohols at ambient temperature and pressure in electrochemical reduction of carbon dioxide at a copper electrode. *Journal of the Chemical Society, Chemical Communications,* 17–19 (1988).

89. Varela, A. S., Kroschel, M., Reier, T. & Strasser, P. Controlling the selectivity of CO_2 electroreduction on copper: The effect of the electrolyte concentration and the importance of the local pH. *Catalysis Today* **260,** 8–13 (2016).

90. Dunwell, M. *et al.* The central role of bicarbonate in the electrochemical reduction of carbon dioxide on gold. *Journal of the American Chemical Society* **139,** 3774–3783 (2017).

91. Yano, J. & Yamasaki, S. Pulse-mode electrochemical reduction of carbon dioxide using copper and copper oxide electrodes for selective ethylene formation. *Journal of applied electrochemistry* **38,** 1721 (2008).

92. Roberts, F. S., Kuhl, K. P. & Nilsson, A. High selectivity for ethylene from carbon dioxide reduction over copper nanocube electrocatalysts. *Angewandte Chemie* **127,** 5268–5271 (2015).

93. Kwon, Y., Lum, Y., Clark, E. L., Ager, J. W. & Bell, A. T. CO_2 Electroreduction with Enhanced Ethylene and Ethanol Selectivity by Nanostructuring Polycrystalline Copper. *ChemElectroChem* (2016).

94. Chen, C. S. *et al.* Stable and selective electrochemical reduction of carbon dioxide to ethylene on copper mesocrystals. *Catalysis Science & Technology* **5,** 161–168 (2015).

95. Ogura, K., Oohara, R. & Kudo, Y. Reduction of CO_2 to ethylene at three-phase interface effects of electrode substrate and catalytic coating. *Journal of the Electrochemical Society* **152,** D213 (2005).

96. Yano, H., Tanaka, T., Nakayama, M. & Ogura, K. Selective electrochemical reduction of CO_2 to ethylene at a three-phase interface on copper (I) halide-confined Cu-mesh electrodes in acidic solutions of potassium halides. *Journal of Electroanalytical Chemistry* **565,** 287–293 (2004).

97. Gao, D., Scholten, F. & Roldan Cuenya, B. Improved CO_2 electroreduction performance on plasma-activated Cu catalysts via electrolyte design: halide effect. *Acs Catalysis* **7,** 5112–5120 (2017).

98. Cheng, T., Xiao, H. & Goddard, W. A. Full atomistic reaction mechanism with kinetics for CO reduction on Cu (100) from ab initio molecular dynamics free-energy calculations at 298 K. *Proceedings of the National Academy of Sciences* **114,** 1795–1800 (2017).

99. Grosse, P., Yoon, A., Rettenmaier, C., Chee, S. W. & Cuenya, B. R. Growth Dynamics and Processes Governing the Stability of Electrodeposited Size-Controlled Cubic Cu Catalysts. *The Journal of Physical Chemistry C* (2020).

100. Mistry, H. *et al.* Exceptional size-dependent activity enhancement in the electroreduction of CO_2 over Au nanoparticles. *Journal of the American Chemical Society* **136,** 16473–16476 (2014).

101. Mistry, H., Varela, A. S., Kühl, S., Strasser, P. & Cuenya, B. R. Nanostructured electrocatalysts with tunable activity and selectivity. *Nature Reviews Materials* **1,** 16009 (2016).

102. Mistry, H. *et al.* Tuning catalytic selectivity at the mesoscale via interparticle interactions. *ACS Catalysis* **6,** 1075–1080 (2016).

103. Hammer, B., Morikawa, Y. & Nørskov, J. K. CO chemisorption at metal surfaces and overlayers. *Physical review letters* **76,** 2141 (1996).

104. Teschner, D., Wild, U., Schlögl, R. & Paál, Z. Surface state and composition of a disperse Pd catalyst after its exposure to ethylene. *The Journal of Physical Chemistry B* **109,** 20516–20521 (2005).

105. Amakawa, K. *et al.* How strain affects the reactivity of surface metal oxide catalysts. *Angewandte Chemie International Edition* **52,** 13553–13557 (2013).

106. Ma, Y. *et al.* Facets Matching of Platinum and Ferric Oxide in Highly Efficient Catalyst Design for Low-Temperature CO Oxidation. *ACS applied materials & interfaces* **10,** 15322–15327 (2018).

107. Tauster, S., Fung, S. & Garten, R. L. Strong metal-support interactions. Group 8 noble metals supported on titanium dioxide. *Journal of the American Chemical Society* **100,** 170–175 (1978).

108. Tauster, S., Fung, S., Baker, R. & Horsley, J. Strong interactions in supported-metal catalysts. *Science* **211,** 1121–1125 (1981).

109. Tauster, S. Strong metal-support interactions. *Accounts of Chemical Research* **20,** 389–394 (1987).

110. Logan, A. D., Braunschweig, E. J., Datye, A. K. & Smith, D. J. Direct observation of the surfaces of small metal crystallites: Rhodium supported on titania. *Langmuir* **4,** 827–830 (1988).

111. Reske, R., Mistry, H., Behafarid, F., Roldan Cuenya, B. & Strasser, P. Particle size effects in the catalytic electroreduction of CO_2 on Cu nanoparticles. *Journal of the American Chemical Society* **136,** 6978–6986 (2014).

112. Manthiram, K., Beberwyck, B. J. & Alivisatos, A. P. Enhanced electrochemical methanation of carbon dioxide with a dispersible nanoscale copper catalyst. *Journal of the American Chemical Society* **136,** 13319–13325 (2014).

113. Loiudice, A. *et al.* Tailoring copper nanocrystals towards C2 products in electrochemical CO_2 reduction. *Angewandte Chemie International Edition* **55,** 5789–5792 (2016).

114. Eren, B. *et al.* Activation of Cu (111) surface by decomposition into nanoclusters driven by CO adsorption. *Science* **351,** 475–478 (2016).

115. Kim, D., Kley, C. S., Li, Y. & Yang, P. Copper nanoparticle ensembles for selective electroreduction of CO_2 to C2–C3 products. *Proceedings of the National Academy of Sciences* **114,** 10560–10565 (2017).

116. Osowiecki, W. T. *et al.* Factors and Dynamics of Cu Nanocrystal Reconstruction under CO_2 Reduction. *ACS Applied Energy Materials* **2,** 7744–7749 (2019).

117. Li, Y. *et al.* Electrochemically scrambled nanocrystals are catalytically active for CO_2-to-multicarbons. *Proceedings of the National Academy of Sciences* **117,** 9194–9201 (2020).

118. De Gregorio, G. L. *et al.* Facet-dependent selectivity of Cu catalysts in electrochemical CO_2 reduction at commercially viable current densities. *ACS catalysis* **10,** 4854–4862 (2020).

119. Wang, Z., Yang, G., Zhang, Z., Jin, M. & Yin, Y. Selectivity on etching: Creation of high-energy facets on copper nanocrystals for CO_2 electrochemical reduction. *ACS nano* **10,** 4559–4564 (2016).

120. Song, Y. *et al.* High-selectivity electrochemical conversion of CO_2 to ethanol using a copper nanoparticle/N-doped graphene electrode. *ChemistrySelect* **1,** 6055–6061 (2016).

121. Ning, H. *et al.* N-doped reduced graphene oxide supported Cu_2O nanocubes as high active catalyst for CO_2 electroreduction to C_2H_4. *Journal of Alloys and Compounds* **785,** 7–12 (2019).

122. Gao, D. *et al.* Enhancing CO_2 electroreduction with the metal–oxide interface. *Journal of the American Chemical Society* **139,** 5652–5655 (2017).

123. Rogers, C. *et al.* Synergistic enhancement of electrocatalytic CO_2 reduction with gold nanoparticles embedded in functional graphene nanoribbon composite electrodes. *Journal of the American Chemical Society* **139,** 4052–4061 (2017).

124. Hori, Y., Kikuchi, K., Murata, A. & Suzuki, S. Production of methane and ethylene in electrochemical reduction of carbon dioxide at copper electrode in aqueous hydrogencarbonate solution. *Chemistry Letters* **15,** 897–898 (1986).

125. Hashiba, H., Yotsuhashi, S., Deguchi, M. & Yamada, Y. Systematic analysis of electrochemical CO_2 reduction with various reaction parameters using combinatorial reactors. *ACS combinatorial science* **18,** 203–208 (2016).

126. Kaneco, S. *et al.* Electrochemical conversion of carbon dioxide to methane in aqueous NaHCO3 solution at less than 273 K. *Electrochimica Acta* **48,** 51–55 (2002).

127. Kaneco, S. *et al.* High-efficiency electrochemical CO_2-to-methane reduction method using aqueous KHCO 3 media at less than 273áK. *Journal of Solid State Electrochemistry* **7,** 152–156 (2003).

128. Azuma, M., Hashimoto, K., Hiramoto, M., Watanabe, M. & Sakata, T. Electrochemical reduction of carbon dioxide on various metal electrodes in low-temperature aqueous KHCO 3 media. *Journal of the Electrochemical Society* **137,** 1772 (1990).

129. Ahn, S. T., Abu-Baker, I. & Palmore, G. T. R. Electroreduction of CO_2 on polycrystalline copper: Effect of temperature on product selectivity. *Catalysis Today* **288,** 24–29 (2017).

130. Hara, K., Tsuneto, A., Kudo, A. & Sakata, T. Electrochemical Reduction of CO_2 on a Cu Electrode under High Pressure: Factors that Determine the Product Selectivity. *Journal of the Electrochemical Society* **141,** 2097 (1994).

131. Gao, D. *et al.* Plasma-activated copper nanocube catalysts for efficient carbon dioxide electroreduction to hydrocarbons and alcohols. *ACS nano* **11,** 4825–4831 (2017).

132. Lin, S.-C. *et al.* Operando time-resolved X-ray absorption spectroscopy reveals the chemical nature enabling highly selective CO_2 reduction. *Nature communications* **11,** 1–12 (2020).

133. Kim, D. *et al.* Insights into an autonomously formed oxygen-evacuated Cu 2 O electrode for the selective production of C 2 H 4 from CO_2. *Physical Chemistry Chemical Physics* **17,** 824–830 (2015).

134. Handoko, A. D. *et al.* Mechanistic insights into the selective electroreduction of carbon dioxide to ethylene on Cu_2O-derived copper catalysts. *The Journal of Physical Chemistry C* **120,** 20058–20067 (2016).

135. Tang, W. *et al.* The importance of surface morphology in controlling the selectivity of polycrystalline copper for CO_2 electroreduction. *Physical Chemistry Chemical Physics* **14,** 76–81 (2012).

136. Ma, M., Djanashvili, K. & Smith, W. A. Controllable hydrocarbon formation from the electrochemical reduction of CO_2 over Cu nanowire arrays. *Angewandte chemie international edition* **55,** 6680–6684 (2016).

137. Yang, K. D. *et al.* Morphology-directed selective production of ethylene or ethane from CO_2 on a Cu mesopore electrode. *Angewandte Chemie* **129,** 814–818 (2017).

138. Scholten, F., Sinev, I., Bernal, M. & Roldan Cuenya, B. Plasma-modified dendritic Cu catalyst for CO_2 electroreduction. *ACS catalysis* **9,** 5496–5502 (2019).

139. Sastre, G. & Corma, A. The confinement effect in zeolites. *Journal of Molecular Catalysis A: Chemical* **305,** 3–7 (2009).

140. Boronat, M. & Corma, A. What is measured when measuring acidity in zeolites with probe molecules? *ACS catalysis* **9,** 1539–1548 (2019).

141. Pan, X. & Bao, X. The effects of confinement inside carbon nanotubes on catalysis. *Accounts of chemical research* **44,** 553–562 (2011).

142. Kalz, K. F. *et al.* Future challenges in heterogeneous catalysis: understanding catalysts under dynamic reaction conditions. *ChemCatChem* **9,** 17 (2017).

143. Seh, Z. W. *et al.* Combining theory and experiment in electrocatalysis: Insights into materials design. *Science* **355** (2017).

144.   Molenbroek, A. M., Helveg, S., Topsøe, H. & Clausen, B. S. Nano-particles in heterogeneous catalysis. *Topics in Catalysis* **52,** 1303–1311 (2009).

145.   Houk, L. R., Challa, S. R., Grayson, B., Fanson, P. & Datye, A. K. The definition of "critical radius" for a collection of nanoparticles undergoing Ostwald ripening. *Langmuir* **25,** 11225–11227 (2009).

146.   Simonsen, S. B. *et al.* Ostwald ripening in a Pt/SiO2 model catalyst studied by in situ TEM. *Journal of catalysis* **281,** 147–155 (2011).

147.   Karapinar, D. *et al.* Electroreduction of CO_2 on single-site copper-nitrogen-doped carbon material: selective formation of ethanol and reversible restructuration of the metal sites. *Angewandte Chemie International Edition* **58,** 15098–15103 (2019).

148.   Plodinec, M. *et al.* Versatile homebuilt gas feed and analysis system for operando TEM of catalysts at work. *Microscopy and Microanalysis* **26,** 220–228 (2020).

149.   Popović, S. *et al.* Stability and degradation mechanisms of copper-based catalysts for electrochemical CO_2 reduction. *Angewandte Chemie International Edition* **59,** 14736–14746 (2020).

150.   Ertl, G. Oscillatory kinetics and spatio-temporal self-organization in reactions at solid surfaces. *Science* **254,** 1750–1755 (1991).

151.   Argyle, M. D. & Bartholomew, C. H. Heterogeneous catalyst deactivation and regeneration: a review. *Catalysts* **5,** 145–269 (2015).

152.   Lunkenbein, T. *et al.* Bridging the time gap: a copper/zinc oxide/aluminum oxide catalyst for methanol synthesis studied under industrially relevant conditions and time scales. *Angewandte Chemie International Edition* **55,** 12708–12712 (2016).

153.   Topalov, A. A. *et al.* Dissolution of platinum: limits for the deployment of electrochemical energy conversion? *Angewandte Chemie International Edition* **51,** 12613–12615 (2012).

154.   Cherevko, S. Stability and dissolution of electrocatalysts: Building the bridge between model and "real world" systems. *Current Opinion in Electrochemistry* **8,** 118–125 (2018).

155.   Beermann, V. *et al.* Real-time imaging of activation and degradation of carbon supported octahedral Pt–Ni alloy fuel cell catalysts at the nanoscale using in situ electrochemical liquid cell STEM. *Energy & Environmental Science* **12,** 2476–2485 (2019).

156.   Somorjai, G. Surface reconstruction and catalysis. *Annual Review of Physical Chemistry* **45,** 721–751 (1994).

157.   Coulman, D. J., Wintterlin, J., Behm, R. & Ertl, G. Novel mechanism for the formation of chemisorption phases: The (2×1) O-Cu (110)"added row"reconstruction. *Physical review letters* **64,** 1761 (1990).

158.   Avanesian, T. *et al.* Quantitative and atomic-scale view of CO-induced Pt nanoparticle surface reconstruction at saturation coverage via DFT calculations coupled with in situ TEM and IR. *Journal of the American Chemical Society* **139,** 4551–4558 (2017).

159.   Zhan, W. *et al.* Crystal structural effect of AuCu alloy nanoparticles on catalytic CO oxidation. *Journal of the American Chemical Society* **139,** 8846–8854 (2017).

160. Zou, L. *et al.* Atomically visualizing elemental segregation-induced surface alloying and restructuring. *The journal of physical chemistry letters* **8,** 6035–6040 (2017).

161. Greiner, M. T. *et al.* Phase coexistence of multiple copper oxides on AgCu catalysts during ethylene epoxidation. *ACS Catalysis* **8,** 2286–2295 (2018).

162. Weckhuysen, B. M. Operando spectroscopy: fundamental and technical aspects of spectroscopy of catalysts under working conditions. *Physical chemistry chemical physics* **5,** vi–vi (2003).

163. Bañares, M. A. Operando methodology: combination of in situ spectroscopy and simultaneous activity measurements under catalytic reaction conditions. *Catalysis today* **100,** 71–77 (2005).

164. Guerrero-Pérez, M. O. & Banares, M. A. From conventional in situ to operando studies in Raman spectroscopy. *Catalysis today* **113,** 48–57 (2006).

165. Eaton, P. & West, P. Atomic force microscopy. *Atomic force microscopy* (2010).

166. Hell, S. W. & Wichmann, J. Breaking the diffraction resolution limit by stimulated emission: stimulated-emission-depletion fluorescence microscopy. *Optics letters* **19,** 780–782 (1994).

167. Binnig, G., Rohrer, H., Gerber, C. & Weibel, E. Surface Studies by Scanning Tunneling Microscopy. *Phys. Rev. Lett.* **49,** 57–61 (1 July 1982).

168. Binnig, G., Quate, C. F. & Gerber, C. Atomic force microscope. *Physical review letters* **56,** 930 (1986).

169. Quate, C., Gerber, C. & Binnig, C. Atomic force microscope. *Phys. Rev. Lett* **56,** 930–933 (1986).

170. Rugar, D. & Hansma, P. Atomic force microscopy. *Physics today* **43,** 23–30 (1990).

171. Hansma, 4. *et al.* Tapping mode atomic force microscopy in liquids. *Applied Physics Letters* **64,** 1738–1740 (1994).

172. Putman, C. A., Van der Werf, K. O., De Grooth, B. G., Van Hulst, N. F. & Greve, J. Tapping mode atomic force microscopy in liquid. *Applied physics letters* **64,** 2454–2456 (1994).

173. Lantz, M., O'shea, S. & Welland, M. Force microscopy imaging in liquids using ac techniques. *Applied physics letters* **65,** 409–411 (1994).

174. Schäffer, T., Cleveland, J., Ohnesorge, F., Walters, D. & Hansma, P. Studies of vibrating atomic force microscope cantilevers in liquid. *Journal of applied physics* **80,** 3622–3627 (1996).

175. LaGraff, J. R. & Gewirth, A. A. Enhanced electrochemical deposition with an atomic force microscope. *The Journal of Physical Chemistry* **98,** 11246–11250 (1994).

176. Wen, R., Hong, M. & Byon, H. R. In situ AFM imaging of Li–O2 electrochemical reaction on highly oriented pyrolytic graphite with ether-based electrolyte. *Journal of the American Chemical Society* **135,** 10870–10876 (2013).

177. Khalakhan, I. *et al.* In-situ electrochemical atomic force microscopy study of aging of magnetron sputtered Pt-Co nanoalloy thin films during accelerated degradation test. *Electrochimica Acta* **211,** 52–58 (2016).

178. Deng, X., Galli, F. & Koper, M. T. In situ electrochemical AFM imaging of a Pt electrode in sulfuric acid under potential cycling conditions. *Journal of the American Chemical Society* **140,** 13285–13291 (2018).

179. Deng, X., Galli, F. & Koper, M. T. In Situ AFM Imaging of Platinum Electrode Surface during Oxidation–Reduction Cycles in Alkaline Electrolyte. *ACS Applied Energy Materials* **3,** 597–602 (2019).

180. Ikemiya, N., Kubo, T. & Hara, S. In situ AFM observations of oxide film formation on Cu (111) and Cu (100) surfaces under aqueous alkaline solutions. *Surface science* **323,** 81–90 (1995).

181. Cruickshank, B. J., Sneddon, D. D. & Gewirth, A. A. In situ observations of oxygen adsorption on a Cu (100) substrate using atomic force microscopy. *Surface science* **281,** L308–L314 (1993).

182. Grosse, P. *et al.* Dynamic Changes in the Structure, Chemical State and Catalytic Selectivity of Cu Nanocubes during CO_2 Electroreduction: Size and Support Effects. *Angewandte Chemie - International Edition* **57,** 6192–6197 (May 22, 2018).

183. Busch, H. Berechnung der Bahn von Kathodenstrahlen im axialsymmetrischen elektromagnetischen Felde. *Annalen der Physik* **386,** 974–993 (1926).

184. Ruska, E. & Knoll, M. Die magnetische Sammelspule für schnelle Elektronenstrahlen. *The magnetic concentrating coil for fast electron beams.) Z. techn. Physik* **12,** 389–400 (1931).

185. De Broglie, L. *Recherches sur la théorie des quanta* PhD thesis (Migration-université en cours d'affectation, 1924).

186. Zworykin, V. K. The scanning electron microscope. *Scientific American* **167,** 111–113 (1942).

187. McMullan, D. Scanning electron microscopy 1928–1965. *Scanning* **17,** 175–185 (1995).

188. Sharma, R. & Weiss, K. Development of a TEM to study in situ structural and chemical changes at an atomic level during gas-solid interactions at elevated temperatures. *Microscopy Research and Technique* **42,** 270–280 (1998).

189. Boyes, E. & Gai, P. Environmental high resolution electron microscopy and applications to chemical science. *Ultramicroscopy* **67,** 219–232 (1997).

190. He, B., Zhang, Y., Liu, X. & Chen, L. In-situ Transmission Electron Microscope Techniques for Heterogeneous Catalysis. *ChemCatChem* (2020).

191. Franks, R. *et al.* A study of nanomaterial dispersion in solution by wet-cell transmission electron microscopy. *Journal of nanoscience and nanotechnology* **8,** 4404–4407 (2008).

192. Williamson, M., Tromp, R., Vereecken, P., Hull, R. & Ross, F. Dynamic microscopy of nanoscale cluster growth at the solid–liquid interface. *Nature materials* **2,** 532–536 (2003).

193. Creemer, J. *et al.* Atomic-scale electron microscopy at ambient pressure. *Ultramicroscopy* **108,** 993–998 (2008).

194. Ring, E. A. & De Jonge, N. Microfluidic system for transmission electron microscopy. *Microscopy and Microanalysis* **16,** 622 (2010).

195. Zheng, H., Claridge, S. A., Minor, A. M., Alivisatos, A. P. & Dahmen, U. Nanocrystal diffusion in a liquid thin film observed by in situ transmission electron microscopy. *Nano letters* **9,** 2460–2465 (2009).

196. De Jonge, N., Peckys, D. B., Kremers, G. & Piston, D. Electron microscopy of whole cells in liquid with nanometer resolution. *Proceedings of the National Academy of Sciences* **106,** 2159–2164 (2009).

197. Wu, J. *et al.* In situ environmental TEM in imaging gas and liquid phase chemical reactions for materials research. *Advanced Materials* **28,** 9686–9712 (2016).

198. Taheri, M. L. *et al.* Current status and future directions for in situ transmission electron microscopy. *Ultramicroscopy* **170,** 86–95 (2016).

199. Tao, F. & Crozier, P. A. Atomic-scale observations of catalyst structures under reaction conditions and during catalysis. *Chemical reviews* **116,** 3487–3539 (2016).

200. Hwang, S., Chen, X., Zhou, G. & Su, D. In Situ Transmission Electron Microscopy on Energy-Related Catalysis. *Advanced Energy Materials* **10,** 1902105 (2020).

201. Boniface, M., Plodinec, M., Schlögl, R. & Lunkenbein, T. Quo Vadis Micro-Electro-Mechanical Systems for the Study of Heterogeneous Catalysts Inside the Electron Microscope? *Topics in Catalysis,* 1–21 (2020).

202. Chee, S. W., Lunkenbein, T. L., Schlögl, R. & Cuenya, B. R. In situ and operando electron microscopy in heterogeneous catalysis–Insights into multi-scale chemical dynamics. *Journal of Physics: Condensed Matter* (2021).

203. Schneider, N. M. *et al.* Electron–water interactions and implications for liquid cell electron microscopy. *The Journal of Physical Chemistry C* **118,** 22373–22382 (2014).

204. De Jonge, N., Houben, L., Dunin-Borkowski, R. E. & Ross, F. M. Resolution and aberration correction in liquid cell transmission electron microscopy. *Nature Reviews Materials* **4,** 61–78 (2019).

205. Grosse, P. *et al.* Dynamic Transformation of Cubic Copper Catalysts during CO_2 Electroreduction and its Impact on Catalytic Selectivity. *Submitted* (2021).

206. Teo, B. & Joy, D. EXAFS spectroscopy. *Techniques and Applications* (1981).

207. Teo, B. K. in *EXAFS: Basic Principles and Data Analysis* 21–33 (Springer, 1986).

208. Rehr, J. J. & Albers, R. C. Theoretical approaches to x-ray absorption fine structure. *Reviews of modern physics* **72,** 621 (2000).

209. Rehr, J. J. *et al.* Ab initio theory and calculations of X-ray spectra. *Comptes Rendus Physique* **10,** 548–559 (2009).

210. Rehr, J. J., Kas, J. J., Vila, F. D., Prange, M. P. & Jorissen, K. Parameter-free calculations of X-ray spectra with FEFF9. *Physical Chemistry Chemical Physics* **12,** 5503–5513 (2010).

211. Newville, M. EXAFS analysis using FEFF and FEFFIT. *Journal of synchrotron radiation* **8,** 96–100 (2001).

212. Burhop, E. & Asaad, W. The Auger Effect. *Advances in Atomic and Molecular Physics* **8,** 163–284 (1972).

213. Sawyer, D. T., Sobkowiak, A. & Roberts, J. L. *Electrochemistry for chemists* (Wiley, 1995).

214. Bard, A. J., Faulkner, L. R., *et al.* Fundamentals and applications. *Electrochemical Methods* **2,** 580–632 (2001).

215. Axnanda, S., Cummins, K. D., Goodman, D. W. & Soriaga, M. P. in *Theory and Experiment in Electrocatalysis* 1–23 (Springer, 2010).

216. Compton, R. G. & Banks, C. E. *Understanding voltammetry* (World Scientific, 2018).

217. Aurbach, D. *Nonaqueous electrochemistry* (CRC press, 1999).

218. Glasstone, S. *An introduction to electrochemistry* (Read Books Ltd, 2011).

219. Kas, R. *et al.* Electrochemical CO_2 reduction on Cu 2 O-derived copper nanoparticles: controlling the catalytic selectivity of hydrocarbons. *Physical Chemistry Chemical Physics* **16,** 12194–12201 (2014).

220. Hori, Y., Takahashi, I., Koga, O. & Hoshi, N. Electrochemical reduction of carbon dioxide at various series of copper single crystal electrodes. *Journal of Molecular Catalysis A: Chemical* **199,** 39–47 (2003).

221. Todorova, T. K., Schreiber, M. W. & Fontecave, M. Mechanistic Understanding of CO_2 Reduction Reaction (CO_2RR) Toward Multicarbon Products by Heterogeneous Copper-Based Catalysts (2019).

222. Perez-Gallent, E., Figueiredo, M. C., Calle-Vallejo, F. & Koper, M. T. M. Spectroscopic Observation of a Hydrogenated CO Dimer Intermediate During CO Reduction on Cu(100) Electrodes. *Angewandte Chemie - International Edition* **56,** 3621–3624 (Mar. 20, 2017).

223. Li, H., Li, Y., Koper, M. T. M. & Calle-Vallejo, F. Bond-making and breaking between carbon, nitrogen, and oxygen in electrocatalysis. *Journal of the American Chemical Society* **136,** 15694–15701 (Nov. 5, 2014).

224. Roberts, F. S., Kuhl, K. P. & Nilsson, A. High selectivity for ethylene from carbon dioxide reduction over copper nanocube electrocatalysts. *Angewandte Chemie - International Edition* **54,** 5179–5182 (Apr. 20, 2015).

225. Tanori, J. & Pileni, M. P. Control of the shape of copper metallic particles by using a colloidal system as template. *Langmuir* **13,** 639–645 (Feb. 19, 1997).

226. Feng, Y. *et al.* Laser-Prepared CuZn Alloy Catalyst for Selective Electrochemical Reduction of CO_2 to Ethylene. *Langmuir* **34,** 13544–13549 (Nov. 13, 2018).

227. Liu, D. *et al.* On the impact of Cu dispersion on CO_2 photoreduction over Cu/TiO 2. *Catalysis Communications* **25,** 78–82 (2012).

228. Wang, Z., Liu, Q., Yu, J., Wu, T. & Wang, G. Surface structure and catalytic behavior of silica-supported copper catalysts prepared by impregnation and sol-gel methods. *Applied Catalysis A: General* **239,** 87–94 (2003).

229. Potochnik, S. J., Pehrsson, P. E., Hsu, D. S. & Calvert, J. M. Selective Copper Chemical Vapor Deposition Using Pd-Activated Organosilane Films. *Langmuir* **11,** 1841–1845 (1995).

230. Sloan Roberts, F. *et al.* Formation of Copper Catalysts for CO_2 Reduction with High Ethylene/Methane Product Ratio Investigated with in Situ X-ray Absorption Spectroscopy. *Journal of Physical Chemistry Letters* **7,** 1466–1470 (May 5, 2016).

231. Aran-Ais, R. M. *et al.* Imaging electrochemically synthesized Cu_2O cubes and their morphological evolution under conditions relevant to CO_2 electroreduction. *Nature Communications* **11** (2020).

232. Varela, A. S., Ju, W., Reier, T. & Strasser, P. Tuning the Catalytic Activity and Selectivity of Cu for CO_2 Electroreduction in the Presence of Halides. *ACS Catalysis* **6,** 2136–2144 (Apr. 1, 2016).

233. Krasnikov, G. Y. & Bokarev, V. P. Surface energy and crystal faceting of elemental semiconductors and other substances. *Doklady Physical Chemistry* **382,** 14–17 (2002).

234. Jesús Velasco-Veiez, J.-J. *et al.* The Electro-Deposition/Dissolution of CuSO 4 Aqueous Electrolyte Investigated by In Situ Soft X-ray Absorption Spectroscopy (2017).

235. Siegfried, M. J. J. & Choi, K.-S. S. Elucidating the effect of additives on the growth and stability of Cu 2O surfaces via shape transformation of pre-grown crystals. *Journal of the American Chemical Society* **128,** 10356–10357 (Aug. 16, 2006).

236. Siegfried, M. J. & Choi, K.-S. Directing the Architecture of Cuprous Oxide Crystals during Electrochemical Growth. *Angewandte Chemie* **117,** 3282–3287 (May 20, 2005).

237. Radi, A., Pradhan, D., Sohn, Y. & Leung, K. T. *Nanoscale shape and size control of cubic, cuboctahedral, and octahedral Cu-Cu$_2$O core-shell nanoparticles on Si(100) by one-step, templateless, capping-agent-free electrodeposition* [Online; accessed 2020-06-10]. Mar. 23, 2010.

238. Siegfried, M. J. & Choi, K. S. Elucidation of an overpotential-limited branching phenomenon observed during the electrocrystallization of cuprous oxide. *Angewandte Chemie - International Edition* **47,** 368–372 (Jan. 2008).

239. Hori, Y., Murata, A., Takahashi, R. & Suzuki, S. Enhanced formation of ethylene and alcohols at ambient temperature and pressure in electrochemical reduction of carbon dioxide at a copper electrode. *Journal of the Chemical Society, Chemical Communications* **109,** 17 (1988).

240. Kortlever, R., Shen, J., Schouten, K. J. P., Calle-Vallejo, F. & Koper, M. T. Catalysts and Reaction Pathways for the Electrochemical Reduction of Carbon Dioxide. *Journal of Physical Chemistry Letters* **6,** 4073–4082 (Oct. 15, 2015).

241. Larrazabal, G. O., Martin, A. J. & Perez-Ramirez, J. Building Blocks for High Performance in Electrocatalytic CO_2 Reduction: Materials, Optimization Strategies, and Device Engineering. *Journal of Physical Chemistry Letters* **8,** 3933–3944 (Aug. 17, 2017).

242. Li, C. W. & Kanan, M. W. CO_2 reduction at low overpotential on Cu electrodes resulting from the reduction of thick Cu 2O films. *Journal of the American Chemical Society* **134,** 7231–7234 (May 2, 2012).

243. Appel, A. M. Electrochemistry: Catalysis at the boundaries. *Nature* **508,** 460–461 (Apr. 9, 2014).

244. Calle-Vallejo, F. & Koper, M. T. M. Theoretical Considerations on the Electroreduction of CO to C 2 Species on Cu(100) Electrodes. *Angewandte Chemie* **125,** 7423–7426 (July 8, 2013).

245. Montoya, J. H., Shi, C., Chan, K. & Nørskov, J. K. Theoretical insights into a CO dimerization mechanism in CO_2 electroreduction. *Journal of Physical Chemistry Letters* **6,** 2032–2037 (June 4, 2015).

246. Kas, R., Kortlever, R., Yilmaz, H., Koper, M. T. & Mul, G. Manipulating the Hydrocarbon Selectivity of Copper Nanoparticles in CO_2 Electroreduction by Process Conditions. *ChemElectroChem* **2,** 354–358 (Mar. 11, 2015).

247. Tang, W. *et al.* The importance of surface morphology in controlling the selectivity of polycrystalline copper for CO_2 electroreduction. *Physical Chemistry Chemical Physics* **14,** 76–81 (Dec. 2, 2012).

248. Sandberg, R. B., Montoya, J. H., Chan, K. & Nørskov, J. K. CO-CO coupling on Cu facets: Coverage, strain and field effects. *Surface Science* **654,** 56–62 (Dec. 2016).

249. Zegkinoglou, I. *et al.* Operando Phonon Studies of the Protonation Mechanism in Highly Active Hydrogen Evolution Reaction Pentlandite Catalysts. *Journal of the American Chemical Society* **139,** 14360–14363 (Oct. 4, 2017).

250. Mistry, H., Reske, R., Strasser, P. & Roldan Cuenya, B. Size-dependent reactivity of gold-copper bimetallic nanoparticles during CO_2 electroreduction. *Catalysis Today* **288,** 30–36 (June 15, 2017).

251. Mistry, H. *et al.* Highly selective plasma-activated copper catalysts for carbon dioxide reduction to ethylene. *Nature Communications* **7,** 12123 (June 30, 2016).

252. Reller, C. *et al.* Selective Electroreduction of CO_2 toward Ethylene on Nano Dendritic Copper Catalysts at High Current Density. *Advanced Energy Materials* **7,** 1602114 (June 2017).

253. Eilert, A. *et al.* Subsurface Oxygen in Oxide-Derived Copper Electrocatalysts for Carbon Dioxide Reduction. *Journal of Physical Chemistry Letters* **8,** 285–290 (Jan. 5, 2017).

254. Lee, S., Kim, D. & Lee, J. Electrocatalytic production of C3-C4 compounds by conversion of CO_2 on a chloride-induced Bi-phasic Cu_2O-Cu catalyst. *Angewandte Chemie - International Edition* **54,** 14701–14705 (Dec. 1, 2015).

255. Ren, D. *et al.* Selective Electrochemical Reduction of Carbon Dioxide to Ethylene and Ethanol on Copper(I) oxide catalysts. *ACS Catalysis* **5,** 2814–2821 (May 31, 2015).

256. Xiao, H., Goddard, W. A., Cheng, T. & Liu, Y. Cu metal embedded in oxidized matrix catalyst to promote CO_2 activation and CO dimerization for electrochemical reduction of CO_2. *Proceedings of the National Academy of Sciences of the United States of America* **114,** 6685–6688 (June 27, 2017).

257. Favaro, M., Xiao, H., Cheng, T., Goddard, W. A. & Crumlin, E. J. Subsurface oxide plays a critical role in CO_2 activation by Cu(111) surfaces to form chemisorbed CO_2, the first step in reduction of CO_2. *Proceedings of the National Academy of Sciences of the United States of America* **114,** 6706–6711 (June 27, 2017).

258. Wang, X., Varela, A. S., Bergmann, A., Kühl, S. & Strasser, P. Catalyst Particle Density Controls Hydrocarbon Product Selectivity in CO_2 Electroreduction on CuOx. *ChemSusChem* **10,** 4642–4649 (Aug. 21, 2017).

259. Schouten, K. J. P., Perez Gallent, E. & Koper, M. T. Structure sensitivity of the electrochemical reduction of carbon monoxide on copper single crystals. *ACS Catalysis* **3,** 1292–1295 (June 7, 2013).

260. Loiudice, A. *et al.* Tailoring Copper Nanocrystals towards C2 Products in Electrochemical CO_2 Reduction. *Angewandte Chemie - International Edition* **55,** 5789–5792 (May 4, 2016).

261. Ulissi, Z. W. *et al.* Machine-learning methods enable exhaustive searches for active Bimetallic facets and reveal active site motifs for CO_2 reduction. *ACS Catalysis* **7,** 6600–6608 (Oct. 6, 2017).

262. Liu, X. *et al.* Understanding trends in electrochemical carbon dioxide reduction rates. *Nature Communications* **8,** 15438 (2017).

263. She, Z. W. *et al.* Combining theory and experiment in electrocatalysis: Insights into materials design. *Science* **355,** eaad4998 (2017).

264. Ju, W. *et al.* Understanding activity and selectivity of metal-nitrogen-doped carbon catalysts for electrochemical reduction of CO_2. *Nature Communications* **8,** 944 (2017).

265. De Luna, P. *et al.* Catalyst electro-redeposition controls morphology and oxidation state for selective carbon dioxide reduction. *Nature Catalysis* **1,** 103–110 (Jan. 15, 2018).

266. Jiang, K. *et al.* Metal ion cycling of Cu foil for selective C–C coupling in electrochemical CO_2 reduction. *Nature Catalysis* **1,** 111–119 (Feb. 15, 2018).

267. Eren, B., Weatherup, R. S., Liakakos, N., Somorjai, G. A. & Salmeron, M. Dissociative Carbon Dioxide Adsorption and Morphological Changes on Cu(100) and Cu(111) at Ambient Pressures. *Journal of the American Chemical Society* **138,** 8207–8211 (July 6, 2016).

268. Le Duff, C. S., Lawrence, M. J. & Rodriguez, P. Role of the adsorbed oxygen species in the selective electrochemical reduction of CO_2 to alcohols and carbonyls on copper electrodes. *Angewandte Chemie International Edition* **56,** 12919–12924 (Oct. 9, 2017).

269. Gao, D. *et al.* Plasma-Activated Copper Nanocube Catalysts for Efficient Carbon Dioxide Electroreduction to Hydrocarbons and Alcohols. *ACS Nano* **11,** 4825–4831 (May 23, 2017).

270. Biesinger, M. C., Lau, L. W., Gerson, A. R. & Smart, R. S. C. Resolving surface chemical states in XPS analysis of first row transition metals, oxides and hydroxides: Sc, Ti, V, Cu and Zn. *Applied Surface Science* **257,** 887–898 (2010).

271. Timoshenko, J. & Kuzmin, A. Wavelet data analysis of EXAFS spectra. *Computer Physics Communications* **180,** 920–925 (2009).

272. Monzó, J. *et al.* Enhanced electrocatalytic activity of Au@ Cu core@ shell nanoparticles towards CO_2 reduction. *Journal of Materials Chemistry A* **3,** 23690–23698 (2015).

273. Behafarid, F. *et al.* Structural and electronic properties of micellar Au nanoparticles: Size and ligand effects. *ACS Nano* **8,** 6671–6681 (2014).

274. Tang, Y. & Cheng, W. Key parameters governing metallic nanoparticle electrocatalysis. *Nanoscale* **7,** 16151–16164 (2015).

275. Koper, M. T. Structure sensitivity and nanoscale effects in electrocatalysis. *Nanoscale* **3,** 2054–2073 (2011).

276. Rizo, R. & Roldan Cuenya, B. Shape-controlled nanoparticles as anodic catalysts in low-temperature fuel cells. *ACS energy letters* **4,** 1484–1495 (2019).

277. Arán-Ais, R. M., Gao, D. & Roldan Cuenya, B. Structure-and electrolyte-sensitivity in CO_2 electroreduction. *Accounts of chemical research* **51,** 2906–2917 (2018).

278. Mangione, G., Huang, J., Buonsanti, R. & Corminboeuf, C. Dual-Facet Mechanism in Copper Nanocubes for Electrochemical CO_2 Reduction into Ethylene. *The journal of physical chemistry letters* **10,** 4259–4265 (2019).

279. Liu, L. & Corma, A. Metal catalysts for heterogeneous catalysis: from single atoms to nanoclusters and nanoparticles. *Chemical reviews* **118,** 4981–5079 (2018).

280. Sui, Y. *et al.* Low temperature synthesis of Cu_2O crystals: shape evolution and growth mechanism. *Crystal growth & design* **10,** 99–108 (2010).

281. Gou, L. & Murphy, C. J. Controlling the size of Cu 2 O nanocubes from 200 to 25 nm. *Journal of Materials Chemistry* **14,** 735–738 (2004).

282. Yoon, S., Kim, S.-D., Choi, S.-Y., Lim, J.-H. & Yoo, B. Hierarchical shape evolution of cuprous oxide micro-and nanocrystals by surfactant-assisted electrochemical deposition. *Crystal Growth & Design* **15,** 4969–4974 (2015).

283. Ko, W.-Y., Chen, W.-H., Cheng, C.-Y. & Lin, K.-J. Architectural growth of cu nanoparticles through electrodeposition. *Nanoscale research letters* **4,** 1481–1485 (2009).

284. Siegfried, M. J. & Choi, K.-S. Electrochemical crystallization of cuprous oxide with systematic shape evolution. *Advanced Materials* **16,** 1743–1746 (2004).

285. Arán-Ais, R. M., Vidal-Iglesias, F. J., Solla-Gullón, J., Herrero, E. & Feliu, J. M. Electrochemical Characterization of Clean Shape-Controlled Pt Nanoparticles Prepared in Presence of Oleylamine/Oleic Acid. *Electroanalysis* **27,** 945–956 (2015).

286. De Jonge, N. & Ross, F. M. Electron microscopy of specimens in liquid. *Nature nanotechnology* **6,** 695–704 (2011).

287. Wang, C.-M., Liao, H.-G. & Ross, F. M. Observation of materials processes in liquids by electron microscopy. *MRS Bulletin* **40,** 46 (2015).

288. Radisic, A., Ross, F. & Searson, P. In situ study of the growth kinetics of individual island electrodeposition of copper. *The Journal of Physical Chemistry B* **110,** 7862–7868 (2006).

289. White, E. R. *et al.* In situ transmission electron microscopy of lead dendrites and lead ions in aqueous solution. *Acs Nano* **6,** 6308–6317 (2012).

290. Gu, M. *et al.* Demonstration of an electrochemical liquid cell for operando transmission electron microscopy observation of the lithiation/delithiation behavior of Si nanowire battery anodes. *Nano Letters* **13,** 6106–6112 (2013).

291. Unocic, R. R. *et al.* Direct visualization of solid electrolyte interphase formation in lithium-ion batteries with in situ electrochemical transmission electron microscopy. *Microscopy and Microanalysis* **20,** 1029–1037 (2014).

292. Sacci, R. L. *et al.* Direct visualization of initial SEI morphology and growth kinetics during lithium deposition by in situ electrochemical transmission electron microscopy. *Chemical Communications* **50,** 2104–2107 (2014).

293. Chee, S. W. *et al.* Studying localized corrosion using liquid cell transmission electron microscopy. *Chemical Communications* **51,** 168–171 (2015).

294. Mehdi, B. L. *et al.* Observation and quantification of nanoscale processes in lithium batteries by operando electrochemical (S) TEM. *Nano letters* **15,** 2168–2173 (2015).

295. Tan, S. F. *et al.* Intermediate Structures of Pt–Ni Nanoparticles during Selective Chemical and Electrochemical Etching. *The journal of physical chemistry letters* **10,** 6090–6096 (2019).

296. Zheng, H. *et al.* Observation of single colloidal platinum nanocrystal growth trajectories. *science* **324,** 1309–1312 (2009).

297. Liao, H.-G., Niu, K. & Zheng, H. Observation of growth of metal nanoparticles. *Chemical Communications* **49,** 11720–11727 (2013).

298. Liao, H.-G. *et al.* Facet development during platinum nanocube growth. *Science* **345,** 916–919 (2014).

299. Radisic, A., Vereecken, P., Searson, P. & Ross, F. The morphology and nucleation kinetics of copper islands during electrodeposition. *Surface science* **600,** 1817–1826 (2006).

300. Radisic, A., Vereecken, P. M., Hannon, J. B., Searson, P. C. & Ross, F. M. Quantifying electrochemical nucleation and growth of nanoscale clusters using real-time kinetic data. *Nano Letters* **6,** 238–242 (2006).

301. Oshima, Y., Tsuda, T., Kuwabata, S., Yasuda, H. & Takayanagi, K. Development of an electrochemical cell for in situ transmission electron microscopy observation. *Journal of Electron Microscopy* **63,** 481–486 (2014).

302. Ortiz Peña, N. *et al.* Morphological and Structural Evolution of Co3O4 Nanoparticles Revealed by in Situ Electrochemical Transmission Electron Microscopy during Electrocatalytic Water Oxidation. *ACS nano* **13,** 11372–11381 (2019).

303. Hua, Q. *et al.* Morphological evolution of Cu$_2$O nanocrystals in an acid solution: stability of different crystal planes. *Langmuir* **27,** 665–671 (2011).

304. Kuo, C.-H. & Huang, M. H. Fabrication of truncated rhombic dodecahedral Cu$_2$O nanocages and nanoframes by particle aggregation and acidic etching. *Journal of the American Chemical Society* **130,** 12815–12820 (2008).

305. Wiley, B., Herricks, T., Sun, Y. & Xia, Y. Polyol synthesis of silver nanoparticles: use of chloride and oxygen to promote the formation of single-crystal, truncated cubes and tetrahedrons. *Nano Letters* **4,** 1733–1739 (2004).

306. Xia, Y., Xiong, Y., Lim, B. & Skrabalak, S. E. Shape-controlled synthesis of metal nanocrystals: simple chemistry meets complex physics? *Angewandte Chemie International Edition* **48,** 60–103 (2009).

307. Xia, Y., Xia, X. & Peng, H.-C. Shape-controlled synthesis of colloidal metal nanocrystals: thermodynamic versus kinetic products. *Journal of the American Chemical Society* **137,** 7947–7966 (2015).

308. Kim, M. H., Lim, B., Lee, E. P. & Xia, Y. Polyol synthesis of Cu 2 O nanoparticles: use of chloride to promote the formation of a cubic morphology. *Journal of Materials Chemistry* **18,** 4069–4073 (2008).

309. Gao, D. *et al.* Selective CO$_2$ Electroreduction to Ethylene and Multicarbon Alcohols via Electrolyte-Driven Nanostructuring. *Angewandte Chemie International Edition* **58,** 17047–17053 (2019).

310. Arjmand, F. & Adriaens, A. Influence of pH and chloride concentration on the corrosion behavior of unalloyed copper in NaCl solution: a comparative study between the micro and macro scales. *Materials* **5,** 2439–2464 (2012).

311. Yin, Z. *et al.* Cu3N Nanocubes for Selective Electrochemical Reduction of CO$_2$ to Ethylene. *Nano Letters* **19,** 8658–8663 (2019).

312. Friend, C. M. & Xu, B. Heterogeneous catalysis: a central science for a sustainable future. *Accounts of chemical research* **50,** 517–521 (2017).

313. De Luna, P. *et al.* What would it take for renewably powered electrosynthesis to displace petrochemical processes? *Science* **364** (Apr. 26, 2019).

314. Kim, D. *et al.* Electrochemical activation of CO$_2$ through atomic ordering transformations of AuCu nanoparticles. *Journal of the American Chemical Society* **139,** 8329–8336 (2017).

315. Huang, J. *et al.* Potential-induced nanoclustering of metallic catalysts during electrochemical CO$_2$ reduction. *Nature communications* **9,** 1–9 (2018).

316. Jung, H. *et al.* Electrochemical fragmentation of Cu$_2$O nanoparticles enhancing selective C–C coupling from CO$_2$ reduction reaction. *Journal of the American Chemical Society* **141,** 4624–4633 (2019).

317. Ross, M. B. *et al.* Designing materials for electrochemical carbon dioxide recycling. *Nature Catalysis* **2,** 648–658 (2019).

318. Ross, F. M. Opportunities and challenges in liquid cell electron microscopy. *Science* **350** (2015).

319. Zhu, G.-Z. *et al.* In situ liquid cell TEM study of morphological evolution and degradation of Pt–Fe nanocatalysts during potential cycling. *The Journal of Physical Chemistry C* **118,** 22111–22119 (2014).

320. Impagnatiello, A. *et al.* Degradation Mechanisms of Supported Pt Nanocatalysts in Proton Exchange Membrane Fuel Cells: An Operando Study through Liquid Cell Transmission Electron Microscopy. *ACS Applied Energy Materials* **3,** 2360–2371 (2020).

321. Vavra, J., Shen, T.-H., Stoian, D., Tileli, V. & Buonsanti, R. Real-time Monitoring Reveals Dissolution/Redeposition Mechanism in Copper Nanocatalysts during the Initial Stages of the CO_2 Reduction Reaction. *Angewandte Chemie International Edition* (2020).

322. Hodnik, N., Dehm, G. & Mayrhofer, K. J. Importance and challenges of electrochemical in situ liquid cell electron microscopy for energy conversion research. *Accounts of chemical research* **49,** 2015–2022 (2016).

323. Trindell, J. A., Duan, Z., Henkelman, G. & Crooks, R. M. Well-defined nanoparticle electrocatalysts for the refinement of theory. *Chemical reviews* **120,** 814–850 (2019).

324. Möller, T. *et al.* reduction on CuO x nanocubes tracking the evolution of chemical state, geometric structure, and catalytic selectivity using Operando Spectroscopy. *Angew. Chem., Int. Ed* (2020).

325. Chang, K. *et al.* Improving CO_2 electrochemical reduction to CO using space confinement between gold or silver nanoparticles. *The journal of physical chemistry letters* **11,** 1896–1902 (2020).

326. Reske, R., Mistry, H., Behafarid, F., Roldan Cuenya, B. & Strasser, P. Particle size effects in the catalytic electroreduction of CO_2 on Cu nanoparticles. *Journal of the American Chemical Society* **136,** 6978–6986 (May 14, 2014).

327. Vayenas, C. G., White, R. E. & Gamboa-Aldeco, M. E. *Modern Aspects of Electrochemistry 42* (Springer Science & Business Media, 2008).

328. Han, N. *et al.* Self-templated synthesis of hierarchical mesoporous SnO 2 nanosheets for selective CO_2 reduction. *Journal of Materials Chemistry A* **7,** 1267–1272 (2019).

329. Kim, C. *et al.* Alloy nanocatalysts for the electrochemical oxygen reduction (ORR) and the direct electrochemical carbon dioxide reduction reaction (CO_2RR). *Advanced Materials* **31,** 1805617 (2019).

330. Huang, J., Mensi, M., Oveisi, E., Mantella, V. & Buonsanti, R. Structural sensitivities in bimetallic catalysts for electrochemical CO_2 reduction revealed by Ag–Cu nanodimers. *Journal of the American Chemical Society* **141,** 2490–2499 (2019).

331. Vasileff, A., Xu, C., Jiao, Y., Zheng, Y. & Qiao, S.-Z. Surface and interface engineering in copper-based bimetallic materials for selective CO_2 electroreduction. *Chem* **4,** 1809–1831 (2018).

332. Zhong, H. *et al.* Synergistic electroreduction of carbon dioxide to carbon monoxide on bimetallic layered conjugated metal-organic frameworks. *Nature communications* **11,** 1–10 (2020).

333. Choi, J. *et al.* Electrochemical CO_2 reduction to CO on dendritic Ag–Cu electrocatalysts prepared by electrodeposition. *Chemical Engineering Journal* **299,** 37–44 (2016).

334. Kim, D., Resasco, J., Yu, Y., Asiri, A. M. & Yang, P. Synergistic geometric and electronic effects for electrochemical reduction of carbon dioxide using gold–copper bimetallic nanoparticles. *Nature communications* **5,** 1–8 (2014).

335. Whipple, D. T. & Kenis, P. J. Prospects of CO_2 utilization via direct heterogeneous electrochemical reduction. *The Journal of Physical Chemistry Letters* **1,** 3451–3458 (2010).

336. Kondratenko, E. V., Mul, G., Baltrusaitis, J., Larrazábal, G. O. & Pérez-Ramirez, J. Status and perspectives of CO_2 conversion into fuels and chemicals by catalytic, photocatalytic and electrocatalytic processes. *Energy & environmental science* **6,** 3112–3135 (2013).

337. Zhang, Y.-J., Sethuraman, V., Michalsky, R. & Peterson, A. A. Competition between CO_2 reduction and H2 evolution on transition-metal electrocatalysts. *Acs Catalysis* **4,** 3742–3748 (2014).

338. Gao, D., Cai, F., Wang, G. & Bao, X. Nanostructured heterogeneous catalysts for electrochemical reduction of CO_2. *Current Opinion in Green and Sustainable Chemistry* **3,** 39–44 (2017).

339. Bertheussen, E. *et al.* Acetaldehyde as an intermediate in the electroreduction of carbon monoxide to ethanol on oxide-derived copper. *Angewandte Chemie International Edition* **55,** 1450–1454 (2016).

340. Kattel, S., Yan, B., Yang, Y., Chen, J. G. & Liu, P. Optimizing binding energies of key intermediates for CO_2 hydrogenation to methanol over oxide-supported copper. *Journal of the American Chemical Society* **138,** 12440–12450 (2016).

341. Verdaguer-Casadevall, A. *et al.* Probing the active surface sites for CO reduction on oxide-derived copper electrocatalysts. *Journal of the American Chemical Society* **137,** 9808–9811 (2015).

342. Engelbrecht, A., Hämmerle, M., Moos, R., Fleischer, M. & Schmid, G. Improvement of the selectivity of the electrochemical conversion of CO_2 to hydrocarbons using cupreous electrodes with in-situ oxidation by oxygen. *Electrochimica Acta* **224,** 642–648 (2017).

343. Ye, J.-S., Chen, C.-W. & Lee, C.-L. Pd nanocube as non-enzymatic glucose sensor. *Sensors and Actuators B: Chemical* **208,** 569–574 (2015).

344. Ye, J.-S., Hsu, S.-Y. & Lee, C.-L. Sequential and transient electrocatalysis of glucose oxidation reactions by octahedral, rhombic dodecahedral, and cubic palladium nanocrystals. *Electrochimica Acta* **211,** 1024–1032 (2016).

345. Chen, C. S., Wan, J. H. & Yeo, B. S. Electrochemical reduction of carbon dioxide to ethane using nanostructured Cu_2O-derived copper catalyst and palladium (II) chloride. *The Journal of Physical Chemistry C* **119,** 26875–26882 (2015).

346.   Goodpaster, J. D., Bell, A. T. & Head-Gordon, M. Identification of possible pathways for C–C bond formation during electrochemical reduction of CO_2: new theoretical insights from an improved electrochemical model. *The journal of physical chemistry letters* **7,** 1471–1477 (2016).

347.   Montoya, J. H., Peterson, A. A. & Nørskov, J. K. Insights into C-C Coupling in CO_2 Electroreduction on Copper Electrodes. *ChemCatChem* **5,** 737–742 (2013).

348.   Politano, A., Marino, A. & Chiarello, G. Alkali-promoted stabilization of subsurface oxygen on Cu (1 1 1). *Chemical Physics* **367,** 148–151 (2010).

349.   Huang, H. *et al.* Understanding of strain effects in the electrochemical reduction of CO_2: using Pd nanostructures as an ideal platform. *Angewandte Chemie* **129,** 3648–3652 (2017).

350.   Liu, M. *et al.* Enhanced electrocatalytic CO_2 reduction via field-induced reagent concentration. *Nature* **537,** 382–386 (2016).

351.   Chen, L. D., Urushihara, M., Chan, K. & Nørskov, J. K. Electric field effects in electrochemical CO_2 reduction. *Acs Catalysis* **6,** 7133–7139 (2016).

352.   Grosse, K., Schulz-von der Gathen, V. & von Keudell, A. Nanosecond pulsed discharges in distilled water: I. Continuum radiation and plasma ignition. *Plasma Sources Science and Technology* **29,** 095008 (2020).

353.   Chen, X., McCrum, I. T., Schwarz, K. A., Janik, M. J. & Koper, M. T. Co-adsorption of cations as the cause of the apparent pH dependence of hydrogen adsorption on a stepped platinum single-crystal electrode. *Angewandte Chemie International Edition* **56,** 15025–15029 (2017).

354.   Diaz-Morales, O., Hersbach, T. J., Badan, C., Garcia, A. C. & Koper, M. T. Hydrogen adsorption on nano-structured platinum electrodes. *Faraday discussions* **210,** 301–315 (2018).

355.   Bondue, C. J. & Koper, M. T. A DEMS approach for the direct detection of CO formed during electrochemical CO_2 reduction. *Journal of Electroanalytical Chemistry* **875,** 113842 (2020).

356.   Grosse, K., Breilmann, W., Maszl, C., Benedikt, J. & von Keudell, A. *Time resolved ion energy distribution functions of non-reactive and reactive high power impulse magnetron sputtering of titanium* in *APS Annual Gaseous Electronics Meeting Abstracts* (2016), HT6–069.

357.   Grosse, K., Held, J., Kai, M. & von Keudell, A. Nanosecond plasmas in water: ignition, cavitation and plasma parameters. *Plasma Sources Science and Technology* **28,** 085003 (2019).

358.   Chee, S. W., Anand, U., Bisht, G., Tan, S. F. & Mirsaidov, U. Direct observations of the rotation and translation of anisotropic nanoparticles adsorbed at a liquid–solid interface. *Nano letters* **19,** 2871–2878 (2019).

359. Woehl, T. J. & Prozorov, T. The mechanisms for nanoparticle surface diffusion and chain self-assembly determined from real-time nanoscale kinetics in liquid. *The Journal of Physical Chemistry C* **119,** 21261–21269 (2015).

13 Appendix

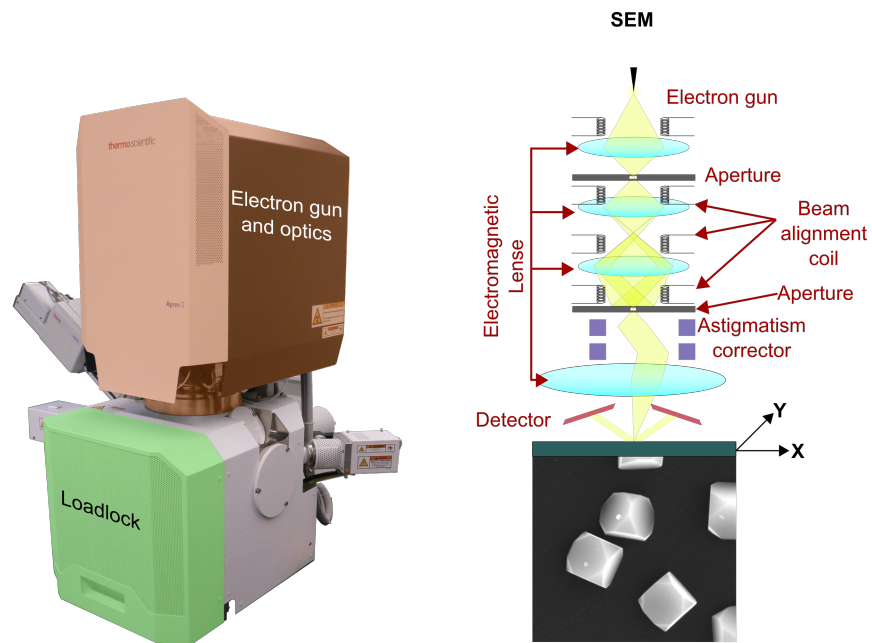## 13.1 List of Tables

List of Tables

13.2   Appendix Chapter 3

Figure 13.1: Left: Image showing a typical SEM (here APREO S from Thermo scientific) that was used in most of the measurements in this work. The electron gun and electron optics are placed in the top compartment. The sample is located below and can be accessed via the loadlock. Right: Schematic of the SEM electron optics that are in the top part.
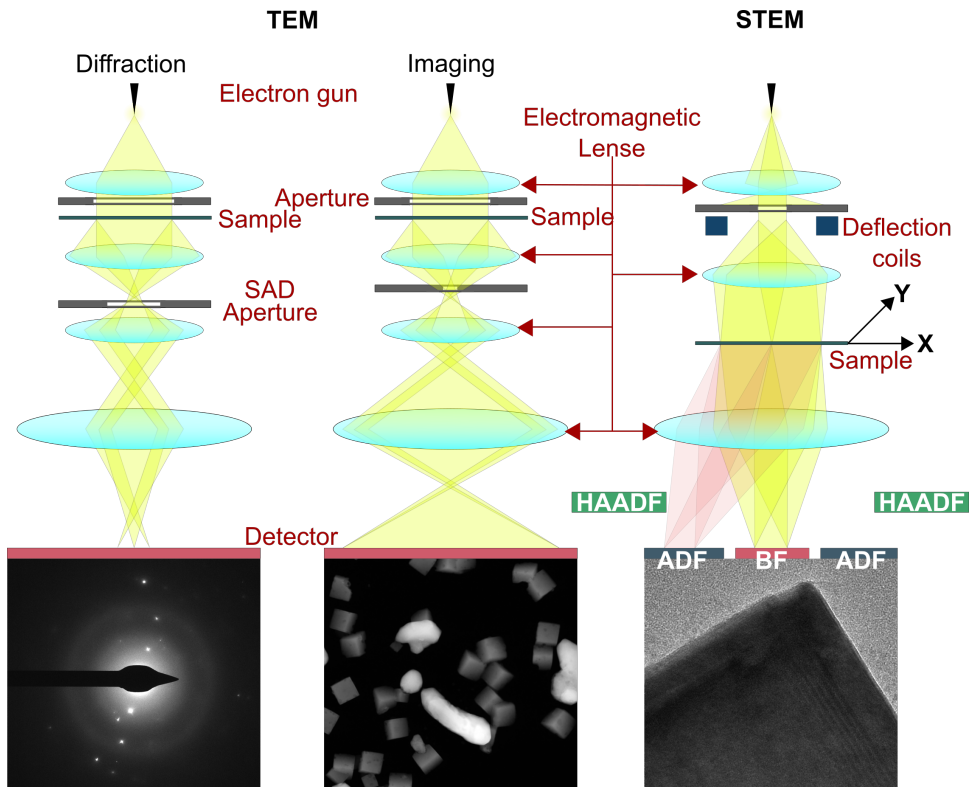
Figure 13.2: Left and middle: schematic of the two different TEM modes selected area diffraction with inserted SAD aperture and DF/BF imaging. Right: schematic of STEM mode with HAADF, angular dark filed (ADF), and bright field detector.

13.3 Appendix Chapter 4
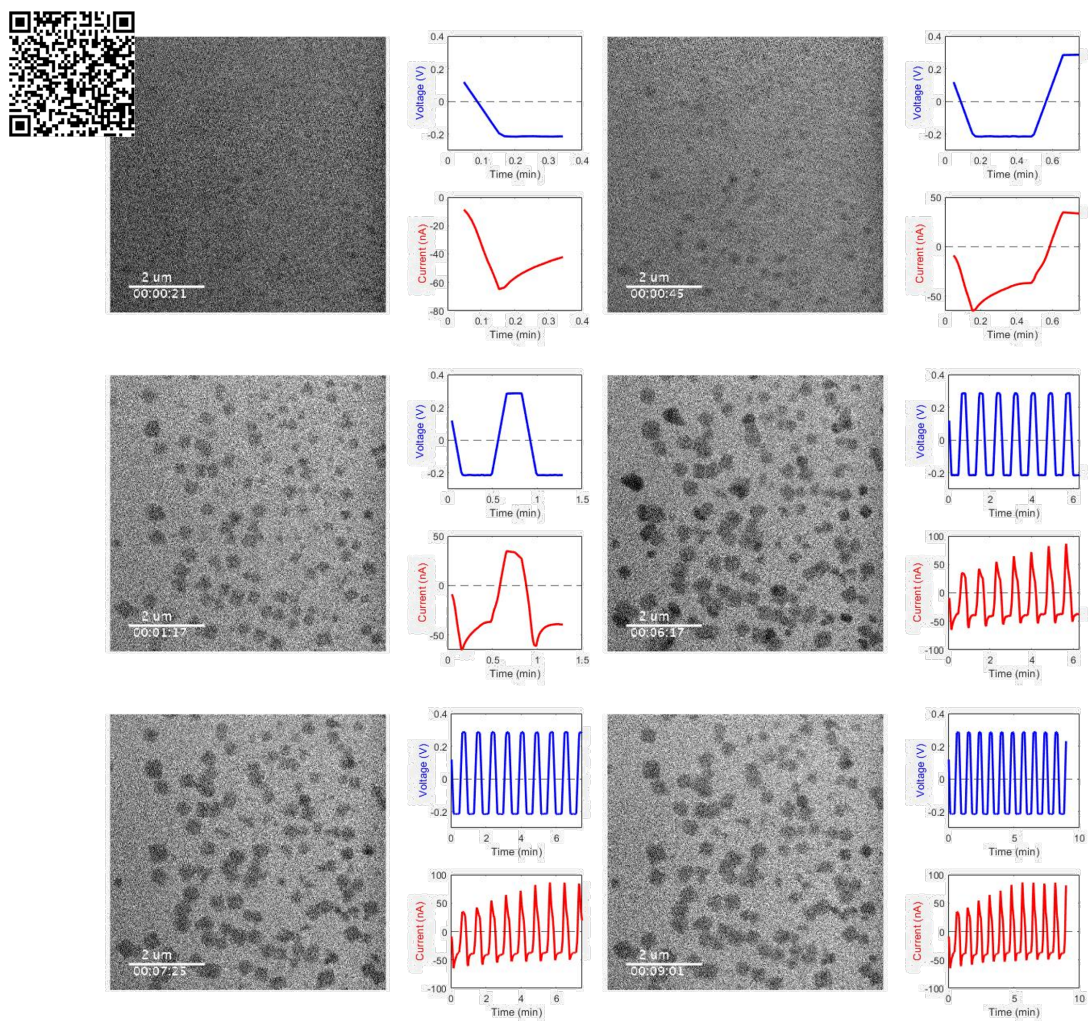
Figure 13.3: *Operando* liquid phase electron microscopy video of Cu cube electrodeposition synchronized with the voltage and current plot over time. The QR code on the top left corner provides the link to download the movie.
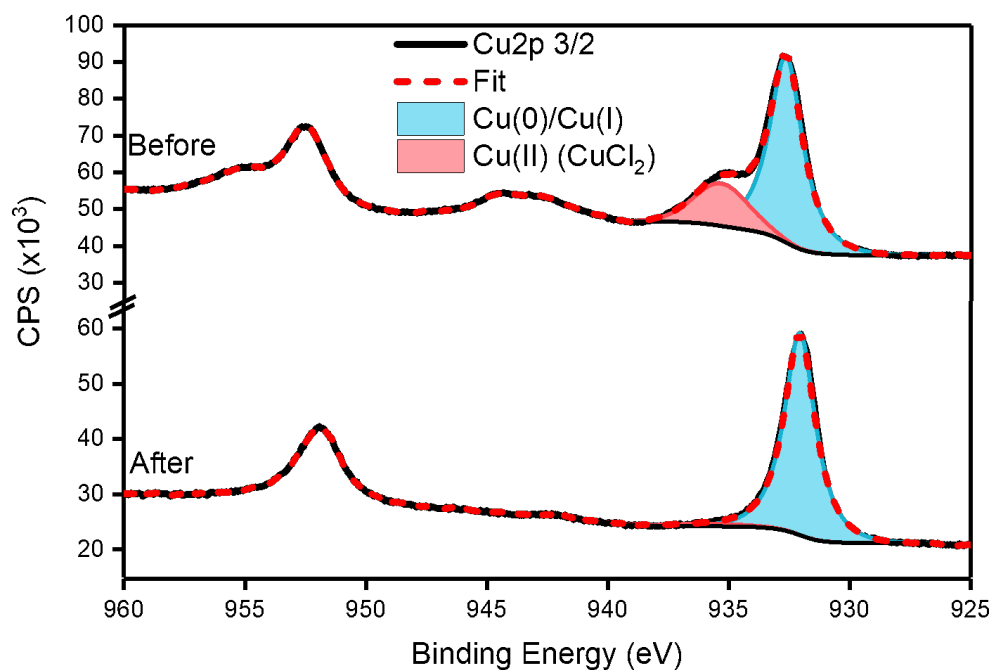
Figure 13.4: Quasi *in situ* XPS Cu-2p core level spectra from a pristine Cu nanocube sample and the same sample measured after 1 h CO$_2$RR at −1.1 V vs RHE, fitted with two doublets corresponding to Cu(0)/Cu(I) species (indistinguishable) and Cu(II). Satellite oxide features were also considered in the fits for the Cu(II) species.
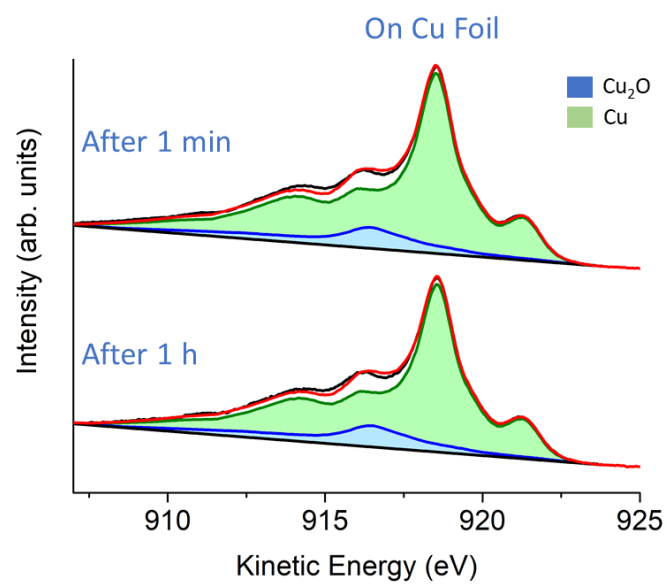
Figure 13.5: Cu AES LMM spectra of 250 nm Cu-Cubes on a Cu foil measured quasi *in situ* after 1 minute and 1 hour of CO_2RR at -1.0 V vs RHE.

13.5 Appendix Chapter 6
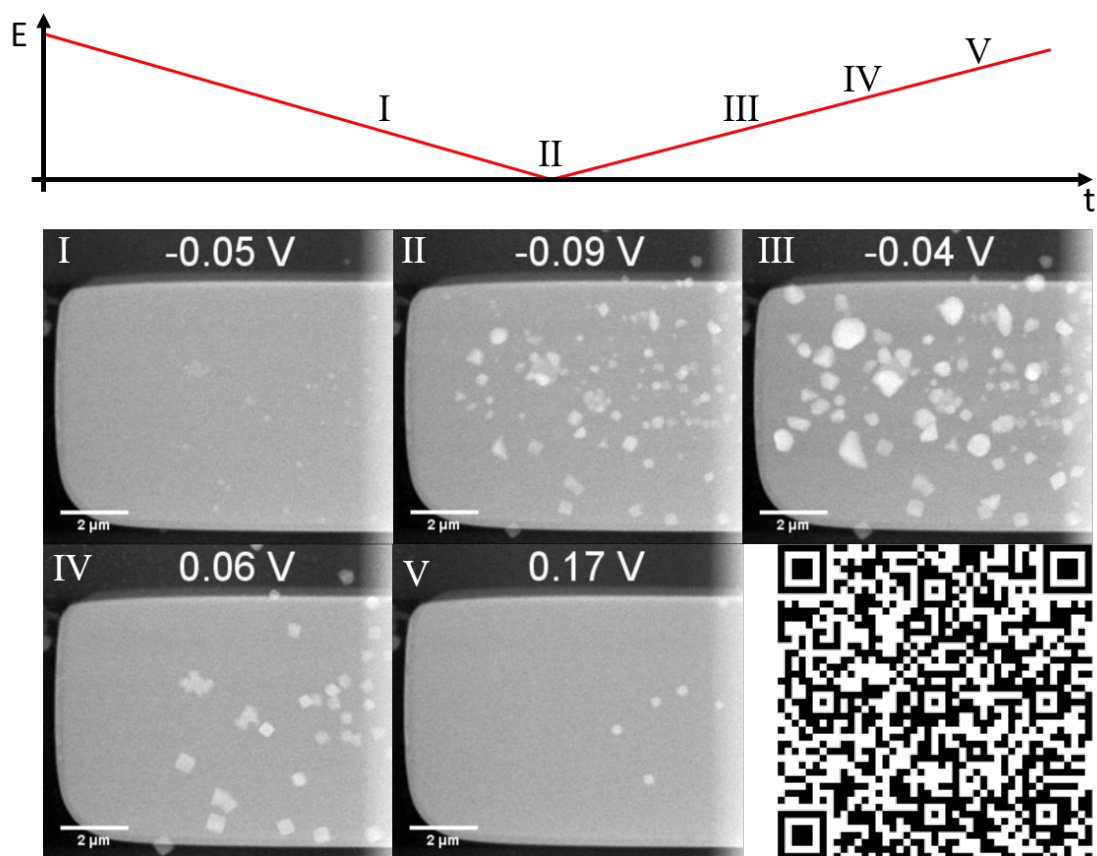
Figure 13.6: **Video of a LSV on the electrode.** The video shows a single cycle of the synthesis protocol where the potential is sweeped from $0.20\,V$ to $-0.10\,V$ vs. ref. and back at $5\,mV\,s^{-1}$. The cubic structures have a higher stability and dissolve later than the amorphous Cu structures. The QR code on the right bottom corner provides the movie download link.
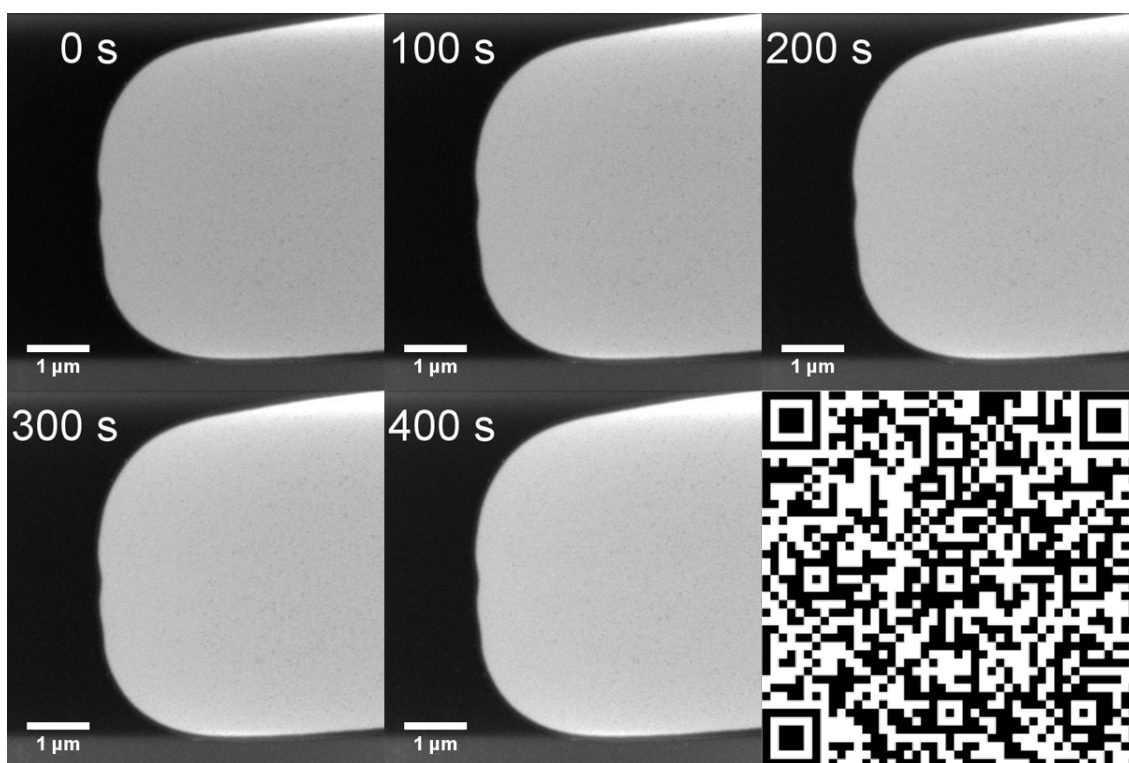
Figure 13.7: **Video of the electrode under OCP** at typical imaging magnification. The QR code at the bottom right provides the movie download link.
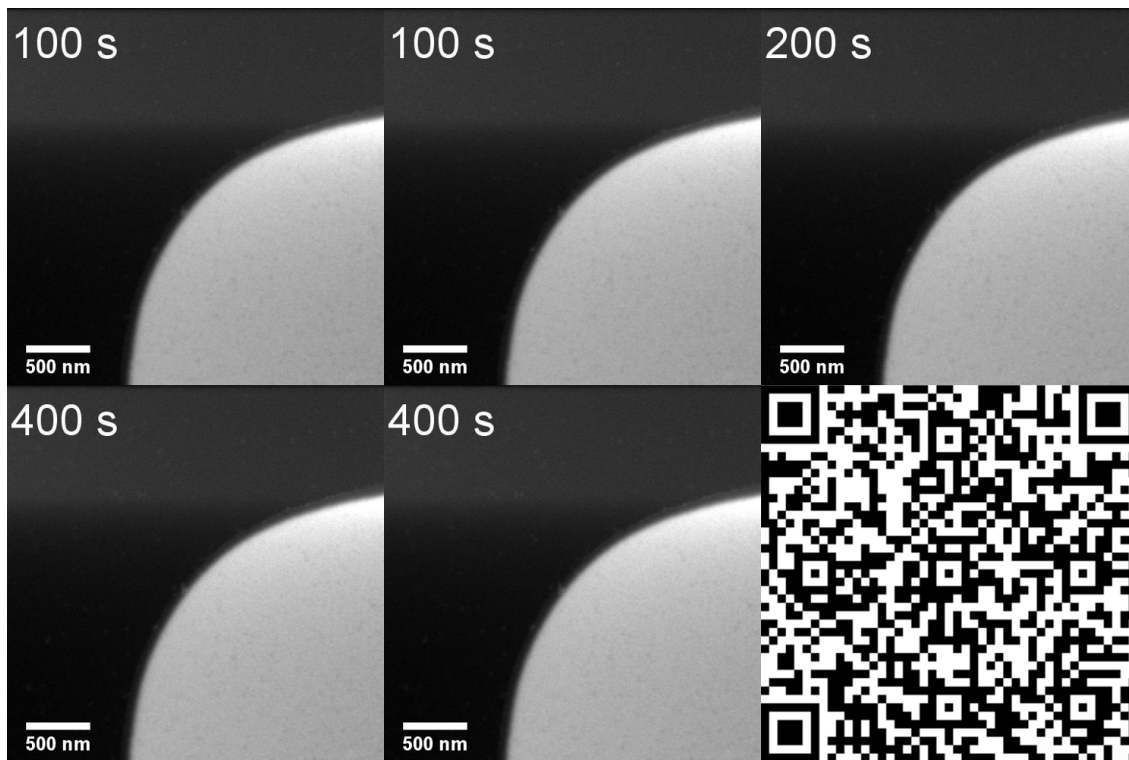
Figure 13.8: **Video of the electrode under OCP** at higher imaging magnification. The QR code at the bottom right provides the movie download link.
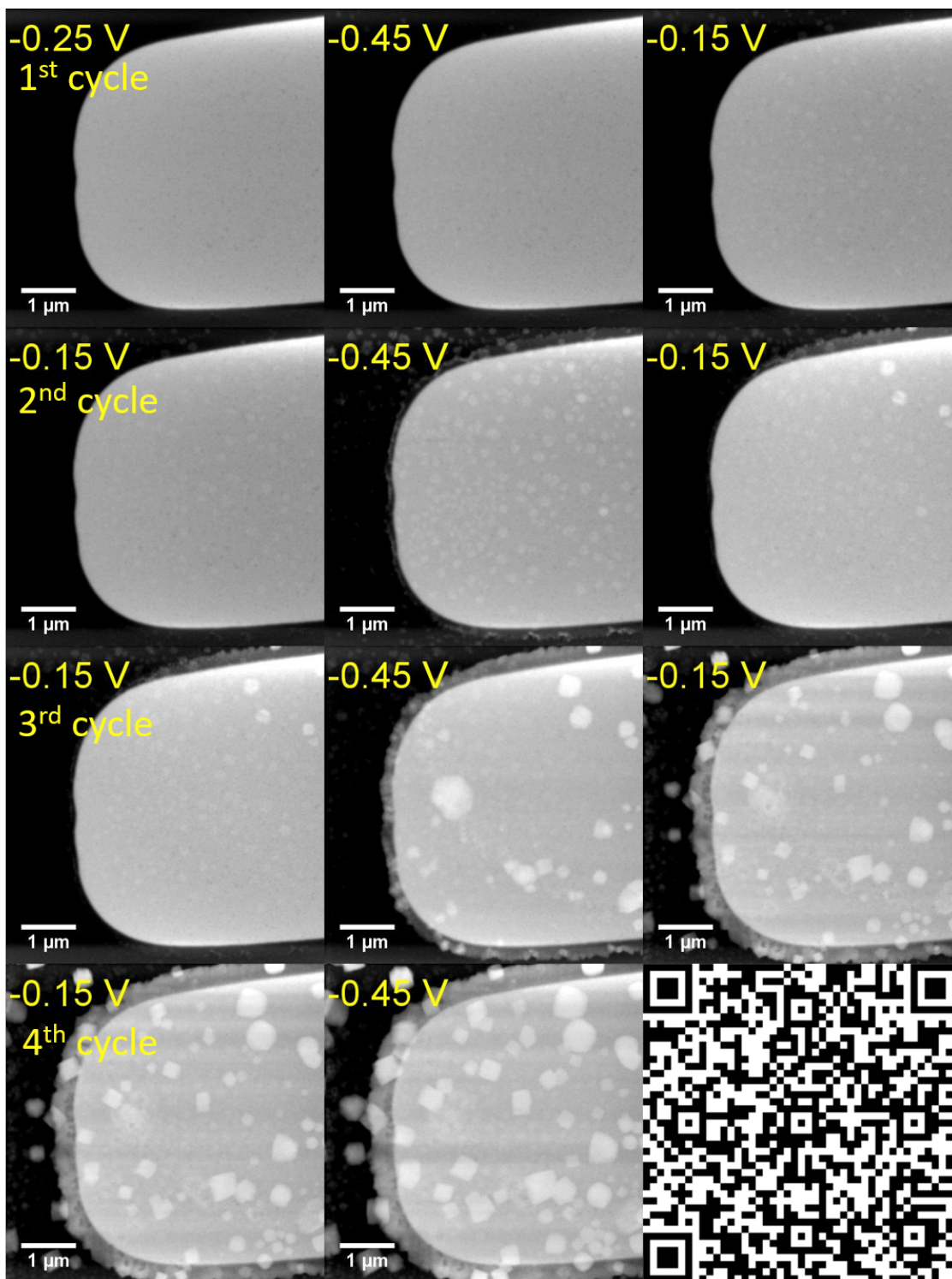
Figure 13.9: **Movie frames showing a Pt electrode** electrochemically cycled at a potential (−0.10 V) where the particles did not fully dissolve from the working electrode. The QR code at the bottom right provides the movie download link.
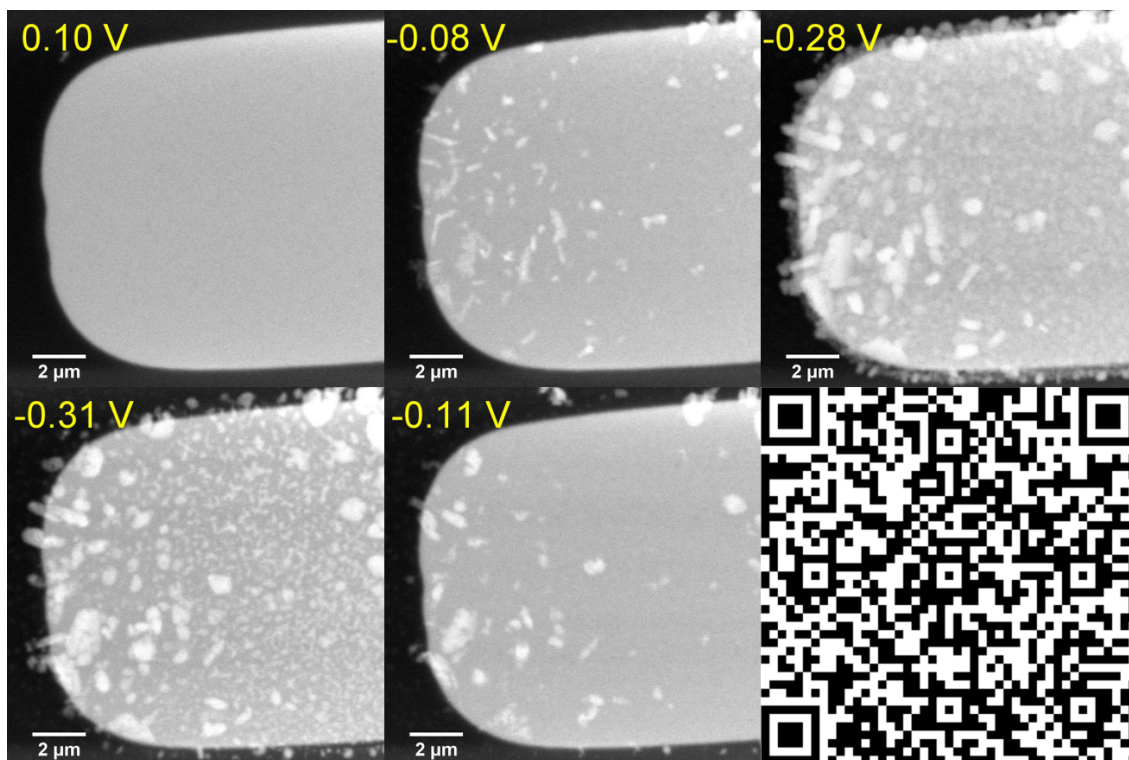
Figure 13.10: **Movie depicting the growth and dissolution of particles** using a 5 mM $CuSO_4$ solution with no KCl added. The QR code at the bottom right provides the movie download link.
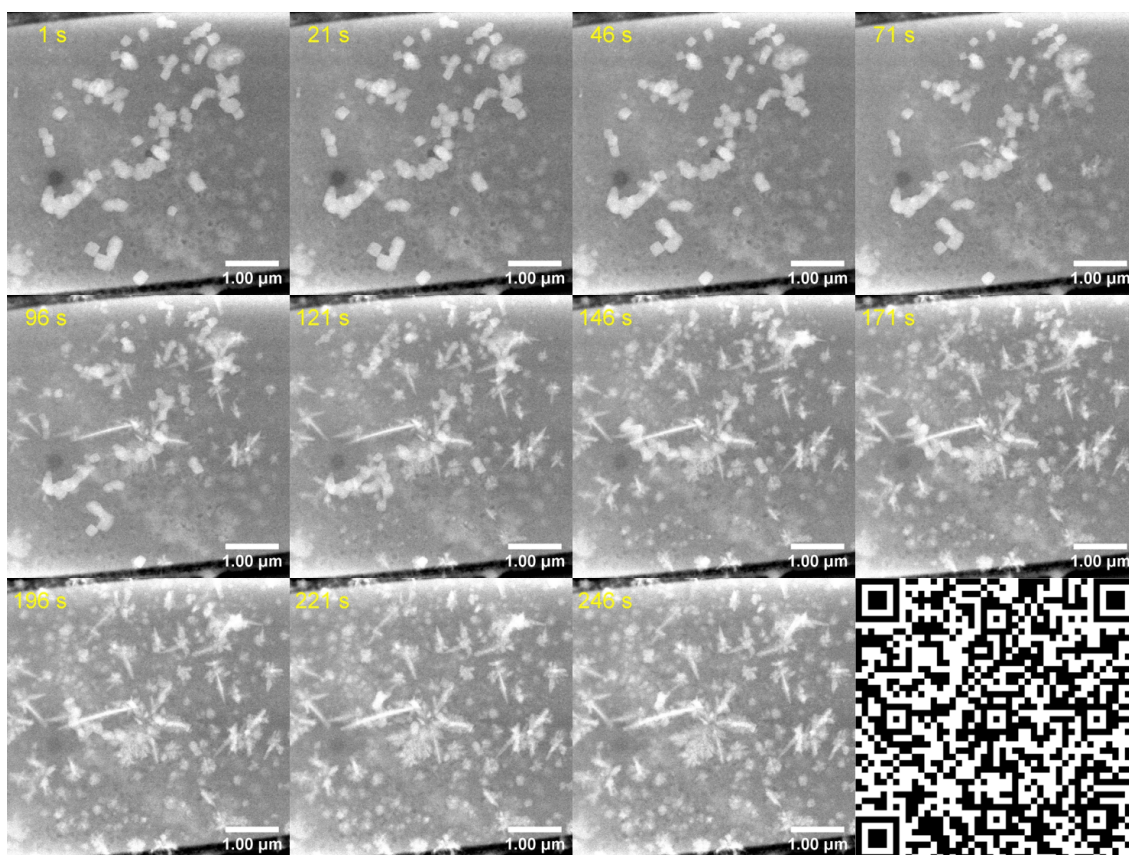
Figure 13.11: **Cu cubes on Pt electrode** at $-0.7\,V_{Pt}$. The QR code provides the movie download link.

13.6   Appendix Chapter 7

The following section shows the effects of radiolysis on samples from chapter 7, where we measured Cu cubes on a carbon support *in situ* with liquid phase EC-TEM.

"Electron beam-related effects are always a concern for liquid cell TEM experiments and so, we have adopted a low electron dose imaging protocol to minimize these artifacts. In our previous work,[313] we determined the electron flux limits for observing noticeable beam-induced effects in our TEM and we stayed under those limits in the current experiments. Appendix Figure 13.12 further compares the after-reaction morphologies observed in the imaged area with those observed in areas that were not imaged and therefore not exposed to the electron beam. The cubes located in the two areas do not exhibit significant differences in morphology, indicating that the extended imaging did not significantly alter the cubes. Hence, we can conclude that we were able to avoid significant electron beam-induced artifacts with our low electron dose protocol, even with extended imaging times of about an hour.
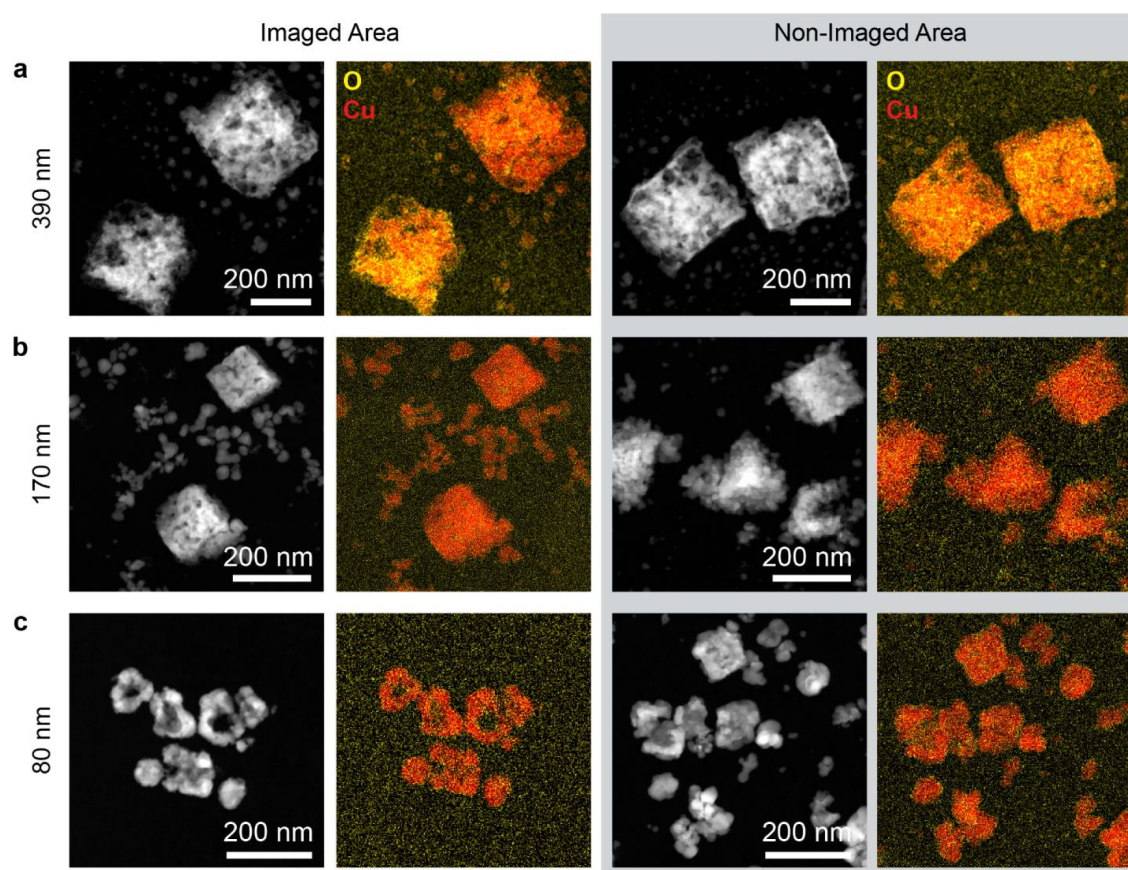

Figure 13.12: **Ex situ STEM-EDX images of areas imaged by the electron beam and those that are not.** The pairs of STEM images and EDX maps compares Cu_2O cubes found on the area of the working electrode that was imaged during the *in situ* experiment and cubes found on areas that were not imaged. Images of each set are at the same magnification.

There appears, however, to be subtle effects caused by the extended electron beam exposure, since there seems to be more secondary NPs in the imaged area as compared to non-imaged areas. It is known that the electron beam, even at low fluxes, can cause NPs to be more mobile,[358,359] which can lead to faster aggregation dynamics[359]. Nevertheless, this effect does not affect the conclusions of our work. The motion and aggregation of these secondary NPs are also consistent with the behavior found in our *ex situ* SEM experiments described in [...] subsection 7.2.7."[205]
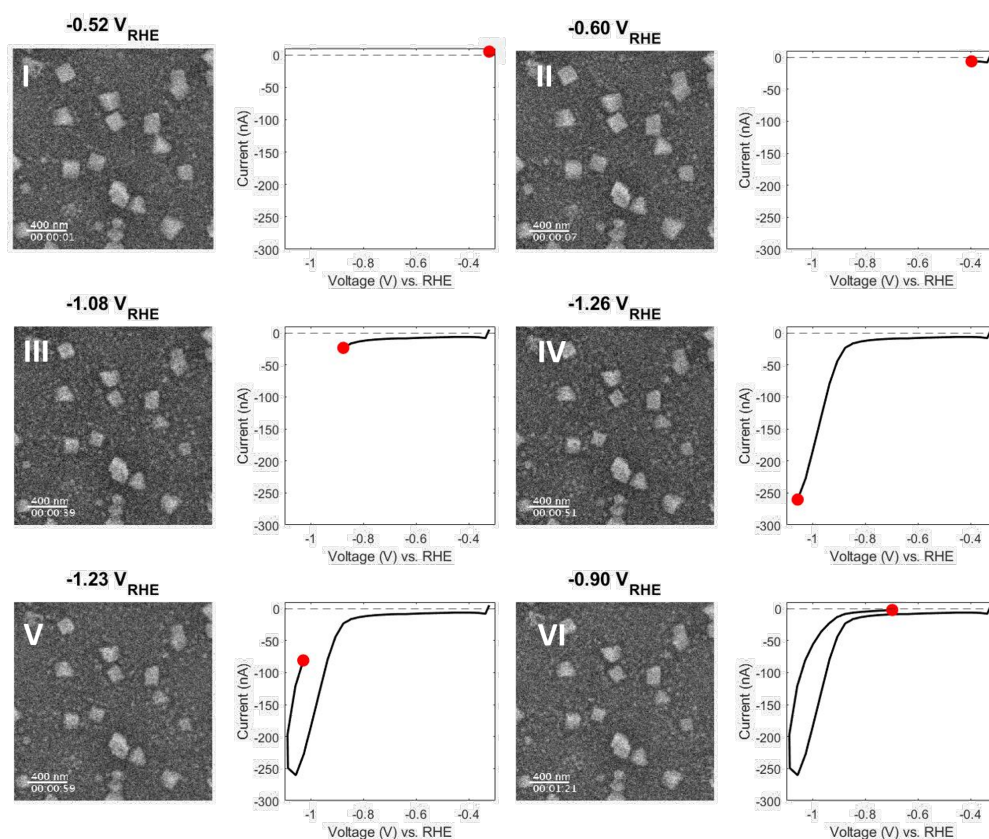
Figure 13.13: EC-TEM movie describing the structural changes in the Cu cubes during the linear sweep voltammetry from -0.3 to -1.0 V_{RHE}. The plot on the right shows the electrochemical response as a function of the applied potential. The image sequence was first drift-corrected and then, two frames were averaged to create one frame of the movie. The movie playback rate is x40 times real time.
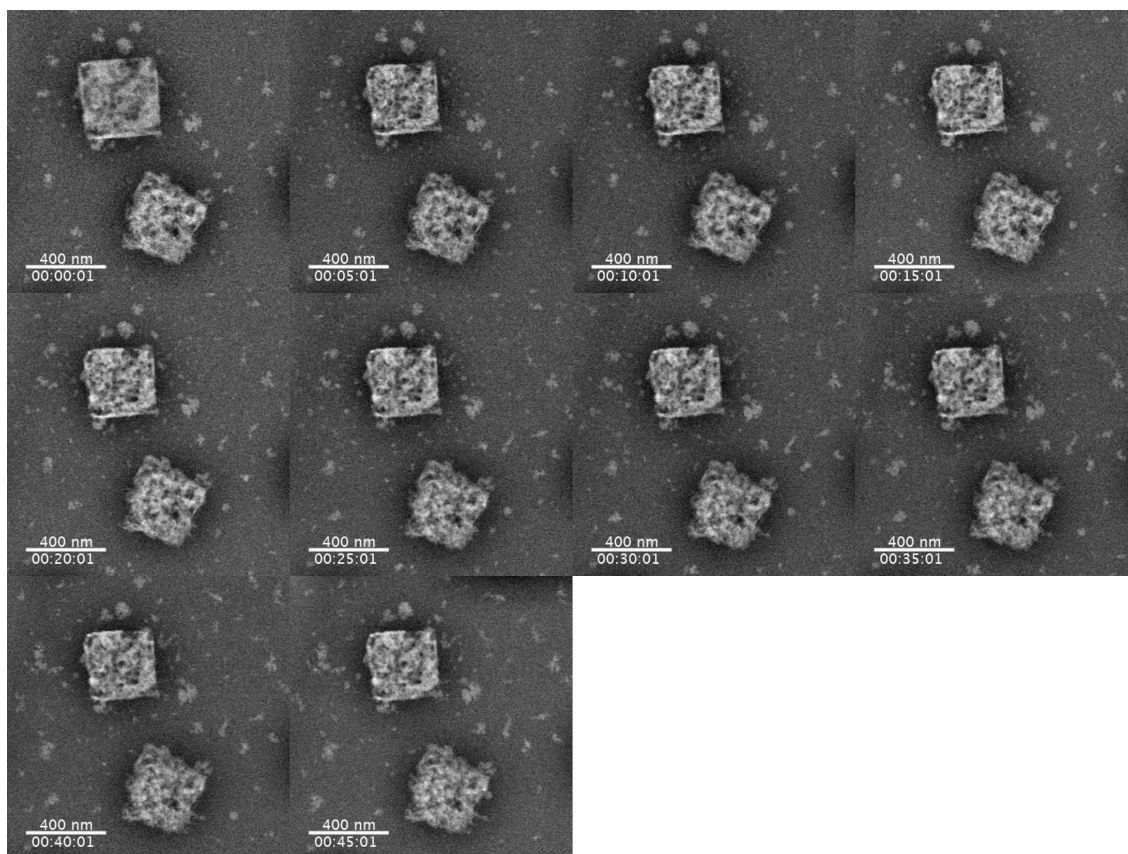
Figure 13.14: Image sequence extracted from an EC-TEM movie describing the structural changes in the 390 nm Cu cubes during 1 h of chronoamperometry at -0.9 V_{RHE} in 0.1 M KHCO$_3$. The recording rate of the movie was 1 frame per second. 5 frames were averaged to create one frame of the movie. The movie playback rate is x100 times real time.
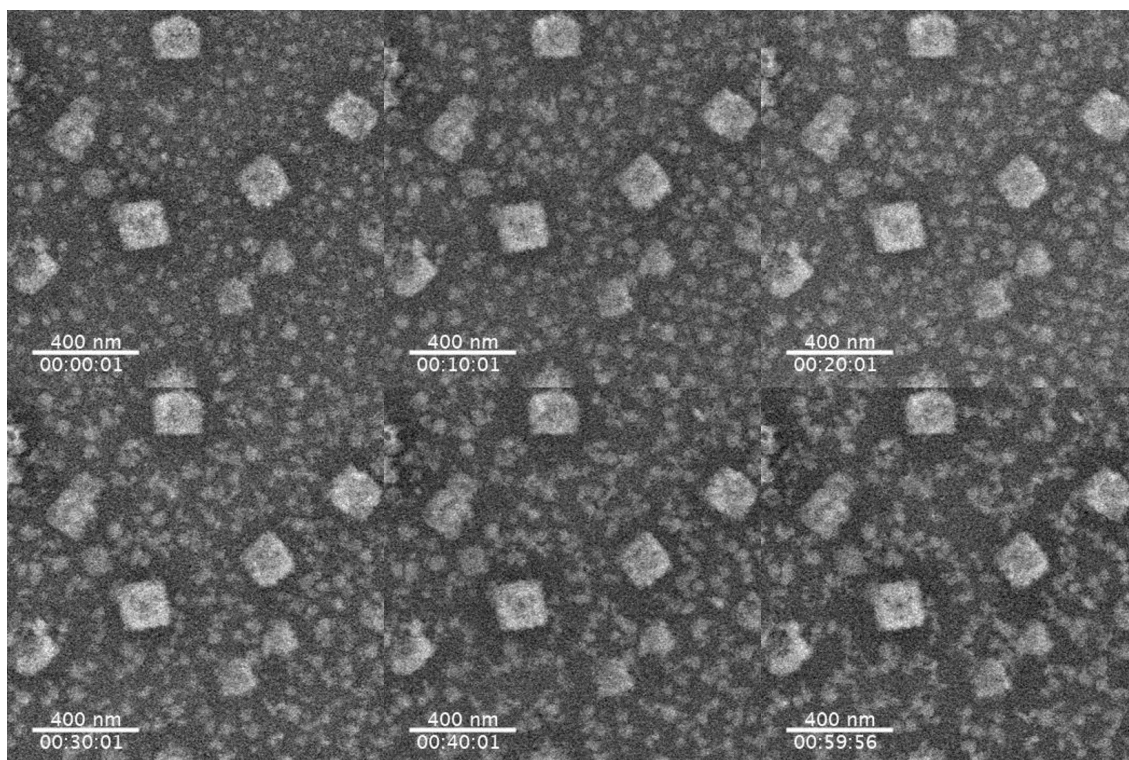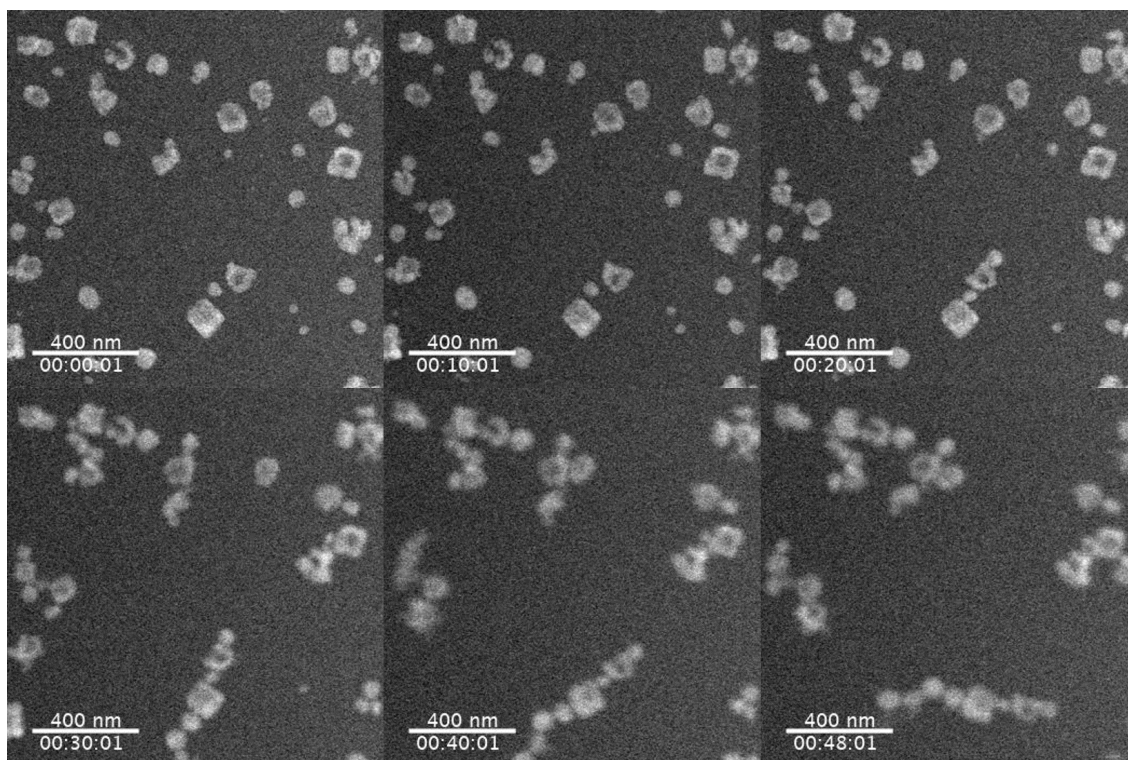
Figure 13.15: Image sequence extracted from an EC-TEM movie describing the structural changes in the 170 nm Cu cubes during 1 h of chronoamperometry at -0.9 V_{RHE} in 0.1 M $KHCO_3$. The recording rate of the movie was 1 frame per second. 5 frames were averaged to create one frame of the movie. The movie playback rate is x100 times real time.

Figure 13.16: Image sequence extracted from an EC-TEM movie describing the structural changes in the 80 nm Cu cubes during 50 min of chronoamperometry at -0.9 V_{RHE} in 0.1 M KHCO$_3$ from an area that has mostly cubes. The recording rate of the movie was 1 frame per second. 5 frames were averaged to create one frame of the movie. The movie playback rate is x100 times real time.
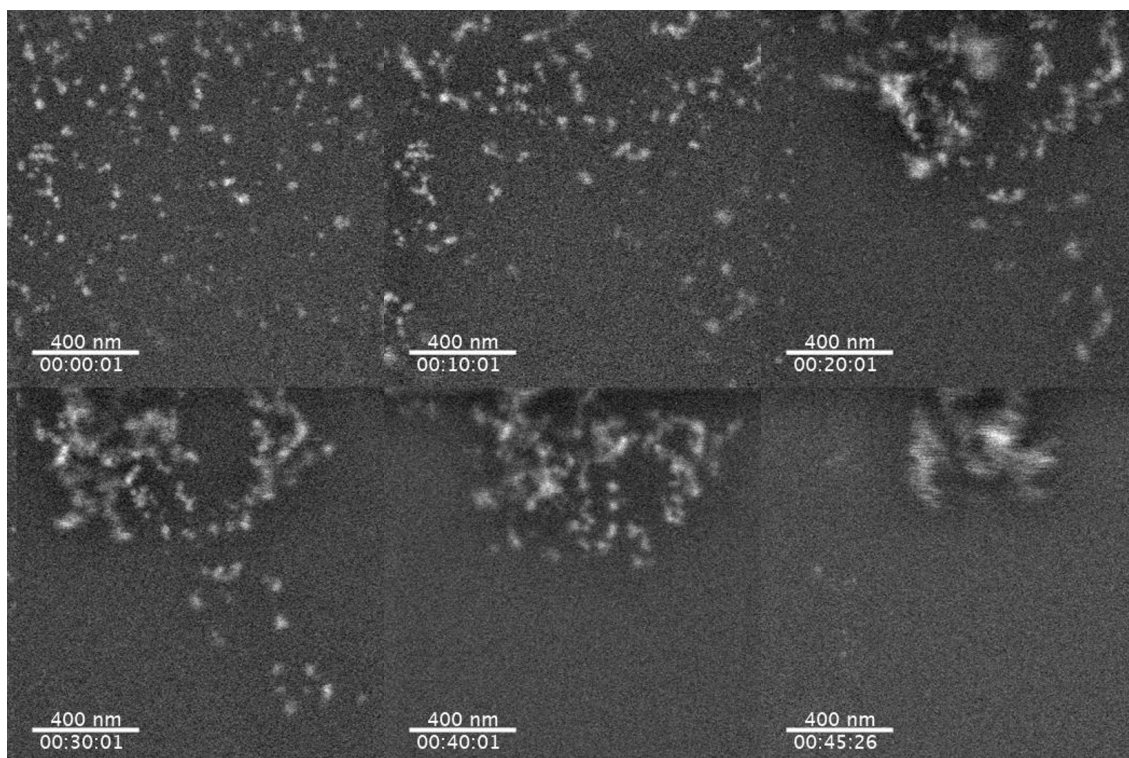
Figure 13.17: Image sequence extracted from an EC-TEM movie describing the structural changes in the 80 nm Cu cubes during 45 min of chronoamperometry at -0.9 V_{RHE} in 0.1 M KHCO$_3$ from an area that has mostly partial cube fragments and re-deposited NPs. The recording rate of the movie was 1 frame per second. 5 frames were averaged to create one frame of the movie. The movie playback rate is x100 times real time.
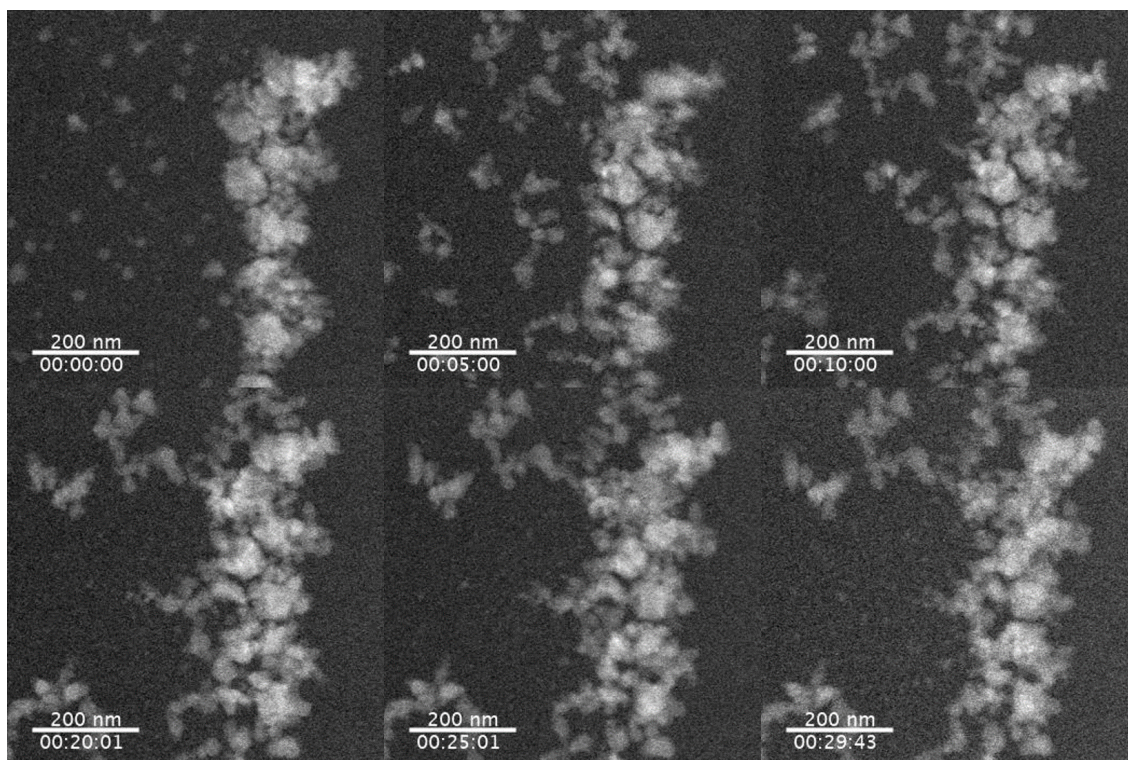
Figure 13.18: Image sequence extracted from an EC-TEM Movie describing the structural changes in the 30 nm Cu cubes synthesized by colloidal chemistry during 30 min of chronoamperometry at -0.9 V_{RHE} in 0.1 M KHCO$_3$. The recording rate of the movie was 1 frame per second. 5 frames were averaged to create one frame of the movie. The movie playback rate is x100 times real time.